Schweizerische Eidgenossenschaft
Confédération suisse
Confederazione Svizzera
Confederaziun svizra

Eidgenössisches Departement für Umwelt, Verkehr, Energie und Kommunikation UVEK
Département fédéral de l'environnement, des transports, de l'énergie et de la communication DETEC
Dipartimento federale dell'ambiente, dei trasporti, dell'energia e delle comunicazioni DATEC

Bundesamt für Strassen
Office fédéral des routes
Ufficio federale delle Strade

Tunnel face stability and tunnelling induced settlements under transient conditions

Ortsbruststabilität und Oberflächensetzungen infolge Tunnelvortrieb unter transienten Bedingungen

Estimation de la stabilité du front de taille et des tassements en surface induits par le creusement du tunnel en conditions transitoires

ETH Zürich, Professur für Untertagbau
Prof. Dr. G. Anagnostou
Dr. R. Schuerch
Dr. P. Perazzelli
Dr. A. Vrakas
MSc ETH Civ Eng P. Maspoli
MSc ETH Civ Eng R. Poggiati

Forschungsprojekt FGU 2012/002 auf Antrag der Arbeitsgruppe Tunnelforschung (AGT)

December 2016 **1592**

Schweizerische Eidgenossenschaft
Confédération suisse
Confederazione Svizzera
Confederaziun svizra

Eidgenössisches Departement für Umwelt, Verkehr, Energie und Kommunikation UVEK
Département fédéral de l'environnement, des transports, de l'énergie et de la communication DETEC
Dipartimento federale dell'ambiente, dei trasporti, dell'energia e delle comunicazioni DATEC

Bundesamt für Strassen
Office fédéral des routes
Ufficio federale delle Strade

Tunnel face stability and tunnelling induced settlements under transient conditions

Ortsbruststabilität und Oberflächensetzungen infolge Tunnelvortrieb unter transienten Bedingungen

Estimation de la stabilité du front de taille et des tassements en surface induits par le creusement du tunnel en conditions transitoires

ETH Zürich, Professur für Untertagbau
Prof. Dr. G. Anagnostou
Dr. R. Schuerch
Dr. P. Perazzelli
Dr. A. Vrakas
MSc ETH Civ Eng P. Maspoli
MSc ETH Civ Eng R. Poggiati

Forschungsprojekt FGU 2012/002 auf Antrag der Arbeitsgruppe Tunnelforschung (AGT)

December 2016 **1592**

Impressum

Forschungsstelle und Projektteam

Projektleitung
Georg Anagnostou

Mitglieder
Roberto Schuerch
Paolo Perazzelli
Apostolos Vrakas
Pietro Maspoli
Raffaele Poggiati

Begleitkommission

Präsident
Felix Amberg

Mitglieder
Prof. Dr. Anton J. Schleiss
Dr. Marco Ramoni
Dr. Alex Schneider
Heinz Dicht
Christian Gammeter

Antragsteller

Arbeitsgruppe Tunnelforschung (AGT)

Bezugsquelle

Das Dokument kann kostenlos von http://www.mobilityplatform.ch heruntergeladen werden.

Inhaltsverzeichnis

Impressum ... **3**
Zusammenfassung ... **7**
Résumé ... **11**
Summary ... **15**

1 Introduction ... **19**
1.1 Problem definition ... 19
1.1.1 On the relevance of transient conditions ... 19
1.1.2 Stand-up time ... 20
1.1.3 Surface settlements ... 22
1.2 Current state of research on the delayed failure ... 25
1.2.1 Numerical studies ... 25
1.2.2 Field tests and physical modelling ... 26
1.3 Current state of research on transient surface settlements ... 27
1.3.1 Numerical studies ... 27
1.3.2 Field observations ... 29
1.4 Structure of the Report ... 29
1.5 Publications ... 31
1.6 Contributions ... 31

2 Manifestations of delayed failure ... **33**
2.1 Introduction ... 33
2.2 Problem setup and computational model ... 34
2.3 Stability under undrained or drained conditions ... 34
2.4 Coupled analysis for dilatant plastic behaviour ... 37
2.4.1 Displacement rate ... 37
2.4.2 Pore pressure, stress and strain development ... 40
2.4.3 Comments on the steady state ... 40
2.4.4 Estimating stand-up time for $\psi > 0$ ... 41
2.5 Coupled analysis for isochoric plastic behaviour ... 41
2.5.1 Displacement rate ... 41
2.5.2 Development of pore pressures, strains and stresses ... 43
2.5.3 Reason of numerical instability ... 45
2.5.4 Estimating stand-up time for $\psi = 0$ ... 45
2.6 Conclusions ... 45

3 Mesh dependency of the stand-up time ... **47**
3.1 Introduction ... 47
3.2 Underwater vertical cut ... 47
3.2.1 Critical strength parameters ... 48
3.2.2 Stand-up time ... 49
3.3 Biaxial problem ... 51
3.3.1 Problem definition ... 51
3.3.2 Analytical solution for the estimation of the stand-up time ... 52
3.3.3 Numerical estimation of the stand-up time ... 53
3.4 Conclusions ... 56

4 Experimental investigation of stand-up time: uniaxial loading tests ... **57**
4.1 Introduction ... 57
4.2 Experimental study ... 57
4.2.1 Material and methods ... 57
4.2.2 Results ... 61
4.3 Numerical study ... 64

4.3.1 Computational model 64
4.3.2 Computational steps 65
4.3.3 MCC model results 65
4.3.4 Test interpretation by MC model....70
4.4 Conclusions 72

5 Experimental investigation of stand-up time: centrifuge tests....73
5.1 Introduction 73
5.2 Centrifuge modelling 75
5.2.1 Material and methods 75
5.2.2 Experimental results 79
5.3 Numerical modelling 83
5.3.1 Computational model 83
5.3.2 Simulation procedure 84
5.3.3 Results 85
5.4 Mesh dependency....92
5.5 Conclusions 94

6 Stand-up time of tunnel face....95
6.1 Introduction 95
6.2 Computational model 95
6.3 Undrained and drained tunnel face stability....97
6.3.1 Numerical investigation....97
6.3.2 Comparison with analytical solutions....100
6.4 Tunnel face stability under transient conditions....100
6.5 On the transient tensile failure of the ground....105
6.6 On some factors influencing stand-up time 108
6.6.1 Cohesion....108
6.6.2 Friction angle 110
6.6.3 *In situ* horizontal effective stress....112
6.6.4 Depth of cover....113
6.7 Design diagrams 115
6.8 Application example....122
6.9 The influence of the support pressure on the stand-up time 123
6.10 Critical advance rate 124
6.11 Conclusions 127

7 Surface settlements under transient conditions 129
7.1 Introduction 129
7.2 Computational models 129
7.2.1 Initial conditions 133
7.3 Dimensional analysis 138
7.3.1 MC model....138
7.3.2 MCC model 138
7.4 Surface settlements for the borderline cases of a very high or a very low permeability .139
7.4.1 MC model....139
7.4.2 MCC model 144
7.5 Surface settlements in medium permeability soils....148
7.5.1 MC model....148
7.5.2 MCC model 158
7.6 Practical estimation of transient settlements 167
7.7 Conclusions 168

Notation.... 169
References.... 173
Projektabschluss 177
Verzeichnis der Berichte der Forschung im Strassenwesen.... 181

Zusammenfassung

Wichtige Voraussetzungen eines erfolgreichen Tunnelvortriebs im überbebauten Gebiet sind die Gewährleistung der Ortsbruststabilität und die Beschränkung der Geländesetzungen. Eine Instabilität der Ortsbrust ist das folgenreichste Gefährdungsbild. Bei geringer Überlagerung kann sich die Instabilität bis zur Geländeoberfläche fortpflanzen und so zu einem Tagbruch führen. Unzulässige Setzungen an der Oberfläche können auch ohne Tagbruch auftreten. Sie entstehen aufgrund der Verformbarkeit des Baugrundes in Kombination mit den vortriebsbedingten Spannungsumlagerungen oder, in wasserführendem Baugrund, einer drainagebedingten Konsolidation.

Oft reagiert der Baugrund verzögert auf den Tunnelvortrieb.. Im wasserführenden Lockergestein ist diese Zeitabhängigkeit auf den Konsolidationsprozess zurückzuführen. Stark durchlässige Böden (z.B. Sand oder Kies) reagieren sofort auf den Vortrieb. Wenig durchlässige Böden (wie Ton) reagieren hingegen sehr langsam. Die Verformungen des Baugrundes sind verknüpft mit Änderungen in Porenvolumen und Wassergehalt, die das Zusickern oder Wegsickern von Porenwasser bedingen. Solche Sickerströmungsvorgänge treten aber – abhängig von der Durchlässigkeit des Bodens – rascher oder langsamer auf. In einem Baugrund geringer Durchlässigkeit bleibt der Wassergehalt kurzfristig praktisch konstant (sogenannt „undrainierte Bedingungen“). Es entstehen kurzfristig Porenwasserüber- oder -unterdrucke, die eine transiente Sickerströmung zum Tunnel hin auslösen. In der Folge werden die Porenwasserüber- oder -unterdrucke abgebaut. Der vollständige Abbau der Porenwasserüber- oder -unterdrucke bzw. der wiedererlangte stabile Zustand des Strömungsfeldes markiert das Ende des Konsolidationsprozesses (sogenannt «drainierte Bedingungen»).

Kiesige Böden mit hoher Durchlässigkeit bzw. praktisch undurchlässige tonige Böden stellen zwei Grenzfälle bezüglich der während des Vortriebs herrschenden Bedingungen dar. Wie oben erwähnt, sind die Bedingungen in diesen zwei Grenzfällen „drainiert“ bzw. „undrainiert“. Allerdings kann der Baugrund eine mittlere Durchlässigkeit aufweisen. Das hat zur Folge, dass der Konsolidationsvorgang mässig schnell abläuft und dass während des Vortriebs Bedingungen herrschen, die zwischen den zwei Extremfällen von drainierten bzw. undrainierten Bedingungen liegen. Das vorliegende Forschungsprojekt befasst sich mit Ortsbruststabilität und Oberflächensetzungen beim Tunnelbau unter solchen „transienten“ oder "teilweise drainierten" Bedingungen. Letztere sind bei Böden mittlerer Durchlässigkeit zu erwarten und somit für Lockergesteine relevant, die im Schweizerischen Mittelland sehr verbreitet sind (z.B. Moränen oder siltige Seeablagerungen).

Das kurzfristige Verhalten dieser Böden („undrainierte Bedingungen“) ist günstiger als das langzeitige Verhalten („drainierte Bedingungen“). Die Ortsbrust kann anfänglich stabil sein und erst nach einer gewissen Zeit instabil werden; die Setzungen nehmen mit der Zeit zu. Instabile Verhältnisse können eine Baugrundverbesserung oder das Aufbringen eines Stützdrucks erfordern (beispielsweise mittels Druckluft oder druckbeaufschlagter Bentonitsuspension). Da derartige Massnahmen kostspielig, zeitaufwändig und baubetrieblich folgenreich sein können, ist die Frage der Standzeit – definiert als die Zeitspanne zwischen Ausbruch und dem Auftreten einer Instabilität – für die Praxis wichtig. Die Standzeit und somit die Möglichkeit eines Verzichts auf Bauhilfsmassnahmen hängt wesentlich von den Festigkeitseigenschaften und der Durchlässigkeit des Baugrunds ab.

Das Verhalten von gering- oder hochdurchlässigen Böden im Bereich der Tunnelortsbrust ist weitestgehend bekannt und kann anhand der beiden Grenzfälle von drainierten oder undrainierten Bedingungen untersucht werden. Hingegen wurde bislang für Böden mittlerer Durchlässigkeit sehr wenig Forschung betrieben und es sind nahezu keine systematischen Untersuchungen vorhanden. Die vereinfachenden Annahmen von entweder drainierten oder undrainierten Bedingungen können im Falle solcher Böden unwirtschaftlich bzw. unsicher sein. Folglich ist es aus Wirtschaftlichkeits- und

Sicherheitsgründen essentiell, das Verhalten von Böden mittlerer Durchlässigkeit unter den im kritischen Ortsbrustbereich herrschenden transienten Bedingungen zu verstehen und zu quantifizieren. Das Forschungsprojekt strebt das Schliessen der in diesem Bereich vorhandenen Wissenslücken an. Die diesbezüglich relevanten Fragestellungen betreffen die Standzeit der Ortsbrust; den Einfluss der Vortriebsgeschwindigkeit auf das Endmass und die zeitliche Entwicklung der Oberflächensetzungen; und die bzgl. Ortsbruststabilität kritische Vortriebsgeschwindigkeit.

Das Hauptziel dieses Projekts war die Ausarbeitung von Empfehlungen und vereinfachten Berechnungsverfahren zur Beurteilung der Ortsbruststabilität und die Abschätzung der Oberflächensetzungen unter transienten Bedingungen. Während der Umsetzung des Projektes sind aber fundamentale Fragen über die grundlegenden physikalischen Mechanismen aufgetreten, deren Beantwortung vertiefte theoretische und experimentelle Untersuchungen erfordert hat. Letztere betrafen das Phänomen des verzögerten Bruchs und die Wechselwirkung zwischen der ausbruchbedingten Erzeugung von Porenwasserüberdrucken und der nahezu gleichzeitig ablaufenden Dissipation derselben.

Voruntersuchungen, die unter gängigen Annahmen über das mechanische Baugrundverhalten durchgeführt wurden, haben gezeigt, dass numerische Simulationen das Phänomen des verzögerten Bruchs nicht immer reproduzieren können und zudem ihre Prognosen von der räumlichen Diskretisierung des numerischen Lösungsverfahrens abhängig sind (je feiner das Netz, desto kürzer die Standzeit). Diese vorläufigen Ergebnisse warfen die Frage auf, ob es überhaupt möglich ist, die Standzeit zu prognostizieren. In einer ersten Phase mussten deshalb die Gründe für das ungenügende Modellverhalten untersucht und das Problem der Netzabhängigkeit der numerischen Resultate behoben werden. Diese Untersuchungen haben aufgezeigt, dass die Annahme der plastischen Dilatanz ausschlaggebend ist, um eine verzögerte Instabilität zu reproduzieren. Unter der in der Praxis oftmals getroffenen, jedoch bekanntlich vereinfachenden Annahme eines konstanten Dilatanzwinkels, führen die gekoppelten Analysen unvermeidlich zu einer konstanten Verformungsrate beim Versagen (während Versagen üblicherweise mit beschleunigenden Verschiebungen assoziiert wird). Realistischere Stoffgesetze, welche die experimentelle Beobachtung berücksichtigen, dass die Scherdeformationen im Grenzzustand volumentreu erfolgen, führen zu beschleunigenden Verschiebungen beim Versagen und erlauben somit die Ermittlung der Standzeit. Solche Modelle weisen jedoch nahe dem Versagenszustand inhärenterweise numerische Stabilitätsprobleme auf, da keine Lösung existiert, welche die zugrundeliegenden kontinuumsmechanischen Gleichungen erfüllt. Aufgrund dieser numerischen Probleme erfordert die Ermittlung der Standzeit eine Auswertung der Gesamtheit der numerischen Resultate.

Auf der Grundlage analytischer Herleitungen konnte nachgewiesen werden, dass die erwähnte Netzabhängigkeit der Standzeit hauptsächlich auf die sogenannte strukturelle Entfestigung zurückzuführen ist, die selbst in einem idealplastischen Material auftritt, wenn das Fliessgesetz nichtassoziiert ist. In numerischen Simulationen lokalisieren sich die Verformungen in einer Scherfuge mit einer Stärke von 1–2 finiten Elementen. Je gröber das Netz, umso breiter ist die numerisch prognostizierte Scherfuge, umso geringer sind die Scherverformungen, umso weniger ausgeprägt ist die strukturelle Entfestigung und umso höher ist die prognostizierte Standzeit. Bei sehr groben Netzen bleibt die strukturelle Entfestigung praktisch aus und die Standzeit tendiert zu einer oberen Grenze. Umgekehrt erlauben sehr feine Netze eine beträchtliche strukturelle Entfestigung bis hin zu Werten, die reinem plastischem Abscheren entsprechen und die Standzeit tendiert zu einer unteren Grenze. Diese zwei Grenzen der Standzeit lassen sich bei relativ einfachen Problemstellungen analytisch bestimmen. Die numerischen Simulationen zeigen, dass bei einer hinreichend feinen räumlichen Diskretisierung die Standzeit in einer nahezu linearen Abhängigkeit zur Elementgrösse steht. Diese Erkenntnis ist wertvoll, denn sie ermöglicht eine Bestimmung der Standzeit durch Berechnungen mit relativ feinen Netzen und Extrapolation der erzielten Ergebnisse auf die Netzgrösse, die der erwarteten korngrössenabhängigen Stärke der Scherfuge entspricht (praktisch null im Hinblick auf die Dimensionen typischer geotechnischer Systeme).

Diese theoretischen Untersuchungen haben gezeigt, dass es zumindest qualitativ möglich ist, das Phänomen des verzögerten Versagens zu reproduzieren und die Standzeit von *numerischen Modellen* zu ermitteln. Jedoch war es fraglich, ob die Modellprognosen auch quantitativ ausreichend genau waren. Demzufolge war es erforderlich, physikalische Versuche durchzuführen, die es erlauben, die Entwicklung der Instabilität an einfachen geotechnischen Systemen unter kontrollierten Bedingungen zu beobachten und die Standzeit mit den numerischen Prognosen zu vergleichen. Die experimentellen Untersuchungen beinhalteten einerseits einachsige Druckversuche andererseits Zentrifugenversuche. Die Versuchsergebnisse wurden numerisch interpretiert, wobei Materialkonstanten angenommen wurden, welche unabhängig experimentell bestimmt wurden (sogenannte „A Klasse" Modell-Validierung). Es wurde festgestellt, dass die einfachen jedoch häufig verwendeten linear-elastischen, vollkommen plastischen Modelle mit Mohr-Coulomb-Fliessflächenbedingungen (MC-Modell) im allgemeinen einen zu geringen Wert für die Standzeit ergeben. Auf der anderen Seite überschätzt das Modified Cam Clay-Modell (MCC) die Standzeit, wenn es in Verbindung mit rechnerisch zu bewältigender räumlicher Diskretisierung eingesetzt wird (d.h. zwar engmaschig, aber noch nicht in dem Masse, wie es aufgrund der experimentell beobachteten sehr dünnen Scherbänder erforderlich wäre). Es liefert jedoch Standzeiten, die den beobachteten Zeiten sehr nahe kommen, wenn die numerischen Ergebnisse auf die Grösse der Scherfuge extrapoliert werden, wodurch ausreichend genaue Prognosen erzielt werden können.

Diese fundamentalen Erkenntnisse ermöglichten es, mit dem ersten Hauptthema des Forschungsprojekts, der Zeitabhängigkeit der Ortsbruststabilität, voranzugehen. Die Untersuchungen wurden aus nachfolgenden Gründen unter Annahme des MC-Modells durchgeführt: Es ist weitverbreitet in der Praxis, man ist mit den hierfür benötigten Parametern vertraut, und – wie oben bereits erwähnt – liefert es (in Kombination mit einer feinen, jedoch immer noch beherrschbaren räumlichen Diskretisierung) eine konservative Schätzung der Standzeit. Im Rahmen des Forschungsprojektes hat man die Auswirkungen der einzelnen geotechnischen Parameter (Kohäsion, Reibungswinkel, Durchlässigkeit, Überlagerung etc.) systematisch untersucht, eine umfassende Parameterstudie durchgeführt, die eine grosse Bandbreite an geotechnischen Bedingungen abdeckt, und dimensionslose Bemessungsdiagramme erstellt. Letztere ermöglichen eine Abschätzung der Standzeit von oberflächennahen Tunnels unter gegebenen geotechnischen Bedingungen und stellen folglich eine nützliche Entscheidungshilfe für die Planung und die Durchführung von Tunnelvortrieben im Lockergestein dar.

Die ermittelten Standzeiten können ebenfalls für eine vereinfachte Beurteilung der Ortsbruststabilität beim laufenden Tunnelvortrieb verwendet werden. Wie im Bericht gezeigt wird, kann die kritische Vortriebsgeschwindigkeit dem Verhältnis von Tunneldurchmesser über die Standzeit gleichgesetzt werden.

Das zweite Hauptthema des Forschungsprojektes, die transienten Oberflächensetzungen betreffend, wurde durch eine Serie von hydraulisch-mechanisch gekoppelten numerischen 3D Berechnungen untersucht. Letztere bestätigten die Hypothese, dass die Vortriebsgeschwindigkeit *v*, die Dauer der Stillstände und die Drainagebedingungen an der Tunnellaibung und an der Ortsbrust für die ausbruchbedingten Setzungen in Lockergesteinen mittlerer Durchlässigkeit wichtig sind.

Sickerströmungen in Richtung einer durchlässigen Verkleidung führen eine langfristige Porenwasserdruckverteilung rund um den Tunnel herbei, die sich signifikant von der ursprünglichen, hydrostatischen Druckverteilung unterscheidet. Sickerströmungen und eine Entspannung von Porenwasserüberdruck führen zu wesentlich höheren Oberflächensetzungen, besonders bei hohen initialen Porenwasserdrucken und müssen vermieden werden, obwohl dies eine höhere Belastung der Verkleidung bedingt. Vergleichende Berechnungen zeigen, dass Setzungen, die bei einem Vortrieb unter voller Kompensation des hydrostatischen Drucks entstehen, um eine Grössenordnung kleiner sein können als diejenigen, die unter atmosphärischem Druck entstehen. Die Kompensation des hydrostatischen Drucks könnte folglich für eine Begrenzung der

Oberflächensetzungen unabdingbar sein, selbst wenn der Scherwiderstand des Baugrunds für die Ortsbruststabilität ausreichen würde.

Die Oberflächensetzungen hängen stark davon ab, ob die Bedingungen in der Umgebung der Ortsbrust drainiert, undrainiert oder teilweise drainiert sind. Beispielsweise ist ein rascher Vortrieb (kontinuierlich oder mit kurzen Stillständen) günstig bzgl. Setzungsbeschränkung, da die für den Konsolidationsprozess im Bereich der Ortsbrust verfügbare Zeit kurz ist. Deshalb ist es aus praktischer Sicht nützlich beurteilen zu können, welche Bedingungen beim Vortrieb zu erwarten sind. Basierend auf einer umfassenden Parameterstudie, die mit zwei weitverbreiteten Stoffgesetzen (dem MC Modell und dem MCC Modell) und unter Berücksichtigung einer vernünftigen Bandbreite von Baugrundparametern, Überlagerung und Permeabilität der Verkleidung durchgeführt wurde, konnte gezeigt werden, dass die Bedingungen im Bereich der Ortsbrust von der dimensionslosen Vortriebsgeschwindigkeit $v\gamma_w D/kE$ abhängig sind (wobei γ_w, D, k und E das spezifische Gewicht von Wasser, dem Tunneldurchmesser, dem Durchlässigkeitsbeiwert des Baugrunds und dem Elastizitätsmodul, das im Falle eines MCC Baugrunds als initialer Elastizitätsmodul auf Höhe der Tunnelachse definiert wird, bezeichnen). Konkret sind die Bedingungen praktisch undrainiert, wenn $v\gamma_w D/kE > 1000$ und praktisch drainiert, wenn $v\gamma_w D/kE < 0.01$.

Für $v\gamma_w D/kE$ zwischen 0.1 und 100 ist die Berücksichtigung der Zeitabhängigkeit durch transiente numerische Berechnungen unabdingbar. Undrainierte und drainierte Berechnungen sind relativ einfach, transiente Analysen sind hingegen anspruchsvoller in Bezug auf Berechnungszeit und Modellierungsaufwand. Es konnte jedoch gezeigt werden, dass die transienten Setzungen auch ohne solche aufwändigen Berechnungen abgeschätzt werden können. Konkret konnte eine Gleichung aufgestellt werden, die die transiente Setzung als Funktion der oben eingeführten dimensionslosen Vortriebsgeschwindigkeit sowie der Setzungen, die für die relativ einfachen Grenzfälle von undrainierten und drainierten Bedingungen berechnet werden können, darstellt.

Zusammenfassend, trägt dieses Forschungsprojekt zur Verbesserung der Sicherheit und Wirtschaftlichkeit des Tunnelbaus bei, indem einfach anwendbare Methoden zur Verfügung gestellt werden um, (i), die Standzeit der Ortsbrust abzuschätzen; (ii), die Ortsbruststabilität beim laufenden Vortrieb in Baugrund mit mittlerer Durchlässigkeit zu beurteilen; (iii), basierend auf Resultaten von relativ einfachen drainierten und undrainierten Analysen die Setzungen unter transienten Bedingungen zu beurteilen.

Résumé

Les dangers les plus graves associés aux travaux souterrains dans des roches faibles sont liés à l'effondrement du front de taille. Dans les tunnels peu profonds, l'instabilité peut se transmettre jusqu'à la surface. Cela peut même y engendrer la formation d'un cratère. Les tassements inadmissibles à la surface peuvent survenir, néanmoins, même sans une défaillance du front de taille, à cause d'une redistribution des contraintes (provoquée par l'excavation du tunnel) ou de la consolidation (causée par l'effet de drainage du tunnel). La réponse des sols à haute perméabilité est pratiquement instantanée, tandis que les sols peu perméables montrent une forte dépendance temporelle due au procès d'écoulement transitoire. Celui-ci est provoqué par l'excavation du tunnel et évolue lentement. Généralement, le comportement à court terme (« conditions non-drainées ») de ces sols est plus favorable que celui à long terme (« conditions drainées ») : le front de taille peut s'avérer instable au début et céder après un certain temps ; les tassements augmentent avec le temps.

Des conditions instables peuvent nécessiter une amélioration ou un renforcement du sol ou un soutènement (par exemple à l'aide de l'air comprimé ou d'une suspension de bentonite). Puisque ces mesures peuvent être désavantageuses économiquement et opérationnellement, la question d'une très grande importance pratique, qui se pose est de savoir, si ou pour combien de temps l'excavation peut demeurer stable sans soutènement. La durée de stabilité (qui représente la durée entre l'excavation et la défaillance) – et ainsi la faisabilité de l'absence du renforcement du sol, de l'amélioration et du soutènement – dépend essentiellement de la résistance du sol et de sa perméabilité.

Le comportement des sols à haute ou faible perméabilité dans les environs du front de taille est connu, et peut être analysé en considérant respectivement les cas limites en conditions drainées et non-drainées. Néanmoins, pour les sols à perméabilité moyenne, très peu de recherches ont été effectuées et pratiquement aucune analyse systématique n'est disponible. Pour ces sols, les hypothèses simplificatrices concernant les conditions drainées et non-drainées peuvent être soit pas rentables soit dangereuses. Par conséquent, la compréhension ainsi que la quantification du comportement des sols à perméabilité moyenne dans des conditions transitoires prévalant dans la zone critique, autour du font de taille, est ainsi essentielle pour la sécurité et les coûts de construction. Ce projet de recherche a pour objectif de combler les lacunes des connaissances à cet égard. Les questions typiques, auxquelles nous devons répondre, concernent l'effet du taux d'avancement sur les tassements à la surface, le taux d'avancement critique à l'égard de la stabilité du front de taille, le développement temporelle des tassements à la surface, la perte de la stabilité pendant une période d'arrêt et la durée de stabilité du front de taille.

La pertinence du projet est évidente pour la sécurité et pour les coûts de construction, compte tenu de la présence fréquente des sols à perméabilité moyenne (par exemple les sols alluviaux en Suisse) et l'utilisation toujours plus intense des espaces souterrains urbains.

L'objectif principal de ce projet est de développer des recommandations ainsi que des méthodes d'analyse simplifiées afin d'évaluer la stabilité du front de taille et d'estimer les tassements dans des conditions transitoires. Ces problèmes de dimensionnement pratiques des tunnels ont engendré une série de questions théoriques concernant les mécanismes physiques et ont nécessité une quantité considérable de recherche fondamentale sur le phénomène de la défaillance retardée ainsi que l'interaction des deux procès simultanés : la génération des surpressions interstitielles (due à l'avancement du tunnel) et la dissipation pratiquement simultanée de ces pressions à cause de la consolidation.

Plus précisément, des enquêtes préliminaires, qui ont été menées sous différentes suppositions sur le comportement mécanique du sol, ont démontrées que, (i) les

simulations numériques ne reproduisent pas toujours le phénomène de la défaillance retardée et (ii) les prédictions théoriques dépendent de la discrétisation spatiale adoptée pour la solution numérique (plus le maillage est fin, plus la durée de stabilité est basse), ainsi remettant en cause la possibilité de prédire la durée de stabilité. Par conséquent, dans un premier temps, il était nécessaire d'examiner les raisons pour le comportement insatisfaisant du modèle et de résoudre le problème de la dépendance du maillage sur les résultats numériques.

L'enquête effectuée a révélé que la supposition décisive, afin de reproduire la défaillance retardée, est celle de la dilatance plastique du sol. Considérant la supposition d'un angle de dilatance constant, souvent considéré dans la pratique de dimensionnement, l'analyse couplée (avec l'hydraulique et la mécanique) mène inévitablement à un taux de déformation constant au point de défaillance, bien que la défaillance soit couramment associée à des déplacements accélérés. Des modèles constitutifs plus réalistes - qui représentent le fait, observé expérimentalement, que le cisaillement au point de défaillance se produit à un volume constant - mènent à des déplacements accélérés au point de défaillance, permettant de déterminer la durée de stabilité. Cependant, ces modèles posent foncièrement des problèmes de stabilité numérique proche de l'état de défaillance, parce qu'il n'existe aucune solution qui satisfasse les équations principales de la mécanique des milieux continus. En raison de ces problèmes de stabilité numérique, la détermination de la durée de stabilité nécessite une co-évaluation de l'intégralité des résultats numériques.

En ce qui concerne la dépendance du maillage sur les résultats numériques, mentionnée précédemment, il a pu être démontré à l'aide de considérations théoriques et de calculs analytiques, que la raison est un ramollissement de la structure, qui se produit dans un matériel parfaitement plastique tant que la règle d'écoulement est non-associée. Dans les simulations numériques, les déformations de cisaillement sont localisées dans une bande qui a une épaisseur de 1 à 2 éléments finis. Plus le maillage d'éléments finis est grossier, plus la bande de cisaillement prédite numériquement est épaisse, plus les déformations de cisaillement sont petites, plus le ramollissement de la structure est prononcé et plus la durée de stabilité prédite est grande. Pour les maillages grossiers d'éléments finis (qui empêchent pratiquement le ramollissement de la structure), la durée de stabilité a une limite supérieure. Vice-versa, des maillages très fins permettent un ramollissement de structure considérable (jusqu'à celui correspondant au cisaillement purement plastique) et la durée de stabilité a une limite inférieure. Ces deux limites de la durée de stabilité peuvent être estimées analytiquement dans le cas de problèmes relativement simples. Les simulations numériques montrent que la durée de stabilité dépend presque linéairement de la taille de l'élément pour une discrétisation suffisamment petite. Ce résultat est très important d'un point de vue pratique, puisqu'il permet de déterminer la durée de stabilité en exécutant plusieurs calculs avec un maillage relativement fin et d'extrapoler leurs résultats à la taille du maillage qui correspond à la bande estimée de cisaillement dépendante de la taille des grains (qui est pratiquement zéro, considérant les dimensions des structures géotechniques typiques).

Ces analyses théoriques ont démontré qu'il est possible de reproduire au moins qualitativement le phénomène de la défaillance retardée et de déterminer la durée de stabilité des modèles numériques. Cependant, il est discutable si les prédictions des modèles sont quantitativement assez précises. Par conséquent, il était nécessaire d'effectuer quelques tests physiques afin d'observer l'évolution de la défaillance de simples systèmes géotechniques dans des conditions contrôlées et de comparer la durée de stabilité observée avec les prédictions numériques. Les études expérimentales se composaient d'essais de compression sous charge uniaxiale et d'essais de centrifugeuse des modèles physiques. Les résultats expérimentales ont été interprétés numériquement, en utilisant des constantes de matériaux qui ont été déterminées expérimentalement, indépendamment des essais de défaillance retardée (appelés validation de modèle « classe A »). Il a été constaté que le modèle simple, mais souvent utilisé, assumant un comportement élastique linéaire, parfaitement plastique au critère de défaillance de Mohr-Coulomb (modèle MC) généralement sous-estime la durée de stabilité. D'autre part, le modèle Modified Cam Clay (MCC) surestime la durée de stabilisation, s'il est utilisé en combinaison avec une discrétisation spatiale gérable (c'est-à-dire, fine, toutefois moins fine qu'elle devrait l'être à cause des bandes de cisaillement observées, très minces), mais fournit des durées de stabilité semblables à celles observées lorsqu'on extrapole les résultats numériques à la taille de la bande de cisaillement, ce qui permet d'établir une prédiction raisonnable et précise de la durée de stabilité.

Ces résultats fondamentaux ont permis à procéder au premier sujet principal de ce projet de recherche, c'est-à-dire à la dépendance temporelle de la stabilité du front de taille. Les recherches ont été effectuées avec le modèle MC pour les raisons suivantes : il est utilisé fréquemment ; les ingénieurs connaissent très bien ses paramètres ; et, comme mentionné auparavant, il fournit (en combinaison avec une discrétisation spatiale fine, mais néanmoins gérable) une estimation prudente de la durée de stabilisation. Les effets des paramètres géotechniques individuels (cohésion, angle de frottement interne, perméabilité, couverture du tunnel, etc.) ont été étudiés systématiquement, une étude de paramètres complète couvrant un large nombre de conditions géotechniques a été effectuée et des tableaux de dimensionnement ont été développés, se basant sur une analyse dimensionnelle. Ce dernier permet d'estimer la durée de stabilité de tunnels peu profonds pour une situation géotechnique, aidant ainsi à prendre des décisions pendant la planification et réalisation des tunnels dans des sols faibles.

Les durées de stabilité indiquées peuvent aussi être utilisées afin d'estimer les conditions de stabilité du front de taille pendant l'avancement du tunnel. Comme le montre ce rapport, le taux d'avancement critique peut être choisi de manière à être égal au rapport entre le diamètre du tunnel et la durée de la stabilité.

Le deuxième sujet principal de ce projet de recherche, les tassements transitoires à la surface, a été analysé à l'aide d'une série d'analyses numériques, tridimensionnelles et couplés (avec l'hydraulique et la mécanique). Les analyses ont confirmé l'hypothèse que le taux d'avancement v, la durée d'une période d'arrêt et les conditions de drainage à la bordure du tunnel et au front du taille sont importants pour le contrôle des tassements à la surface, suite à l'excavation du tunnel dans des sols à perméabilité moyenne.

L'écoulement en direction du revêtement perméable provoque une distribution de la pression de l'eau interstitielle à long terme autour du tunnel, qui est considérablement différente de la distribution initiale et hydrostatique. L'écoulement ainsi que la réduction de la pression de l'eau interstitielle causent des tassements considérablement élevés à la surface, particulièrement dans le cas de pression initiale d'eau interstitielle élevée et, qui doivent être évités, même si ceci entraîne des forces plus élevées sur le revêtement du tunnel. Les calculs comparatifs démontrent que les tassements suite à l'avancement du tunnel avec une compensation totale de la pression hydrostatique peuvent être d'un ordre de grandeur plus petit que ceux qui se produisent sous une pression atmosphérique. La compensation de la pression hydrostatique peut ainsi être indispensable dans le but de limiter les tassements à la surface, même si la résistance du sol au cisaillement serait suffisamment élevée et le front de taille serait stable sans soutènement.

Les tassements à la surface calculés en considérant des conditions non-drainées, drainées et transitoires peuvent être très différents. Par exemple, une excavation rapide (continue ou avec des temps d'arrêts courts) est favorable par rapport aux limitations des tassements, parce que le temps disponible pour le procès de consolidation à proximité du front de taille est court. Par conséquent, d'un point de vue pratique, il est important d'évaluer quelles conditions doivent être supposées pendant l'avancement du tunnel. En se fondant sur une étude paramétrique complète avec deux modèles constitutifs particulièrement répandus (modèles MC et MCC), considérant une série raisonnable de paramètres du sol, de couverture du tunnel et de perméabilité du revêtement, il a pu être démontré que les conditions autour du front de taille dépendent de la valeur du taux d'avancement normalisé $v\gamma_w D/kE$ (où γ_w, D, k et E représentent respectivement le poids spécifique de l'eau, le diamètre du tunnel, la perméabilité du sol et le module de Young, qui est défini par le module d'élasticité initiale à l'axe du tunnel dans le cas d'un sol MCC). Spécifiquement, les conditions sont pratiquement non-drainées si $v\gamma_w D/kE > 1000$ et pratiquement drainées si $v\gamma_w D/kE < 0.01$.

Pour des valeurs de $v\gamma_w D/kE$ entre 0.1 et 100, il est indispensable de considérer la dépendance temporelle. Les analyses de tassement drainées et non-drainées sont relativement simples. Cependant, les analyses transitoires sont exigeantes en termes du temps d'ordinateur et d'effort de modélisation. Toutefois, il a pu être démontré qu'une estimation préliminaire des tassements transitoires peut être faite sans effectuer une telle analyse exigeante. Plus spécifiquement, une équation a pu être développée qui exprime les tassements transitoires en fonction du taux d'avancement normalisé et des tassements calculés pour les cas limites relativement simples en conditions drainées et non-drainées.

En résumé, ce projet de recherche contribue à améliorer la sécurité et les coûts de construction en fournissant des méthodes faciles à utiliser, afin, (i), d'estimer la durée de stabilité du front de taille d'un tunnel ; (ii), d'évaluer la stabilité du front de taille pendant l'excavation dans des sols de perméabilité moyenne ; (iii), d'évaluer les tassements en conditions transitoires se basant sur les résultats des analyses relativement simples en conditions drainées et non-drainées.

Summary

The most serious hazards in soft ground tunnelling are associated with a collapse of the tunnel face. In shallow tunnels, the instability may propagate towards the surface, thereby creating a crater on the ground surface. Inadmissible surface settlements may occur, however, even without a face failure, as a consequence of excavation-induced stress redistribution or soil consolidation caused by the drainage action of the tunnel. The response of high-permeability soils is practically instantaneous, while low-permeability soils exhibit pronounced time-dependency due to the transient seepage flow process, which is triggered by the tunnel excavation and develops slowly over the course of time. In general, the short-term behaviour ("undrained conditions") of these soils is more favourable than the long-term one ("drained conditions"): the tunnel face may be stable initially and fail only after some time; the settlements increase with time.

Unstable conditions may necessitate improvement or reinforcement of the ground or the application of a support (e.g. by compressed air or pressurized bentonite slurry). As such measures may present economical and operational disadvantages, the question of whether and for how long the excavation can remain stable without support is of great practical relevance. The stand-up time (time lapsing between end of the excavation and the occurrence of failure), and thus the feasibility of refraining from ground reinforcement, improvement or support, depends essentially on soil strength and permeability.

The behaviour of high- or low-permeability soils around the advancing tunnel face is well understood and can be analysed by considering the borderline cases of drained or undrained conditions, respectively. For medium permeability soils, however, very little research work has been done and there are hardly any systematic investigations available. The simplifying assumptions involving drained or undrained conditions may be uneconomical or unsafe, respectively, for such soils. Understanding and quantifying the behaviour of medium permeability soils under the transient conditions prevailing in the critical region around the advancing tunnel face is therefore essential for construction safety and economy. The research project aims to close the knowledge gaps existing in this respect. Typical questions to be answered concern the effect of the advance rate on surface settlement, the critical advance rate with respect to face stability, the time-development of surface settlement, the loss of stability during a standstill and the stand-up time of the tunnel face.

The relevance of the project in terms of construction safety and cost is evident in view of the frequent occurrence of medium permeability soils (e.g. the many glacial tills in Switzerland) and the increasingly intensive use of urban or sub-urban underground space.

The main goal of the project was working out recommendations and simplified analysis procedures for face stability assessment and settlement estimation under transient conditions. Addressing these practical tunnel design issues raised a series of theoretical questions about the underlying physical mechanisms and necessitated a considerable amount of fundamental research into the phenomenon of delayed failure and the interplay of two concurrent processes: the generation of excess pore pressures (due to tunnel advance) and the practically simultaneous dissipation of these pressures through consolidation.

More specifically, preliminary investigations, which were carried-out under widely made assumptions about the mechanical behaviour of the ground, showed that, (i), numerical simulations do not always reproduce the phenomenon of delayed failure and, (ii), that the theoretical predictions depend on the spatial discretization adopted for the numerical solution (the finer the mesh, the lower the stand-up time), thus putting a question mark on the basic possibility of predicting stand-up time. Therefore, in a first phase, it was necessary to investigate the reasons for the unsatisfactory model behaviour and to resolve the problem of the mesh-dependency of the numerical results.

The performed investigations revealed that the decisive assumption for reproducing delayed failure is the one about the plastic dilatancy of the ground. Under the simplifying, but in design practice frequently made assumption of a constant dilation angle, coupled analyses inevitably lead to a constant deformation rate at failure, although failure is commonly associated with accelerating displacements. More realistic constitutive models, which account for the experimentally observed fact that shearing at failure occurs under constant volume, lead to accelerating displacements at failure, thus allowing determining stand-up time. However, such models inherently exhibit numerical stability problems close to the failure state, because a solution satisfying the governing continuum-mechanical equations does not exist. Due to these numerical stability problems, the determination of the stand-up time necessitates co-evaluation of the entirety of the numerical results.

With regard to the mentioned mesh-dependency of the numerical results, it could be shown by means of theoretical considerations and analytical computations that the reason is the so-called structural softening, which occurs in a perfectly plastic material as long as the flow rule is non-associated. In numerical simulations, the shear strains become localized in a band which is about 1–2 finite elements thick. The coarser the finite element mesh, the thicker the numerically predicted shear band, the smaller the shear strains, the less pronounced the structural softening and the higher the predicted stand-up time. For very coarse finite element meshes (which practically prevent structural softening) the stand-up time tends to an upper limit. Vice-versa, very fine meshes allow for considerable structural softening (up to that corresponding to purely plastic shearing) and the stand-up time tends to a lower limit. These two limits of stand-up time can be estimated analytically in the case of relatively simple problems. The numerical simulations show that for a sufficiently fine spatial discretization, the stand-up time depends almost linearly on the element size. This finding is valuable from the practical viewpoint, as it allows determining stand-up time by performing a few computations with relatively fine meshes and extrapolating their results to the mesh size that corresponds to the expected, grain-size-dependent thickness of the shear band (practically zero considering the dimensions of typical geotechnical structures).

These theoretical investigations showed that it is possible to reproduce at least qualitatively the phenomenon of delayed failure and to determine the stand-up time of the *numerical model*. It was, however, questionable whether the model predictions were quantitatively sufficiently accurate. Therefore, it was necessary to carry-out physical tests allowing to observe the evolution of failure of simple geotechnical systems under controlled conditions and to compare the observed stand-up time with the numerical predictions. The experimental investigations consisted of uniaxial loading tests and centrifuge testing of physical models. The experimental results were interpreted numerically, using material constants which were determined experimentally independently of the delayed failure tests (so-called "class A" model validation). It was found that the simple, but widely used, linearly elastic, perfectly plastic model with Mohr-Coulomb yield condition (MC model) generally underestimates the stand-up time. On the other hand, the Modified Cam Clay (MCC) model overestimates the stand-up time when used in combination with a computationally manageable spatial discretization (*i.e.* fine, but still not as much as it would be necessary on account of the experimentally observed very thin shear bands), but provides stand-up times very close to the observed ones when extrapolating the numerical results to the size of the shear band, thus allowing for a reasonably accurate prediction of the stand-up time.

These fundamental findings made it possible to proceed with the first main subject of the research project, i.e. the time-dependency of tunnel face stability. The investigations were carried-out adopting the MC model for the following reasons: it is widely used in design practice; engineers are very familiar with its parameters; and, as mentioned above, it provides (in combination with a fine, but still manageable spatial discretization) a conservative estimate of the stand-up time. The effects of the individual geotechnical parameters (cohesion, friction angle, permeability, overburden etc.) were studied systematically, a comprehensive parametric study covering a wide range of geotechnical conditions was carried-out and, based upon a dimensional analysis, dimensionless design charts were worked-out. The latter allow estimating stand-up time of shallow tunnels for a given geotechnical situation, thus assisting decision-making during planning and execution of soft ground tunnels.

The given stand-up times can also be used for a simplified estimation of the face stability conditions during tunnel advance. As it is shown in the report, the critical advance rate can be taken equal to the ratio of tunnel diameter to stand-up time.

The second main subject of the research project, i.e. the transient surface settlements, was investigated by a series of 3D coupled hydraulic-mechanical numerical analyses. The analyses confirmed the hypothesis that advance rate v, duration of standstills and drainage conditions at the tunnel boundary and face are important for the control of tunnelling-induced surface settlements in medium permeability soils.

Seepage flow towards a pervious lining induces a long-term pore pressure distribution around the tunnel which is significantly different from the initial hydrostatic one. Seepage flow and pore pressure relief leads to significantly larger surface settlements particularly in the case of high initial pore pressures and must be avoided even if this would result to a higher lining loading. Comparative calculations show that the settlements induced during advance with full compensation of the hydrostatic pressure may be by one order of magnitude smaller than the ones occurring under atmospheric pressure. The compensation of the hydrostatic pressure might thus be indispensable in order to limit the surface settlements, even if the shear strength of the ground would be sufficiently high and the face would be stable without any support.

The surface settlements computed under the assumptions of undrained, drained and transient conditions can be very different. For example, a rapid excavation (continuous or with short standstills only) is favourable with respect to settlement limitation, because the time available to the consolidation process in the vicinity of the advancing face is short. Therefore, it is valuable from the practical viewpoint to be able to assess which conditions have to be expected during advance. Based upon a comprehensive parametric study with two widely-distributed constitutive models (the MC model and the MCC model), i.e. considering a reasonable range for the soil parameters, the overburden and the lining permeability, it could be shown that the conditions around the advancing heading depend on the value of the normalized advance rate $v\gamma_w D/kE$ (where γ_w, D, k and E denote the unit weight of the water, the tunnel diameter, the soil permeability and the Young's modulus, defined as the initial elastic modulus at the tunnel axis in the case of a MCC soil). Specifically, the conditions are practically undrained if $v\gamma_w D/kE > 1000$ and practically drained if $v\gamma_w D/kE < 0.01$.

For $v\gamma_w D/kE$ between 0.1 and 100 it is indispensable to consider time-dependency. Undrained and drained settlement analyses are relatively simple, but transient analyses are demanding in terms of computer time and modelling effort. However, it could be shown that a preliminary estimation of the transient settlements can be made without such a demanding analysis. More specifically, an equation could be established that expresses transient settlement as a function of normalized advance rate and of the settlements computed for the relatively simple borderline cases of undrained and drained conditions.

In conclusion, this research project contributes to tunnel construction safety and economy by providing easy to use methods for, (i), estimating stand-up time of the tunnel face; (ii), assessing face stability during ongoing excavation in medium-permeability soils; (iii), assessing settlements under transient conditions based upon the results of relatively simple drained and undrained analyses.

Introduction

1.1 Problem definition

1.1.1 On the relevance of transient conditions

Saturated, water-bearing ground responds to excavation with a longer or shorter delay depending on its permeability and on the rate of loading [1]. In soft ground, this time-dependency can almost always be traced back to consolidation. The response of high-permeability soils (e.g. sandy or gravelly soil) is practically instantaneous (reaching steady state practically immediately), while low-permeability soils (e.g. clay) exhibit a pronounced time-dependency, which is due to the transient seepage flow process. The latter is triggered by excavation and develops slowly over the course of time: The long-term deformations of the ground include, in general, changes to its water content, which take more or less time, depending on the seepage flow velocity and thus on the soil permeability.

For problems involving "unloading" of the soil, the short-term behaviour (*i.e.* the behaviour under the *undrained* conditions prevailing instantaneously after unloading) is more favourable than the long-term one (*i.e.* the behaviour under the drained conditions prevailing at the end of the consolidation process). Undrained tunnel excavation leads to negative excess pore pressures in the ground as its volume and water content tend to increase. These excess pore pressures dissipate during consolidation, leading to a decrease of effective stresses and thus to decrease of the soil resistance to shearing. Consequently, the short-term behaviour is more favourable than the long-term.

This project deals with the stability of the tunnel face and the development of surface settlements under *transient conditions* (lying somewhere between undrained and drained conditions), where the dissipation of excess pore pressure is not so fast to achieve steady state already during excavation, but on the other hand also not so slow to consider practically undrained conditions within the relevant time period (which depends on the question under investigation). Transient conditions are particularly relevant for soils of medium-low permeability (e.g. the widely-distributed moraines in Switzerland). For example, in soils of this type the tunnel face may be stable only for a limited, not easily quantifiable time period; *failure occurs with a delay*. (A "delayed failure" may also be induced by other events, like intense raining, surcharge at the surface or an earthquake. However, these aspects fall outside the aim of the present work.)

The dominant role of the progressive dissipation of pore pressure in delayed failure in medium-low permeability soils has been widely reported in the literature. Sevaldson [2], Skempton [3], [4], Vaughan and Walbancke [5], Hughes *et al.* [6], Potts *et al.* [7], Lollino *et al.* [8] and Ellis and O'Brien [9] – among others – present several examples of delayed failure of cuttings, while Davis et al. [10] remarked that the assessment of time dependent face stability is a major concern for tunnelling engineers. Shahin and Nakai [11], Callari and Casini [12], Anagnostou [13], Höfle *et al*. [14] and Callari [15] show that for medium-low permeability soils, transient conditions can occur already in the vicinity of the excavation face, so that the surface settlements (and the drawdown of the water level, see Callari [15]), vary with the advance rate.

The behaviour of high- or low-permeability soils is well understood and can be analysed by considering the borderline cases of drained or undrained conditions, respectively. For medium permeability soils, however, very little research work has been done and there are hardly any systematic investigations available. The simplifying assumptions involving drained or undrained conditions may be uneconomical or unsafe, respectively, for such soils.

1.1.2 Stand-up time

The understanding and the assessment of the time dependent stability of excavations in medium-low permeability soils is relevant for both temporary (e.g. open-cut excavations or tunnel face) and permanent (e.g. road or railway cuttings) geotechnical structures. A major point of interest is the assessment of the so-called *stand-up time* (*i.e.*, the time lapsing between the completion of the excavation, Figure 2.1, and failure, Figure 2.2): a long stand-up time allows to refrain from face support or ground improvement works during temporary excavations, thus saving time and cost, while a short stand-up time requires the implementation of costly and time-consuming auxiliary measures (Figure 2.3). Understanding and quantifying the behaviour of medium-low permeability soils under transient conditions is therefore essential for construction safety and economy.

(a) (b)

Figure 2.1 *Stable unsupported vertical cut (a) and tunnel face (b) in low permeability soil (pictures after blog.geotechpedia.com and www.dr-sauer.com, respectively).*

(a) (b)

Figure 2.2 *(a) Collapse of excavation (after cliffs.lboro.ac.uk/downloads/kovacevic.pdf) and (b) collapse of a tunnel face (Lausanne subway, Switzerland; courtesy of H. Stadelmann, Implenia AG) in weak ground.*

(a) (b)

Figure 2.3 *Tunnel face support, (a), by compressed air (entrance to the cutterhead for hyperbaric interventions during the construction of the St Petersburg subway, Russia; courtesy of Salini-Impregilo) and, (b), face bolting (bypass Patras, Greece; courtesy of Prof. G. Anagnostou).*

The stand-up time of an excavation increases with the shear strength of the ground (all other parameters being fixed). Figure 2.4 shows qualitatively the dependency of the stand-up time on cohesion. The two values ($c_{U,lim}$, $c_{D,lim}$) mark the boundary of the transient failure regime. If the cohesion is lower than $c_{U,lim}$, then the excavation would be unstable even under undrained conditions; stand-up time in this case is equal to zero. If, on the other hand, the cohesion is higher than $c_{D,lim}$, then the excavation would be stable also in the long term; for $c \rightarrow c_{D,\mathrm{lim}}^{-}$ stand-up time tends to infinity. The limit cohesion $c_{D,lim}$ represents, therefore, a singularity point. The asymptotic increase in stand-up time indicates a considerable sensitivity of the ground response with respect to cohesion at the upper end of the transient failure regime: Close to the limit cohesion $c_{D,lim}$ a relatively small variation Δc may result in an infinite change in stand-up time (from a finite value to infinity or vice-versa; Figure 2.4).

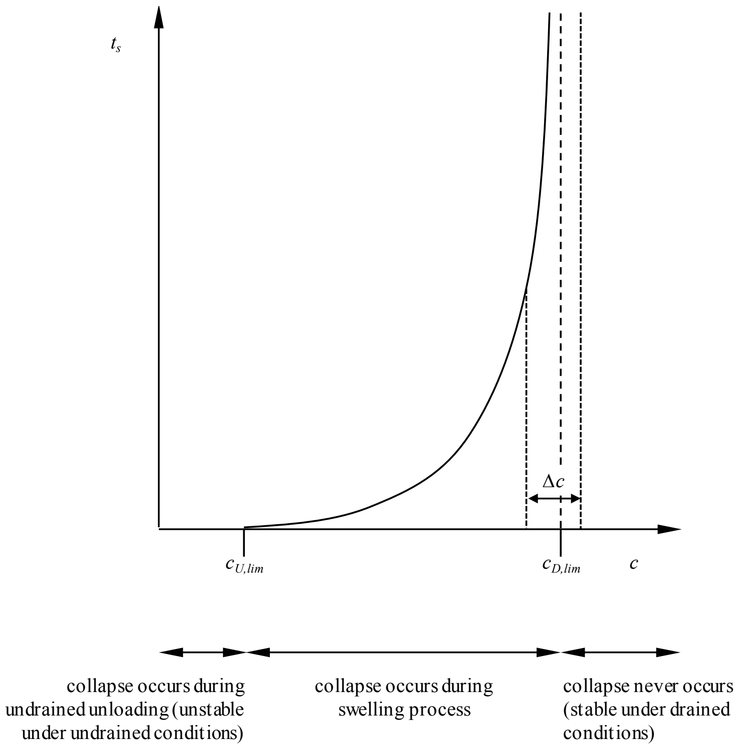

Figure 2.4 *Qualitative dependency of the stand-up time t_s on cohesion c.*

A cohesion change Δc can be due to intrinsically softening behaviour (*i.e.* strength parameters decreasing with shear deformation) or, in the case of non-associated plastic flow, due to the so-called structural softening (the definition of structural softening was introduced by Sterpi [16], the phenomenon was already described by Davis [17]). Structural softening means an apparent reduction of the shear strength (to the so-called “operational strength”) caused by the progressive rotation of the principal stress axes inside the shear band during shearing [17].

Structural softening occurs in perfectly plastic or strain-hardening materials, provided that the flow rule is non-associated [16]. As in FEM analyses the shear deformation depends on the element size (the smaller the element size, the larger the possible rotation), the change in cohesion Δc caused by structural softening is also a function of the element size. This means, in conclusion, that for FEM transient analyses assuming a non-associated plastic flow (and thus affected by structural softening), the stand-up time will increase with increasing mesh size. As discussed above on the basis of Figure 2.4, a significant mesh sensitivity is to be expected at cohesion values just above the limit cohesion $c_{D,lim}$.

1.1.3 Surface settlements

In contrast to the mechanisms underlying face instability, which inherently are localised in the close vicinity of the face, the sources of the tunnelling-induced settlement are manifold.

From the overview of Figure 2.5, it becomes evident that the response of the system may be time-dependent for different reasons: for example, due to the passage of the excavation face or due to long-term consolidation far behind the face. In order to clarify what "transient conditions" does mean in the more narrow sense of the context of the planned research project, let us consider first the borderline cases of a high-permeability ground and of a low-permeability ground.

The deformations underlying the settlement at a specific cross section (e.g. a-a) start to develop before tunnel advance reaches this cross section (i), continue after passage of the excavation front up to about two tunnel diameters behind the face (ii) and may continue to increase far behind the tunnel face and for a long time period after construction (iii).

The deformations ahead of the face (i) are due to the excavation-induced stress redistribution and, in the case of an open face, to the drainage action of the tunnel, which causes a de-pressurisation of the pore water in the ground ahead of the face.

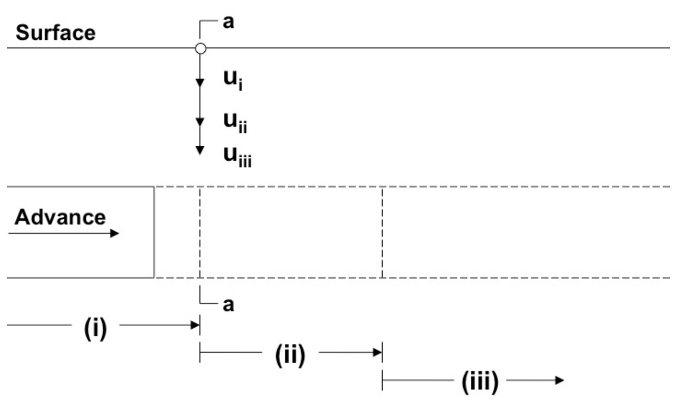

Figure 2.5 *Source of settlement.*

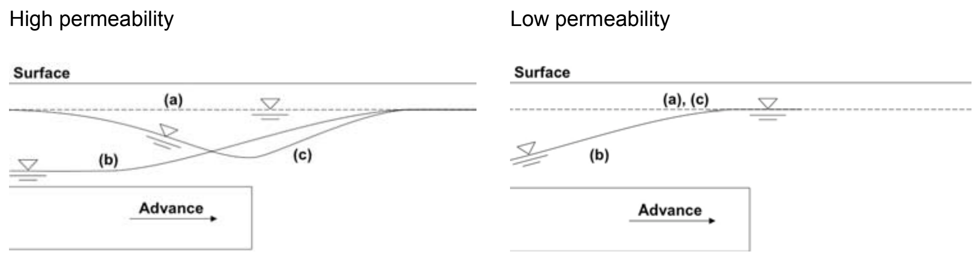

Figure 2.6 *Development of water table in high-permeability ground (left) or in low-permeability ground (right). (a) Closed face, impervious lining; (b) Closed face, drained lining; (c) Open face, impervious lining.*

In the region (ii) up to a distance of 1 – 2 diameters behind the face, the excavation-induced stress re-distribution and the support installation reach completion. The excavation boundary is only partially supported and in general it is allowed to deform (more or less, depending on the construction means and methods).

The important causes of settlement in conventional tunnelling include, e.g., the deformability of the shotcrete shell before ring closure at the invert and the low stiffness of green shotcrete. The ring closure location and the advance rate (which directly influences the loading rate of the green shotcrete) are important factors for controlling settlement.

In mechanised tunnelling, the gap between the shield and the bored profile, as well as the annular gap immediately behind the shield tail, represent sources of deformation and thus of settlement. The pressure of the support medium (compressed air, slurry) and the annulus grouting materials and procedures are decisive factors with respect to settlement control.

The long-term settlements (iii) are due to the time-dependency of the ground response, which in the case of a low-permeability water-bearing ground is associated with excess pore pressure dissipation and the consolidation process. Field measurements (e.g. [18], [19], [20]) and numerical investigations (e.g. [21], [22]) show that the surface settlements can significantly increase several months after lining installation. During this time, the settlement trough widens and deepens [18].

A decisive factor governing the long-term settlement is draining action of the tunnel lining. Wongsaroj *et al*. [21] showed that depending on the ratio between lining and soil permeability and thickness, the tunnel lining may act as a permeable or an impermeable boundary.

In a *high-permeability ground* the hydraulic head field is continuously at a steady state. In the case of closed-shield tunnelling (or of tunnelling under compressed air) with an impervious lining, the hydraulic head remains constant and equal to its initial undisturbed state (Figure 2.6 left (a)). The ground behaviour is not time-dependent, but the system behaviour exhibits a time-dependency due to the advance of the excavation face. The deformations develop instantaneously with the tunnel advance and are associated with the excavation-induced stress redistribution. If the tunnel face is open and the tunnel lining drained, the hydraulic head field adjusts itself practically instantaneously to the hydraulic boundary conditions and moves together with the advancing tunnel face. The deformations in this case are associated also with the groundwater drainage towards the advancing face and the tunnel wall, which causes pore pressure relief or even a draw-down of the water table (Figure 2.6 left (b)). If the tunnel lining is impervious, the pore pressure reduction or the draw-down of the water table will only be temporary, *i.e.* restricted to the vicinity of the advancing face [23]. After the passage of the excavation front and the installation of the lining, the pore pressure increases again and the initial state is restored (Figure 2.6 left (c)): The consolidation (an increase in effective stress due to the lowering of the water table) is followed by swelling (a decrease in effective stresses due to the rising water table).

In the borderline case of a *low-permeability ground*, undrained conditions prevail around the advancing face or during short standstills. The deformations around the face (settlement sources (i) and (ii) in Figure 2.5) therefore occur under constant water content. (Instead of changes in the water content, excess pore pressures develop.) The time-dependency of the system behaviour at this stage is solely due to the advance of the tunnel face. In a second, completely distinct stage far behind the face, the excess pore pressures dissipate and the hydraulic head field adjust itself slowly to the prevailing hydraulic boundary conditions. The time-dependency of the deformations in the second stage is due to the consolidation/swelling process Note that, in contrast to the high-permeability case discussed above, a draw-down of the water table does not occur at all in the present case – neither in the vicinity of the face, nor far behind the face – if the tunnel lining is impervious (Figure 2.6 right (a, c)). If the tunnel lining is pervious, a draw-down of the water table does takes place only far behind the face (Figure 2.6 right (b)).

In the case of a medium-permeability ground, the conditions around the advancing face will be somewhere between “drained” and “undrained”. In contrast to the high-permeability case, the ground exhibits a time-dependent behaviour in the sense that excess pore pressures develop and do not dissipate instantaneously. On the other hand, the medium-permeability case is different from the low-permeability case discussed above insofar as the excess pressure dissipation does not take place with such a long delay, far behind the advancing face, but occurs simultaneously with the face advance. The complexity of such intermediate conditions is due to the fact that two mechanisms of time-dependency overlap here: the advance of the face (which causes a stress-redistribution and excess pore pressure generation) and the consolidation/swelling process (over the course of which the excess pore pressures dissipate/increase).

The role of the advance rate and that of transient conditions with respect to surface settlement in a medium permeability soil become evident when considering that the settlements originating from the face area (sources (i) and (ii) in Figure 2.5) also depend on the type of conditions prevailing there (undrained, drained or somewhere in-between these two) and that, for a given permeability k, the advance rate v governs the type of conditions around the tunnel face. For one and the same ground and construction practice (annulus grouting, support pressure in mechanised tunnelling, excavation and support sequence in conventional tunnelling, etc.), different deformations may occur depending on whether the conditions around the face are drained (low advance rate v), undrained (high advance rate v) or somewhere in-between these two.

Analogously to the issue of face stability, the present research project focuses on intermediate conditions also with respect to surface settlement. The effect of the advance rate on the surface settlement during tunnel advance, excavation standstills and at long-term are key topics in the project.

1.2 Current state of research on the delayed failure

Over the last decades the topic of delayed failure has been investigated numerically and by means of field and physical tests.

1.2.1 Numerical studies

Stability of geotechnical structures is traditionally investigated by means of limit equilibrium models (e.g. [24], [25], [26], [27] for the stability of slopes or trench excavations and [28], [10] for the tunnel face stability). These models are simple but fail to consider soil deformations, which are essential to the time-dependency of ground behaviour in general and to the problem of transient failure in particular. Einstein and Samarasekera [29] investigated the time-dependent stability of a tunnel cross-section in water-bearing soil by estimating the pore pressure field first (using transient seepage flow analyses that do not consider soil deformation) and incorporating it into a numerical stress analysis. This approach is adequate for drained conditions, where the problem – although physically coupled – can also be analysed as uncoupled because the steady state hydraulic head field does not depend on the deformations. For transient problems, however, fully coupled hydraulic-mechanical analyses are essential. Although the need for a coupled approach was pointed out already by Bjerrum and Kjaernsli [30], very few works investigate the issue of delayed failure by means of coupled transient numerical analysis.

Table 2.1 provides an overview of numerical studies on the transient stability of slopes or trenches. With the exception of Banerjee *et al.* [31] (who did not investigate numerical behaviour close to failure) and Borges [32] (whose simulations did not reach the ultimate state for the material constants adopted) the works of Table 2.1 allow the following conclusions to be made: numerical simulations can reproduce a distinct failure under the assumption of isochoric plastic flow, *i.e.* zero plastic volumetric deformation ([33], [34], [35]); the failure occurs more suddenly in the case of a isochoric or contractant flow [36]; and stand-up time decreases with a decreasing dilation angle ([7]; [37]).

Failure of a structure over time is associated with accelerating displacements close to the ultimate state ([38], [39], [40], [41]). However, as mentioned already by Griffiths *et al.* [42], Kirkebø [36] and Potts *et al.* [7], coupled transient analysis models do not exhibit such behaviour under the assumption of a constant positive dilation angle: the numerical solution fulfils equilibrium, while the displacements increase over time at a constant rate. The present report aims to improve the understanding of the causes of this model behaviour and to show which parameters must be evaluated in order to determine stand-up time.

Concerning tunnelling, to the authors' knowledge, no systematic study of the stand-up time of the tunnel face during standstills exists in the literature. Only Ng and Lee [43] and Callari [44] addressed the issue of the time dependent face stability. Ng and Lee [43] estimated the necessary face reinforcement as a function of the consolidation time. The authors showed that the dissipation of the negative excess pore pressure induced by the excavation leads to an increase of the bolting density requirement. Callari [44] discussed the influence of the plastic dilation and of the hardening modulus on the stand-up time. The author showed that positive plastic dilation and hardening behaviour are favourable with respect to the stand-up time. Moreover, Callari [44] observed that FEM analyses of tunnel face stability have difficulties to capture the localization of the strains ahead of the tunnel face near to the ultimate state.

***Table 2.1** Investigations into the issue of delayed failure of cuttings or slopes employing coupled transient numerical analyses.*

Reference	*Problem*	*Constitutive model*
Holt and Griffiths [33] Griffiths and Li [34]	Vertical cut Vertical cut	Linearly elastic, perfectly plastic; Mohr-Coulomb failure criterion; zero dilation
Kirkebø [36]	Slope	Linearly elastic, perfectly plastic; smoothened Mohr-Coulomb failure criterion; dilatant, isochoric and contractant plastic flow
Potts *et al.* [7] (selected results are presented also in Vaughan [45] and Potts and Zdravković [46])	Cut slope	Linearly elastic, perfectly plastic or strain-softening; Mohr-Coulomb yield criterion; dilatant and isochoric plastic flow
Banerjee *et al.* [31]	Vertical cut	Extension of the Modified Cam-Clay model for anisotropic behaviour
Kovacevic et al. [35]	Cut slope	Non-linearly elastic, strain-softening; Mohr-Coulomb yield criterion; zero dilation
Borges [32] (1)	Cut slope	Modified Cam-Clay model
Kovacevic et al. [47] Kovacevic et al. [48]	Cut slope Underwater slope	Critical state model of the Cam-Clay family
Sanavia [37]	Slope	Linearly elastic, strain-softening; Drucker-Prager yield criterion; dilatant and isochoric plastic flow; unsaturated soil

(1) Without investigation of the numerical behaviour close to failure.

Another issue which is strictly related to the stand-up time of the tunnel face is the minimum (“critical”) advance rate for which the face would remain stable during ongoing excavation.

The issue of face stability during ongoing excavation was addressed by Höfle *et al.* [14], [49] and by Sitarenios and Kavvadas [50]. Höfle *et al.* [14] showed that the deformations increase with increasing permeability but pointed out that quantitative statements about face stability cannot be made and mentioned the difficulty of applying the so-called “phi-c-reduction” method for calculating the safety factor under transient conditions. Höfle *et al.* [49] could demonstrate, however, by means of one parametric study with permeability values k = 10^{-6} to 10^{-9} m/s (the advance rate is not given in the paper) that the safety factor of the tunnel face decreases with increasing permeability. Sitarenios and Kavvadas [50] also concluded that the ground permeability has a major relevance on the stability of the tunnel face (more specifically on the required support pressure). The authors showed that for a fixed advance rate of 36 m/day, favourable undrained conditions ahead of the tunnel face occurred when the permeability of the soil is lower than 5 10^{-7} m/s, while for a permeability higher than 10^{-6} m/s drained conditions prevailed around the face.

1.2.2 Field tests and physical modelling

Two major field tests were executed by Banerjee *et al.* [31] and Cooper *et al.* [51]. The authors, investigated the manifestation of delayed failure of an 9.75 m high vertical cut and of an 9 m high slope with inclination 1:2, respectively, by increasing artificially the pore pressure in the ground close to the potential sliding surface (by means of wells). The tests were fully instrumented in order to monitor the evolution over time of the pore pressure (by means of piezometers and/or tensiometers) and of the deformations (by means of inclinometers and extensometers).

Field tests are useful for the understanding of the problem, but at the same time, are expensive and time-consuming (requiring several months before reaching collapse) and, on account of the big number of involved and partially unknown parameters, not reproducible. These issues can be overcome using small scale physical models.

The only works dealing with the physical modelling of time dependent stability of slopes are those of Davies [52] and Deepa and Viswanadham [53]. Both authors investigated the delayed failure of slopes in the centrifuge. Davies [52] investigated the time dependent stability of a slope due to an increase of the surface loading, while Deepa and Viswanadham [53] investigated the stability over time of a nail reinforced slope induced by imposing an increase of pore pressure inside the model. To the authors knowledge, no physical models reproducing a delayed failure as defined in Section 1.1 (delayed failure under constant boundary conditions and loads) exist.

1.3 Current state of research on transient surface settlements

Over the course of the last decades the topic of surface settlements under transient conditions has been investigated numerically and by means of field observations.

1.3.1 Numerical studies

Several Authors studied the transient surface settlements induced by tunnel excavation by means of fully coupled hydraulic-mechanical analyses. Table 2.2 provides an overview of these numerical studies. (For a review of relevant drained and undrained three-dimensional studies see [54].)

O' Reilly *et al*. [18]and Stallebrass *et. al.* [55] investigated the time-dependent surface settlements that take place after an undrained excavation in clay and silty clay formations using plane strain numerical models. Wongsaroj [20], Wongsaroj *et al.* [56], [21] and Kasper and Meschke [22] investigated similar problems using three-dimensional models that consider the advance of the tunnel face. According to these studies the evolution over time and the final distribution of the surface settlements depend on the permeability model assumed for the soil (*i.e.* isotropic, anisotropic, linear or dependent to the soil stress field) and on the pore pressure on the excavation boundaries. The pore pressure on the excavation boundaries as well as the surface settlements varies significantly depending on whether the lining is permeable or impermeable. A systematic study on transient settlements in London Clay by Wongsaroj *et al.* [21] showed that the ground surface heaves in the long term when a tunnel lining is impermeable, as the negative excess pore pressure generated during tunnel excavation dissipates and the clay swells. When a tunnel lining is permeable, the ground surface continues to settle in the long term, owing to the increase in effective stress associated with the decrease in pore pressure around the tunnel [21]. According to Wongsaroj *et al.* [21] the heaves in the long term are significantly affected by the volume loss, while the magnitude and the width of the consolidation settlement profile is found to increase as the soil's horizontal to vertical permeability ratio increases. Wongsaroj [20], Wongsaroj *et al.* [21] and Kasper and Meschke [22] show numerical results close to field observations of long term surface settlements.

Shahin and Nakai [11], Callari and Casini [12], Höfle *et al.* [14], Anagnostou [13], Callari [15] investigated by means 3D numerical analyses the transient surface settlements that take place during a continuous excavation process (*i.e.* without standstills) in low- to medium-permeability grounds. With the exception of Shahin and Nakai [11], all these studies consider atmospheric pressure at the excavation face and make different assumptions for the lining permeability: a highly permeable lining was considered by Anagnostou [13] and Höfle *et al.* [14]; an impermeable lining was considered by Anagnostou [13], Callari and Casini [12], Callari [15]. Unlined tunnels have been analysed by Callari and Casini [12] and Callari [15]. Shahin and Nakai [11] assume impervious excavation face and tunnel walls for simulating a shield TBM advance with a full compensation of the water pressure.

The above studies show that in the case of atmospheric pressure at the excavation boundaries (*i.e.* atmospheric pressure at the tunnel face, unlined tunnel or lined tunnel with a highly permeable lining) the vertical surface settlement in a fixed cross section increases with the advance of the face and for a fixed distance from the face it decreases with the increasing of the advance rate. Similar behaviour was observed also in the case of impermeable excavation boundaries (*i.e.* full compensation of the water pressure). In the case of atmospheric pressure at the tunnel face and impervious lining a more complex behaviour was observed. The vertical surface settlement increases with the advance of the face and decrease with the increasing of the advance rate only in the vicinity of the face. Starting from a certain distance of the face the total surface settlements may decreases (*i.e.* the surface heaves) with the advance of the face and with the decrease of the advance rate. This behaviour is related to the increase of the pore pressures and to the swelling of the ground occurring far from the face due to the presence of an impervious lining and to the distance of the drainage boundary. This behaviour was pointed out by Anagnostou [13] based upon on numerical analysis assuming a linearly elastic soil model. The same author remarks that with a more realistic material model (taking into account the stiffer ground response to unloading), this effect would be less pronounced and the final settlement would be governed by the deformations around the tunnel heading.

Table 2.2 *Investigations into the issue of surface settlements employing coupled transient numerical analyses.*

Reference	***Type of Analysis***	***Constitutive model***
O' Reilly *et al*. [18]	2D plane strain	Modified Cam-Clay model; Elasto-plastic Mohr-Coulomb model; fully saturated soil
Stallebrass *et. al.* [55]	2D plane strain	So-called 3-SKH soil model; fully saturated soil
Wongsaroj [20] Wongsaroj *et al*. [56] Wongsaroj *et al*. [21]	The short-term variables calculated at the "monitoring/instrument" plane by 3D step by step analysis were transferred to a 2D plane strain model for long-term consolidation calculation.	Critical state model with the sub-loading surface concept, non-linear elasticity and cross-anisotropic elasticity; fully saturated soil
Kasper and Meschke [22]	3D step by step	Modified Cam-Clay model; fully saturated soil
Shahin and Nakai [11]	3D step by step	So-called "elasto-plastic sub-loading t_{ij}" model; fully saturated soil
Callari and Casini [12]	3D step by step	Elasto-plastic Drucker-Prager model; fully saturated soil
Höfle *et al*. [14]	3D step by step	Hardening Soil model; fully saturated soil
Anagnostou [13]	3D one step algorithm	Elastic model; fully saturated soil
Callari [15]	3D step by step	Elasto-plastic Drucker-Prager model; fully and partially saturated soil
Cattoni *et al*. [57]	2D plane strain	Modified Cam-Clay model; fully saturated soil

Only few works ([13], [57]) investigated the effect of the advance rate on the ground conditions (drained, undrained or transient) in the vicinity of the heading in shallow tunnels. Based upon comparative calculations considering specific geometrical and geotechnical conditions, highly permeable tunnel lining and different values of the ratio of advance rate v to permeability k, Anagnostou [13] concluded that the soil response in the vicinity of the heading is practically undrained for $v/k > 10^6$, and practically drained for $v/k < 10^2$.

In order to evaluate the ground conditions (drained, undrained or transient) for TBM excavations in Modified Cam Clay (MCC) soils Cattoni *et al.* [57] performed simplified plane strain analyses introducing a dimensionless factor N_1 (so called normalized face advancement rate and defined as $N_1 = vD\gamma_w/kE_{eq}$, where γ_w denotes the water unit weight, D is the tunnel diameter and E_{eq} is an equivalent soil stiffness defined as the total vertical stress at the tunnel axis to the slope of the normal consolidation line). Based upon the results of these plane strain analyses, which refer to specific geometrical and geotechnical conditions, impervious lining and different values of the factor N_1, Cattoni *et al.* [57] concluded that the ground response in the area of the shield can be regarded as practically undrained for $N_1 > 30$ and practically drained for $N_1 < 0.1$. Moreover, according to their results, the advance rate affects only slightly the maximum final settlements.

Plane strain models (as the one assumed by Cattoni *et al.* [57]) are too simplified for analysing excavation processes characterized by no compensation of the water pressure at the tunnel face (e.g. conventional tunnels, TBM operated in open mode or in closed mode with partial compensation of the water pressure), because they cannot take into account the drainage effect of the tunnel face on the hydraulic and stress field. In these cases 3D fully coupled analyses are indispensable. However, no such 3D systematic study (i.e. considering different geotechnical and geometrical conditions) on the effect of advance rate on the ground response (drained, undrained or transient) to tunnel excavation is found in the literature.

1.3.2 Field observations

A very limited number of publications present measurements of water pressures and consolidation displacements induced by tunnelling in low permeability grounds. This is because the timescale required for field-based research is significantly large. The most of publications report experiences in London clay. A recent review of these works can be found in Wongsaroj [20] and Mair [58]. According to Mair [58] segmentally lined tunnels in London Clay act as drains in most cases, despite the linings have been grouted. The settlements generally continue to increase. Trough width also increases because consolidation of clay occurs over a much wider zone than ground loss caused by tunnel excavation. The magnitude, rate and distribution of the reported long-term settlements cover a wide range of values.

Evaluations on the kind of soil response during the tunnel excavation (drained, undrained or transient) supported by measurements of pore pressures have not been found in literature.

1.4 Structure of the Report

The first part of the Report (Chapters 2 and 3) investigates the influence of the constitutive behaviour of the ground (particularly that of plastic dilation) on the mechanism of delayed failure by means of fully coupled hydraulic-mechanical simulations, and the development of a practical method for dealing with the numerical problem of mesh-sensitivity which occurs in any geotechnical structure at failure due to the structural softening.

Chapter 2 investigates *how delayed failure manifests* itself by considering the time dependent stability of an underwater vertical cut. Although the problem is relatively simple, it provides valuable insights into the mechanism of delayed failure. The results presented are thus also relevant to other geotechnical problems, such as the stand-up time of tunnel headings. Emphasis is placed on the effects of plastic dilatancy as it affects ground response not only quantitatively but also qualitatively. Under the frequently made simplifying assumption of a constant positive dilation angle, coupled analyses inevitably lead to a constant deformation rate at failure, while engineers associate failure commonly with accelerating displacements. Models that allow for shearing under constant volume lead to accelerating displacements but inherently exhibit numerical stability problems close to the failure state. In order to determine stand-up time it is essential to evaluate the numerical results in their entirety, including the time-development of the displacement, stress and pore pressure fields.

Chapter 3 investigates the issue of *mesh dependency* starting with the problem of the underwater vertical cut. The results show that when the flow rule is non-associated the stand-up time decreases with decreasing finite element size. As expected according to the qualitative considerations of Section 1.1.2, the mesh dependency becomes particularly relevant when the assumed cohesion approaches the critical value for which the excavation would be stable under drained conditions. Depending on cohesion, the underwater vertical cut may remain stable in the long term for a coarse mesh, but experience delayed failure when adopting a finer discretization. For lower cohesion values, the mesh-dependency is less pronounced and the stand-up time varies almost linearly with the size of the mesh.

The remaining sections of Chapter 3 investigate the influence of the mesh size on the propagation speed of the shear band (and thus of the stand-up time) considering the simple unloading problem of a rectangular domain under biaxial strain conditions. Based upon theoretical considerations and analytical computations it is shown that (for a given problem layout and fixed material constants) the stand-up time must vary between an upper and a lower limit depending on the mesh size. The two limits correspond to two borderline cases with respect to structural softening: for a coarse mesh the stand-up time tends to the upper limit because the amount of the shear deformation is so small that no softening occurs, while for the fine mesh the stand-up time tends to the lower limit because the large shear deformations cause a great decrease in shear strength.

Finally, Chapter 3 suggests a simple practicable way of estimating a lower upper limit of stand-up time without the need to implement regularization techniques. As the stand-up time depends almost linearly on element size for fine meshes, stand-up time can be determined by performing few computations with relatively fine, but computationally manageable meshes and extrapolating their results to the mesh size that corresponds to the expected, grain-size-dependent thickness of the shear band.

The second part of the Report (Chapters 4 to 6) presents an experimental study and the corresponding validation of the computational method and assumptions. The experiments allow observing the phenomenon of delayed failure under controlled conditions and consist of uniaxial loading tests (Chapter 4) and centrifuge tests (Chapter 5). The experimental results were interpreted also numerically, using material constants which were determined independently (mainly by means of laboratory tests, partially based upon theoretical considerations).

The numerical analyses of Chapter 4 and 5 show that the simple, but widely used, linearly elastic, perfectly plastic model with Mohr-Coulomb yield condition (MC model) and isochoric flow rule generally underestimates the stand-up time. The reason is that it does not account for the plastic volumetric strains accompanying shearing, which temporarily perpetuate negative excess pore pressures, thus delaying failure. The MCC model, which is known to overestimate strength on the dry side of the yield surface, generally overestimates the stand-up time when used in combination with computationally manageable spatial discretization (*i.e.* fine, but still not as much as it would be necessary on account of the experimentally observed very thin shear bands). However, stand-up times very close to the observed ones are obtained by extrapolating the numerical results to the size of the shear band. In conclusion, the MCC model allows for a reasonably accurate prediction of the stand-up time in a typical over-consolidated clay, while the MC model in combination with a fine (but still manageable) discretization provides a conservative estimate.

The findings of Chapters 3 – 5 made it possible to investigate systematically the effect of the decisive geotechnical parameters on the time-dependency of tunnel face stability (Chapter 6). Based upon the results of a comprehensive numerical parametric study, dimensionless design charts were worked-out. The diagrams cover a wide range of ground parameters and apply to shallow tunnels (overburden less than four diameters). The results presented are important for tunnel engineering practice, e.g. when estimating the feasibility of atmospheric interventions in the working chamber of a closed shield. Finally, Chapter 6 presents a simplified approach for the estimation of the critical advanced speed required in order to maintain the face stable during ongoing excavation.

The last part of the Report (Chapter 7) investigates by means of 3D coupled hydraulic-mechanical MC and MCC analyses the tunnelling-induced surface settlements under drained, undrained and transient conditions. Comparative computations highlight the influence of the advance rate, standstills, and drainage conditions at the tunnel boundary (lining permeability) as well as at the tunnel face. On the basis of these parametric computations practical guidelines on evaluating the type of the necessary analysis (drained, undrained or transient) as well as on how to consider transient conditions in a preliminary stage are given. More specifically, a simple equation that expresses the time-dependent surface settlements as a function of the settlements computed under the simplest assumptions of undrained and drained conditions is proposed.

1.5 Publications

Parts of the present report have already been communicated by means of scientific publications: Schuerch and Anagnostou [59]; [60], [61]; [62], [63]), Schuerch *et al.* [64], Schuerch [65].

1.6 Contributions

The *Summary* was drafted by R. Schuerch and P. Perazzelli, revised by G. Anagnostou and finally-checked by A. Vrakas.

Chapter 1 was written by R. Schuerch and P. Perazzelli and revised by G. Anagnostou and A. Vrakas.

Chapter 2 was written by R. Schuerch, G. Anagnostou and A. Vrakas. The formulation of the scientific problem was done by G. Anagnostou. The numerical analyses and the post-processing were performed by A. Vrakas and R. Schuerch.

Chapter 3 was written by R. Schuerch and revised by G. Anagnostou. The formulation of the scientific problem was done by R. Schuerch. The analytical solution for the estimation of the stand-up time (Section 3.3.2) was derived by G. Anagnostou and A. Vrakas.

Chapters 4 and 5 were written by R. Schuerch and revised by G. Anagnostou. The conception, planning and supervision of the experiments as well as the design of the experimental apparatus were done by R. Schuerch. The test apparatus was constructed in the IGT workshop (ETH Zurich) by Mr. A. Kieper and Mr. E. Bleiker. The mechanical and technical support during the experiments in the centrifuge was given by Mr. M. Iten. The preliminary experiments required in order to optimize the test procedures were performed by MSc R. Iten, while the final tests reported here were performed by MSc P. Maspoli. Numerical analyses and evaluation of test results were performed by R. Schuerch.

Chapter 6 was written by R. Schuerch and revised by G. Anagnostou. The numerical models used for the computations were created by R. Schuerch. The parametric numerical study, the post-processing and the representation of results into design nomograms were performed by MSc R. Poggiati under the supervision of R. Schuerch.

Chapter 7 was written by P. Perazzelli and revised by G. Anagnostou, A. Vrakas and R. Schuerch. The dimensional analysis was done by P. Perazzelli. The numerical models used for the computations were created and tested by P. Perazzelli and A. Vrakas. The parametric numerical study was performed by P. Perazzelli. The idea of the s-shaped curve for estimating the time-dependent surface settlements (Section 7.6) was proposed by G. Anagnostou.

Finally, the editorial assistance of MSc R. Poggiati and MSc P. Maspoli in preparing this report is greatly appreciated.

2 Manifestations of delayed failure

2.1 Introduction

The present Chapter investigates how failure manifests itself in coupled FEM analyses by studying the relatively simple plane strain problem of an underwater vertical trench excavation (Figure 2.1), which, on account of the chosen material constants, remains stable in the short-term, but collapses before reaching drained conditions. The reason for considering an *underwater* excavation is to keep the problem as simple as possible. More specifically, as the stationary hydraulic head field is hydrostatic in the case of an underwater excavation, it avoids the additional complexity introduced by long-term seepage forces and by the resulting tensile stresses (the influence of the tensile stresses on the manifestation of failure will be discussed in Chapter 6). Although the problem considered is simple and is analysed assuming the standard Mohr-Coulomb (MC) model and employing a commercial finite element code, it provides an illustration of features that are indeed relevant to many practical geotechnical problems, such the face stability of tunnels or the behaviour of retained excavations in low-permeability soils.

Chapter 2 starts with the setup of the problem and an outline of the computational model, and continues with an investigation of the borderline cases of undrained stability and drained stability. The results of this preliminary analysis serve to identify a set of shear strength parameters for which the excavation is unstable in the long term (hereafter referred to as "critical parameters"). Afterwards, transient stability is investigated for this parameter set by means of fully coupled numerical analyses; it will be shown that under the simplifying assumption of a constant non-zero dilation angle the system reaches a steady state that is characterized by constant non-zero rates of displacement and shear strain. The reason for this model behaviour is that an acceleration in the deformations would imply an accelerating increase in the water content in the shear band, which, as explained later, is physically impossible.

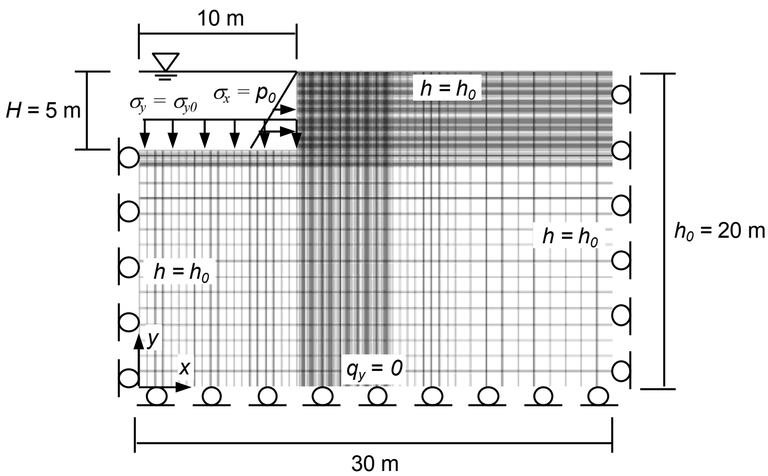

Figure 2.1 *Computational model and boundary conditions.*

Accelerating displacements presuppose that shearing can occur at a constant volume, which is true for most soils (after a certain amount of shearing deformation has taken place) and can be mapped by the appropriate constitutive models. This is illustrated by numerical results for the simplest possible model (a linearly elastic, perfectly plastic material with an isochoric flow rule). The same conclusion applies to models of the critical state family (e.g. Modified Cam Clay model), as shown in Schuerch [65]. Such models exhibit numerical stability problems close to the ultimate state, however, because it is *inherently* impossible to satisfy the equilibrium and the mass balance equations simultaneously.

2.2 Problem setup and computational model

Figure 2.1 shows the geometry and the boundary conditions of the plane strain problem under investigation. The numerical computations are carried-out by means of fully coupled hydraulic-mechanical continuum-mechanical FEM analyses. All analyses executed employing the commercial finite element code Abaqus 6.12 [66]. The resolution of the non-linear equations is carried out by means of the non-linear iteration method after Newton. The initial effective stresses increase linearly with depth depending on the submerged unit weight γ' and a lateral earth pressure coefficient equal to unity.

The soil is modelled as an isotropic, linearly elastic and perfectly plastic material obeying the MC yield criterion with a non-associated flow rule. The integration of the elasto-plastic incremental equations adopts the procedure after Clausen [67]. Seepage flow follows Darcy's law. Table 2.1 and Table 2.2 give the material constants and computational details, respectively.

The undrained excavation was performed over a time interval of 5 h. The numerical simulation procedure is explained in detail in Schuerch [65].

Table 2.1 *Assumed material constants.*

Seepage flow parameters		
Unit weight of water	γ_w [kN/m^3]	10
Permeability	k [m/s]	10^{-9}
Water compressibility	c_w [MPa]	0
Parameters for Mohr-Coulomb material		
Saturated unit weight	γ [kN/m^3]	20
Young's modulus	E' [MPa]	15
Poisson's ratio	ν [-]	0.3
Plasticity parameters	c', φ', ψ	see Figures

Table 2.2 *Computational details.*

Size of computational domain	After Wehnert [68] – see Figure 2.1
Spatial discretization	8-node elements with biquadratic displacement and bilinear pore pressure shape functions
Number of nodes	19,101
Number of degrees of freedom	44,627

2.3 Stability under undrained or drained conditions

The stability (or lack thereof) is evaluated from the displacement of the crest of the excavation (point A in the inset of Figure 2.2b). Figure 2.2b shows the computed displacements of point A as a function of the effective support pressure σ'_x (normalized by the initial effective stress σ'_{x0}) for a specific parameter set.

Under *undrained* conditions (dashed lines) the displacements reach a finite value after complete unloading, which indicates that the excavation is stable. The dilation angle has no influence on the displacements, which is trivial considering that the soil remains practically elastic even after complete unloading (a plastic zone develops only locally at the toe of the vertical cut and at the soil surface, Figure 2.2a).

Under *drained* conditions the displacements become asymptotically infinite at about σ'_x/σ'_{x0} = 13% (solid lines in Figure 2.2b), while a continuous plastic zone develops from the toe of the excavation to the soil surface (Figure 2.2a, solid lines), which indicates that the system has reached the ultimate state.

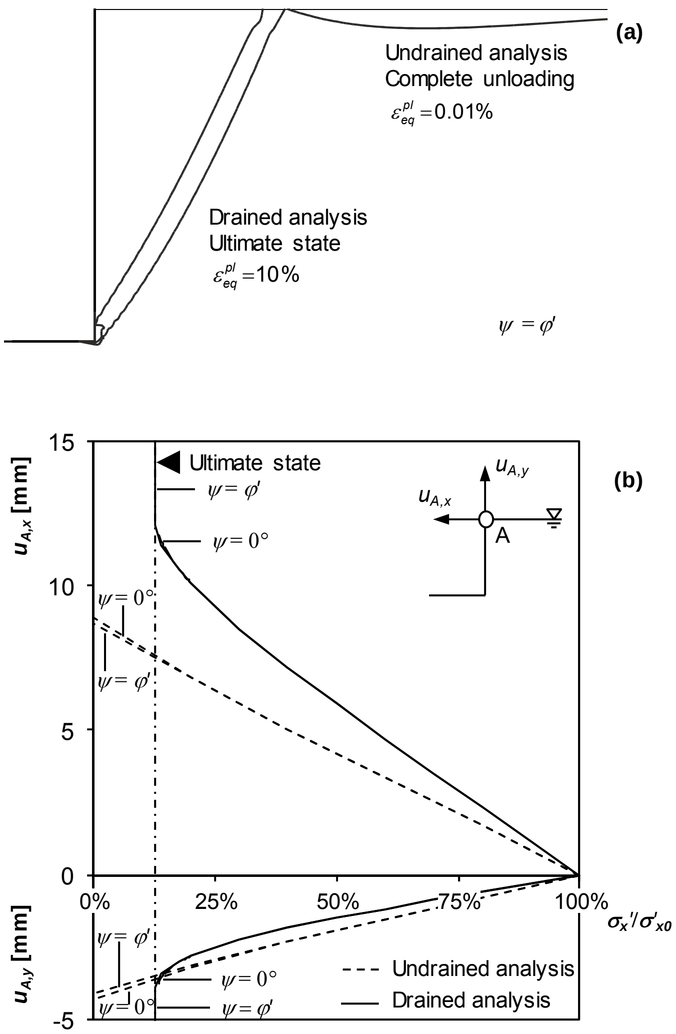

Figure 2.2 *(a) Contour of the plastic zone, i.e. of the region inside which the stress points are located on the yield surface; (c' = 4.5 kPa, φ' = 30°, other parameters according to Table 2.1) and, (b), displacements at the excavation crest (point A) as a function of the normalized effective support pressure.*

According to Figure 2.2b, the plastic dilation angle has a negligible effect on the magnitude of the displacements. The reason is that plastic dilation occurs only inside a relatively narrow shear zone. As expected, the limit pressure for ψ = 0° is slightly higher than for an associated flow rule.

Figure 2.3a shows the results of a parametric study into stability conditions in terms of the effective shear strength parameters c' and φ'. The straight lines were determined analytically according to the active earth pressure theory. The drained stability was computed in terms of effective stresses considering an unsupported vertical cut. The dash-dot applies to the analytical solution proposed by Drescher and Detournay [69] for ψ = 0°, while the dashed line corresponds to the static solution ($\psi = \varphi'$).

The solid line applies to undrained stability and was computed in terms of total stresses, taking account of the support force exerted by the water upon the vertical cut. It is a simple matter to verify [70] that for equilibrium the minimum undrained shear strength

$$s_u = \frac{1}{4}\gamma' H \ , \tag{2.1}$$

where H denotes the height of the cut. Under plane strain conditions and certain simplifying assumptions (no out-of-plane plastic flow, an elastic-perfectly plastic Mohr-Coulomb material with ψ = 0°), the actual average undrained shear strength is related to the effective shear strength parameters and to the *in situ* effective stresses at the mid-height of the vertical cut:

$$s_u = c'\cos\varphi' + \gamma'\frac{H}{2}\frac{(1+K_0)}{2}\sin\varphi' \ . \tag{2.2}$$

Eqs. (2.1) and (2.2) lead to following undrained stability condition in terms of the effective shear strength parameters (solid line in Figure 2.3a):

$$c' = \frac{1-(1+K_0)\sin\varphi'}{4\cos\varphi'}\gamma' H \ . \tag{2.3}$$

The marked points in Figure 2.3a were obtained numerically and agree well with the analytical solutions (lines). The points show combinations of the minimum shear strength parameters under which the unsupported excavation remains stable under drained conditions (white and black circles) or under undrained conditions *for isochoric* plastic behaviour (black diamonds). In the case of *dilatant* plastic behaviour, the excavation always remains stable under *undrained* conditions (due to the unloading-induced suction); for this case (dilatant behaviour, undrained conditions), Figure 2.3a (white diamonds) shows the minimum shear strength parameters that are necessary to prevent the development of a continuous plastic zone from the bottom to the crest of the excavation.

The assumption of an associated flow rule (dilation angle ψ = φ', white markers) leads to slightly lower critical shear strength parameters than that of isochoric plastic flow (ψ = 0°, black markers), both under drained conditions and under undrained conditions (due to structural softening).

The solid and dashed lines in Figure 2.3a delimit three regions: for shear strength pairs (*φ', c'*) within region 1 the excavation is stable in both the short term and the long term (i.e. the stand-up time is equal to infinity); in region 2 the excavation would fail instantaneously (*i.e.* the stand-up time is equal to zero); region 3 exhibits delayed failure (excavation is stable in the short term, but unstable in the long term). As region 3 is quite narrow, Figure 2.3a implies that relatively small variations in the cohesion will result in variations in the stand-up time by orders of magnitude. (The curve in Figure 2.3b was determined numerically after Section 2.5 and illustrates the sensitivity of stand-up time with respect to cohesion for a friction angle of 30°).

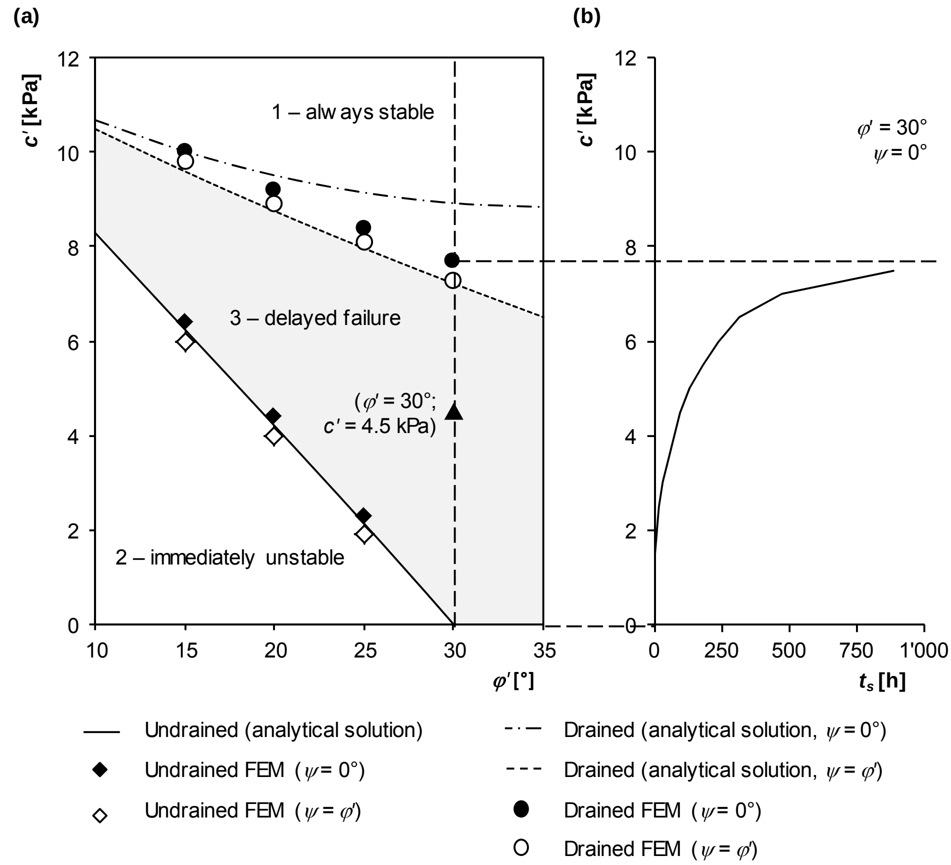

***Figure 2.3** (a) Critical shear strength parameters (c', φ') for undrained and drained stability and, (b), stand-up time t_s as a function of the cohesion c' (parameters according to Table 2.1).*

The transient analyses of the next sections will be carried out for a parameter pair in the delayed failure region (c' = 4.5 kPa, φ' = 30°, marked by a triangle in Figure 2.3a), for which the question of stand-up time arises. The chosen parameter set is representative of soils exhibiting a pronounced time dependency (the shear strength parameters of London Clay after Kovacevic [37]).

2.4 Coupled analysis for dilatant plastic behaviour

2.4.1 Displacement rate

Let first take a material with the associated flow rule ($\psi = \varphi'$). As can be seen from Figure 2.4a, a plastic zone develops progressively over the course of time from the bottom of the vertical cut towards the soil surface, which is reached at about 250 h. As in many other similar problems some early yielding also occurs close to the soil surface. It is associated with the development of tensile stresses at the surface of the model, where the initial stresses are very low [47]. However, although the plastic zone extends up to the surface, thus separating the unstable and stable soil regions, the displacements of the excavation crest (Figure 2.4b, lines for ψ = 30°) do not exhibit the acceleration that one would expect close to the ultimate state, but instead continue to increase at a constant rate.

This happens not only under the assumption of an associated flow rule, but also for any ideal material that does not cease to experience plastic volumetric strains during shearing, *i.e.* under any simplifying constitutive law involving a positive constant non-vanishing dilation angle (see lines for $0 < \psi \leq \varphi'$ in Figure 2.4b). The only difference is that the displacement rate increases with decreasing dilation angle: As shearing is accompanied by plastic volumetric strains, any specific value of the crest displacement is associated with a certain increase in the water content in the plastic zone. The lower the dilation angle, the less the water content must increase in order that the displacement reaches a specific value and, consequently, the earlier the displacement will reach this value or, in other words, the higher the displacement rate will be.

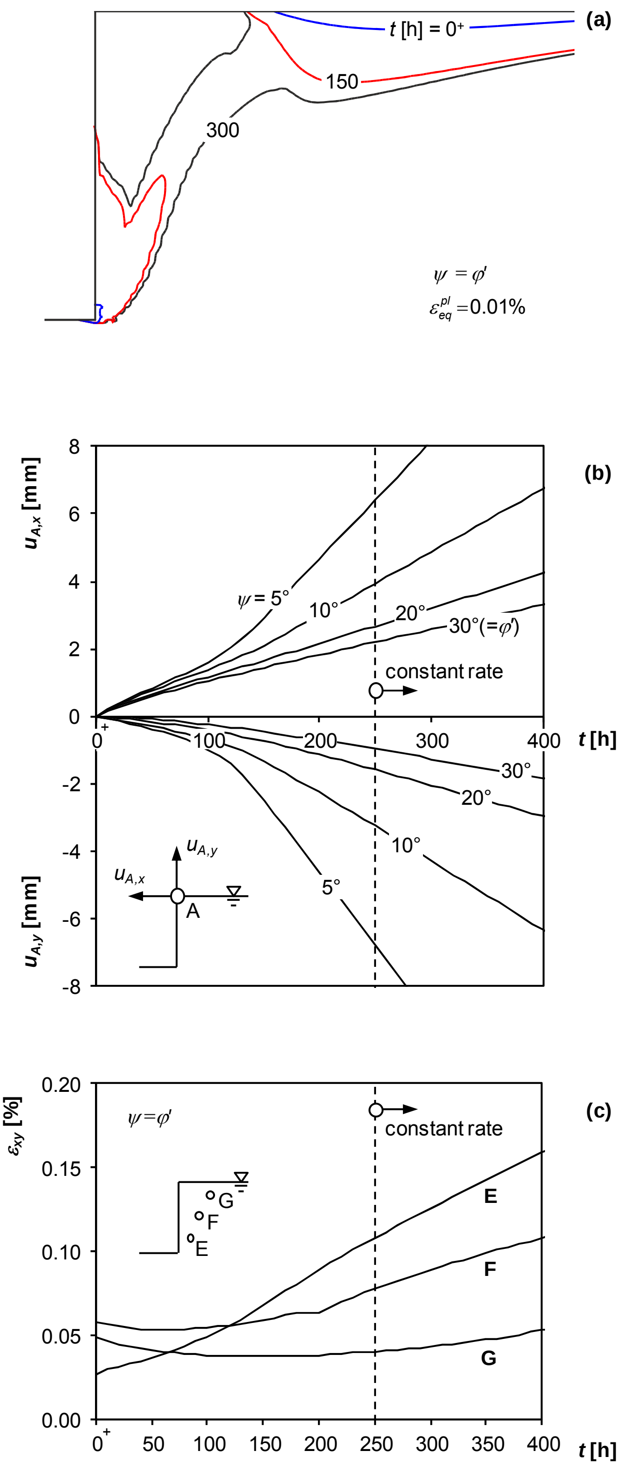

Figure 2.4 *Time-development, (a), of the plastic zone, (b), of the crest displacements and, (c), of the shear strain ε_{xy} at three points in the plastic zone (φ' = 30°, c' = 4.5 kPa, other parameters according to Table 2.1).*

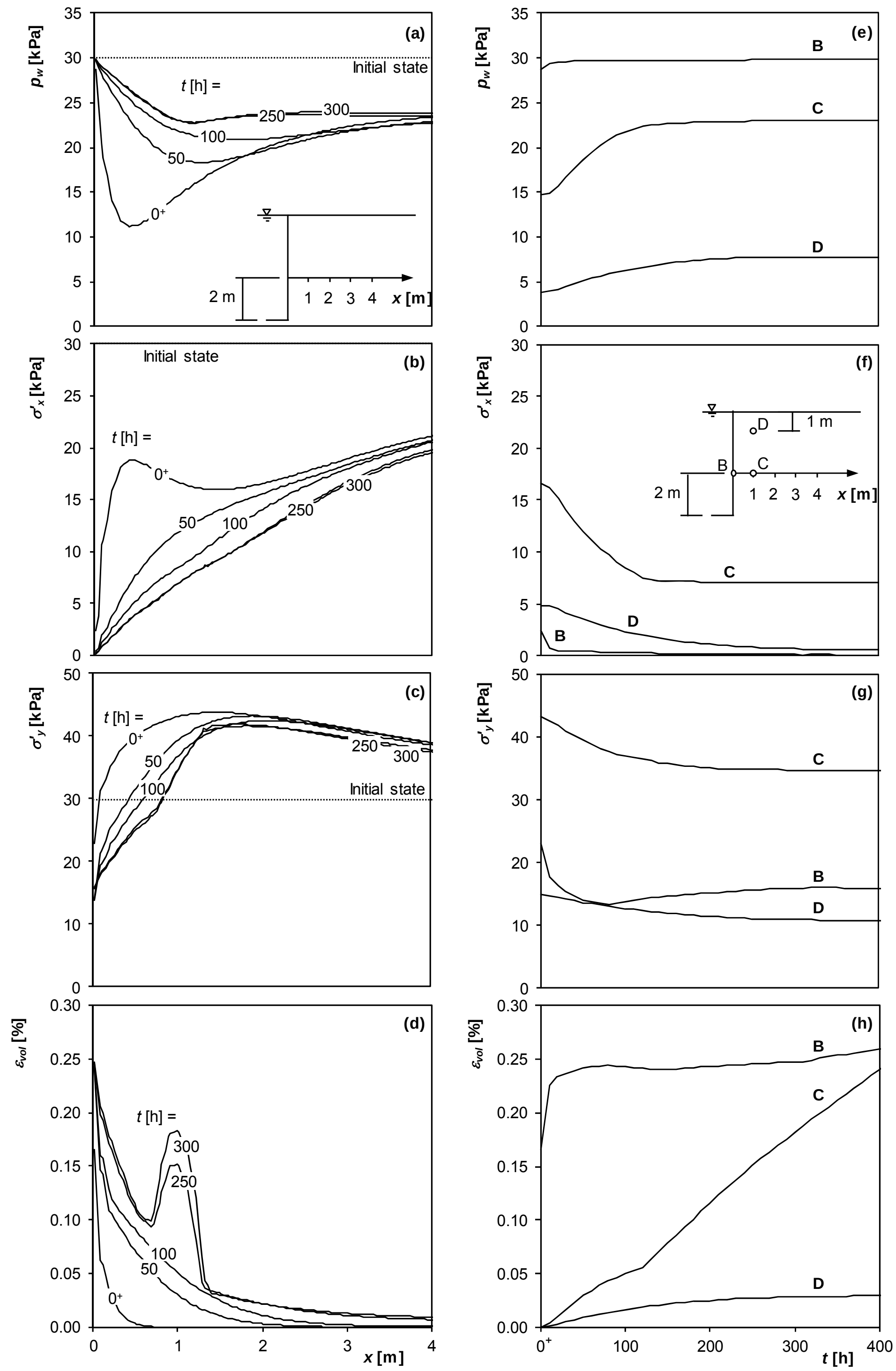

Figure 2.5 *Spatial distribution along a horizontal line (see inset in diagram (a)): (a) pore pressure p_w; (b) effective horizontal stress σ'_x; (c) effective vertical stress σ'_y; (d) volumetric strain ε_{vol}. Time-development at three points (see inset in diagram (e)): (e) pore pressure p_w; (f) effective horizontal stress σ'_x; (g) effective vertical stress σ'_y; (h) volumetric strain ε_{vol} (ψ = φ' = 30°, c' = 4.5 kPa, other parameters according to Table 2.1).*

2.4.2 Pore pressure, stress and strain development

In order to gain more insight into the model behaviour, let study the time-development of pore pressure p_w, the effective stresses (σ'_x, σ'_y) and the volumetric strain ε_{vol}. Figure 2.5 shows the distribution and the time-development of these variables along a horizontal line (see inset in Figure 2.5a) and at selected points (see inset in Figure 2.5e; points B and C are located in the plastic zone, point D is located in the elastic region). Rapid excavation leads to an instantaneous decrease in the pore pressure (Figure 2.5a). The negative excess pore pressures partially counterbalance the excavation-induced decrease in the horizontal effective stress (compare lines for $t = 0^+$ in Figure 2.5a and Figure *2.5*b) and therefore have a stabilizing effect, which manifests itself in the relatively high vertical effective stresses (line for $t = 0^+$ in Figure 2.5c).

The stabilizing effect of the negative excess pore pressures is only temporary because they dissipate over time (Figure 2.5a) according to the imposed boundary condition (hydrostatic pressure), thus leading to a progressive decrease in the horizontal and vertical effective stresses (Figure 2.5b and Figure *2.5*c). After about 250 hours, pore pressures and effective stresses reach a stationary state (Figure 2.5a to Figure *2.5*c, Figure 2.5e to Figure *2.5*g). On the other hand, the volumetric strain in the plastic zone continues to increase at a constant rate (see Figure 2.5d and the lines for points B and C in Figure 2.5h). This is particularly evident in the middle of the plastic zone (point C in Figure 2.5h). As the effective stresses remain constant for t > 250 h, the volumetric strain rate is purely plastic and is associated (due to the assumption of a constant dilation angle) with a constant plastic shear strain rate, which manifests itself macroscopically as a constant velocity of the sliding wedge.

2.4.3 Comments on the steady state

It is remarkable that the dissipation of the excess pore pressures ceases before the pore pressures reach the hydrostatic distribution that would prevail under drained conditions. The steady state is characterized by a *non-hydrostatic* pore pressure distribution or, in other words, by a non-uniform hydraulic head field. The latter fulfils the mass balance equation:

$$-k \cdot \nabla\nabla h = nc_w \dot{p}_w + \dot{\varepsilon}_{vol}^{el} + \dot{\varepsilon}_{vol}^{pl}\,, \tag{2.4}$$

where h, k, n and c_w denote the hydraulic head, permeability, porosity and water compressibility, respectively. At the steady state (*i.e.*, practically, for t > 250 h), the first and the second r.h.s. term disappear (the elastic strain rate is equal to zero because the effective stresses no longer change), while the plastic volumetric strain rate is constant and non-zero. Consequently, Eq. (2.4) becomes

$$-k \cdot \nabla\nabla h = \dot{\varepsilon}_{vol}^{pl}\,. \tag{2.5}$$

According to this equation, the hydraulic head field remains stationary but, rather than being uniform, is consistent with the r.h.s. term, which is imposed by the shearing of the soil at a constant volumetric strain rate. In other words, the shear zone represents a sink. The drop in water pressure in the plastic zone of dilatant materials is known in the literature (e.g. [71]) and has also been observed in laboratory and field tests (e.g. [72], [51]). The gradient of the non-uniform stationary head field causes a permanent seepage flow towards the dilating shear zone, the rate of which controls the rate of displacement. The displacement rate cannot increase continuously, because this would presuppose an accelerating shearing rate and, due to the plastic flow rule, an accelerating water uptake by the plastic zone. The latter would presuppose an accelerating seepage flow rate and, consequently, a continuously increasing hydraulic gradient towards the plastic zone. As the hydraulic boundary conditions are fixed, a continuously increasing hydraulic gradient would be possible only if the hydraulic head in the plastic zone decreased continuously, *i.e.* if the pore pressure in the shear band continued to become more and more negative. This is impossible as it would lead to a continuous increase in shear resistance, thus halting the failure process and contradicting the initial hypothesis of accelerating displacements.

In conclusion, the frequently made, simplifying but nevertheless unrealistic constitutive assumption of a constant non-zero dilation angle not only delays failure in the model, but actually prevents it from reaching the state of accelerating displacements, which is commonly associated with the notion of failure.

It should be noted here that the effect of dilatancy on the displacement rate at failure was first observed by Potts [7] in their numerical investigation into the delayed collapse of cut slopes in stiff clay. They intuitively explained the gradual (rather than sudden) increase in displacement over time as the combined effect of two compensating mechanisms: the decrease in pore water pressure in the rupture zone due to dilation and its increase due to swelling (such that the hydraulic head field becomes stationary, which is the case). Thus, they concluded that '*the drop in pore water pressures due to dilation acts as a partial brake on the rate of post-collapse movement on the slip surface*'.

2.4.4 Estimating stand-up time for $\psi > 0$

Considering the nature of the above limitation in the constitutive assumption (unlimited plastic volumetric strains), stand-up time might be determined by checking when the computed shear strains reach the values at which the soil approaches critical state and, consequently, the assumption of a constant dilation angle becomes absolutely unrealistic. Such an approach does not appear promising because – at least in the computational example under consideration – the displacement rate is already constant at shear strains of less than a few per cent (Figure 2.4c), which are considerably smaller than the values at which the soil would approach a critical state (10 – 40%, *cf.,* e.g. [73]).

On the other hand, considering the prominent role of plastic volumetric behaviour, it may be an oversimplification to define stand-up time as the time lapsing between unloading and the time at which the displacement rate becomes constant. A realistic flow rule, e.g. within the framework of critical state soil mechanics, is indispensable in this respect (see [65]). The following Section investigates the stability of the vertical cut by assuming the simplest possible model, *i.e.* that of a perfectly-plastic material with isochoric behaviour ($\psi = 0°$) right from the start of shearing.

2.5 Coupled analysis for isochoric plastic behaviour

2.5.1 Displacement rate

In contrast to the case of dilatant behaviour (Figure 2.4b), crest displacements increase rapidly to infinity (after about 90 hours, Figure 2.6b). The constitutive assumption concerning plastic dilatancy thus affects the model behaviour not only quantitatively but also qualitatively.

The asymptotic increase in the displacement rate indicates that the system is approaching the ultimate state, and it occurs as soon as a continuous plastic zone forms, delimiting the stable part of the ground from the unstable part (*i.e., t* = 90 h, Figure 2.6a). Once the plastic zone reaches the soil surface, no further stress re-distribution is possible and the excavation collapses.

Failure occurs considerably earlier than the onset of a constant displacement rate in the case of an associated plastic flow (90 h *vs*. 250 h, Figure 2.6b and Figure *2.4*b). These results agree qualitatively with those of Kirkebø [36] and Potts [7], who also found that dilatancy delays the process of pore pressure dissipation. Another remarkable difference between dilatant and isochoric behaviour is that in the latter case shearing occurs within a thin band (see deformed meshes in Figure 2.7) as the plastic deformations are localised in a narrow zone due to the non-associativity of the plastic potential. The localization is not particularly evident in Figure 2.6a because the plotted contour delimits a zone of non-zero, but very small plastic strains.

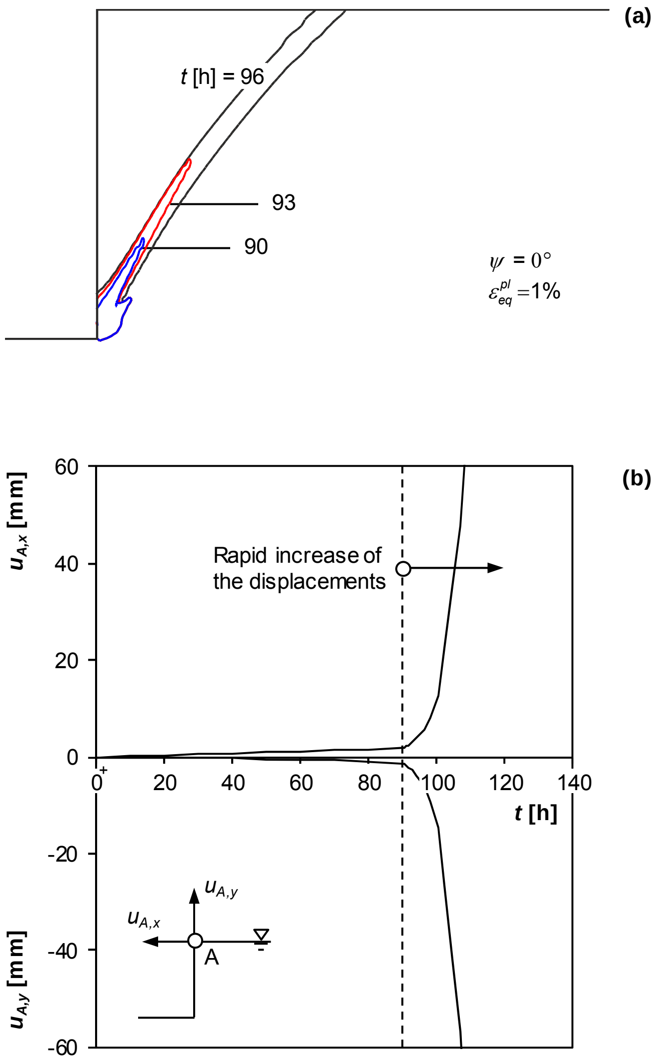

Figure 2.6 *Time-development, (a), of the plastic zone, and, (b), of the crest displacements (ψ = 0°, φ' = 30°, c' = 4.5 kPa, other parameters according to Table 2.1).*

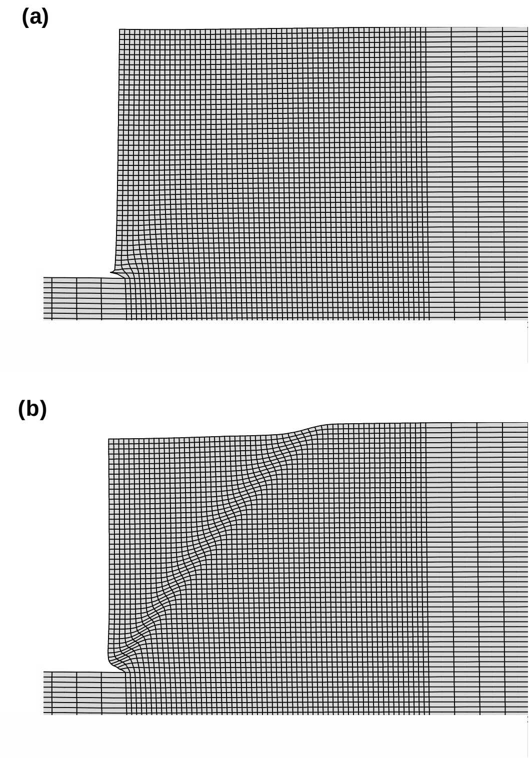

Figure 2.7 *Deformed mesh for associated (a) and isochoric (b) plastic flow at t = 250 and 90 h, respectively (scaled by factor 20).*

2.5.2 Development of pore pressures, strains and stresses

Figure 2.8 shows, in a similar way to Figure 2.5, the spatial distribution and time-development of pore pressure, effective stresses and volumetric strain. The instantaneous response is practically the same as for the case of an associated flow rule.

The evolution of the pore pressure (Figure 2.8a) is similar to the case of an associated flow rule (Figure 2.5a), but the effective stresses decrease faster for $\psi = 0°$ (Figure 2.8b and Figure 2.8c) than for $\psi = \varphi'$ (Figure 2.5b and Figure 2.5c) and, most remarkably, their spatial distribution exhibits oscillations after about 90 hours (Figure 2.8b and Figure 2.8c), while the pore pressure distribution remains almost constant (Figure 2.8a). Kirkebø [36] experienced similar numerical stability problems close to failure. The oscillations are particularly evident in the time-development of the stresses and the volumetric strain in the shear zone after t = 90 h (Figure 2.8f to Figure 2.8h, point C).

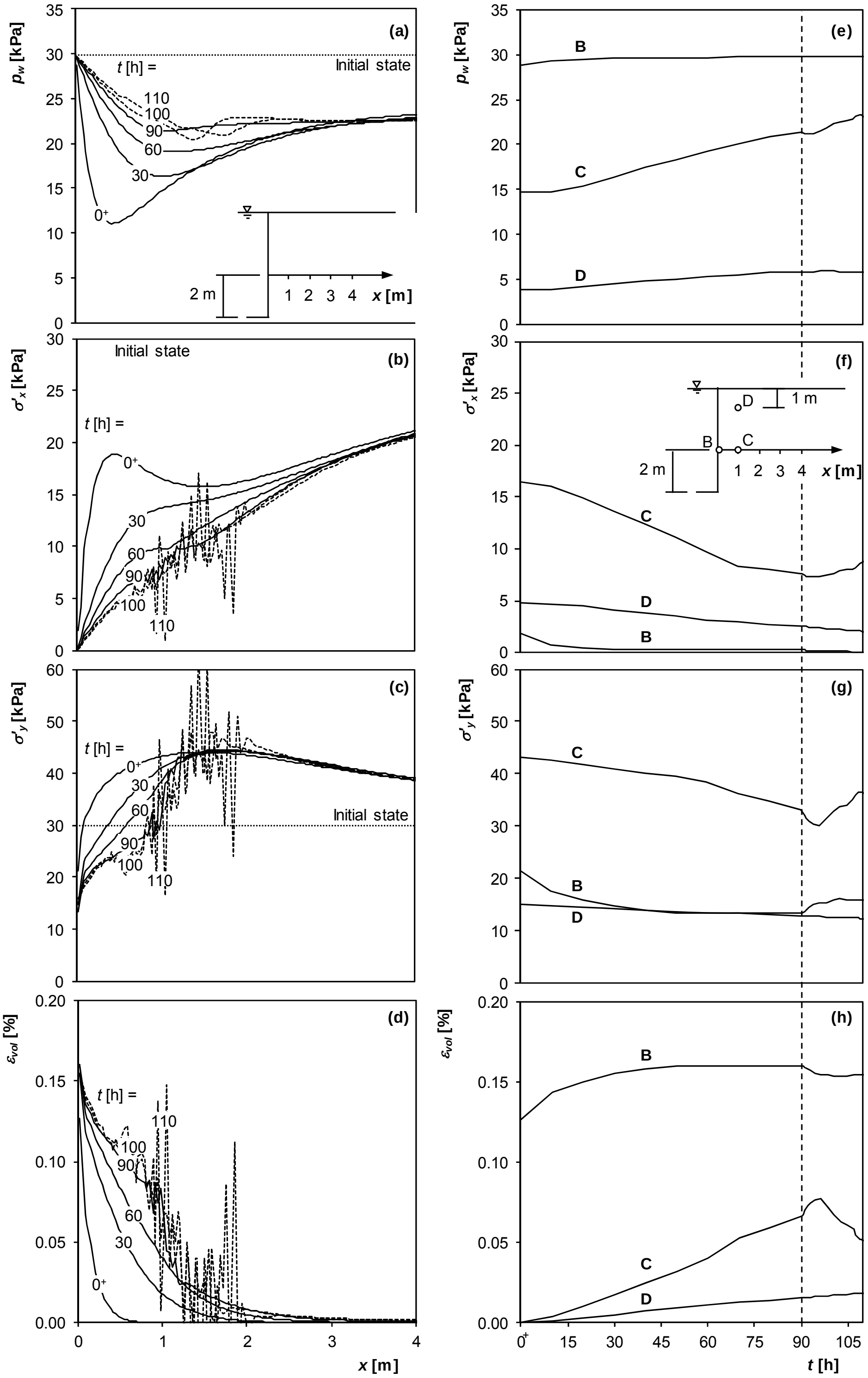

Figure 2.8 *Spatial distribution along a horizontal line (see inset in diagram (a)): (a) pore pressure p_w; (b) effective horizontal stress σ'_x; (c) effective vertical stress σ'_y; (d) volumetric strain ε_{vol}. Time-development at three points (see inset in diagram (e)): (e) pore pressure p_w; (f) effective horizontal stress σ'_x; (g) effective vertical stress σ'_y; (h) volumetric strain ε_{vol} (ψ = 0°, φ' = 30°, c' = 4.5 kPa, other parameters according to Table 2.1).*

2.5.3 Reason of numerical instability

The occurrence of numerical oscillations is related to the inherent impossibility of satisfying both mass balance and equilibrium at the ultimate state for materials exhibiting shearing at constant volume. At the ultimate state, the plastic flow should occur under constant effective stresses and, the elastic volumetric strain rate should therefore become equal to zero. As the plastic volumetric strains are equal to zero as well (ψ = 0°), the source term in the mass balance equation should disappear, *i.e.*

$$-k \cdot \nabla\nabla h = 0\,. \tag{2.6}$$

Eq. (2.6) in combination with the given homogeneous hydraulic boundary conditions implies a uniform hydraulic head field, under which the equilibrium condition cannot be satisfied. This is also the reason why the computed pore pressures (Figure 2.8a and Figure *2.8*e) cannot reach the final hydrostatic distribution according to Eq. (2.6); the source term in the mass balance equation (Eq. 2.4) remains non-zero.

2.5.4 Estimating stand-up time for $\psi = 0$

In conclusion, coupled transient numerical analyses that assume non-dilatant plastic flow can approach, but not reach, the ultimate state. This makes a determination of failure time difficult. In order to estimate stand-up time, one should simultaneously evaluate the time-development and the distribution of displacements, effective stresses and volumetric strains. The ultimate state is characterized by, (i), an increase in the displacement rate of points located within the unstable region of the system, (ii), the development of a continuous plastic zone and, (iii), the onset of spurious oscillations in volumetric strain and effective stresses.

2.6 Conclusions

In order to improve the understanding of the mechanism behind delayed failure and to identify the criteria to be used for determining the stand-up time of the tunnel face, Chapter 2 investigated the relatively simple problem of an underwater vertical cut by means of hydraulic-mechanical coupled finite element analyses.

Starting with the borderline cases of undrained and drained conditions Chapter 2 showed that, depending on the effective shear strength parameters, a vertical cut may either fail during excavation, experience delayed failure (*i.e.* be stable in the short-term but fail in the long term) or be stable in the long term. Stability can be determined by observing the evolution of the displacements at the crest of the vertical cut. It does not depend significantly on the plastic flow rule.

Successively, Chapter 2 studied the transient process under the assumption of dilatant behaviour and a parameter set for which the excavation should experience delayed failure. According to the presented results, the displacements at the ultimate state, rather than accelerating (as in the common conception of a system at failure), continue to increase linearly over time, while the hydraulic head field remains stationary but non-uniform.

This is due to the simplifying constitutive assumption of a constant, non-zero dilatancy angle, which implies that accelerated shearing must be accompanied by an accelerating increase in the water content in the shear zone and thus by negative excess pore pressures of continuously increasing magnitude, which is physically impossible. This behaviour was illustrated here with reference to a simple and widely-used linearly elastic, perfectly plastic constitutive model. However, on account of the underlying mechanism outlined above, softening constitutive models with constant dilation angle would exhibit the same behaviour after reaching residual strength.

In conclusion, the widely made, simplifying but nevertheless unrealistic constitutive assumption of a constant non-zero dilation angle not only delays failure, but actually prevents it from reaching the state of accelerating displacements, which is commonly associated with the notion of failure. The constitutive assumption about plastic dilatancy affects the model behaviour not only quantitatively, but also qualitatively.

In order to obtain accelerating displacements at failure, it is essential to adopt constitutive models that map the soil property to experience shearing at a constant volume (e.g. models from the critical state family). Isochoric shearing leads, however, to numerical stability problems close to failure because it is inherently impossible to satisfy both the equilibrium and the mass balance conditions. In order to estimate the failure time, it is therefore essential to evaluate the evolution of displacements and effective stresses simultaneously, as well as the stability behaviour of the iterative numerical solution algorithm.

3 Mesh dependency of the stand-up time

3.1 Introduction

Materials which exhibit non-associated plastic flow are affected by the so-called structural softening. The structural softening is caused by the rotation of the principal stresses inside shear band: the larger the rotation, the higher the amount of softening. The rotation of the principal stresses depends on the shear deformations. In FEM analyses, the latter depend on the elements size. As qualitatively explained in the Introduction of the present Report, this causes a dependency of the stand-up time to the coarseness of the spatial discretization: the stand-up time decreases with decreasing mesh size because the rotation of the principal axes increases with decreasing mesh size (due to the occurrence of larger shear deformation).

Chapter 3 investigates the influence of the mesh coarseness on the stand-up time on the example of the underwater cut problem of Chapter 2 and, subsequently, for the very simple problem of an axially loaded rectangular specimen under bi-axial strain conditions (hereafter referred to as "biaxial problem"; Section 3.3). The simplicity of the biaxial problem allows, (a), estimating stand-up time also analytically and, (b), performing comparative computations with extremely fine meshes.

The analytical solution derived for the stand-up time of the biaxial problem, considers two borderline concerning amount of structural softening: no softening at all (*i.e.*, no rotation of the principal axes and, consequently, no reduction of the shear strength parameters) and maximum softening (*i.e.*, rotation of the principal axes up to the development of purely plastic shear strains). These two borderline cases provide an upper and a lower limit of the stand-up time, respectively. The numerically predicted stand-up times are between these two bounds.

In order to practically deal with the mesh dependency of the stand-up time, Chapter 3 suggests a way of estimating a lower limit of stand-up time without the need to implement regularization technique: It can be determined by performing few computations with a relatively fine mesh and extrapolating their results to the mesh size that corresponds to the expected, grain-size-dependent thickness of the shear band. The proposed method is based upon the observation that dependency of the stand-up time on the size of the elements becomes almost linear for relatively fine meshes and it is supported by the analytical solution, which shows that there exist a non-zero bound of the stand-up time.

3.2 Underwater vertical cut

The purpose of the present Section is to investigate the role of the discretization on the manifestation of failure and on the stand-up time on the basis of the same problem of Chapter 2.

For the material parameters assumed in Table 2.1, the element size has no influence on the model behaviour (failure manifests itself by an acceleration of the displacements rate to infinity when assuming materials that allow for shearing under constant volume) but influences the stand-up time when considering a non-associated plastic flow: the stand-up time decreases with decreasing element size; the finer the discretization, the earlier the system fails (Figure 3.1).

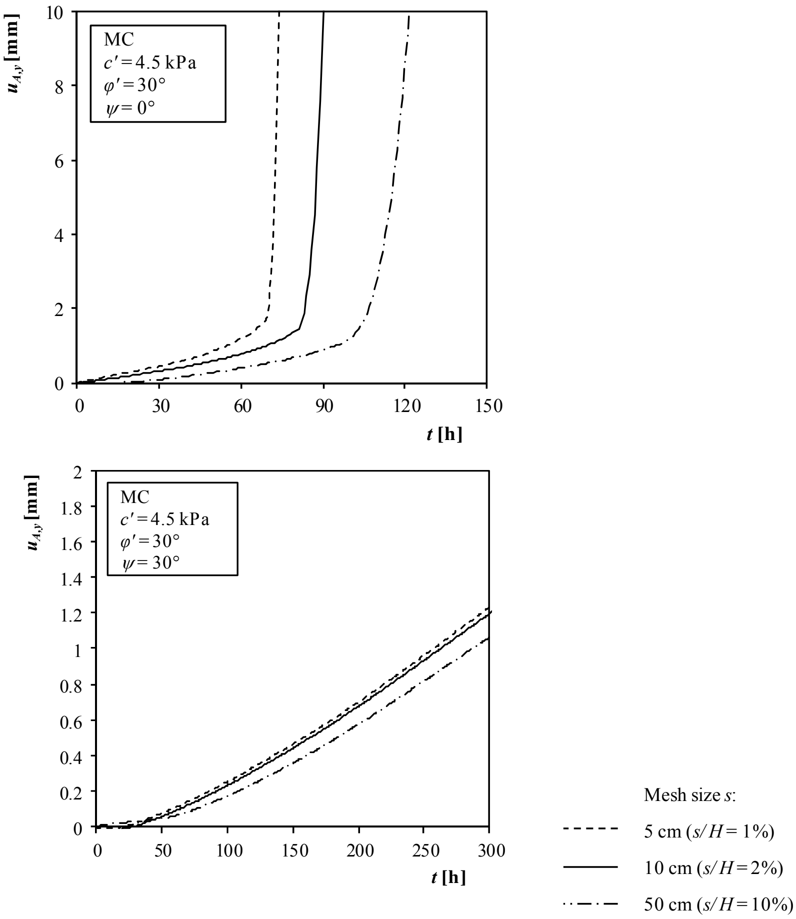

Figure 3.1 *Time-development of the vertical crest displacement for several values of mesh size assuming isochoric and associated plastic flow (parameters according to Table 2.1).*

3.2.1 Critical strength parameters

Figure 3.2a shows the analytical relationships between the friction angle and the cohesion that are required for stability under undrained (solid line) or drained conditions (two upper lines) as well as numerical results for drained stability, φ' = 30° and three mesh sizes (black dots). The dashed and the dot-dashed lines in Figure 3.2 are obtained with and without taking into account the reduction of the strength parameters caused by structural softening (solution derived by Drescher and Detournay [69]), respectively.

With a coarse mesh (50 cm) a critical strength is numerically predicted which is close to the analytical solution obtained disregarding the reduction of the operational strength due to principal axes rotation. The finer the mesh, the closer the numerical prediction to the solution considering the maximum reduction of the shear strength caused by structural softening will be.

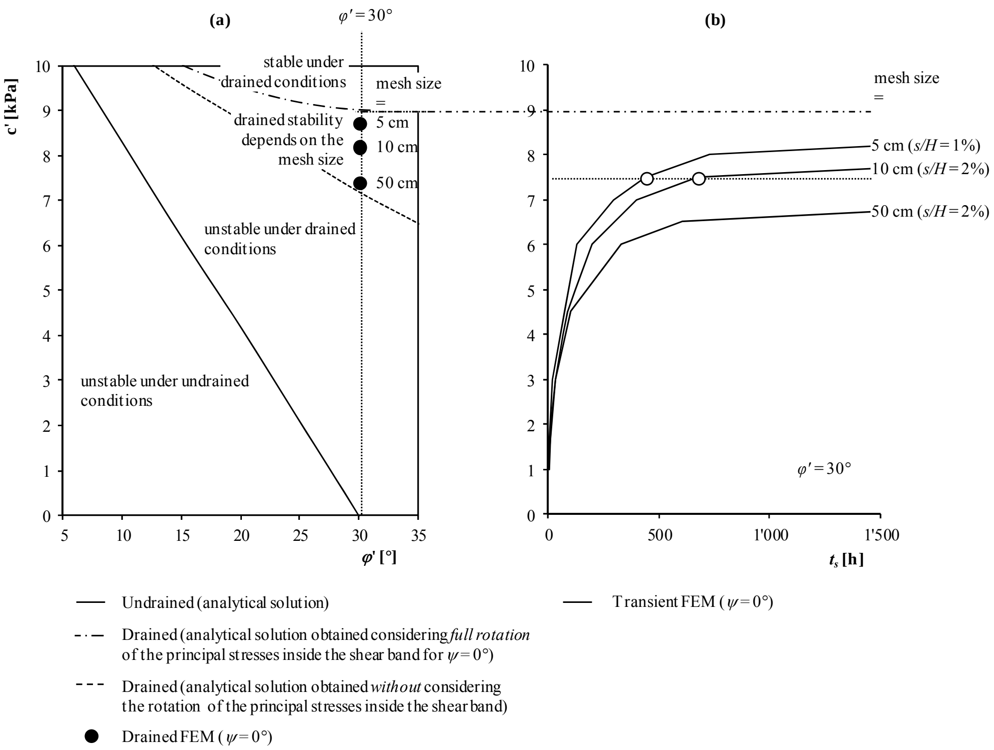

***Figure 3.2** (a) Critical strength parameters for undrained and drained stability and influence of the mesh size for drained FEM stability analyses; (b) Stand-up time as a function of the cohesion for mesh size 5 cm, 10 cm and 50 cm (parameters according to Table 2.1).*

3.2.2 Stand-up time

Figure 3.2b shows the stand-up time as a function of the cohesion for the three mesh sizes. In accordance with the qualitative explanation of Section 1.1.2, the influence of the spatial discretization on the stand-up time is particularly pronounced when the cohesion is close to the critical value for drained stability. For cohesion values of Figure 3.2a in the range bounded by the analytical solutions obtained taking into account or disregarding the effect of structural softening, the stand-up time can be finite or infinite depending on the mesh size. Consider, for example, a cohesion of 7.5 kPa. The stand-up time corresponds to the intersection point (white dots) between the dashed line of Figure 3.2b and the curves obtained for three mesh sizes. The stand-up time amounts to 440 hours and to 670 hours for mesh size 5 cm and 10 cm, respectively. Thus, the increase of mesh size from 5 cm to 10 cm causes a finite increase of stand-up time of about 230 hours. The curve obtained for mesh size 50 cm, however, does not intersect the dashed line corresponding to 7.5 kPa because, the stand-up time increases asymptotically to infinity approaching a cohesion value of about 7 kPa. This means that for mesh size 50 cm and cohesion 7.5 kPa, the stand-up time is infinite, so that the change of stand-up time caused by the increase of mesh size from 10 cm to 50 cm is infinite as well.

The dependency of the stand-up time on the mesh size is additionally illustrated by Figure 3.3. For a cohesion c of 4.5 kPa the stand-up time depends almost linearly on the mesh size; for c = 7 kPa the mesh dependency of the stand-up time becomes strongly non-linear; and, for c = 7.5 kPa, the stand-up time becomes infinite for mesh sizes larger than 20 – 30 cm, which means that the spatial discretisation influences the predicted response qualitatively. The vertical cut is stable for large element size because the mobilized operational strength parameters are high enough in order to satisfy the stability under drained conditions (strength parameters located above the dashed line of Figure 3.2a), while for smaller mesh size the mobilized operational strength parameters are such that, the excavation collapses before reaching drained conditions (strength parameters located below the dashed line of Figure 3.2a).

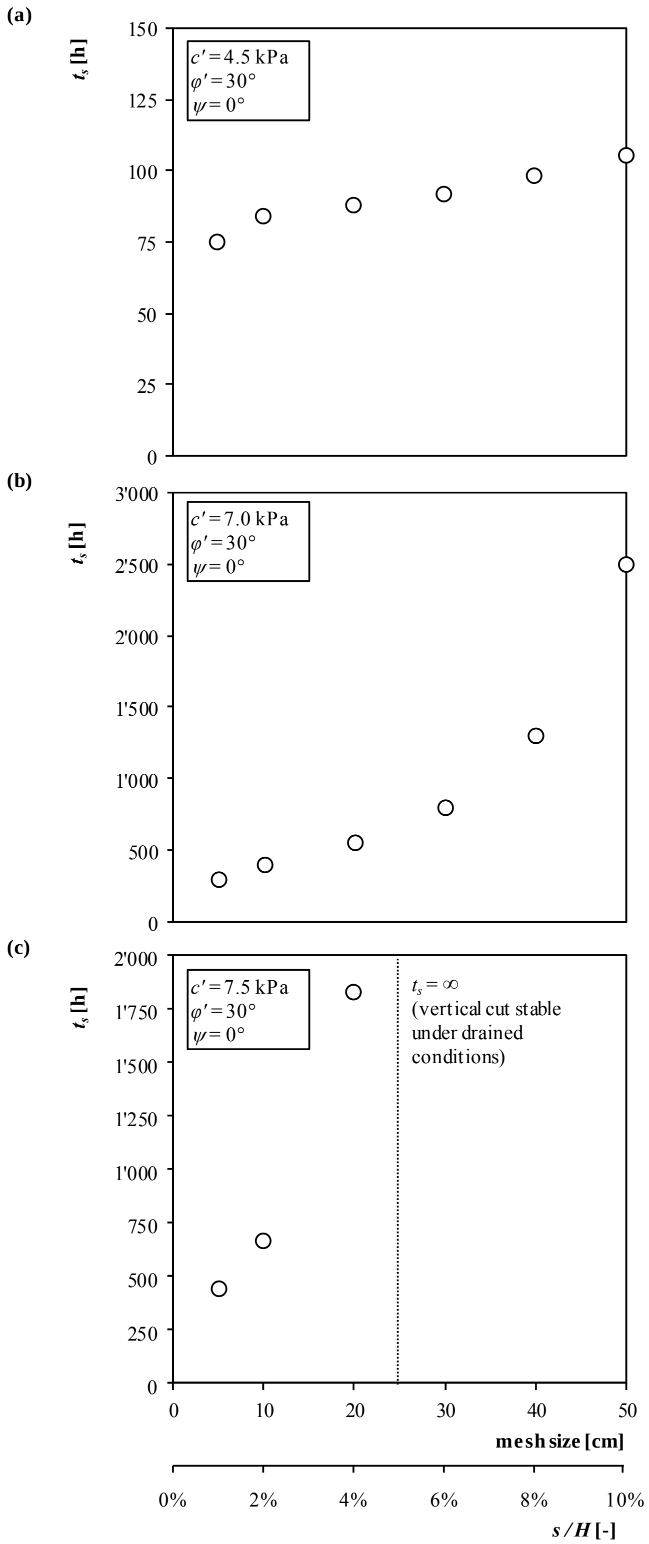

Figure 3.3 *Stand-up time as a function of the mesh size for cohesion (a) 4.5 kPa, (b), 7 kPa and, (c), 7.5 kPa (other parameters according to Table 2.1).*

3.3 Biaxial problem

3.3.1 Problem definition

The problem under consideration is a rectangular specimen under biaxial conditions (Figure 3.4). The specimen is initially under an isotropic total stress of σ_{x0} = σ_{y0} = 300 kPa and a pore pressure of p_{w0} = 100 kPa; subsequently, it is subjected to undrained unloading along its right boundary PQ by reducing the boundary traction s_x from 300 kPa to 100 kPa rapidly (Δs_x = -200 kPa), while keeping the boundary traction s_y along the upper boundary QR constant to 300 kPa. The undrained unloading of the model generates a uniform negative excess pore pressure (see [65]). Subsequently, a pore pressure of 100 kPa (as in the initial state) is prescribed at the drained boundary OP (the remaining boundary PQRO is considered as being impervious), thus initiating an excess pore pressure dissipation process.

The material behaviour is taken linearly elastic, perfectly plastic according to Mohr-Coulomb (MC) yield criterion with isochoric plastic flow (ψ = 0°) and the material constants after Table 3.1.

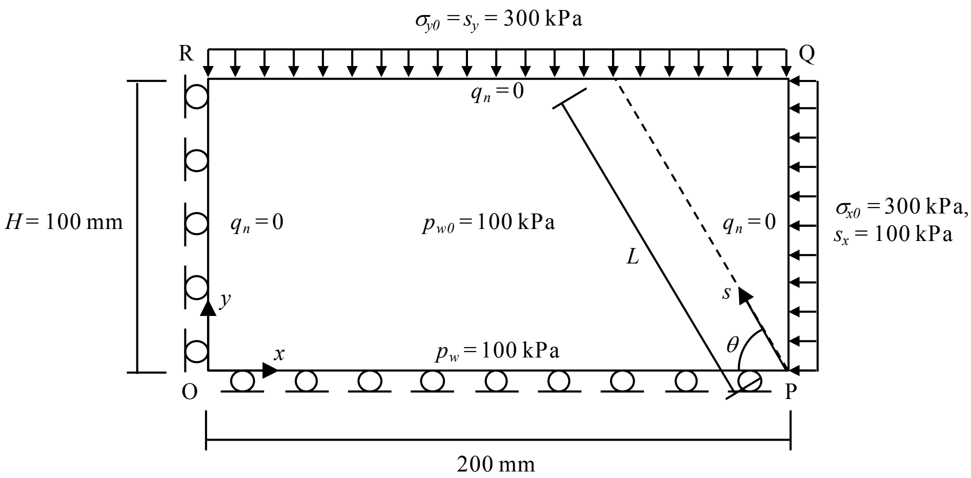

Figure 3.4 *Biaxial problem layout, initial and boundary conditions.*

Table 3.1 *Assumed material constants.*

Unit weight of water	γ_w [kN/m^3]	10
Water compressibility	c_w [MPa]	0
Young's modulus	E [MPa]	100
Poisson's ratio	ν [-]	0.3
Angle of internal friction	φ [°]	30
Dilation angle	ψ [°]	0
Cohesion	c [kPa]	50
Permeability	k [m/s]	10^{-9}

3.3.2 Analytical solution for the estimation of the stand-up time

An analytical solution for the estimation of the stand-up time based upon the limit equilibrium of a sliding wedge (delimited by the dashed line in Figure 3.4) is found in Schuerch [65]:

$$U(t_s) = \frac{1}{p_{w0}} \left(\frac{c}{\tan\varphi} + \sin^2\theta\, s_x + \cos^2\theta\, s_y - \frac{\sin\theta\cos\theta}{\eta\tan\varphi}\left(s_y - s_x\right) \right). \tag{3.1}$$

where p_{w0} is the initial uniform pore pressure in the model, c and φ are the effective strength parameters, s_x and s_y are the boundary stresses, θ is the inclination of the sliding plane and, finale, η is the reduction factor (taking into account the rotation of the principal axes, see [65]).

The Equation has a solution only if its r.h.s. – which is constant – is between 0 and 1. One can easily verify that if the r.h.s. term is negative, then the system would be unstable already at $t = 0^+$ (*i.e.*, under undrained conditions), while if it is higher than 1, then the system would be stable even under drained conditions. In order to avoid the numerical solution of the non-linear Equation (3.1), it is advantageous to solve it with respect to c and compute the cohesion that is required for given stand-up time t_s.

The evaluation of Eq. (3.1) requires an assumption concerning the inclination θ of the sliding surface. The latter corresponds to the angle which minimizes the stand-up time (and so maximizes the required cohesion). For given material parameters and boundary stresses (s_x, s_y), the stand-up time (resulting from the solution of Eq. 3.1) depends only on the reduction factor η. Taking the upper and lower boundary of the reduction factor (see [65]), Equation (3.1) provides an upper and a lower limit of the stand-up time, respectively.

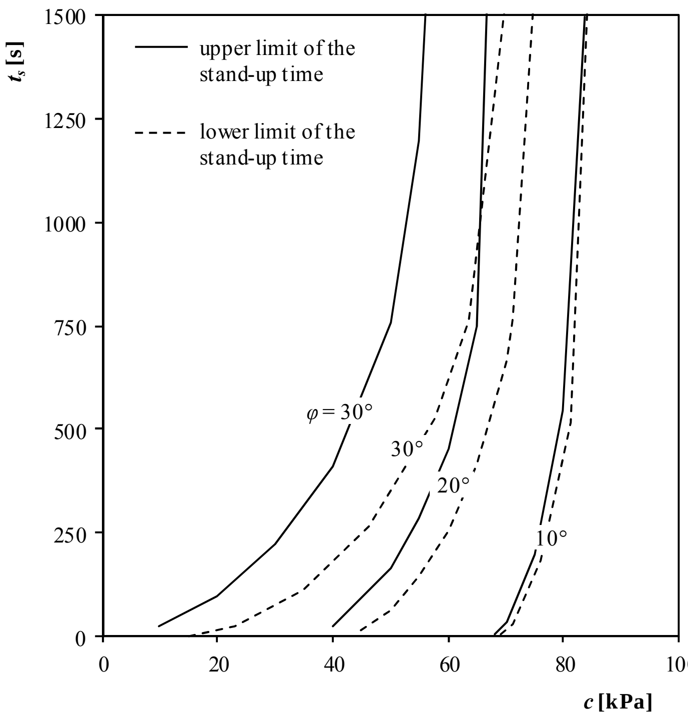

Figure 3.5 *Upper and lower limit of the stand-up time (other parameters according to Tab. 3.1).*

Figure 3.5 shows the upper and the lower limit of the stand-up time computed for three values of friction angle. The influence of the structural softening on the stand-up time increases with the friction angle. As discussed in Section 3.2.2, the difference is particularly pronounced when the cohesion approaches the critical value for which the problem is stable under drained conditions. For such cohesion, the stand-up time is infinite when the rotation of the principal axes is neglected, but reduces to a finite value when taking into account the full rotation of the axes. In conclusion, for cohesion values close to the critical one, the structural softening influences the stand-up time quantitatively and qualitatively.

Finally, for the parameters given in Table 3.1, the upper limit of the stand-up time is 759 s and the lower one 335 s.

3.3.3 Numerical estimation of the stand-up time

Schuerch [65] shows that the occurrence of failure is associated with the formation of a shear band (*i.e.* a region with concentrated intense shear deformation), which propagates from the bottom of the model towards its top over time. Failure occurs when the shear band fully develops through the model. The propagation of the shear band is mainly due to a combination of (i) a reduction of the shear resistance caused by the dissipation of the excess pore pressure (leading to a reduction of the effective stresses) and (ii) a progressive reduction of the operational shear strength caused by structural softening.

Figure 3.6 shows the evolution over time of the displacements at the upper right corner of the model. For the considered problem, failure occurs at t = 530 s. This time point corresponds to the formation of a shear band developing from the bottom to the top of the model (see inset in Figure 3.6). As isochoric plastic flow is assumed, collapse manifests itself by an asymptotic increase to infinity of the displacements of the unstable part of the model (Figure 3.6; *cf.* Chapter 2).

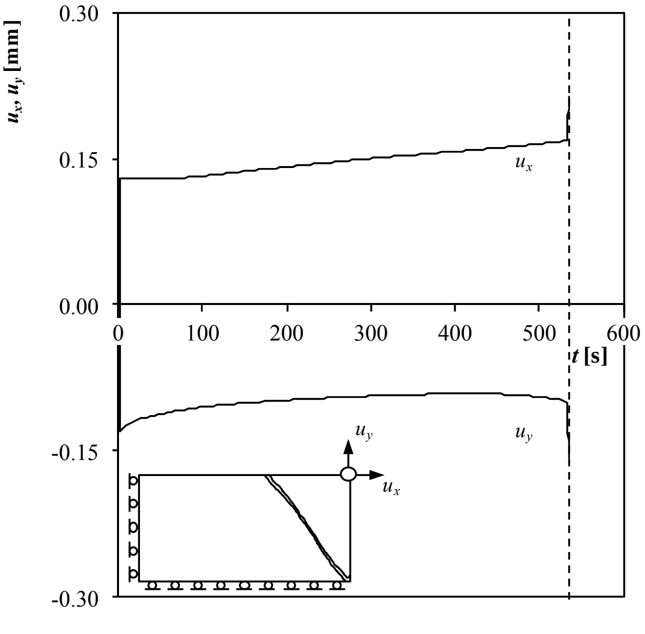

Figure 3.6 *Time-development of the displacements at the top-right corner.*

3.3.3.1 Influence of the element size on the stand-up time

3.3.3.1.1 Numerical results

The model behaviour was investigated for a series of mesh sizes varying between 0.5 mm and 12.5 mm (which is equal to 0.5 – 12.5% of the specimen height and results to a spatial discretization by 400 x 200 – 16x8 elements, respectively). The numerical results (Figure 3.7) allow drawing the following conclusions: The stand-up time increases from 455 s to 685 s with increasing mesh size; the numerically predicted stand-up times are between by the two analytically determined limits; The stand-up time trends to a constant value for large elements, while it depends almost linearly on the element size for small elements reaching a non-zero value as the element size approaches zero.

Comparative coupled analyses with other material parameters allow drawing the same conclusions [65].

3.3.3.1.2 Interpretation

The main cause of mesh-dependency of stand-up time is structural softening. The amount of structural softening increases with increasing shear deformation. Due to localization, the shear deformation increases with decreasing element size. The larger deformation causes a decrease of the operational shear strength, and so a reduction of the stand-up time.

The analytically predicted lower bound of the stand-up time corresponds to an instantaneous decrease of the strength parameters to the operational residual one. Localization occurs also when using large elements, but in this case the shear deformation and the principal axes rotation are so small that softening has almost no influence on the stand-up time.

3.3.3.1.3 Stand-up time estimation for very thin shear bands

The linear dependency of the stand-up time to the mesh size observed for fine meshes in Sections 3.2.2 and 3.3.3.1.1 and the demonstration that the stand-up time tends to a non-zero value for extremely small element sizes, suggest that a practicable way of estimating the stand-up time is to perform few computations with relatively fine, but computationally manageable meshes and extrapolate their results to the mesh size that corresponds to the expected, grain-size-dependent thickness of the shear band (which is practically zero).

As shown in Section 3.2.2 and as depicted exemplary by Figure 3.8, there are situations for which the strength parameters are such that the stand-up time varies very sensitively with the element size (from a finite value to an infinite one). For these cases the linear extrapolation should be carried-out only between the stand-up times obtained with sufficiently small elements (such that the relationship between the stand-up times and the mesh size is almost linear, see e.g. dashed line in Figure 3.8).

Otherwise the inclination of the extrapolated line could result to a negative extrapolated stand-up time, which would be obviously erroneous (see e.g. dot-dashed line of Figure 3.8).

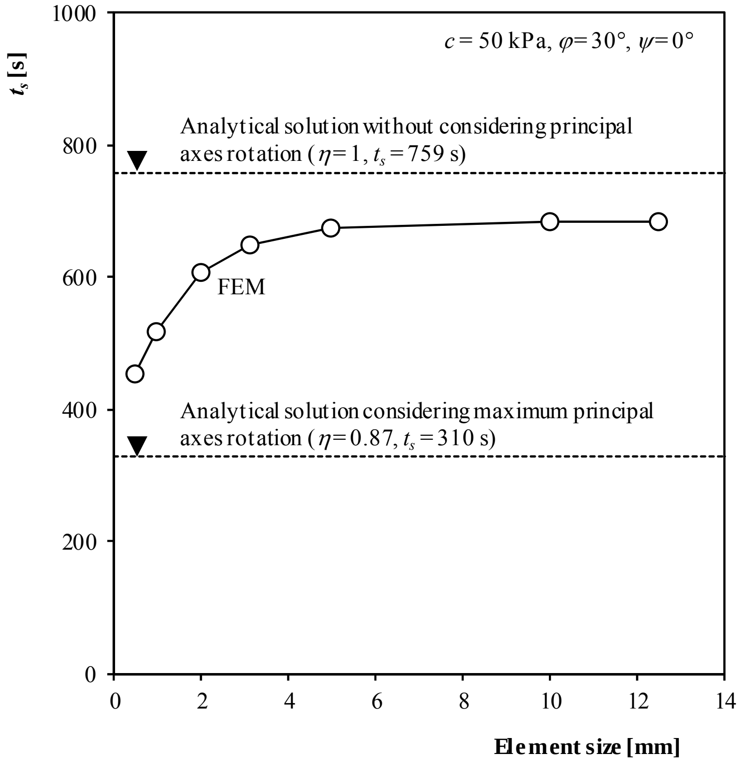

Figure 3.7 *Stand-up time as a function of element size.*

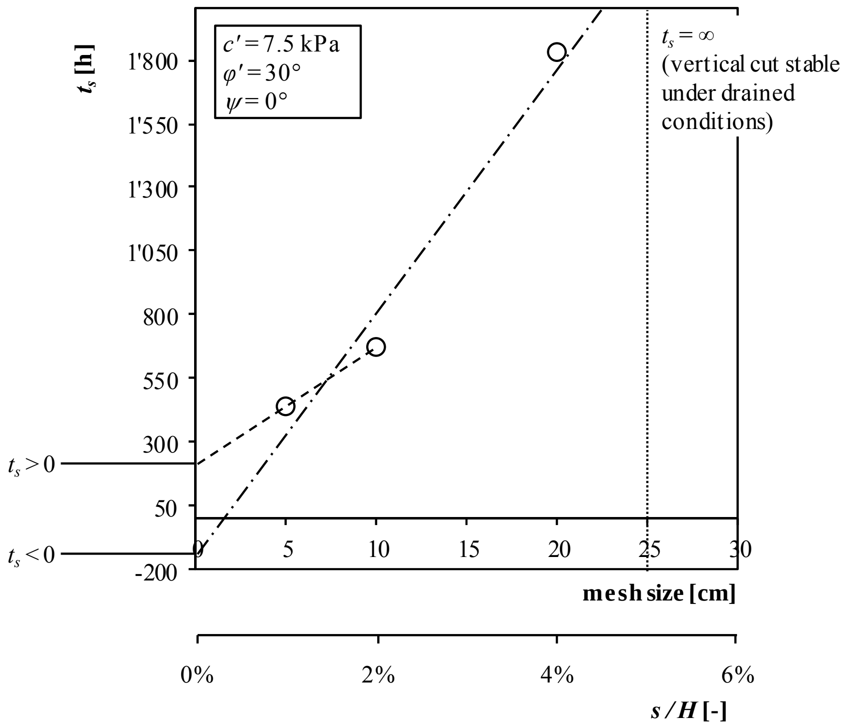

Figure 3.8 *Linear extrapolation of the stand-up time in the example of the underwater vertical cut of Figure 3.3c.*

3.4 Conclusions

The excess pore pressure dissipation causes a gradual reduction of the effective stress both inside and ahead of the shear band. The decrease in the effective stress along the shear band results to a decrease in its shear resistance, which is additionally assisted by structural softening induced by the non-associativity of the flow rule. As the shear stresses decrease inside the shear band, the shear stresses must increase ahead of the shear band in order to satisfy equilibrium, thus causing failure propagation. This stress redistribution process continues until the shear band has progressed through the entire system. Afterwards, the system collapses.

Chapter 3 showed that the coarseness of the spatial discretization generally influences the model behaviour quantitatively but not qualitatively. The assumption of non-associated plastic flow leads to mesh-dependency of the stand-up time: the finer the FE mesh, the earlier the system will fail. An exception occurs when the strength parameters are close to the critical values for drained stability. In this case the occurrence, or not, of instability during the swelling processes depends on the size of the mesh.

The main reason for the mesh dependency of the stand-up time is that the amount of softening increases with the shear deformation, and so with decreasing element size. Chapter 3 analytically showed that, the stand-up time is bounded by an upper and a lower limit, which correspond to zero and maximum softening (as derived by Schuerch [65]), respectively.

Finally, the numerical results showed that the stand-up time depends almost linearly to the mesh size for relative fine meshes. This is a valuable result, as it suggests a practicable way of estimating the stand-up time: It can be determined by performing a few computations with relatively fine, but computationally manageable meshes and extrapolating their results to the mesh size that corresponds to the expected, grain-size-dependent thickness of the shear band.

4 Experimental investigation of stand-up time: uniaxial loading tests

4.1 Introduction

The goal of the present Chapter is to study the delayed failure induced by the transient process of excess pore pressure dissipation by means of a simple experiment and asses the capability of hydraulic-mechanical coupled FEM analyses to reproduce the observed behaviour.

The test consists in loading small prismatic (50 mm x 50 mm x 100 mm) specimens of over-consolidated clay by a constant uniform vertical pressure and leaving the specimens consolidate or swell under constant boundary conditions until failure occurs. The tests are executed underwater.

The short-term stability of the specimen is due to the negative excess pore pressures that prevail in the specimen at the moment at which the vertical load is applied. The negative excess pore pressures are induced by quickly unloading the sample from the oedometer-cell at the end of the preparation phase.

The specimen behaviour is monitored by recording the vertical displacement of the top of the specimen and the pore pressure inside the specimen over time and by taking pictures at regular time intervals.

Section 4.2 focuses on the experimental study. During testing shear bands develop starting from the specimen corners and propagating over time towards the centre of the specimen. The progression of the shear band is due to the dissipation of the negative excess pore pressure that are generated during the pre-test phase and partially perpetuated during uniaxial testing due to the plastic dilation in the shear bands. Failure occurs shortly after the full development of the shear bands throughout the specimen. It manifests itself by an accelerating displacement. The time lapsing from loading to collapse is defined as stand-up time.

Section 4.3 presents the computational assumptions and results of the performed three-dimensional coupled FEM analyses. The MCC model reproduces qualitatively the observed behaviour but it overestimates stand-up time. The MC model (with isochoric flow rule) underestimates the stand-up time because it does not capture the dilatant behaviour of the overconsolidated material.

4.2 Experimental study

4.2.1 Material and methods

4.2.1.1 Specimen preparation

Specimen preparation consists of 4 main phases: over-consolidation of the clay, extraction of the consolidated material, cutting of the samples and, finally, sample storage (Figure 4.1).

Birmensdorf Clay – a reconstituted natural high plasticity clay [74] – was used in the experiments. The clay was initially mixed with water (initial water content of the clay mixture = 100%) under vacuum and then poured into a large oedometer cell with diameter 250 mm (filling height about 217 mm). In order to avoid sticking, the internal wall of the oedometer cell was covered with a thin plastic sheet lubricated with paraffin oil.

Afterwards the clay was loaded to 100 kPa in 5 loading steps (4 kPa, 15 kPa, 25 kPa, 50 kPa and 100 kPa), then unloaded (in one step) and, finally, left to consolidate at 50 kPa, thus obtaining an uniform OCR of 2. The total consolidation time (loading up to 100 kPa and successive unloading to 50 kPa) took about 30 days.

After the consolidation phase, the material was quickly unloaded and removed from the oedometer cell (Figure 4.1b). The undrained unloading generates a negative excess pore pressure (see [65]).

The material was subsequently cut in 12 prismatic samples, 10 cm high with a base 5 cm x 5 cm (cutting scheme in Figure 4.1c). In order to obtain a precise geometry and limit sample disturbance, the cutting was executed using a thin cutting wire, which was vertically guided by an aluminium frame (Figure 4.1d). Sand was inserted in the open cuts during cutting of the consolidated material in order to avoid the re-sticking of the clay (this also facilitated the handling of the samples in the subsequent preparation phases).

For the period between sample preparation and uniaxial testing, the samples were sealed by a cellophane film and closed in an aluminium formwork (Figure 4.1e) in order to protect them and to limit premature dissipation of the excess negative pore pressure. This sealing system proved to be effective (see [65]).

4.2.1.2 Installation of pore pressure transducers

Pore pressure was measured during consolidation and uniaxial testing by means of micro pore pressure transducers (ppts). The ppts are of type Keller (type 2MIX/2bar/81840.1) and consist of a small sensor (diameter 7 mm, length 11.6 mm) and a data transfer cable (diameter 0.6 mm).

In order to measure pore pressure as reliably as possible, the consolidated material should be disturbed as less as possible. For this reason, the ppts were installed in the clay right from the start (*i.e.* in the initial water - clay mixture).

The supporting system is such that only the sensors and their cables remain inside the material at the end of the consolidation phase. In this system, the ppts are fixed by means of vertical auxiliary wires (Figure 4.2a), which ensure that the ppts maintain their position during the filling of the oedomenter cell with the clay - water mixture and avoid tension between sensors and cables.

Small diameter mono-braid wires (0.4 mm) composed by Dyneema fibers (BR8 by CLIMAX) were used to hang the ppts to an upper support plate (Figure 4.2b). The used wires have a high axial stiffness and tensile strength. The ppts were kept fixed in their initial position until the end of the consolidation step at 25 kPa. After this step the vertical hanging wires were cut, thus leaving the sensors to move freely together with the consolidating soil. The initial elevation of the ppts was chosen such that they reach the centre of the sample at the end of consolidation.

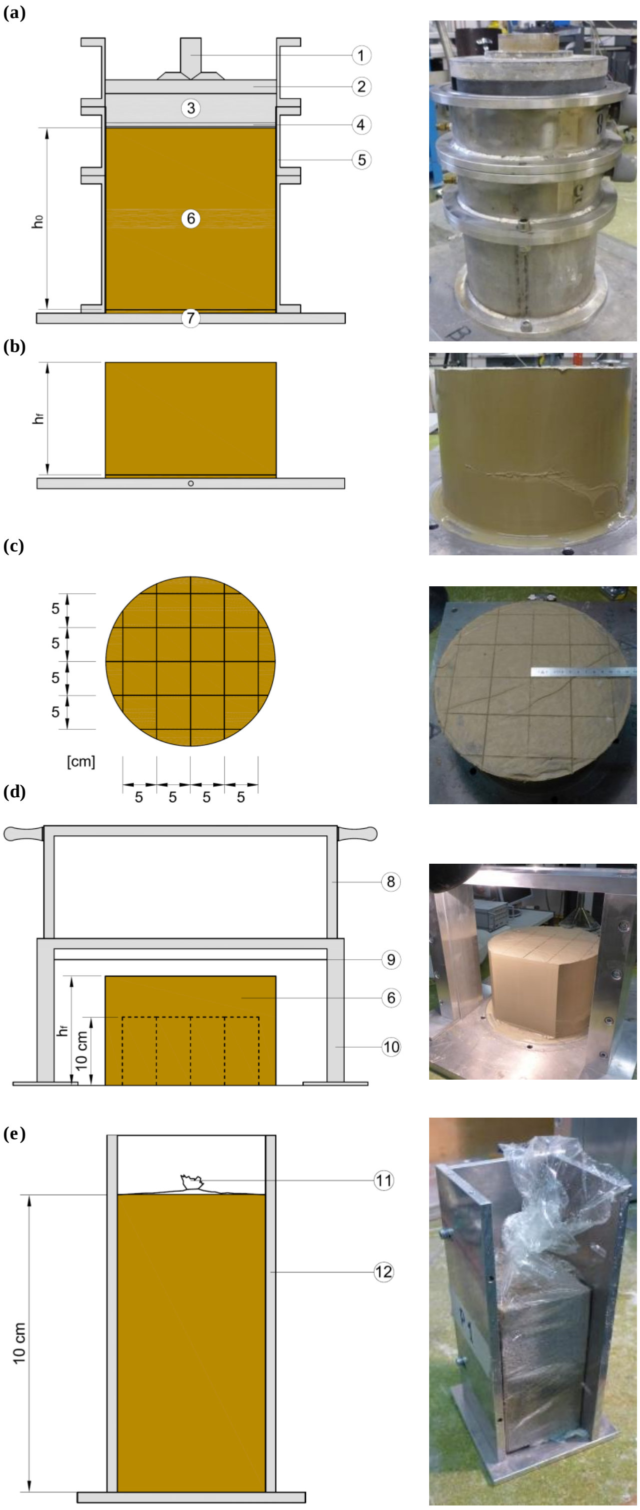

Legend:

1	Load piston
2	Load plate
3	Filter plate
4	Textile and paper filters
5	Oedometer cell
6	Clay
7	Drainage plate
8	Cutting device
9	Cutting wire
10	Cutting guide
11	Cellophane film
12	Formwork

Figure 4.1 *Sample preparation (pre-test phase). (a) oedometer cell, (b) consolidated clay cylinder, (c) cutting scheme, (d) cutting device, (e) sample storage.*

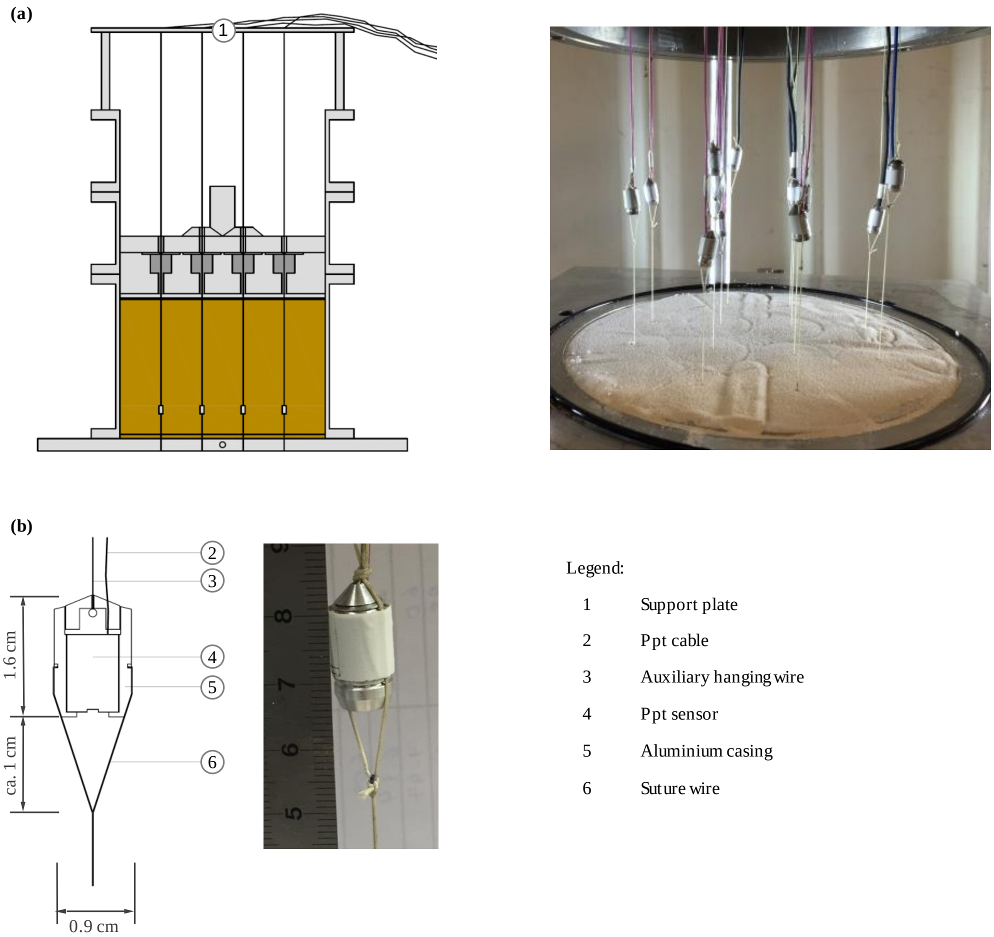

Figure 4.2 *Installation of ppts by means of auxiliary hanging and suture wire. (a) hanging structure and, (b), detail of ppt fixation.*

The ppts were connected to the bottom plate by means of 0.48 mm diameter synthetic absorbable surgical suture wires (type Vicryl Rapide by ETHICON) which dissolve over time (after about 40 days and 90 days in water and clay, respectively). The advantage of the selected wires is that they offer a high short-term resistance (thus ensuring a fixed position of the ppts during filling the oedometer) but, as they dissolve, allow an easy separation of the material from the bottom drainage plate after the consolidation.

For additional details on the model preparation we refer to Schuerch [65].

4.2.1.3 Testing device and procedure

The test consisted of a rapid uniaxial loading by a uniform vertical pressure of 33.3 kPa (applied within about 2 s), followed by a swelling stage under constant load and hydraulic boundary conditions. The test ended after certain time with the failure of the specimen.

The specimen behaviour was monitored by measuring the vertical displacement of the load cylinder and the pore pressure in the specimen centre (by laser and ppts, respectively). In addition, pictures of the deformed specimen were taken at regular time intervals (about every 5 min).

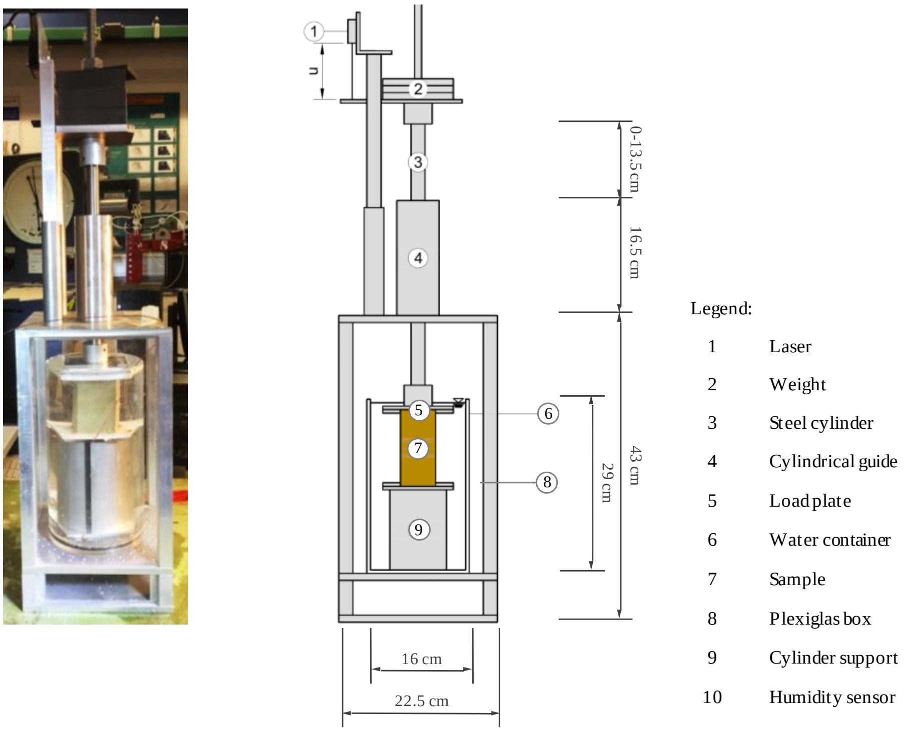

***Figure 4.3** Test device.*

Figure 4.3 shows the apparatus specifically developed for the tests. In order to control the hydraulic boundary conditions, the tests were executed within a chamber, which was composed by an aluminium frame and removable Plexiglas walls. The loading device was outside the chamber; the load was transferred to the sample by means a loading plate that was connected to a vertical steel cylinder. The latter was vertically guided by a tube which was fixed to the upper plate of the chamber. The tube was equipped with two miniature metric ball bushing bearings (MM12WW by Thomson) at its extremities in order to eliminate friction.

4.2.1.4 Material parameters

Table 4.1 gives the parameters of the Birmensdorf clay in terms of the Mohr-Coulomb (MC) and Modified Cam Clay (MCC) models. With the exception of the effective cohesion of the MC model, the values were obtained by means of laboratory tests. The effective cohesion was estimated assuming that the soil behaves as MCC and considering the theoretical effective stress path expected during testing [65].

4.2.2 Results

Figure 4.4a and Figure 4.4b show the time-development of the vertical displacement at the top of the specimen and of the pore pressure in its centre, respectively. Figure 4.4c shows images of the specimen at several times (t = 0 is the time immediately before loading).

The vertical loading of the specimen, causes an instantaneous settlement by 0.5 mm, followed by a time-dependent settlement. The displacement rate is almost constant over the first 3.5 minutes (0.5 mm/min) and increases continuously afterwards (Figure 4.4a). The displacement starts to accelerate when shear bands develop at the corners of the specimen (Figure 4.4c). The shear bands are about 0.1 mm thick and extend over the entire width of the specimen. On the specimen side perpendicular to the plane shown in Figure 4.4c, no shear bands develop.

Table 4.1 *Material constants.*

Saturated unit weight	γ [kN/m^3]	18.2
Unit weight of water	γ_w [kN/m^3]	10
Liquid limit	w_l [%]	58
Plastic limit	w_p [%]	19
Plasticity index	I_p [%]	39
Void ratio (at σ_v = 1 kPa)	e_0 [-]	2
Seepage flow parameters		
Permeability	k [m/s]	1.5 10^{-9}
Water compressibility	c_w [MPa]	0
Parameters for linearly elastic, perfectly plastic MC material		
Young's modulus	E [MPa]	18
Poisson's ratio	ν [-]	0.3
Cohesion	c' [kPa]	9 (see [65])
Friction angle	φ' [°]	24.5
Dilation angle	ψ [-]	0
Parameters for Modified Cam Clay material		
Gradient of swelling line	κ [-]	0.01 (see [65])
Gradient of compression line	λ [-]	0.21 (see [65])
Intercept of compression line	e_1[-]	2
CSL slope in p'-q plane	M [-]	0.96
Poisson's ratio	ν [-]	0.3

The shear bands progress over time toward the specimen centre. The displacement rate increases with increasing shear bands length (compare Figure 4.4a and Figure *4.4*c). At t = 5.7 min the rate increases rapidly and the specimen fails. This happens shortly after the shear bands completely develop through the model.

Figure 4.4b shows that the pore pressure in the centre of the model at t = 0 amounts to -32 kPa. This value is higher than the pore pressure expected theoretically after unloading in the pre-load phase (*i.e.* -50 kPa). The higher value indicates that the excess negative pore pressure partially dissipated during the time lapsing from the unloading and the test execution [65].

Due to the loading of the specimen by 33 kPa, pore pressure increases to -21 kPa (Figure 4.4b, t = 2 s). The loading-induced excess pore pressure of 11 kPa agrees with the value expected for fully undrained loading (Δp_w = 33 kPa / 3=11 kPa).

As the test is executed underwater (*i.e.* the boundary pore pressure is atmospheric), one might expect that the pore pressure would increase continuously to zero. The observed time-development of the pore pressure (in the centre of the specimen) is nevertheless complex: Pore pressure starts to increase, reaches a maximum at t = 0.4 min, then decreases with almost constant rate (-2.1 kPa/min) for about 5 min and shortly before failure starts again to increase.

The decrease in pore pressure after t = 0.4 min is probably due to the partially constrained plastic dilation in the middle of the specimen. This hypothesis is supported by the photographs (Figure 4.4c), which show a slight horizontal expansion of the specimen, and will be validated by means of numerical analyses in Section 4.3. Also the zero rate of pore pressure observed briefly before to failure seems to be related with the plastic shearing: when the material at the centre of the specimen reaches critical state, the shearing continues at constant plastic volume so that no further negative excess of pore pressure is generated.

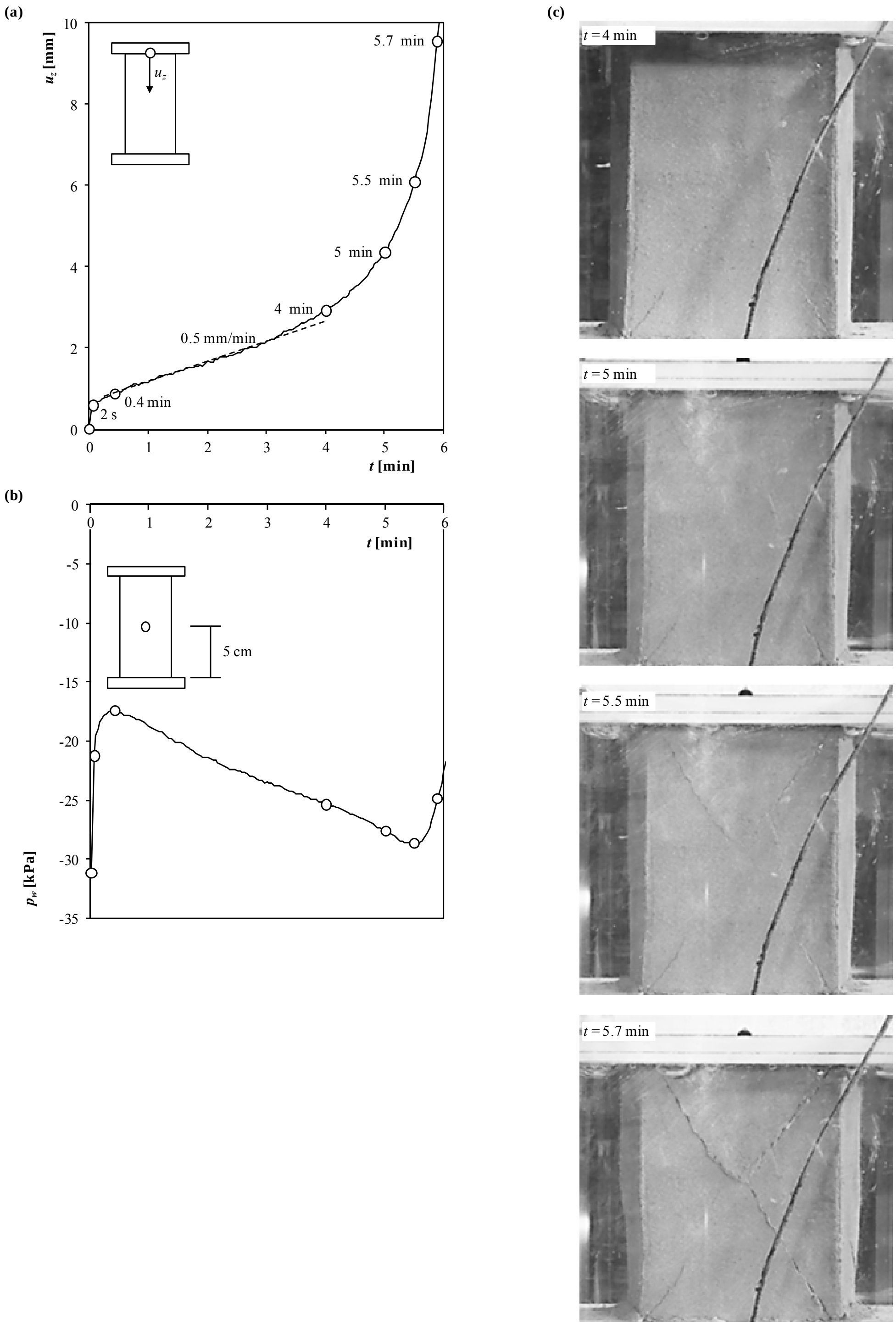

Figure 4.4 *Typical results of underwater tests: Time-development of, (a), vertical displacement of the top specimen boundary and, (b) of the pore pressure in the centre of the specimen (ppt installed with auxiliary hanging and suture wire); (c) lateral view of the deformed sample at several times (the black line in the Figure is the ppt cable).*

4.3 Numerical study

4.3.1 Computational model

The performed tests were simulated by means of three-dimensional analyses. The model was discretized by means of 8-node cubic elements with side length 5 mm and trilinear displacement and pore pressure shape functions (Figure 4.5a).

Figure 4.5b and Figure 4.5c show the boundary conditions and the load applied to the model during the simulation of the consolidation phase in the oedometer and during the uniaxial loading test, respectively. Considering the testing setup, the nodes of the bottom boundary of the model were fixed, while a very high stiffness, simulating the load plate, was assigned to the two uppermost element rows. This modelling of the load plate allows the transfer of the vertical load σ_v (acting on the upper boundary of the numerical model) to the soil, ensuring at the same time a uniform vertical settlement of the upper boundary of the specimen.

The clay is modelled either as a saturated porous medium according to the Modified Cam Clay (MCC) model or as an isotropic, linearly elastic and perfectly plastic material obeying the Mohr-Coulomb yield criterion with isochoric plastic flow (MC model). The seepage flow follows the Darcy's law.

Due to the small size of the specimen, the weight of the soil is not considered in the analyses.

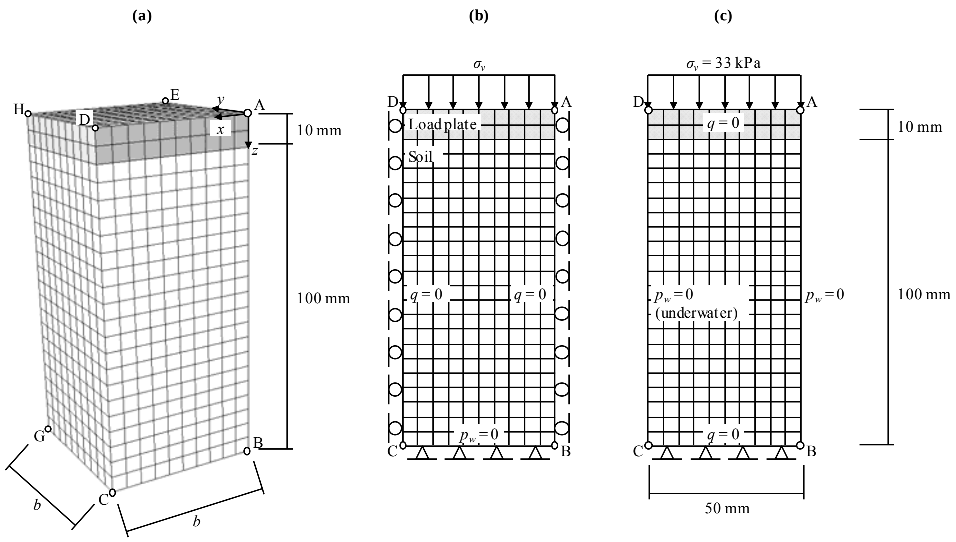

Figure 4.5 *(a) Geometry of the 3D numerical model; (b) boundary conditions and load applied during the consolidation phase; (c) boundary conditions and load applied during the test.*

4.3.2 Computational steps

4.3.2.1 MCC model

In the case of the MCC model one must take into account the stress path and the volumetric changes occurring in the oedometer. This is done in 4 simulation steps:

i) Liquid clay in the oedometer: Initialization of the numerical model considering a uniform and hydrostatic stress of 1 kPa and atmospheric pore pressure;
ii) Consolidation to 100 kPa: Stepwise drained loading of the numerical model up to a vertical pressure σ_v of 100 kPa;
iii) Unloading and swelling to 50 kPa: Stepwise drained unloading to 50 kPa.
iv) Extraction of the consolidated clay from the oedometer, cutting of the specimen and storage of the samples: Deactivation of the rollers along the lateral boundaries and complete unloading of the model in one time step of 2 hours (transient analysis with no-flow condition at the model boundaries).

The simulation of the actual test phase (uniaxial loading) consists of 2 steps:

v) Loading of the sample: Increase in the vertical load from zero to 33 kPa over a time period of 2 s (transient analysis).
vi) Swelling under constant load: transient analysis after instantaneous change of the hydraulic boundary conditions at the lateral surface of the model (Figure 4.5c).

4.3.2.2 MC model

The initial state considered in the simulations with the MC model are those prevailing in the specimen just before uniaxial loading. Consequently, the initial total stresses are taken equal to zero, while the initial pore pressure is considered as uniform and equal to -50 kPa (theoretical suction induced by the undrained unloading after quick removal of the material from the oedometer).

The uniaxial loading is simulated as for the MCC model.

4.3.3 MCC model results

Atmospheric pore pressure is imposed to the lateral boundaries in step (vi) (swelling phase after uniaxial loading).

In order to have a fixed slope of the CSL, and so for the better understanding of the results, the computations assume a circular yield function and plastic potential in the deviatoric plane, taking the slope of the critical state line *M* equal to 0.96 (see [65]), which assumes a Lode's angle of -30° (triaxial compression). The latter assumption is reasonable for the considered problem, so that the difference with the results that would be obtained by assuming a more realistic shape of the yield surface and of the plastic potential (e.g. according to MC) is expected to be small.

Figure 4.6a shows the effective (solid line) and total (dashed line) stress paths in the centre of the specimen in the plane *p'*-*q* and *p*-*q*, respectively. Figure 4.6b and Figure 4.6c show the time-development of the pore pressure in the centre of the specimen and of the vertical settlements at the top boundary of the model, respectively.

The initial deviatoric stress *q* is equal to zero and the initial mean stress is equal to 1 kPa (point i). The consolidation at 100 kPa causes hardening of the material and expansion of the yield surface to its maximum size (yield surface passing through point ii characterized *p'* = 85 kPa, *q* = 22.3 kPa and K_0 = 0.76). As the process is drained, the effective mean stress at this stage is equal to the total mean stress. The subsequent drained unloading to 50 kPa is elastic. At the end of the unloading (point iii), the over-consolidation ratio (defined by the ratio between the maximum vertical effective stress experienced in the past and the current vertical effective stress) amounts to 2.0. It is interesting, that the deviatoric stress decreases considerably during unloading (from 22.3 kPa to 2 kPa; state ii and iii, respectively), while (as expected on account of the over-consolidation) the coefficient of lateral pressure increases from 0.78 to 1.04.

The last step of the sample preparation is simulated by a complete unloading of the model under undrained conditions (from state iii to state iv). During the undrained unloading the effective mean stress remains constant, while the total mean stress and the deviatoric stress decrease to zero (Figure 4.6a). The unloading-induced suction is equal to -53 kPa (Figure 4.6b). This value is higher than the measured value (about -30 kPa) and slightly lower than the theoretical expected value (*i.e.* - 50 kPa, see [65]).

The practically instantaneous loading of the specimen by 33 kPa (from state iv at t = 0 to state v at t = 2 s) causes an increase in the deviatoric stress from zero to the applied pressure. As the loading is undrained the mean effective stress remains equal to zero, while the pore pressure and the mean total stress increase by 11 kPa (*i.e.*, the suction decreases from 53 to 42 kPa). The settlement occurring at this stage is equal to 0.2 mm (Figure 4.6c), *i.e.* about half as measured experimentally.

During the swelling process (t > 2 s) the excess negative pore pressure dissipates and, consequently, the effective stress state moves leftward toward the drained equilibrium point $p \approx q_v / 3$ = 11 kPa, while the deviatoric stress remains almost constant (also in this case, the small change in the deviatoric stress is probably due to the non-uniform stress state caused by the mechanical boundary conditions). During this period the specimen slight expands in the vertical direction (swelling due to the decrease in the mean effective stress). This heave was not observed in the laboratory tests; it may be related to the inability of the used constitutive model to capture the higher stiffness of the material at small strain [75].

At t = 4 min the effective stress path reaches the yield surface. The plastic dilation accompanying yielding results to decreasing pore pressure in the centre of the model (Figure 4.6b), and consequently an increase of the mean effective stress (Figure 4.6a), so that the effective stress state moves back towards the critical state line. During this process the deviatoric stress slightly increases.

Figure 4.7a shows the time-development of the plastic zone in the vertical symmetry plane of the model. Yielding starts to occur at the model corners already at t = 1 min. After 4 minutes, a plastic zone develops in the middle of the model. The two plastic zones merge after about 20 minutes. Differently to the experimental results, no localization of the deformation and of the plastic zone occurs in the numerical model. It should be noted that localization does not occur even when imposing a lower strength to the corner elements.

After 23 min, the effective stress path reaches the critical state line, which means that further plastic shearing would occur under constant plastic volumetric strain (Figure 4.6a). However, as further shearing does not produce a stabilizing decrease in pore pressure, the system reaches the ultimate state. This is evident from the rapid displacement acceleration at t = 23 min (Figure 4.6c).

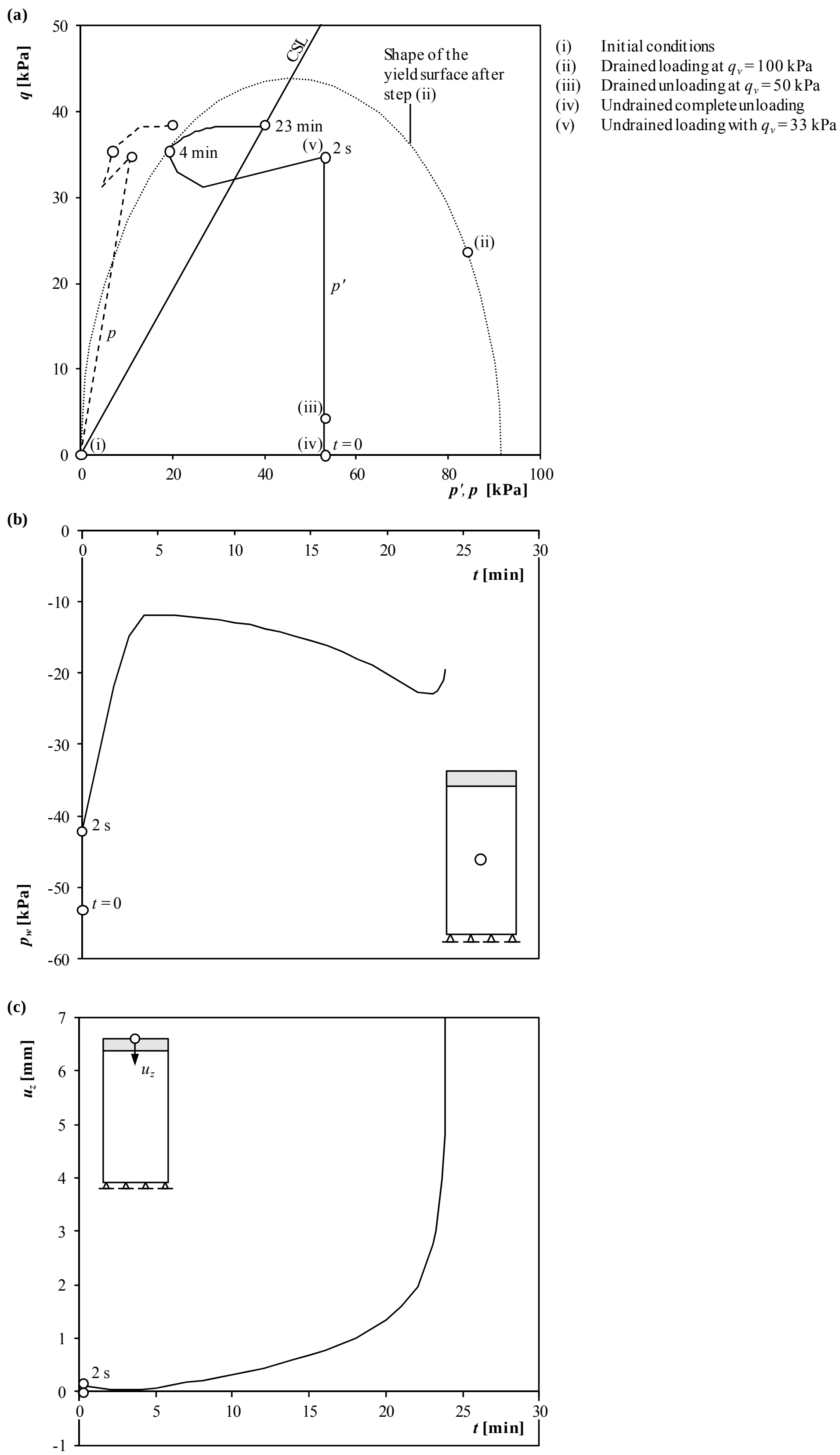

Figure 4.6 *Results obtained for an underwater test with MCC model (a) Effective (solid line) and total (dashed line) stress path of a point located in the centre of the model in p'-q and p-q diagram, (b) evolution over the test time of the pore pressure in the centre of the specimen and (c) of the vertical settlements at the top of the model.*

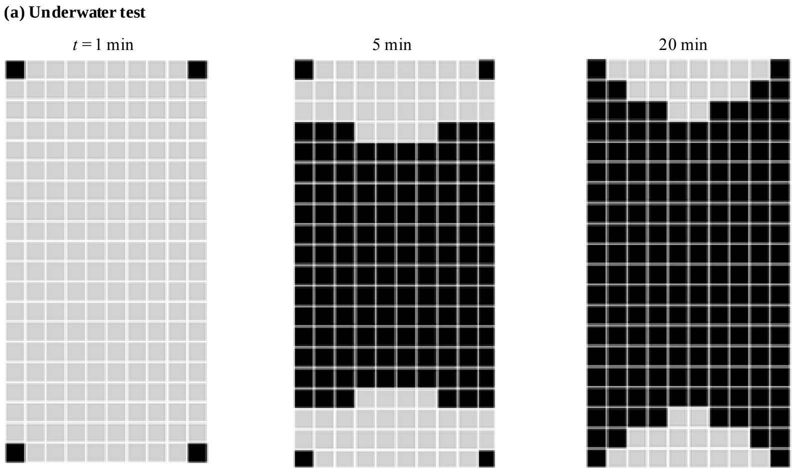

Figure 4.7 *Plastic zone on the mid plane of the sample at several times for test executed (a) underwater and (b) under water vapour (MCC model).*

The time-development of the vertical displacement and of the pore pressure qualitatively agrees with the experimental observations (*cf.* Figure 4.6 with Figure 4.4). This is true particularly concerning the complex evolution of the suction over time (decreasing initially, then increasing and finally, just before failure, decreasing again). However, the numerical analysis predicts a much slower process than observed; the predicted stand-up time (23 minutes) is by factor 3.5 longer than the average of all 8 tests (6.5 minutes).

As mentioned above the measured initial suction (32 kPa) is lower than the theoretically expected suction (50 kPa) and this indicates that some excess pore pressure dissipation might have occurred before the uniaxial loading. So, the question arises whether the difference between computed and measured stand-up time might be due to the different initial suction. Schuerch [65] numerically shows that the consideration of an initial partial dissipation of the negative excess pore pressure results to earlier yielding (2 *vs.* 4 min) and to a slightly shorter stand-up time (19 *vs.* 23 min). Consequently, a partial dissipation of the initial pore pressure does not explain the observed difference between predicted and observed behaviour.

It has been shown that, for the problem under investigation, the MCC model overestimates the stand-up time. The main reason for the overestimation must be related to the shape of the yield surface of the MCC model; it is well known [76] that the MCC model overestimates yield strength on the dry side (the actual yield surface is less expanded). This means that the stress path between undrained unloading and yield surface as well as back from the yield surface to the CSL is longer, and so that the plastic dilative shearing is overestimated. This causes a longer the stand-up time. In addition, the obtained numerical results differ from the experimental observations in that they do not reproduce the observed localization of the deformation.

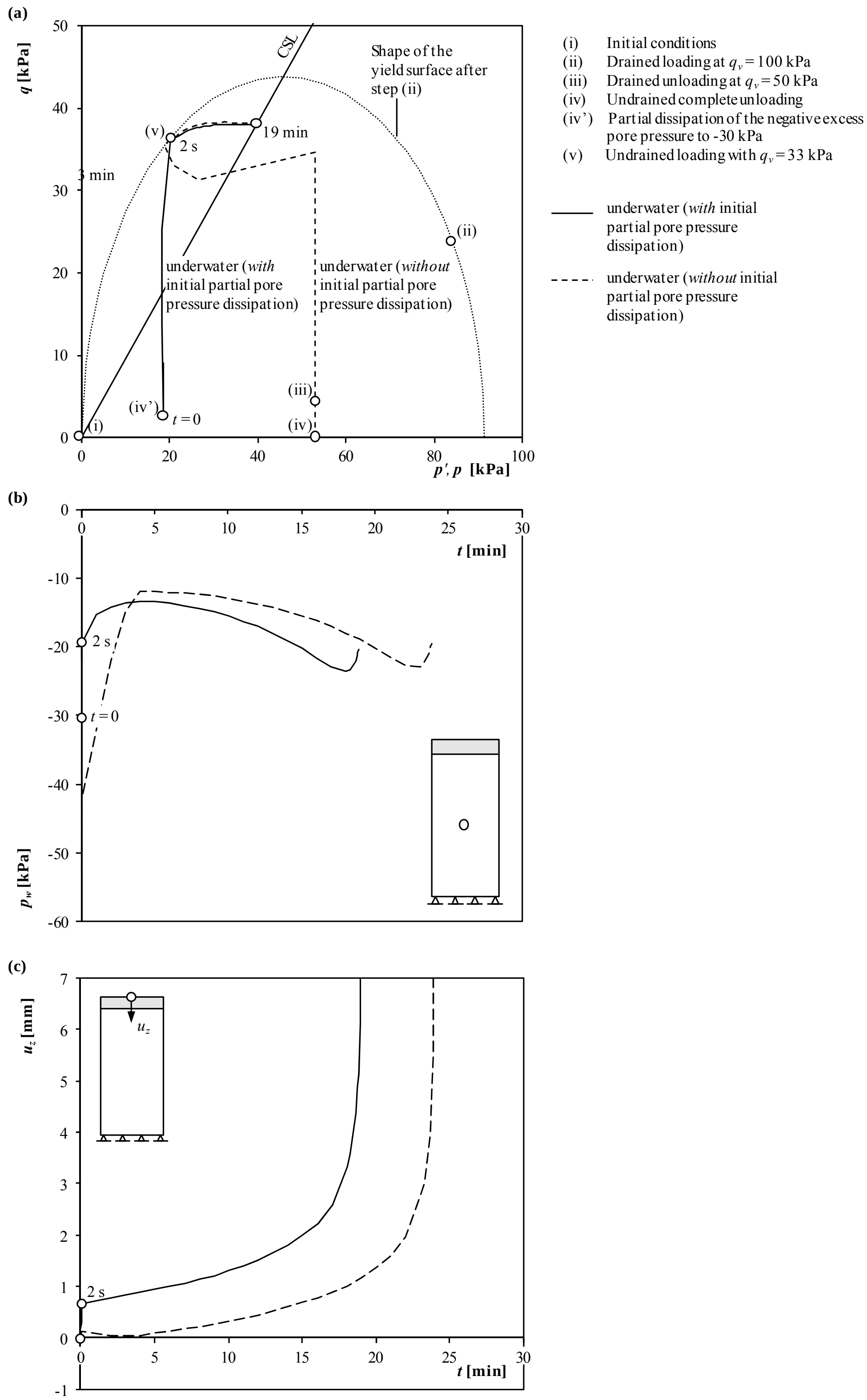

***Figure 4.8** Results obtained considering or not an initial partial dissipation of the pore pressure (solid and dashed lines, respectively) for an under-water test with MCC model (a) effective (solid line) and total (dashed line) stress path of a point located in the centre of the model in p'-q and p-q diagram, (b) evolution over the test time of the pore pressure in the centre of the specimen and (c) of the vertical settlements at the top of the model.*

4.3.4 Test interpretation by MC model

Figure 4.9 presents computational results analogously to the previous Section (Figure 4.6), considering an effective cohesion of 9 kPa, which is theoretically consistent with the material strength according to MCC model (see Section 4.2.1.4). The effect of cohesion on stand-up time will be discussed at the end of the present Section.

As explained for the MCC model, the failure process is driven by the dissipation of the negative initial excess pore pressure (Figure 4.9b). The increase in pore pressure results to a decrease in the effective stresses, which, for the given deviatoric stress, leads to yielding. The latter occurs in the model centre at t = 1.4 min (Figure 4.9a). At the same time, the model collapses (Figure 4.9c).

The predicted stand-up time of 1.4 min is by about factor 15 shorter than predicted by the MCC model and by about factor 4.5 shorter than observed in the laboratory tests. The main difference to the MCC model is that the MC model (with isochoric flow rule) does not takes account of the plastic dilatant shearing, which, as shown by the MCC simulations, delays failure. In the case of MCC model (which considers dilatant behaviour), negative excess pore pressure develop after yielding, *i.e.* the pore pressure decreases (Figure 4.6b), thus increasing the mean effective stress (Figure 4.6a) and stabilizing the system until the stress state reaches the CSL (Figure 4.6a). This cannot happen in the isochoric MC model. This is shown clearly by the time-development of pore pressure Figure 4.9b: Contrary to the MCC model and to the experimental observations, pore pressure increases monotonically until failure. The predicted time-development of the vertical displacement, too, differs qualitatively from the MCC predictions and from the observed behaviour: the MC model predicts that heave (swelling) rather than settlement occurs during the pore pressure dissipation; this trend reverses to accelerating settlement only very close to the ultimate state (Figure 4.9c).

Figure 4.10 shows the influence of the effective cohesion (the only parameter that was not measured experimentally) on the stand-up time. The sensitivity of the stand-up time to the cohesion is high: the model collapses immediately after loading for a cohesion of 2 kPa (minimum cohesion required for short-term stability) while, it remains stable even in the long term for cohesion higher than $c_{D,lim}$ = 10.6 kPa.

For cohesion values between 2 and 10 kPa, the predicted stand-up time is less than 4 minutes (0 – 2.4 min with average 0.76 min), and so rather shorter than stand-up time of the physical models (2.2 – 8.2 min with average about 4 min, see Schuerch 2016). This means that, considering a cohesion slightly different than 9 kPa, the MC model with isochoric plastic behaviour will underestimate the stand-up observed experimentally. The underestimation of the stand-up time would be even higher if considering the formation of shear bands observed experimentally could not be reproduced numerically (a localization does not occur even when imposing a lower resistance to the element rows located at upper and lower corners of the model). As explained in Chapter 3, localization would lead to a decrease in the operational strength parameters and thus also in the stand-up time.

In conclusion, based upon the comparison between the measured data (pore pressure and vertical settlement) and the numerical one it can be concluded that, for the present example, the MC model with isochoric plastic behaviour underestimates the stand-up time when the cohesion is lower or slightly higher than the one estimated based upon theoretical consideration. The underestimation occurs because the MC model does not capture the plastic dilation that occurs after yielding. However, if the assumed cohesion is close to $c_{D,lim}$, the MC model may lead to the overestimation of the stand-up time. In the extreme case, in which the assumed cohesion is higher than $c_{D,lim}$, the MC model leads to infinite stand-up time and so, to an erroneous interpretation of the model behaviour.

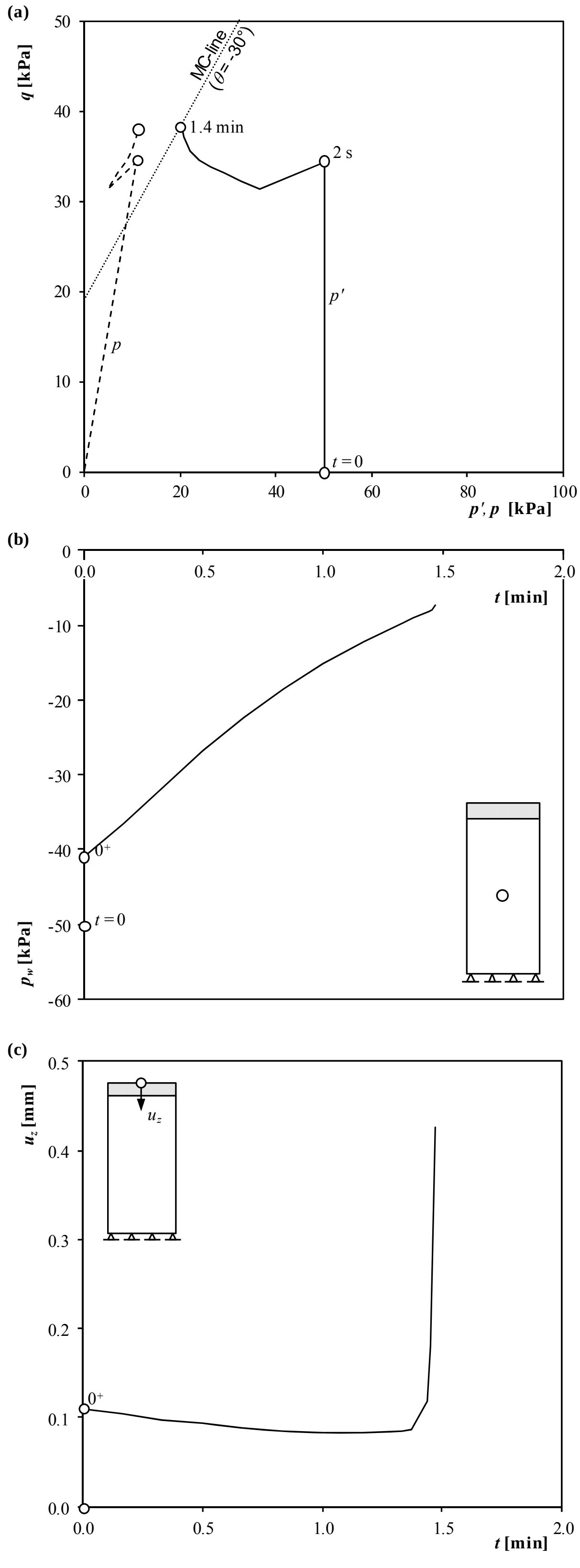

Figure 4.9 *Results obtained for an underwater test with MC model (a) Effective (solid line) and total (dashed line) stress path of a point located in the centre of the model in p'-q and p-q diagram, (b) evolution over the test time of the pore pressure in the centre of the specimen and (c) of the vertical settlements at the top of the model.*

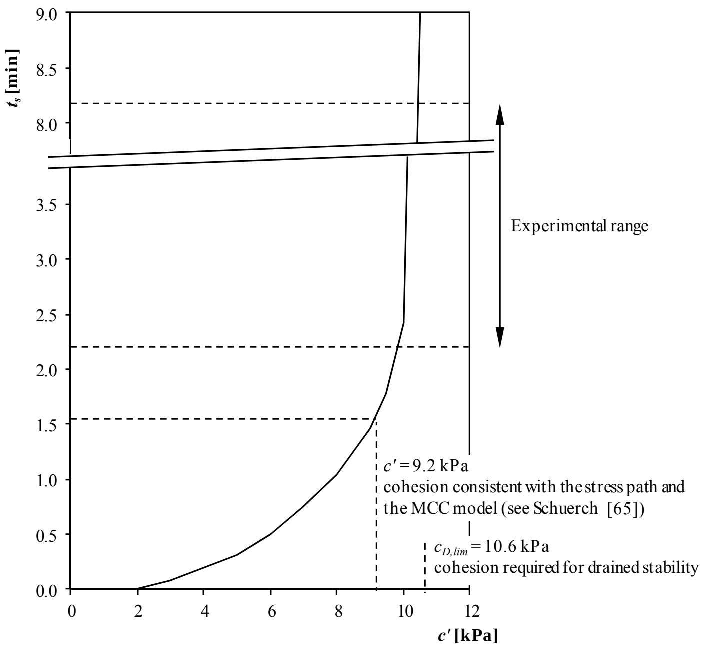

Figure 4.10 *Influence of the effective cohesion on the stand-up time (MC model, underwater tests).*

4.4 Conclusions

Chapter 4 investigated the problem of delayed failure induced by the transient swelling process by means of simple uniaxial tests.

The experimental tests showed that shear bands develop in the corners of the specimen and progress toward its centre over the time; failure occurs shortly after a continuous shear band develops through the specimen. The occurrence of failure manifests itself by a rapid acceleration of the vertical displacement.

The numerical interpretation of the measured pore pressure in the centre of the specimen showed that failure is driven by the dissipation of the negative initial excess pore pressure and delayed by the plastic dilation that occurs after the onset of yielding.

The numerical simulations showed, furthermore, that the use of the MCC model allows to qualitatively reproduce the behaviour observed experimentally in terms of pore pressure and settlements evolution over time (but not the observed localization of deformations). However, the MCC simulations overestimate the stand-up time (mainly because of the overestimation of the plastic dilation). The isochoric MC model besides failing to reproduce the observations qualitatively underestimates the stand-up time, as it does not consider dilatant shearing. This result is relevant under the practical point of view, as it suggest that the simple and widely used MC model represents a simple and “safe” approach for the estimation of the stand-up time for problems characterized by stress paths similar to the one reproduced in the present laboratory test. However, care must be paid on the selection of the effective cohesion; its overestimation or underestimation may lead to an erroneous interpretation of the model behaviour (let assume that a finite stand-up time physically exists. If the cohesion assumed in the computation is lower than $c_{D,lim}$, the computed stand-up time will be probably shorter than the physical one; if the assumed cohesion is higher than $c_{D,lim}$, the stand-up time will be infinite, and so the model behaviour will be interpreted erroneously). In the opinion of the authors, a parametric study investigating the sensitivity of the stand-up time on the cohesion (for the plausible cohesion range) should be always performed when adopting the MC model and, as safe engineering assumption, the stand-up time should be taken equal to the lowest one.

5 Experimental investigation of stand-up time: centrifuge tests

5.1 Introduction

Numerical investigations of delayed failure of cuttings were presented among others by Kirkebø [36], Potts [7], Kovacevic [35], Ellis and O'Brien [9] and Lollino [8]. The listed authors investigated the progressive evolution of deep-seated failures in overconsolidated clays (or tills) due to a combination of pore pressure increase and intrinsic softening behaviour (see e.g. [7]). In the mentioned literature works, the verification of the models and of the constitutive laws is performed calibrating the parameters and the boundary conditions (e.g. the seepage boundary condition on the excavated surface; [35]) in order to reproduce already occurred delayed failures of man-made cuts in natural soils (intrinsically characterized by heterogeneity and variability of the ground parameters). As described by Lambe [77], this approach (so-called *C-type* prediction) is useful in order to improve the understanding of a problem, but it should not be used in order to prove that a prediction technique is correct; in other words the methods are numerically sophisticated but at the same time require assumptions that are uncertain at the field-scale, making thus them validation not robust.

In order to reduce the uncertainties (homogeneity of the soil, material parameters, boundary conditions, …) of the analysed problem, small-scale (reproducible) physical models are required. Physical models at laboratory scale allow to control the model parameters and the boundary conditions during the execution of the test. For the purpose of delayed failure investigation, centrifuge modelling is the most attractive method because it allows to reproduce the stress level of real scale problem (so-called *prototype*) and, at the same time, to reproduce the diffusion process driving the instability (*i.e.* the swelling process) much faster than at the prototype scale (real time).

The present Chapter investigates the delayed failure of a 7 m high underwater vertical cut (Figure 5.1) in over-consolidated clay by means of physical tests executed under well-controlled conditions and numerical coupled hydraulic-mechanical FEM analyses. Differently form the works of Deepa and Viswanadham [53] and Davies [52] (in which transient failure was induced by an artificial change of boundary conditions and of loading, respectively), the delayed failure of the proposed physical model occurs due to swelling process only (*i.e.* under constant boundary conditions and loads).

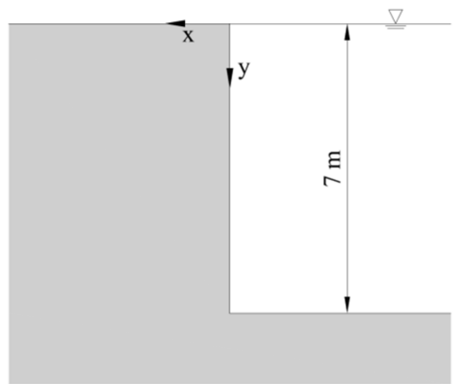

Figure 5.1 *Problem layout (at prototype scale).*

The experiments have been carried-out in the drum centrifuge of ETH [78]. The simulation of the excavation during the test was achieved retracting a support wall installed – prior acceleration – against the vertical cut (Figure 5.2). The soil used in the present experiments is a natural reconstituted high plasticity clay coming from Birmensdorf (Switzerland) overconsolidated at 100 kPa (same material used for the uniaxial tests presented in Chapter 4).

The FEM analyses have been carried-out with material constants, which have been determined independently on the centrifuge test results (with laboratory tests or based upon theoretical considerations, see [65]).

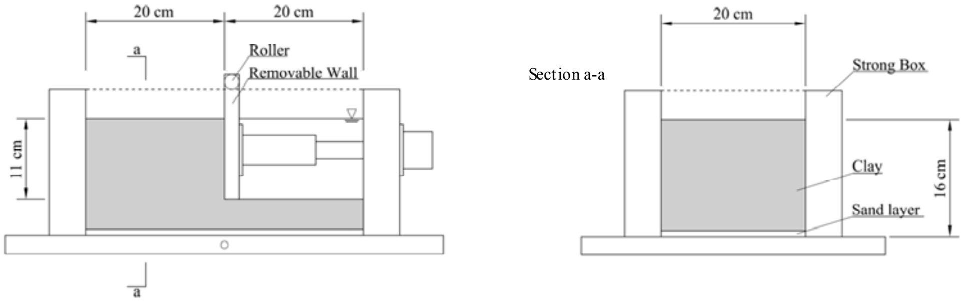

Figure 5.2 *Model set-up.*

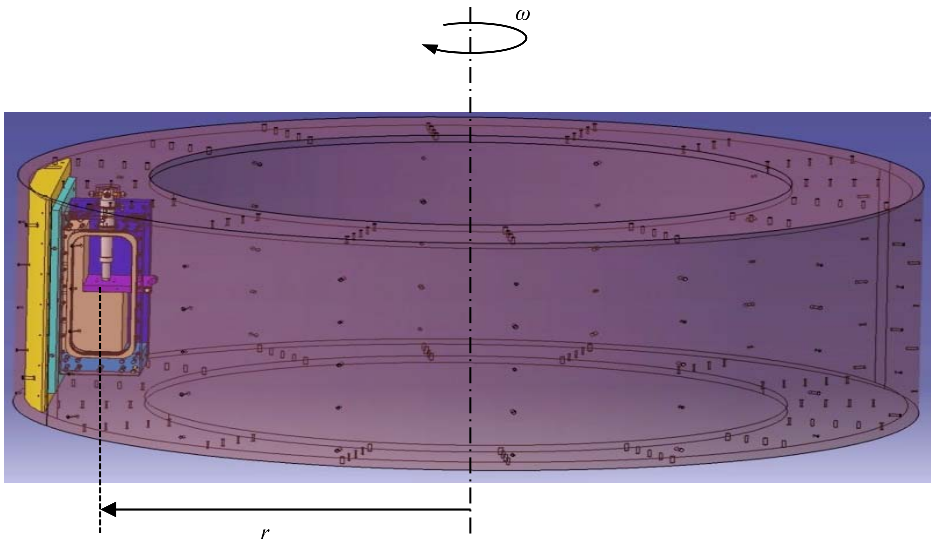

Figure 5.3 *Drum centrifuge with assembled model.*

5.2 Centrifuge modelling

5.2.1 Material and methods

5.2.1.1 Scaling laws and model dimensions

The scaling laws (see Table 5.1 for an overview) define the relationship between the prototype scale and the model scale (physical models in the centrifuge) as function of *n* (where *n* expresses the centrifuge acceleration as a multiple of the earth gravity *g*).

The centrifuge acceleration is obtained by rotating the model with a constant angular speed of:

$$\omega = \sqrt{\frac{ng}{r}}\frac{60}{2\pi}, \tag{5.1}$$

where r = 0.874 m is the radial distance between the centre of rotation and the middle height of the excavation (see Figure 5.3).

Table 5.1 *Scaling laws prototype/model (being n the number of g's) according to Schofield* [79].

Acceleration	n
Stress and pressure	1
Density	1
Length	$1/n$
Velocity	1
Volume	$1/n^3$
Mass	$1/n^3$
Force	$1/n^2$
Time (diffusion)	$1/n^2$
Time (dynamic)	$1/n$

Table 5.2 *Model height h and corresponding centrifugal acceleration n and rotational speed ω.*

	h [cm]	n [-]	ω [rpm]
Test 1 (reference case)	11.0	63.5	255
Test 2	10.7	65.7	259
Test 3	10.2	68.6	265
Test 4	11.2	62.5	253

Table 5.2 shows the height of the vertical cut and the corresponding centrifuge acceleration – required in order to reproduce a 7 m height vertical cut – for the four executed centrifuge tests.

5.2.1.2 Model preparation

The preparation of the model consisted of 5 phases: consolidation of the clay, excavation of the vertical cut at 1 *g*, installation of the supporting wall, drawing of lateral contrast lines and, finally, installation in the centrifuge.

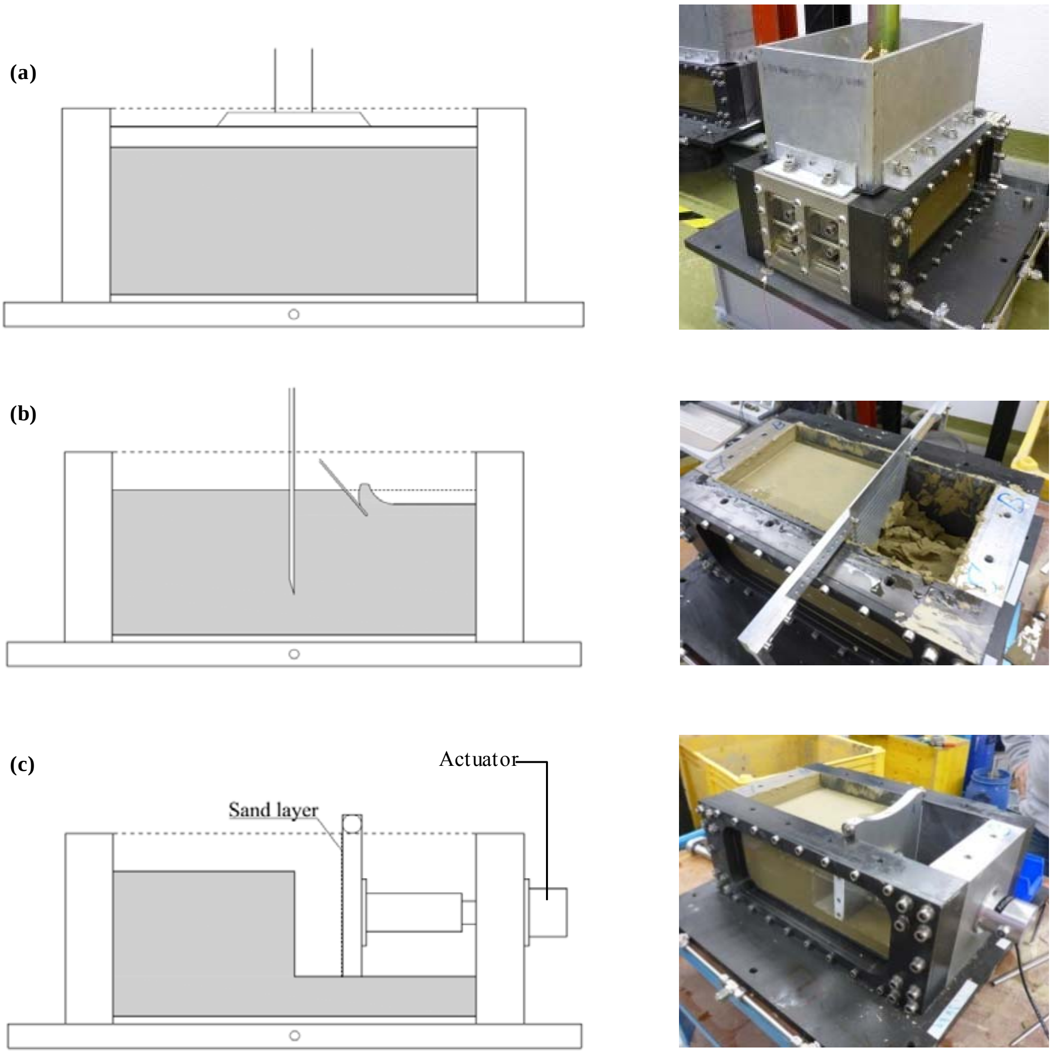

Figure 5.4 *Model preparation: (a) consolidation, (b), excavation and, (c), insertion of the retaining wall.*

The natural clay was initially mixed under vacuum with water (in order to remove the air contained in the mixture) until reaching an homogeneous slurry with 100% water content. The slurry was then poured into the strongbox and consolidated up to 100 kPa (Figure 5.4a). The consolidation was carried-out by means of an hydraulic press in 5 steps: 4 kPa, 15 kPa, 25 kPa, 50 kPa and 100 kPa. The total consolidation time amounted to about 25 days. In order to eliminate friction between soil and strongbox (during both the consolidation and the test phase), the longitudinal walls of the box where initially lubricated by means of paraffin oil.

The material in front of the vertical cut was excavated at the end of the consolidation phase (Figure 5.4b). A sharped aluminium blade was temporarily installed in the middle of the model. In order to assure an accurate geometry of the cut and protect it during the excavation.

The support wall was installed in the model after excavation (Figure 5.4c). The longitudinal movement of the support wall was controlled by an electric actuator. In order to avoid sticking of the material during the execution of the centrifuge test (particularly during the retraction of the wall), the wall was covered by oily sand.

The strongbox has a removable Plexiglas window on one of its longer sides, which allows to observe the overall model behaviour during the centrifuge test (see photography in Figure 5.4). After the installation of the supporting wall, the window was temporarily removed and horizontal white lines spaced 1 cm were drawn on the lateral boundary of the model.

Before installation in the centrifuge, small plastic pipes (4 mm in diameter) were installed in the corners of the model. The plastic pipes were connected to the bottom plate of the strongbox (drainage plate) in order to reduce the time required for the rise of the water level inside the model during the initial phase of the centrifuge test. An overflow pipe was connected to the drainage plate and fixed against the external wall of the strongbox. This allowed – in combination to a constant water inflow through the drainage plate of the strongbox – to keep a constant water level during the duration of the centrifuge test.

Finally, the strongbox was installed in the drum centrifuge (note that the model stands vertically, see Figure 5.3) and connected to the external water supply system.

5.2.1.3 Instrumentation

The model was instrumented with laser distance meter and micro pore pressure transducers (ppts) measuring the vertical settlement and the pore pressure, respectively. Moreover, in order to observe the overall model behavior during testing, two fast cameras were fixed on the lateral and upper sides of the strongbox.

A total of seven ppts of type Druck (type PDCR81) and Keller (type 2MIX/2bar/81840.1) were used. Six of them were placed into the clay and one was connected to the water supply system, in order to monitor the hydraulic head in the drainage plate during the test.

Four out of the six ppts were placed near the theoretical lowest inclination of the failure surface (*i.e.* 45°) at a depth of 4 cm (2 ppts) and 8.5 cm (2 ppts), respectively (Figure 5.5). The selected position allowed to collect data near the potential sliding plane without influencing the failure mechanism. The remaining two ppts were installed near the strongbox back wall (same elevation as described above) as control of the pore pressure field in a larger distance from the failure plane.

The ppts were installed into the clay at the end of the consolidation step of 50 kPa as follows: drilling the clay by means of a borer through the strongbox back wall (special openings were disposed in the wall); introduction of the sensor in the hole; and, finally, filling the hole with liquid slurry by means of a syringe equipped with a long injection micro pipe. In order to avoid the risk of trapping air bubbles inside the hole, the slurry was injected from the end of the hole (similarly to the grouting procedure used for rock bolts grouted by mortar). After filling the hole, the opening was sealed by means of a rubber ring and closed with a screwed steel cylinder. Finally, the vertical pressure was increased to 100 kPa, allowing thus the fresh slurry (injected around the sensor and the cable of the ppts) to consolidate (ensuring thus a reliable pore pressure measurement during the tests in the centrifuge).

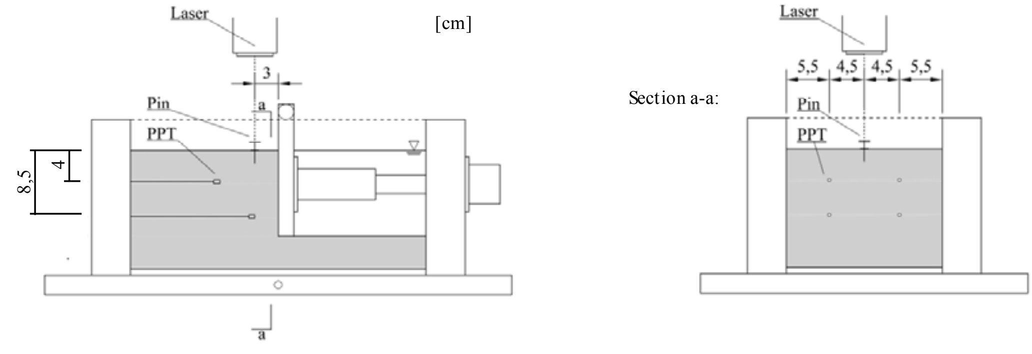

Figure 5.5 *Model instrumentation.*

A short range distance sensor (high precision laser distance meter) was used for the measurement of the vertical settlement of a fixed point located at the crest of the wall (Figure 5.5). In order to avoid the measurement errors associated with the refraction of the laser on the wet clay surface, the target point was located on an aluminium pin with flat circular head. The pin was constructed with a ring at its mid-height, which stabilized the pin and prevented its penetration into the soil during testing, thus ensuring that the pin displacement is equal to that of the soil surface. Due to the small size of the pin and to the low unit weight of aluminium, the pin weight is negligible compared to the stresses in the soil and does not influence the failure mechanism.

5.2.1.4 Test procedure

The centrifuge test started with rising of the water level in the model. This was carried-out at a rotational speed of 100 rpm (corresponding to a centrifugal force of 10 *g*). After the water level reached the top of the vertical cut, the rotational speed was increased to its final value (255 rpm for a 11 cm high wall; Table 5.2).

The acceleration of the model caused the generation of positive excess pore pressure in the clay. Therefore, after the acceleration phase, a consolidation phase of about 8 hours was required in order to reach hydrostatic pore pressure distribution. The latter was controlled by means of the micro pore pressure transducers. Finally, the supporting wall was quickly retracted (thus simulating a rapid excavation) and the model behaviour was monitored until failure.

5.2.1.5 Determination of the material parameters

Table 5.3 gives the parameters of the clay (Birmensdorf clay) used in the centrifuge tests for the Mohr-Coulomb (MC) and the Modified Cam Clay (MCC) Model. With the exception of the effective cohesion of the soil, the values were obtained by means of the laboratory tests described in Schuerch [65]. The effective cohesion is estimated assuming that the soil behaves as MCC and considering the theoretical effective stress path expected during testing [65].

Table 5.3 *Material constants.*

Saturated unit weight	γ [kN/m^3]	18.2
Unit weight of water	γ_w [kN/m^3]	10
Liquid limit	w_l [%]	58
Plastic limit	w_p [%]	19
Plasticity index	I_p [%]	39
Void ratio (at σ_v = 1 kPa)	e_0 [-]	2
Seepage flow parameters		
Permeability	k [m/s]	1.5 10^{-9}
Water compressibility	c_w [MPa]	0
Parameters for linearly elastic, perfectly plastic MC material		
Young's modulus	E [MPa]	18
Poisson's ratio	ν [-]	0.3
Cohesion	c' [kPa]	8 kPa (see [65])
Friction angle	φ' [°]	24.5
Dilation angle	ψ [-]	0
Parameters for Modified Cam Clay material		
Gradient of swelling line	κ [-]	0.01 (set 1) / 0.022 (set 2)
Gradient of compression line	λ[-]	0.21 (set 1) / 0.152 (set 2)
Intercept of compression line	e_1[-]	2
CSL slope in p'-q plane	M [-]	0.96
Poisson's ratio	ν [-]	0.3

5.2.2 Experimental results

Figure 5.6, Figure 5.7 and Figure 5.8a show the time-development of the vertical settlement, photographs of the model at two times and the time-development of the pore pressure, respectively, for test No. 1. For sake of completeness, Figure 5.8b additionally shows the pore pressure evolution over time of all four centrifuge tests (ten rather than twelve curves are shown, because some ppts stopped measuring during execution of Tests 2, 3 and 4).

The reference state (t = 0) for the presented vertical settlement is the one prevailing just before retracting the supporting wall. Pore pressure distribution at t = 0 is hydrostatic (28 kPa and 52 kPa at the highest and lowest ppts elevation, respectively – points B and C in Figure 5.8a).

The quick retraction of the supporting wall (which simulates an undrained excavation) causes a practically instantaneous settlement of the soil surface (by about 2 mm; Figure 5.6) as well as negative excess pore pressures (of about 55 kPa and 115 kPa, at points B and C, respectively; Figure 5.8a). The development of negative excess pore pressures can be explained as a consequence of the excavation-induced reduction of the horizontal total stress along the vertical cut; pore pressure decreases more at the elevation of the deeper ppt, because the *in situ* stresses (and thus the excavation-induced decrease in total stress) increase over depth.

The negative excess pore pressures dissipate over time (Figure 5.8a). As one might expect for a dissipation process, its rate decreases over time initially, but reaches a constant value after about 2 min (upper ppt) or 3 min (lower ppt).

At t = 17 min a tensile crack develops at the crest of the excavation in a distance of about half the height of the cut. The development of such cracks during progressive failure is observed also in the field (e.g. Banerjee [31], Cooper [51], Hughes [6], Lollino [8]). At t = 18.5 min a thin shear band starts to develop at the toe of the excavation; it is probably associated with a high stress concentration over there.

The settlement increases at an approximately constant rate over a long period and starts to accelerate significantly shortly after the above-mentioned first signs of failure (at about t = 22 min; Figure 5.6). Cooper [51] defined this time as the end of the “apparent overall stability”. The measured displacement evolution – characterized by an initial phase of low displacement rate followed by a phase of acceleration – was also observed in the field by Cooper [51] and Kovacevic [48].

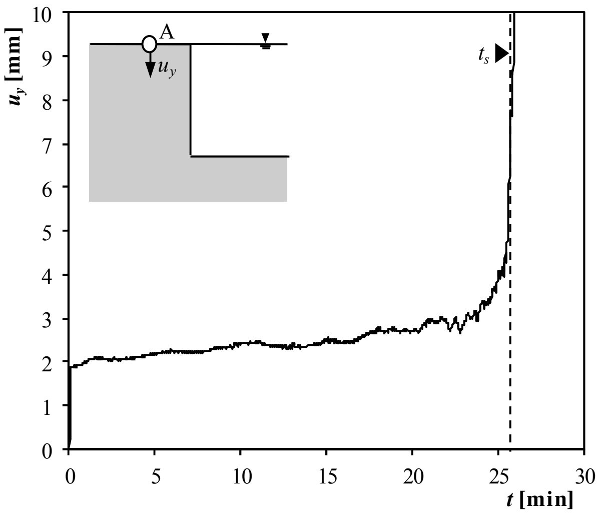

Figure 5.6 *Evolution over time of the vertical displacement after retraction of the supporting wall (Test No.1).*

(a)

(b)

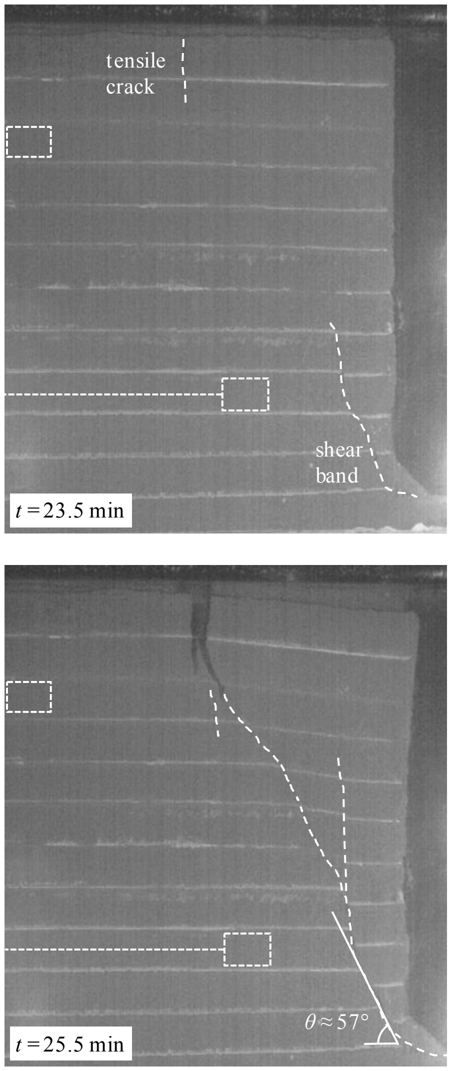

Figure 5.7 *Deformed model at, (a), 23.5 minutes and, (b), 25.5 minutes (Test No.1).*

At t = 25.5 min the tensile crack and the shear band join (Figure 5.7b) and the cut collapses (see settlement acceleration in Figure 5.6); the stand-up time in this test is thus equal to 25.5 minutes. At ultimate state, a wedge slides on a plane inclined by 57°, which is close to Coulomb's inclination (45°+ φ'/2 = 57.3°). Vermeer [80], too, observed that the shear band inclination in finely grained soils is close to the Coloumb's inclination.

It is interesting to note that, shortly before failure, the pore pressure measured by the lower ppt decreases (C; Figure 5.8a), while the pore pressure at the upper ppt first decreases and then increases. This may be due to an increase of the total stresses caused by stress re-distribution, which occurs after tensile failure.

Finally, the model behaviour was both qualitatively and quantitatively reasonably good reproducible, which indicates a high quality of the tests. The variability of the measured pore pressures and displacements was small (Figure 5.8b and Figure 5.9, respectively). The average stand-up time of the four centrifuge tests amounts to 24.5 minutes (Figure 5.9a), which corresponds (taking account of the scaling laws and centrifuge accelerations; Table 5.1 and Table 5.2) to 72.4 days at the prototype scale (Figure 5.9b).

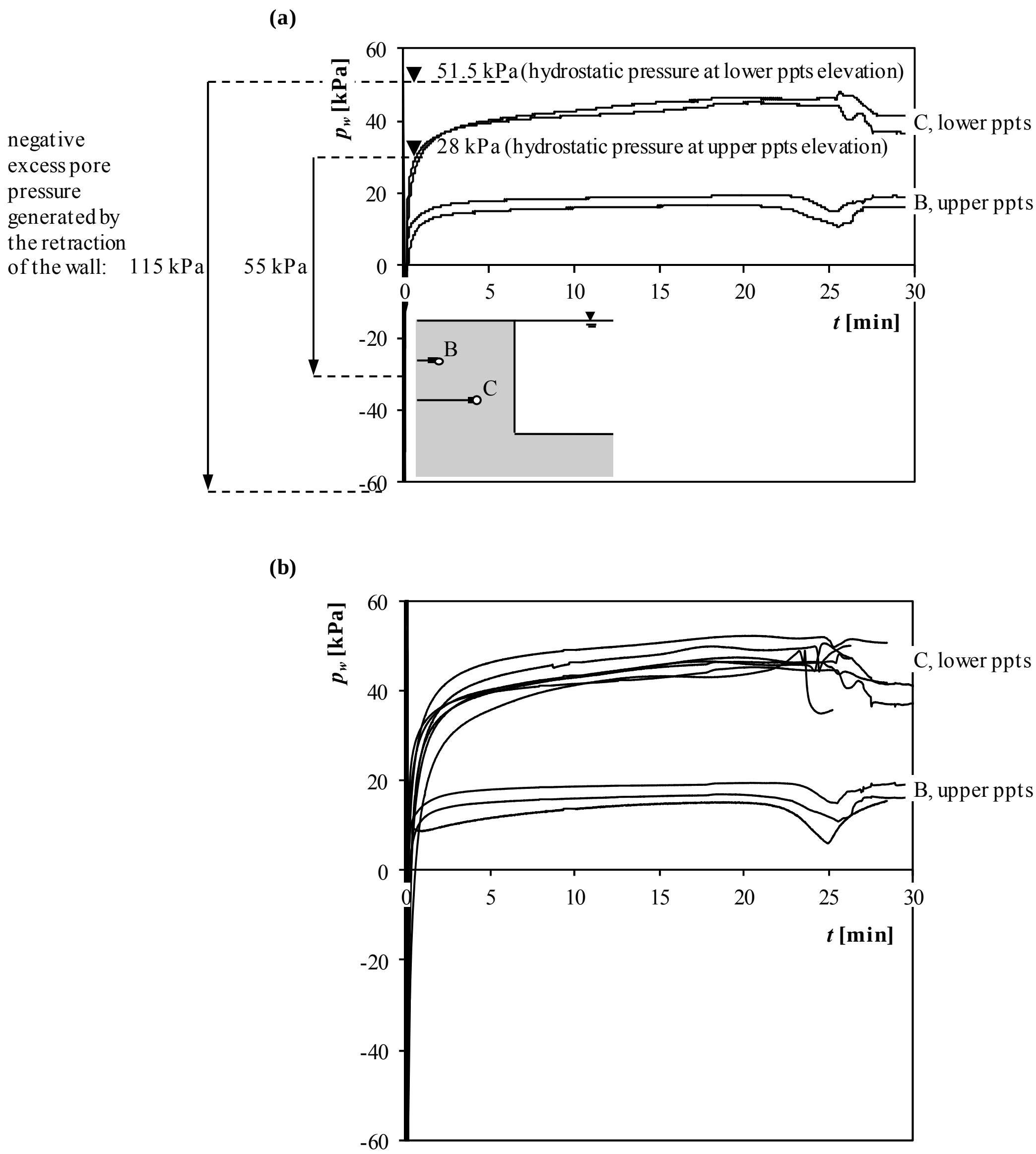

***Figure 5.8** Evolution over time of the pore pressure for, (a), the Test No.1 and, (b), all centrifuge tests.*

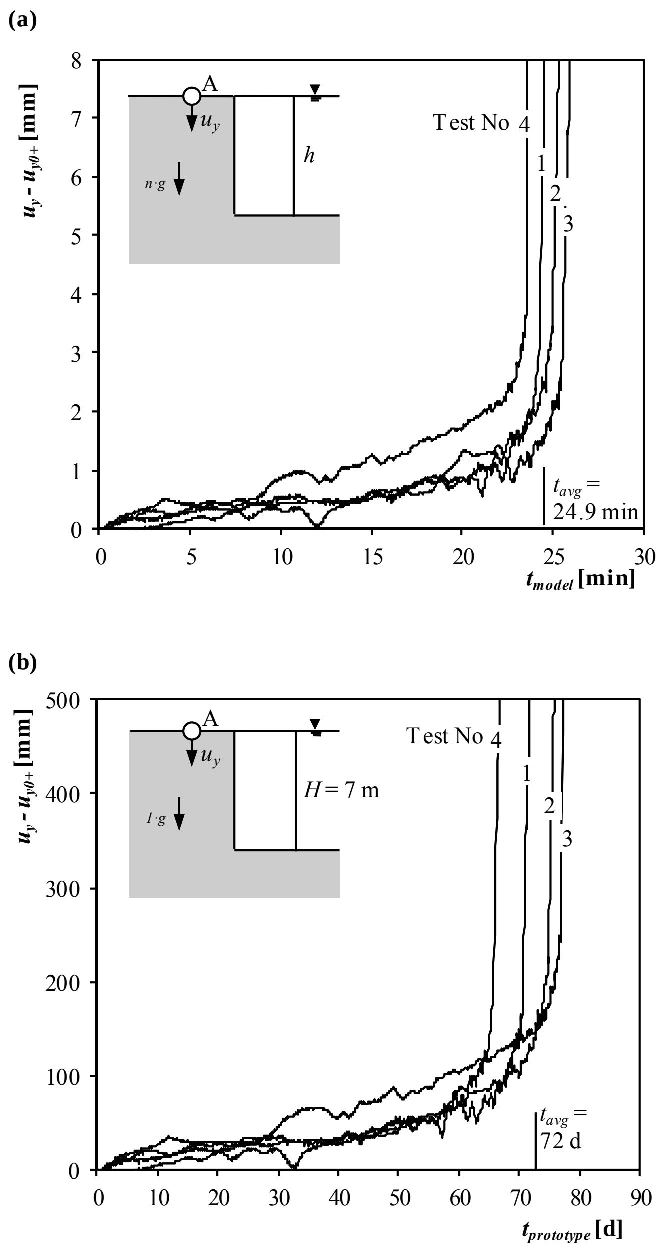

***Figure 5.9** Evolution over time of the vertical displacement of all 4 tests at, (a), the model and, (b), the prototype scale.*

5.3 Numerical modelling

5.3.1 Computational model

The problem is formulated in plane strain at the prototype scale. Figure 5.10 shows the geometry and the boundary conditions of the problem under investigation.

The soil is modelled either as an isotropic, linearly elastic and perfectly plastic material obeying the Mohr-Coulomb yield criterion with isochoric plastic flow or as a Modified Cam Clay material (Table 5.3). The seepage flow follows the Darcy's law.

The shape of the yield function for the MCC model in the deviatoric plane is taken according to the Gudehus [81] expression:

$$g\left(\theta_L\right) = \frac{2b}{1+b+(1-b)\cos\left(3\theta_L\right)}\,, \tag{5.2}$$

where θ_L is the Lode's angle and *b* is the convexity factor (assumed equal to 0.8). The present example adopts the Gudehus formulation for the MCC model in order to capture the possible small changes of the Lode's angle during the stress re-distribution process, and so, reproduce as best as possible the expected material response. As shown by Schuerch [65] for a similar problem, a circular yield surface with slope of the CSL matching plane strain conditions would be also a reasonable assumption for the problem under consideration.

The spatial discretization employs 8-node square elements with biquadratic displacement and bilinear pore pressure shape functions. The element side length is equal to 50 cm, which means that the height of the vertical cut is discretized by 14 elements (Figure 5.10); the effect of the mesh size on the stand-up time is studied in Section 5.4.

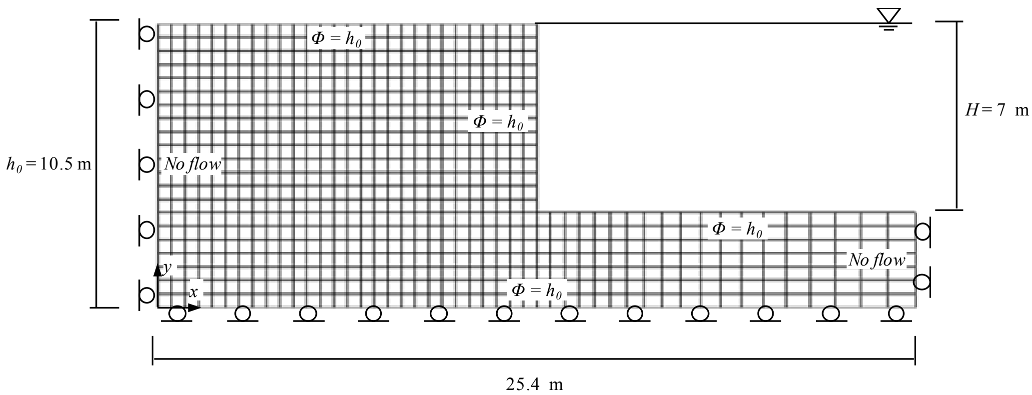

Figure 5.10 *Numerical model and boundary conditions imposed during the simulation of the delayed failure.*

As the ppts are fixed to the strongbox by means of micro-cables, they cannot move horizontally towards the cut and this may have an influence on the pore pressure field. The potential effect of the ppts on the model behaviour was investigated by comparative computations with and without horizontally fixing the nodes along the two horizontal lines between the strongbox and the ppts. This represents a simplifying assumption that probably overestimates the effect of the ppts.

5.3.2 Simulation procedure

5.3.2.1 MC model

The initial conditions represent the state just before excavation. The initial effective stresses increase linearly with depth according to the submerged unit weight and a lateral earth pressure coefficient equal to unity. The latter is consistent with the value at the mid-height of the vertical cut (see [65]).

The excavation is simulated by reducing the horizontal effective stresses at the vertical excavation boundary and the effective vertical stress at the bottom boundary of the excavation from its initial value to zero in one short time step of 3600 s, while the water pressure along the boundaries of the model is kept equal to hydrostatic one. Afterwards, a transient analysis starts.

5.3.2.2 MCC model

The MCC model requires assumptions on the spatial distribution of the initial void ratio and of the initial effective stresses (particularly of the K_0 coefficient) consistent with the constitutive model itself and with the construction history of the physical model.

i) Initialization of the numerical model: The initial conditions represent the state at the end of the consolidation at 100 kPa. As the latter was carried-out outside the centrifuge and the effect of a gravity acceleration of 1*g* is negligible in the model scale, gravity is disregarded in the model initialization, too, although the numerical problem is formulated at the prototype scale. Therefore, uniform initial pore pressure, vertical effective stress and void ratio e_0 are considered (equal to zero, 100 kPa and 1.1, respectively). The coefficient of horizontal stress is taken after Jaky [82] ($K_0 = 1 - \sin\varphi' = 0.58$), because the soil is normally consolidated at this state.

ii) This step simulates the complete vertical unloading of the physical model and the excavation of the vertical cut under 1*g*. Therefore, the gravitational forces are not activated yet in numerical model. The complete unloading is simulated by setting all boundary tractions equal to zero and performing a steady state analysis (pore pressure remains equal to zero). Subsequently, in view of the next simulation step, the soil elements in front of the vertical cut are deactivated and nodes on the vertical cut fixed in the horizontal direction in order to simulate the supporting wall.

The next steps simulate the test phases in the centrifuge:

iii) The acceleration in the centrifuge and the successive consolidation is simulated by activating the gravitational forces, fixing the boundary pore pressures equal to the hydrostatic pressure and performing a steady state analysis.

iv) The rapid excavation of the vertical cut is simulated by deactivating the horizontal fixity of the nodes located along the vertical cut and performing a transient analysis for one short time step (3600 s).

v) The phase of excess pore pressure dissipation is simulated by a transient analysis as for the MC model.

5.3.3 Results

5.3.3.1 MC model

First, the results obtained without fixing the nodes at the elevation of the ppts will be discussed. The solid line in Figure 5.11a represents the predicted time-development of the vertical displacement at the location of the pin used for the laser measurement. The predicted stand-up time is equal to approximately 32 days, which is in the same order of magnitude as the actual one (66 – 77 days with an average of 72 days). However, differences exist between observation and prediction with respect to the deformation pattern and to the time-development of settlement. These differences are discussed below.

The predicted deformation pattern (Figure 5.11b) is that of one sliding wedge – without the observed tension crack (Figure 5.7) – and this along a plane, which is less inclined than the actual one (53° *vs.* 57°). The reason for the absence of a tension crack in the numerical simulation is that tensile failure is not taken into account by the adopted MC model. Tension cracks shorten drainage paths and, consequently, tentatively accelerate excess pore pressure dissipation and failure. However, according to the experimental results, the tension crack started to develop very late, which means that its effect is relevant only close to failure. The results of the Chapters 2 and 3 show that, the inclination of the slip line increases with the fineness of the mesh. This could explain the difference with respect to the inclination of the sliding plane: the latter is slightly underestimated by the numerical analyses because the chosen discretization is not fine enough.

According to the numerical simulation, the soil surface heaves at a low rate over a long period of time (Figure 5.11a), while the monitoring results show a settlement right from the start (Figure 5.11c). The predicted heave is probably due to an overestimation of the soil swelling by the MC model, which assumes a constant Young's Modulus, thus underestimating the stiffness of the soil in unloading.

Swelling occurs due to the continuous increase in the pore pressure until few days before failure (solid lines in Figure 5.12a). The predicted time-development of the pore pressure agrees qualitatively well with the measurements (Figure 5.12b), but the predicted excavation-induced instantaneous drop in pore pressure (about 8 kPa and 20 kPa at point B and C, respectively) is considerably less than measured (about 55 kPa and 115 kPa at point B and C, respectively).

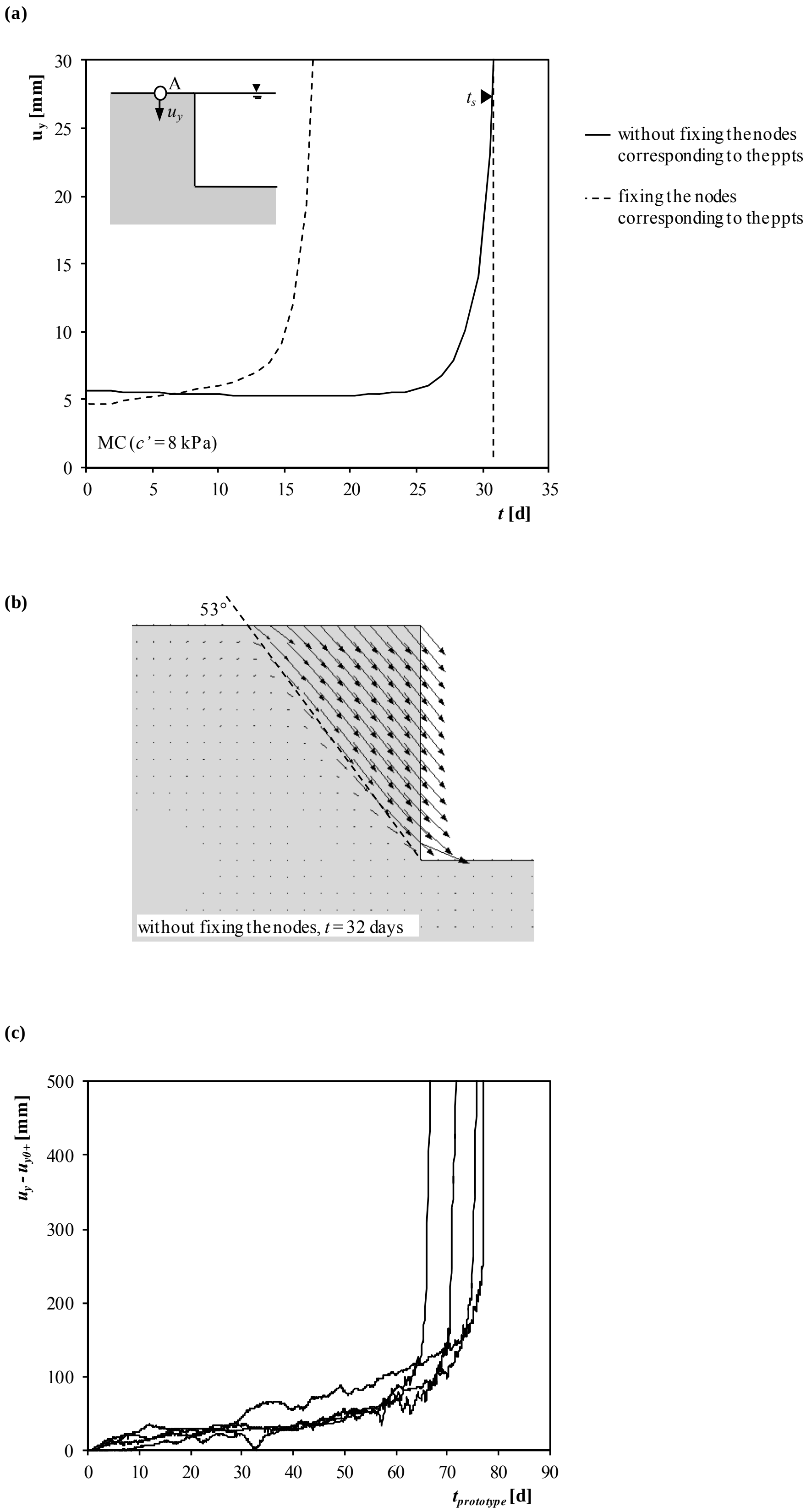

***Figure 5.11** MC model: (a) evolution over time of the vertical displacement at point A, (b), displacement vectors at failure and, (c), monitoring results at prototype scale.*

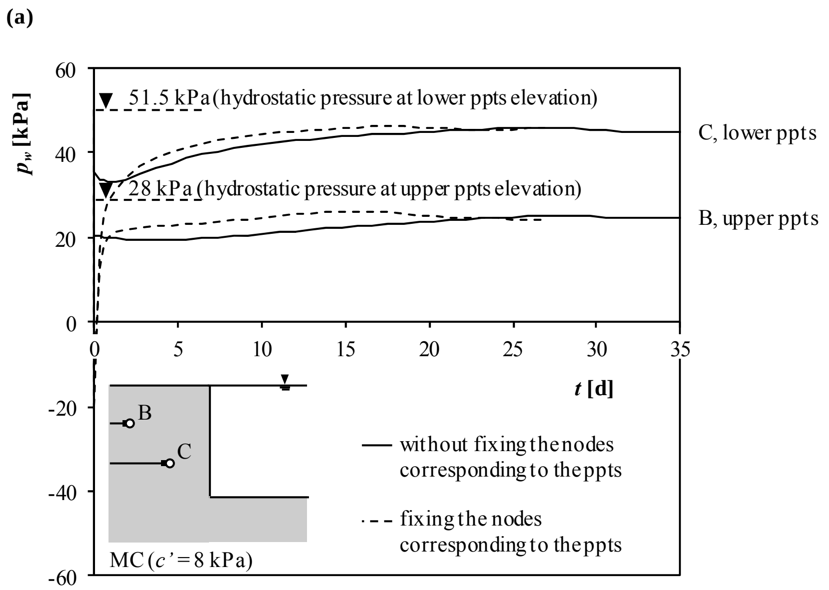

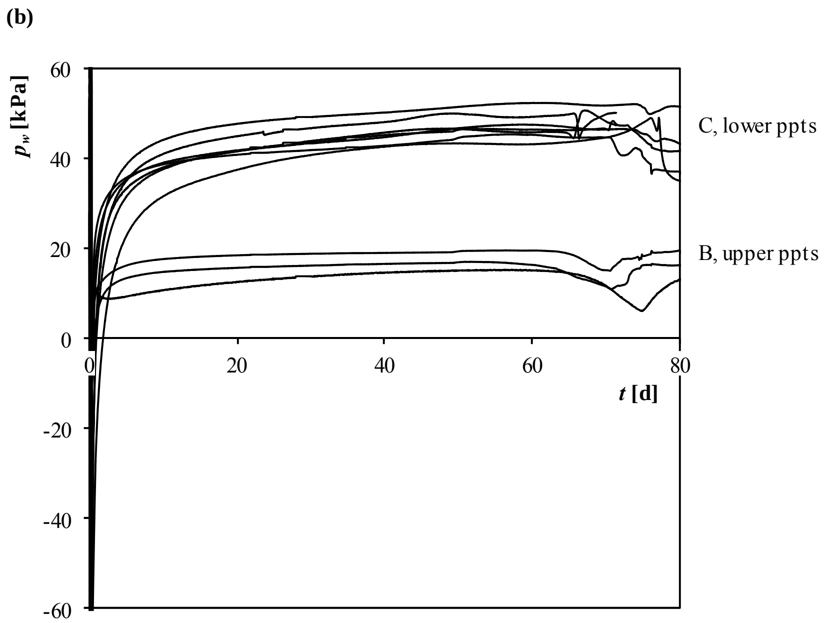

***Figure 5.12** MC model: (a) evolution over time of the pore pressure at the ppts locations (points B and C) and, (b), monitoring results at prototype scale.*

This difference seems to be due the fact that the ppts represent an obstacle to horizontal displacements of the soil in their close vicinity. In fact, the comparative computations with fixed nodes predict an excavation-induced instantaneous drop in pore pressure by about 39 kPa and 72.5 kPa (at point B and C, respectively; dashed lines in Figure 5.12a) which is closer to the monitored values.

After the initial phase of the excess pore pressure dissipation process (about 5 – 10% of t_s), the pore pressures obtained with fixed nodes become quite similar to those obtained without fixing the nodes (Figure 5.12a).

The simulation with fixed nodes results to a stand-up time of about 17 days (Figure 5.11a, dashed line), *i.e.* the difference between observed and predicted stand-up time is bigger than in the case of free nodes.

The computation with fixed nodes provides a possible interpretation of the excavation-induced instantaneous drop in pore pressure measured experimentally. The comparison of the results obtained with and without fixed nodes also indicates that the ppts locally influence the pore pressure field (the effect of the ppts is limited to the vicinity of their tips). This means that the measured pore pressure may not be representative of the pore pressure acting in the model (the size of the ppts is small compared to the width of the model).

In search of possible reasons for the difference between predicted and observed stand-up time, the sensitivity of the simulation results with respect to cohesion, Young's modulus *E* and permeability *k* was investigated, whereby only the product *Ek* is significant on account of the structure of the consolidation equations (Figure 5.13). For the reasonable cohesion range (7 – 9 kPa, see [65]) and *Ek* after Table 5.3, the stand-up time is equal to 12.5 – 100 days (4 – 130 d when considering a variation by ±30% in *Ek*), which is in the order of the measured time (70 – 80 d), but mostly lower. A simulation with a finer mesh discretization would predict an even lower stand-up time (Section 5.4). As shown in Chapter 4, the reason for the underestimation of the stand-up time by the isochoric MC model is that it does not consider the plastic dilation which delays the excess pore pressure dissipation process.

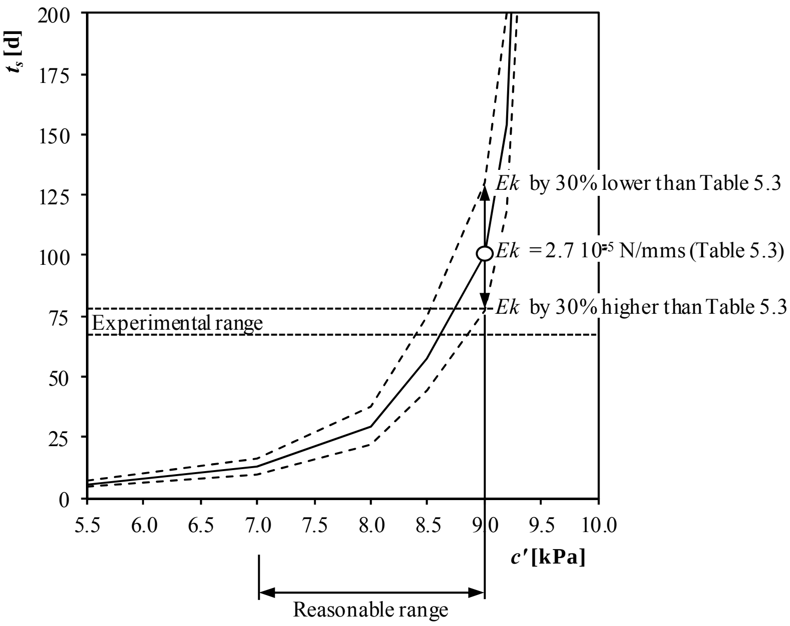

Figure 5.13 *MC model. Stand-up time as a function of the effective cohesion.*

5.3.3.2 MCC model

Selected computational results are presented in Figure 5.14 and Figure 5.15. The time-development of settlement is qualitatively the same for both parameter sets and agrees qualitatively well with the experimental results (Figure 5.14c). Quantitative differences exist with respect to the initial instantaneous settlement and the stand-up time. As expected according to the elastic stiffness of the material, the initial settlement computed for set 2 is almost double of the one obtained for set 1. According to the expectations, the stand-up time is higher for set 1 than for set 2 (410 days *vs.* 130 days). For both materials set the stand-up time is higher than the actual stand-up time (72 d at the prototype scale). The settlement close to failure (about 100 mm for both parameter sets) is about half the measured one (Figure 5.14c). As in the MC simulations (and for the same reasons), a wedge (without tension crack) develops at ultimate state (Figure 5.14b) and the sliding plane is less inclined than observed in the experiments (52.5° and 54° for set 1 and 2, respectively, *vs*. 57° in the experiments).

In conclusion, the MCC model predicts the observed settlement much better than the MC model. However, the stand-up time computed with the MCC model is longer than the observed one.

As explained in Chapter 4, a first reason for the different stand-up time could be related the shape of the MCC yield surface, which overestimates the resistance of the soil on the dry side of the critical state line. A higher resistance means that a bigger stress change is required in order to reach the yield surface, and successively to soften to the CSL. As the stress change in the considered problem is mainly due to the swelling process, a higher resistance leads to a longer swelling time. Another reason is the sensitivity of the stand-up time to the mesh size. As it will show in Section 5.4, with finer meshes (that are able to map the development of a thin shear band) the model predicts stand-up times very close to the actual ones.

As the soil at the ppt locations (points B and C) remains elastic immediately after unloading, the excavation-induced instantaneous pore pressure drop is for both parameter sets close to the one computed with the MC model. It is lower than the measured instantaneous negative excess pore pressure for the reasons explained in Section 5.3.3.1. The predicted time-development of the pore pressure is different from the observed time-development in that it increases only at the beginning of the process; over the last two thirds of the process, pore pressure decreases. The decrease in pore pressure is associated with the plastic dilation that accompanies shearing and occurs over such a long period (much longer than observed) because, as explained above, the MCC overestimates the size of the yield surface on the dry side (and thus the amount of shearing and plastic dilation needed to reach the CSL). As plastic dilation has a stabilizing effect, the overestimation of the plastic dilation results to an overestimation of the stand-up time.

Summarizing, the MCC well captures qualitatively the deformation behaviour observed experimentally. However, the pore pressure evolution (and thus of the settlement rate) is affected by the simplified shape of the yield surface, which, for the considered problem (unloading an over-consolidated soil) overestimates the resistance of the ground. This inherently leads to an overestimation of the stand-up time.

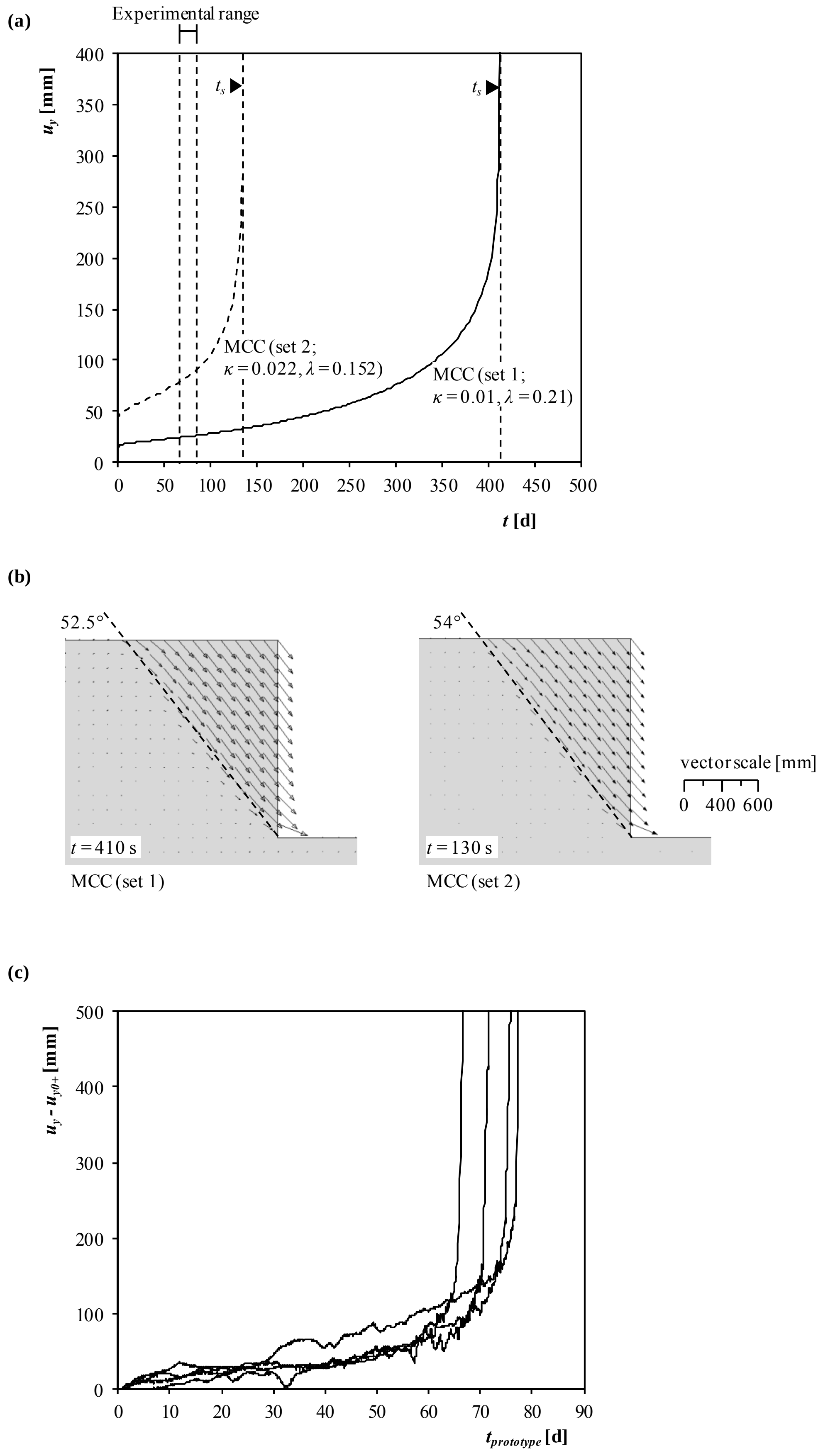

Figure 5.14 *MCC model: (a) evolution over time of the vertical displacement at point A, (b), displacement vectors at failure and, (c), monitoring results at prototype scale.*

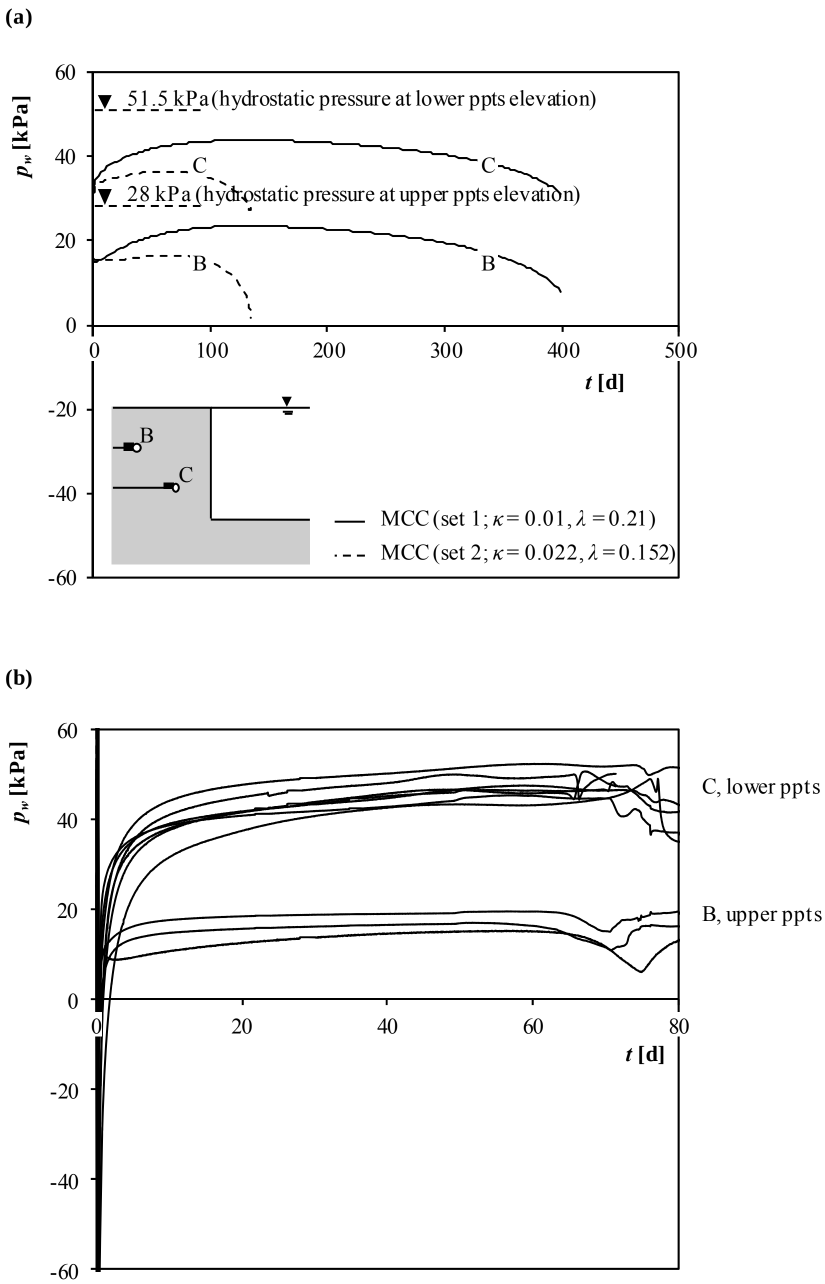

***Figure 5.15** MCC model: (a) evolution over time of the pore pressure at the ppts locations (points B and C) and, (b), monitoring results at prototype scale.*

5.4 Mesh dependency

As explained in Chapter 3, the finer the mesh, the shorter the stand-up time. This is confirmed also by a series of numerical simulations of the centrifuge test, which were performed with different meshes. The mesh dependency is pronounced particularly for the MCC model (Figure 5.16). The finest considered discretization consists of square elements of side length 0.20 m, which means that the vertical cut is 35 elements high. It is obvious that selecting an element size in the order of few mm (the size of the shear band) is hardly feasible as it would require an extremely log computational time (Figure 5.17 exemplary shows the non-linear increase of the computational time with decreasing element size). The stand-up time for thin shear bands can be estimated by linear extrapolation (Figure 5.16) and amounts to 9 – 11 days for the isochoric MC model (which is by factor 8 less than observed) and to 43 – 80 days for the MCC model, which agrees reasonably well with the observed stand-up times.

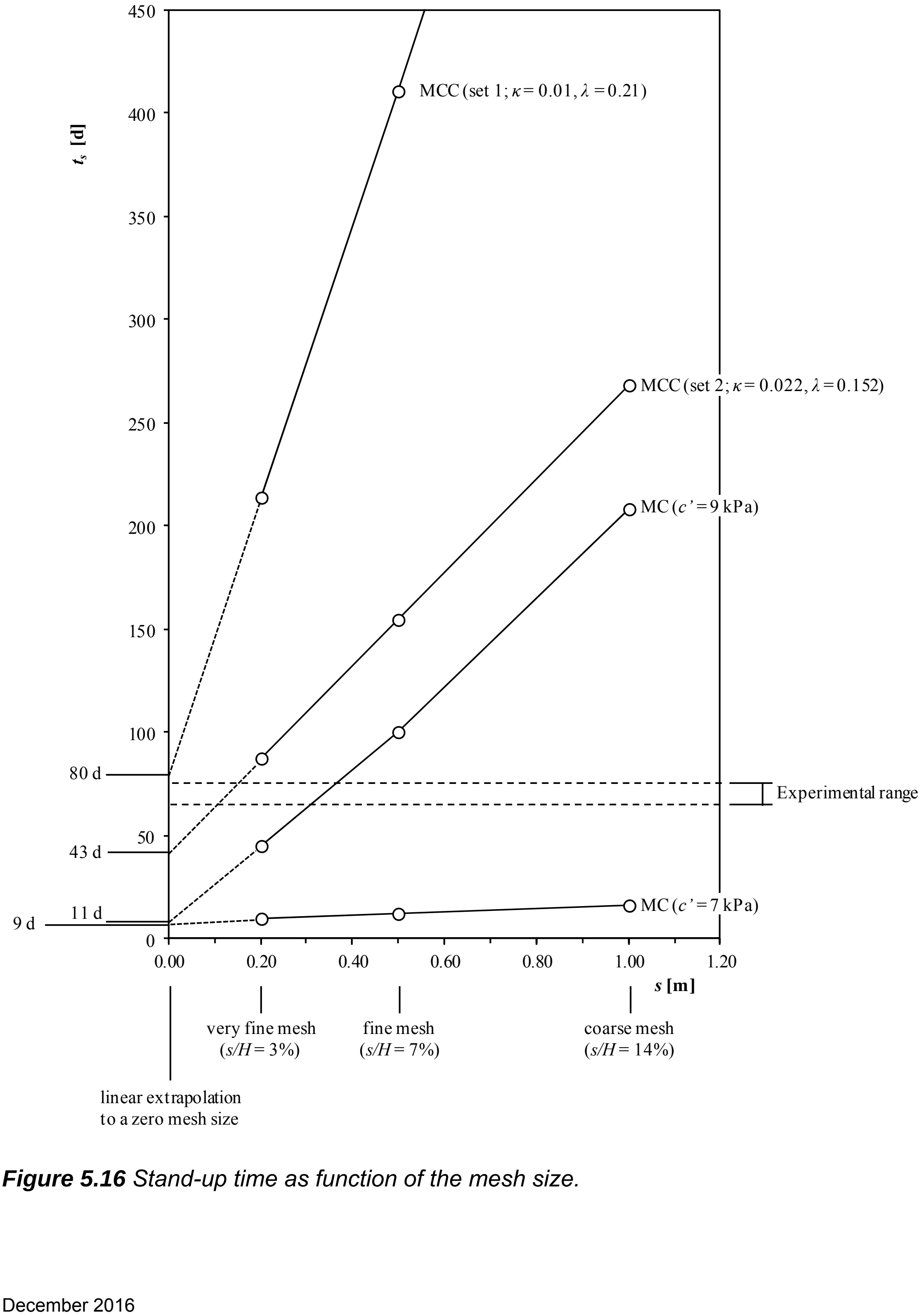

Figure 5.16 *Stand-up time as function of the mesh size.*

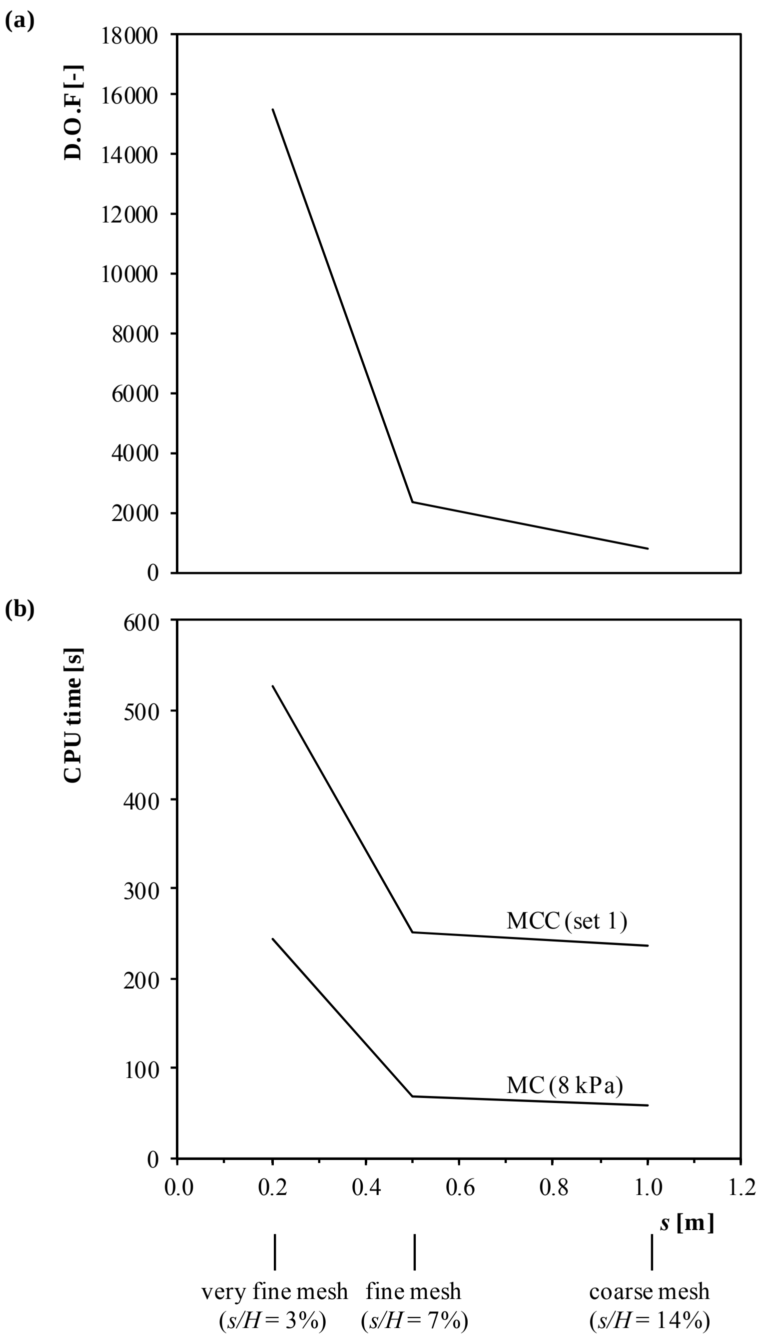

Figure 5.17 *(a) Degree of freedom as a function of the element size and, (b), total CPU time required for two computations adopting MC and MCC models, respectively (64-bit operating system, processor Intel® Xeon® CPU E3-1245 V2 3.4 GHz parallel processing, RAM 16 GB).*

5.5 Conclusions

Chapter 5 investigated experimentally and numerically the stand-up time of an underwater vertical excavation in over-consolidated clay. Although the problem considered is simple, it provides an illustration of features that are indeed relevant to the time dependent face stability of tunnels in low-permeability soils.

The experimental tests were executed in a drum centrifuge that allows to reproduce a prototype height of the unsupported excavation of 7 m. The tests showed a very good reproducibility, both with respect to settlement and pore pressure evolution.

These physical models showed that collapse occurs due to a combination of shear and tensile failure. Failure manifests itself with rapid settlement acceleration. The average stand-up time was 25 minutes at the model scale, which corresponds – according to the scaling laws – to 72 days at the prototype scale.

The numerical computations were carried-out by means of coupled FEM analyses. The behaviour was studied for two constitutive models: the Modified Cam Clay model and the linearly elastic perfectly plastic Mohr Coulomb model with isochoric plastic flow.

The material parameters used in the numerical analyses were mostly estimated or validated in advance based upon laboratory tests or determined based upon theoretical considerations.

The MC model led to a stand-up time generally shorter than the actual, and gives displacements that are much smaller than the measured one. The MCC model generally led to an overestimation of the stand-up time, but better reproduced the physical model behaviour. Taking into account the mesh sensitivity of the results by extrapolating the stand-up time to the mesh size corresponding to the thickness of the shear band the underestimation of the stand-up time increased for the MC model, while the stand-up time computed with the MCC model got close to the experimental results. In spite of the observed differences the simulation predictions were very good considering that they were class A predictions.

In conclusion, Chapter 5 confirmed that the estimation of the stand-up time, although being a highly complex phenomenon, can be approximated numerically by hydraulic-mechanical coupled FEM analyses, even using a simple constitutive model (the stand-up time has the same order of magnitude than the one observed experimentally). The selection of a MC model with isochoric plastic flow generally leads to an underestimation of the stand-time (particularly when extrapolating the results to the thickness of the shear band), while the assumption of a MCC model leads to an overestimation of the stand-up time if the results are not extrapolated to the size of the shear band.

6 Stand-up time of tunnel face

6.1 Introduction

The most serious hazards in soft ground tunnelling are associated with a collapse of the tunnel face. In shallow tunnels the instability may propagate towards the surface, thereby creating a crater. Experience shows that an unsupported tunnel face may remain stable for a certain period after excavation. Under such conditions the question arises upon the stand-up time. The assessment of the stand-up time is important for both mechanised and conventional tunnelling, particularly under the economical point of view: a short stand-up time would require the implementation of ground improvement or reinforcement or, in the case of mechanized tunnelling, hyperbaric interventions, while a long stand-up time would allow to refrain from such costly and time consuming measures.

Chapter 6 investigates numerically the time dependent stability of the tunnel face assuming that all time effects are due to the excess pore pressure dissipation process in the ground. This assumption is reasonable for shallow tunnels crossing water-bearing soils. The stand-up time is estimated by means of coupled hydraulic-mechanical spatial analyses making use of the findings of the fundamental investigations of the previous Chapters. The computational results are presented in the form of easy to use dimensionless design charts for the assessment of the face stability in shallow tunnelling. The diagrams cover a wide range of ground parameters and allow to estimate quickly the stand-up time of the face, representing thus a valuable decision-making aid in tunnel engineering practice.

6.2 Computational model

The ground is discretized by 8-node brick elements (Figure 6.1). The element size varies from 0.5 m (close to the tunnel face) to 8 m (at the model boundary). The influence of spatial discretization is investigated in Section 6.7.

The water table is taken equal to the elevation of the ground surface (H_w = H). The hydraulic potential is fixed to its initial value at the far field boundaries as well as at the level of the water table. The latter is true if there is no draw-down of the water table, which presupposes sufficient ground water recharge. No-flow conditions are imposed at the symmetry plane as well as at the tunnel wall, which is true for a practically impervious lining, *i.e.* a lining having a permeability much lower than that of the soil (by a factor of at least 1000; [20]). Consider for example a shotcrete with permeability 10^{-12} m/s [83], the condition of no-flow apply if the soil permeability is lower than 10^{-15} m/s (which corresponds to very low permeability clay). For segmental lining with watertight joints or shotcrete combined with waterproof membrane (double lining), the permeability of the support is such that the conditions of no-flow apply for all type of soils.

In the case of a more permeable lining or of water table draw-down, the computational results are on the safe side, because the hydraulic heads on the ground around the tunnel face are tentatively lower.

Mixed conditions are imposed at the tunnel face (*i.e.* no-flow in case of negative pore pressure, and drainage-surface elsewhere). This condition allows the water to flow from the ground toward the tunnel, but not *vice-versa* (which would be physically impossible). The tunnel lining is simulated in a simplified way by fixing all nodal displacements at the excavation boundary.

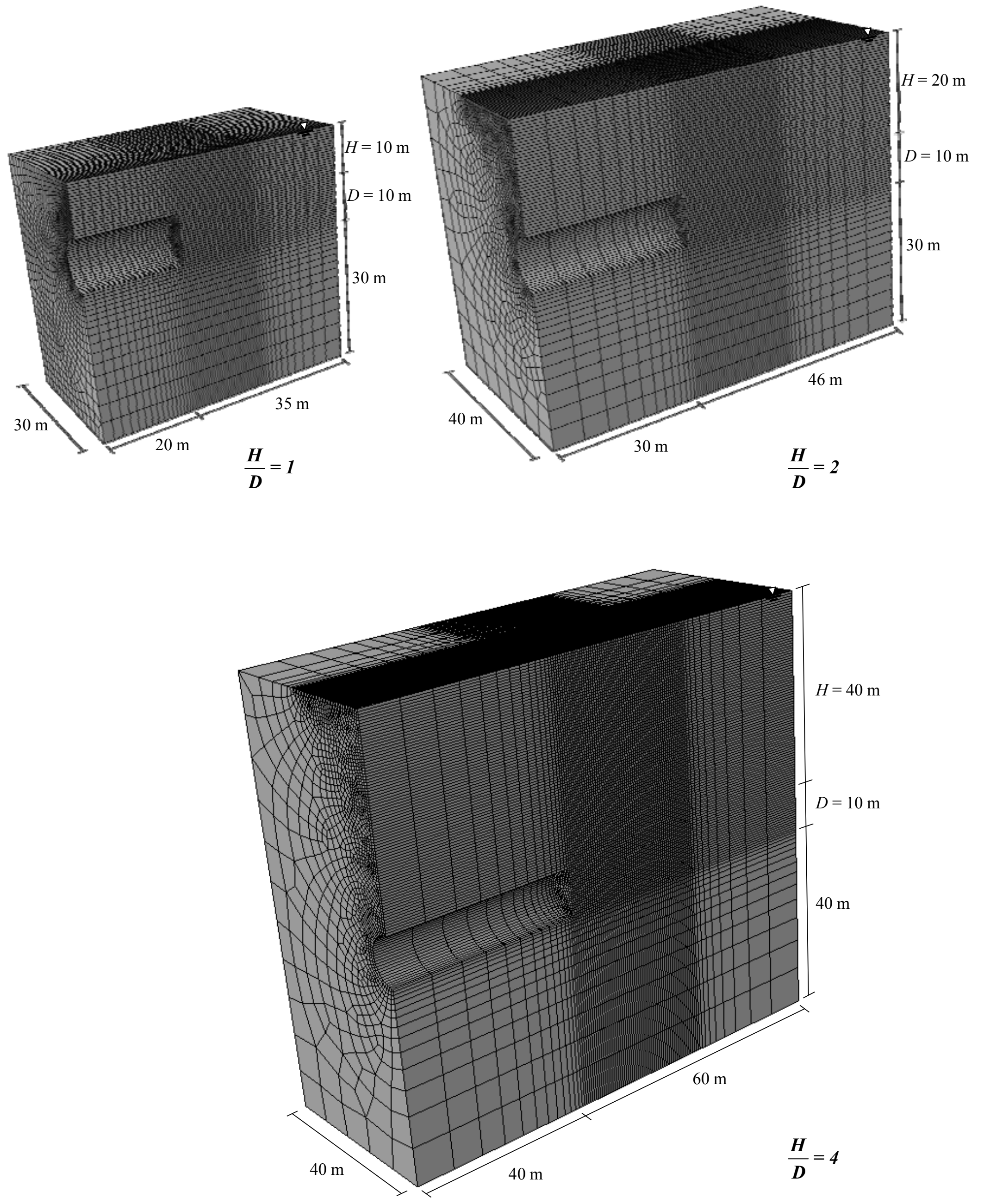

Figure 6.1 *Numerical models.*

The initial stress field corresponds to the overburden pressure at each point. The analyses have been performed for two values of coefficient of lateral pressure (K_0 = 0.5 and 1.0).

The ground is modelled as an isotropic, linearly elastic and perfectly plastic material obeying the Mohr-Coulomb yield criterion with isochoric plastic behaviour *without* tension cut-off. This assumption presupposes that the ground exhibits a tensile strength, and so the presence of cementation bonds between the grains. Otherwise, tensile failure would occur in the form of progressive ravelling of the ground at the face. In order to take into account the absence of tensile strength, a tension cut-off has to be considered in the constitutive model (see Figure 6.8b). The influence of the tension cut-off on the results is investigated in Section 6.5. The results show that a tensile cut-off prevents failure to manifests with an increase of the displacements rate. In the present Chapter, the stand-up time in a no-tension ground is taken equal to the time at which tensile stresses start to develop in the model.

The reasons for selecting the MC model are: it is widely used in engineering practice; there is considerable experience in practice about its parameters; it provides in general conservative estimates of the stand-up time (see Chapters 4 and 5). The integration of the elasto-plastic incremental equations is performed according to Clausen [67]. Table 6.1 summarizes the parameters considered in the analysis.

Table 6.1 *Assumed material constant (in case of multiple values the number in brackets is the assumed default parameter).*

Saturated unit weight	γ [kN/m^3]	20
Lateral pressure coefficient	K_0 [-]	0.5, (1.0)
Unit weight of water	γ_w [kN/m^3]	10
Seepage flow parameters		
Permeability	k [m/s]	10^{-7}
Water compressibility	c_w [MPa]	0
Parameters for linearly elastic, perfectly plastic material		
Young's modulus	E [MPa]	20
Poisson's ratio	ν [-]	0.3
Cohesion	c' [kPa]	5-40, (20)
Friction angle	φ' [°]	15, (25), 35
Dilation angle	ψ [-]	0

6.3 Undrained and drained tunnel face stability

6.3.1 Numerical investigation

First the borderline cases of face stability under undrained and drained conditions will be considered on the example of a 10 m diameter tunnel, 10 m deep. Since the goal of the later Sections is to study the evolution of face stability over time, the ground parameters are selected such that the unsupported tunnel face is stable under undrained conditions, but fails under drained conditions.

Undrained stability is investigated by reducing practically instantaneously the total stresses σ_n normal to the face (hereafter referred to as "total face support pressure") from their initial value σ_{n0} (horizontal *in situ* stress) to zero. Typical results are presented in Figure 6.2a and Figure 6.3a. The plastic zone is limited to a small area in front of the tunnel face (Figure 6.2a) and the displacements stabilize to finite values even in the case of an unsupported tunnel face (Figure 6.3a), thus indicating that the latter is stable in the short term.

Drained stability is analysed as follows. In a first step, a steady state analysis is carried-out fixing the pore pressure at the tunnel face and the effective stress normal to the face (hereafter referred to as "effective support pressure") equal to atmospheric and to the initial horizontal effective stress σ'_{n0}, respectively. Subsequently, the effective face support pressure is reduced stepwise, while the pore pressure field is fixed to the steady-state field obtained in the first step. The results are presented in Figure 6.2b and Figure *6.3*b. The depressurization of the pore water in the first step causes consolidation of the ground, face extrusion and surface settlement although the effective face support pressure is kept fixed to its initial value (Figure 6.3b; lines for points A and B; displacements at σ'_n/σ'_{n0} =100%). With decreasing effective face support pressure σ'_n, the displacements increase and the plastic zone ahead of the face becomes larger (Figure 6.2b). Contrary to the undrained analysis, the displacement of the face (point A) does not reach a finite value, but increases asymptotically to infinity when the effective support pressure σ'_n approaches a critical value of about 25% σ'_{n0} (Figure 6.3b; state marked by "(iii)"). This indicates that the system has reached its ultimate state; re-distribution of the effective stresses is no longer possible and the face becomes unstable. It is noteworthy that the plastic zone at the ultimate state does not reach the ground surface (Figure 6.2b, state (iii)). A localized failure ahead of the face presupposes the development of tensile stresses above the unstable region of material. The latter develop in the model because of the adoption of the MC model without tension cut-off.

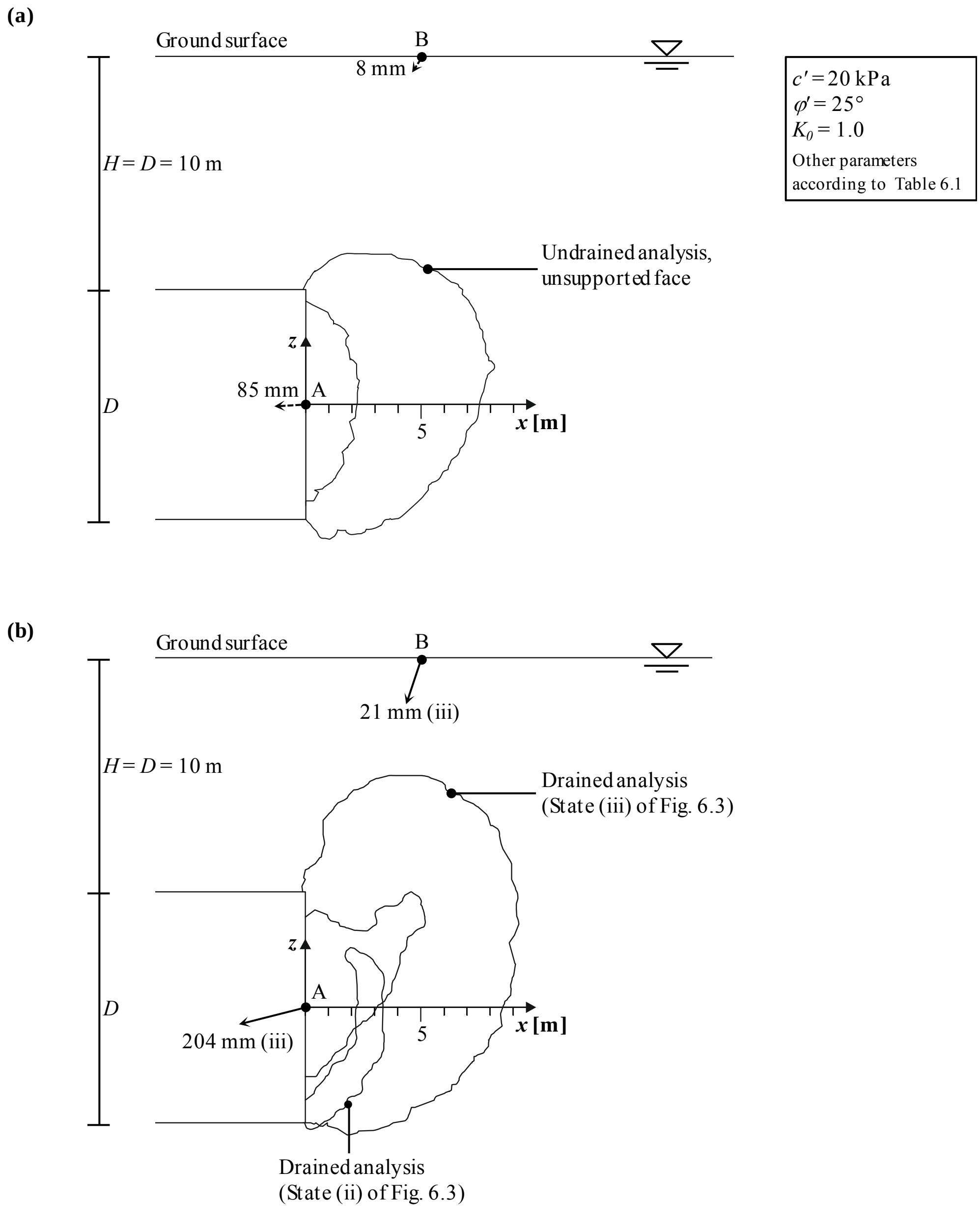

***Figure 6.2** Boundary of the plastic zone and displacement vectors of the points A and B, (a), at the end of the undrained excavation and, (b), short before failure under drained conditions.*

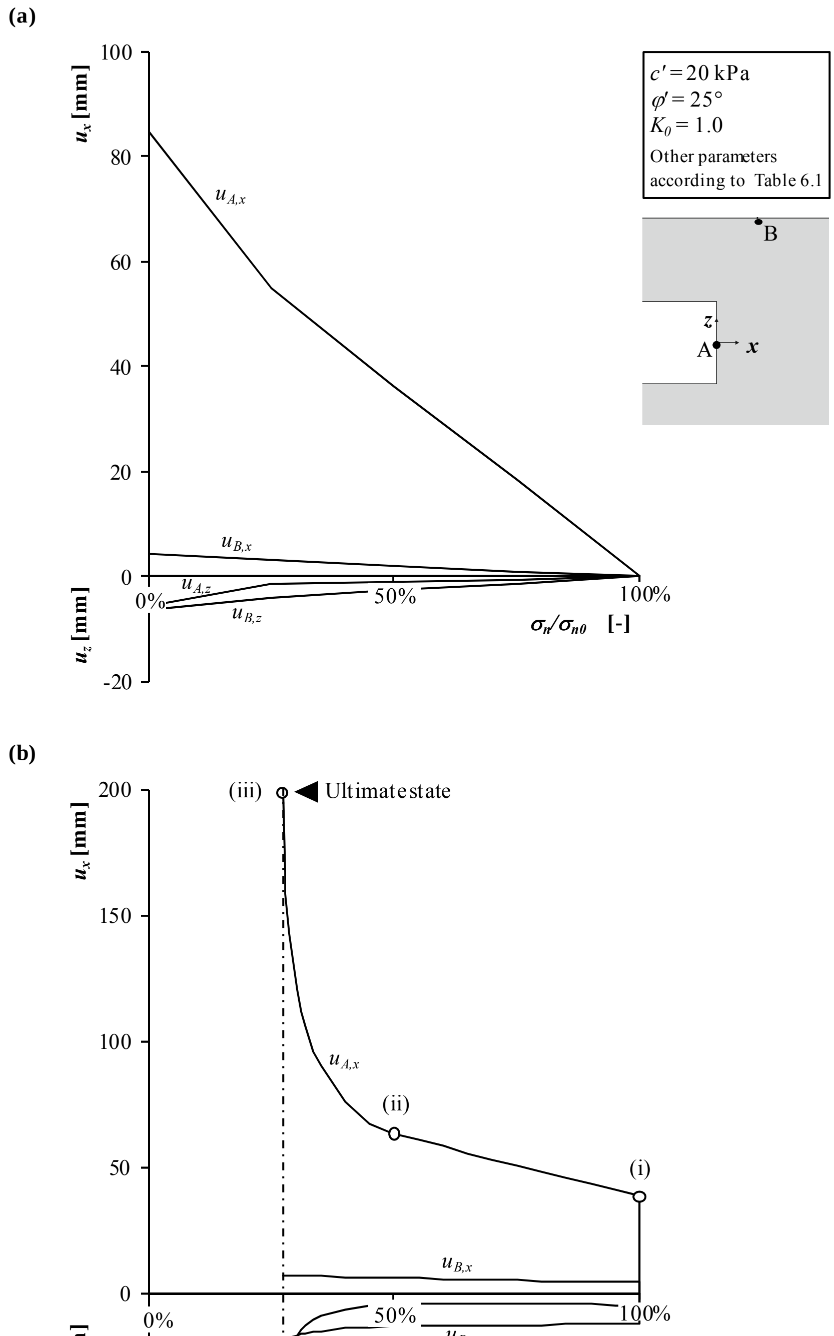

***Figure 6.3** Displacement of points A and B as a function of the normalized total face support pressure or the normalized effective face support pressure for, (a) undrained analysis and, (b), drained analysis, respectively.*

6.3.2 Comparison with analytical solutions

The prediction of stable undrained conditions agrees with the results obtained by applying the static solution of Davis [10], according to which the required face support pressure

$$p_s = \sigma_{v,0}(z = H + 0.5D) - N_s\ s_u\ , \tag{6.1}$$

where $\sigma_{v,0}$ is the mean *in situ* total stress at the tunnel axis (= 300 kPa in the present example), N_s is the so-called stability number (= 4.5 for H/D = 1; Davis [10]) and s_u is the undrained shear strength. For a uniform undrained shear strength s_u of 82 kPa (after Eq. (2.2) of Section 2, taking into account the mean effective stress at the tunnel axis elevation), the required support pressure is negative (-69 kPa), which means that the face is stable without support.

The stability of the tunnel face under drained conditions is investigated after Perazzelli [84], according to which the required support pressure

$$p_s = P_1\ \gamma_w\ \Delta h + P_2\ \gamma' H - P_3\ c'\ , \tag{6.2}$$

where Δh denotes the difference in hydraulic head between water table and tunnel axis (15 m in the present example), γ' (= 10 kN/m^3) is the submerged unit weight of the soil, c' is the effective cohesion and the coefficients P_1, P_2, P_3 are functions of the friction angle and of the inclination of the sliding wedge (determined such that it maximizes p_s).

For the strength parameters of the present problem (c' = 20 kPa and φ' = 25°), P_1 = 0.47, P_2 = 0.11, P_3 = 2.07 and the required effective support pressure is equal to to 37.9 kPa, which is very close to the numerically predicted limit pressure (25% x 15 m x 10 kN/m^3 = 37.5 kPa). The required support pressure was obtained for a critical inclination of the sliding wedge of 36°.

The critical cohesion, *i.e*. the cohesion required for drained stability of an unsupported face, can be obtained from Eq. (6.2) by setting the support pressure equal to zero,

$$c'_{D,\lim} = \frac{P_1\ \gamma_w\ \Delta h + P_2\ \gamma' H}{P_3}\ , \tag{6.3}$$

and is equal to 38 kPa in the present case.

6.4 Tunnel face stability under transient conditions

In the example of Section 6.3 the unsupported tunnel face is stable in short-term (undrained conditions) but unstable in long-term (drained conditions). Next, the evolution of face stability over time will be studied and the stand-up time t_s of the tunnel face will be estimated.

The tunnel face stability is simulated by means of a transient analysis following the undrained excavation (as described in the previous Section). The assumption of undrained conditions – prevailing at the beginning of the transient analysis – represents a reasonable assumption in the following cases: (i) rapid advance rate compared to the soil permeability (ratio between advance rate and ground permeability of about 5000 – 10000 for a tunnel of 10 m diameter; [13] – e.g. for a clayey soil with permeability 10^{-9} m/s, undrained condition would prevail around the tunnel face progressing with a rate higher than 0.5 – 1 m/day); (ii) closed shield tunnelling with full compensation of the initial stresses (*i.e.*, where the stress and hydraulic fields around the tunnel during advance correspond to the *in situ* one) followed by rapid depressurization of the face (a rather theoretical case). The influence of the advance rate on the face stability is discussed in Section 6.10.

As explained in Chapter 2, stand-up time is estimated co-evaluating the time-development of the stresses and pore pressures (Figure 6.4 and Figure 6.7), of the plastic zone (Figure 6.5a), of the equivalent plastic and total volumetric strain (Figure 6.5b and Figure *6.6*b, respectively) and of the displacements of selected points (Figure 6.6a).

In spite of the excavation-induced unloading of the tunnel face, the axial effective stress σ'_x at the face is compressive (Figure 6.4b), which is favourable for stability. The reason is that negative excess pore pressures develop due to the excavation (Figure 6.4a). As the horizontal effective stress practically coincides with the minor principal stress, the effective stresses in the axial direction govern the magnitude of the effective stresses in the vertical and in the transverse directions (Figure 6.4c and Figure 6.4d), which explains the similarity in the distribution of σ'_z and σ'_y.

During the dissipation of the negative excess pore pressures (Figure 6.4a) the effective stresses (and thus also the shear resistance of the ground) decrease (Figure 6.4b, c and d). A plastic zone develops ahead of the tunnel face, progresses upwards and reaches the ground surface at about t = 11.3 h (Figure 6.5a). The shape of the failure zone agrees reasonably well with the wedge and prism mechanism that is often assumed by limit equilibrium analyses (e.g. [28]), nevertheless with a curved slip surface. This is visible also from the contour lines of the total equivalent plastic strain $\varepsilon_{eq,pl}$ (Figure 6.5b). The latter is defined as (e.g. [85])

$$\varepsilon_{eq,pl} = \int_0^t \sqrt{\frac{2}{3}\dot{\varepsilon}_{ij}^p \dot{\varepsilon}_{ij}^p}\, dt \,, \tag{6.4}$$

and provides an overall measure of the shearing of the ground. The shape of the contour lines indicates an average inclination of the sliding surface (assumed as the surface with the maximum equivalent plastic strain, *i.e.* of the most intense shearing) of about 39° (which is only 3° higher than the angle predicted by the limit equilibrium analysis of Section 6.3.2).

It interesting to note that at the ultimate state the ground remain elastic close to the tunnel face (around point A) as well as close to the ground surface above the central part of the failure mechanism (around point C); shearing localizes along the boundaries of a wedge and prism failure mechanism. The ground remains elastic around point A due to the negative excess pore pressures that developed in the proximity of the tunnel face during undrained unloading but have not dissipated yet (thus keeping the effective stresses sufficiently high) and because of the small amount of shear deformation. Point B is located in the elastic region delimited by the shear bands, which – at the ultimate the failure – develop from the tunnel face up to the ground surface.

Failure occurs at about t = 11.3 hrs. The latter is indicated by (Section 2.5.2):

- the time-development of displacements, which start to increase rapidly at t = 11.3 h and tend to infinity at about t = 12.3 h (Figure 6.6a);

- the extent of the plastic zone (it reaches the ground surface at t = 11.3 hrs, Figure 6.5a);

- the almost constant rate of the volumetric strain and the effective stresses (observed particularly in points D, C and A' at about 11.3 hours, see Figure 6.6b and Figure 6.7, respectively);

- numerical convergence problems shortly before collapse (for t > 11.3 hrs, the volumetric strains at point D as well the horizontal effective stress σ'_y and the vertical stress σ'_z decrease instead of remaining constant; Figure 6.6b and Figure 6.7).

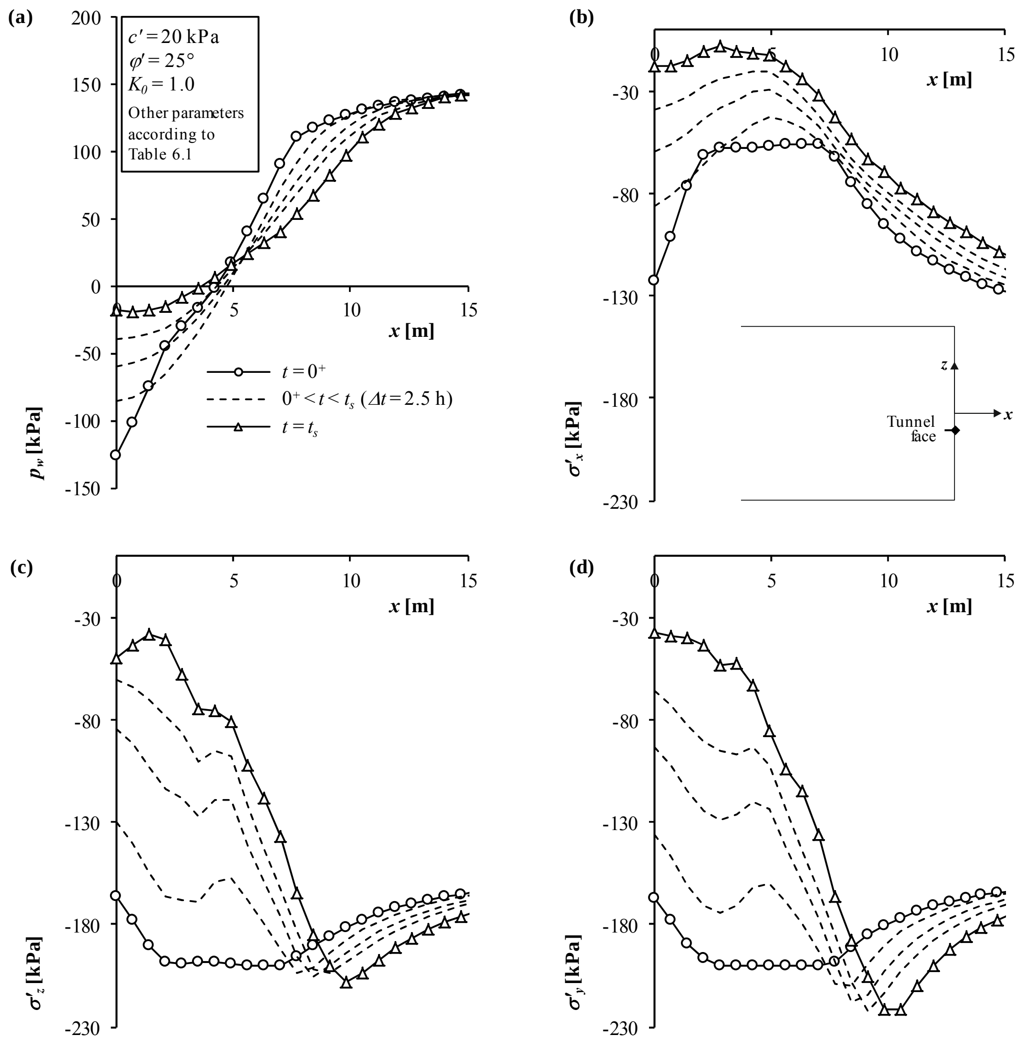

Figure 6.4 *Spatial distribution (along the tunnel axis ahead of the face) of: (a) pore pressure p_w (nodal values); (b) effective horizontal stress σ'_x; (c) effective vertical stress σ'_z; (d) effective out of plane stress σ'_y (effective stress values averaged at the element centroid).*

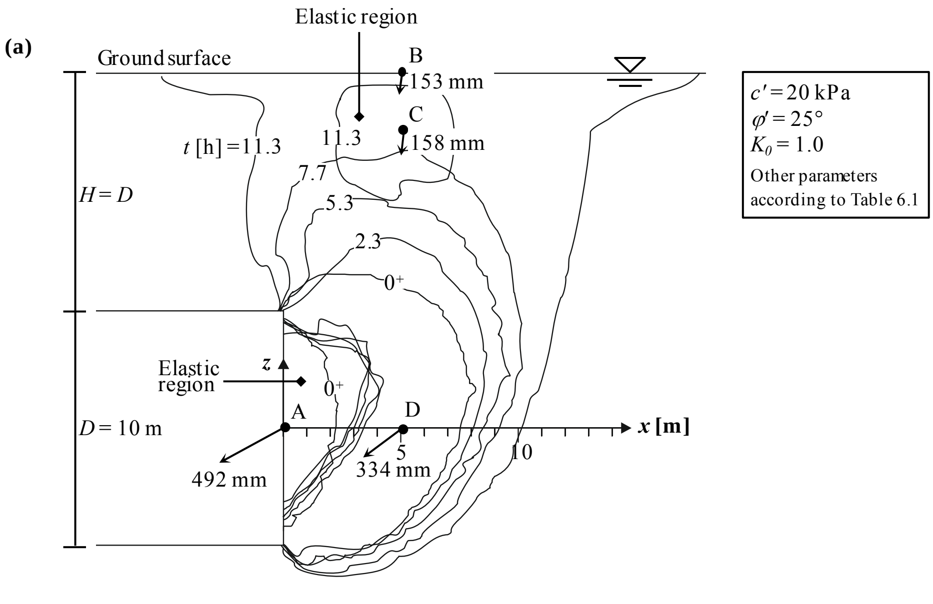

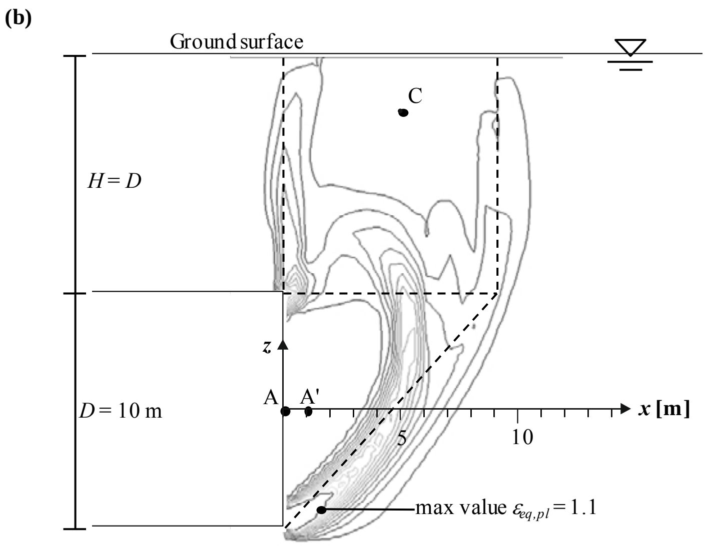

***Figure 6.5** Contour of, (a), the plastic zone at different time and displacement vectors of points A, B, C and D at $t = t_s = 11.3$ h (ultimate state) and, (b), the total equivalent plastic strain $\varepsilon_{eq,pl}$ at failure. The dashed lines indicate the shape of the failure mechanism.*

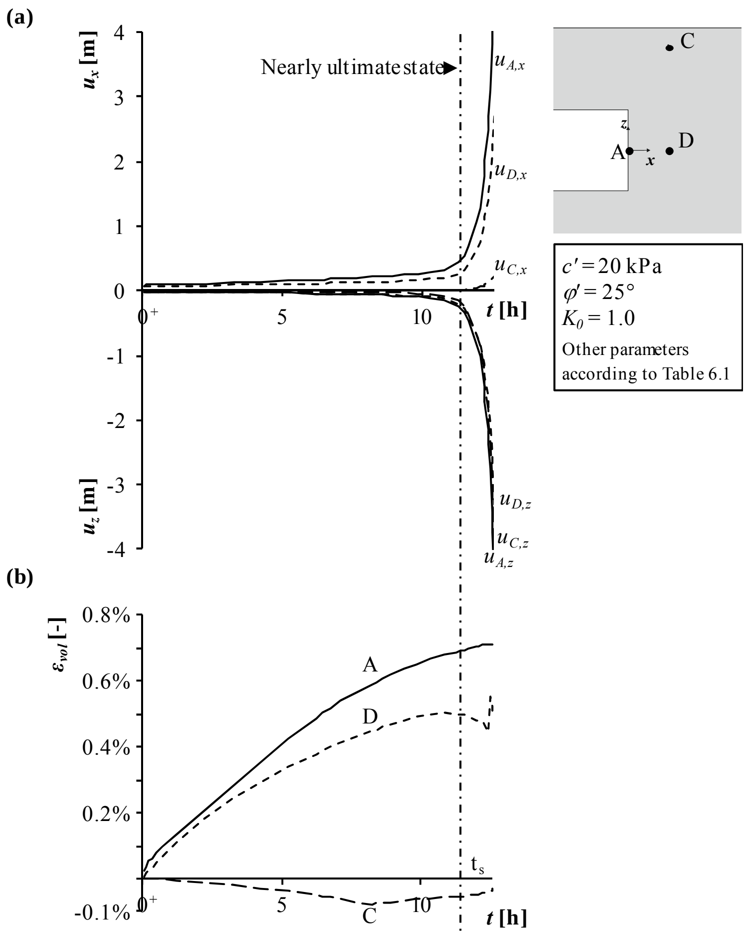

Figure 6.6 *(a) Evolution of the displacements (u_x, u_z) and of (b) the volumetric strain (ε_{vol}) at points A, C and D over time. The dashed vertical line crossing the time axis at t = t_s = 11.3 h corresponds to the near ultimate state.*

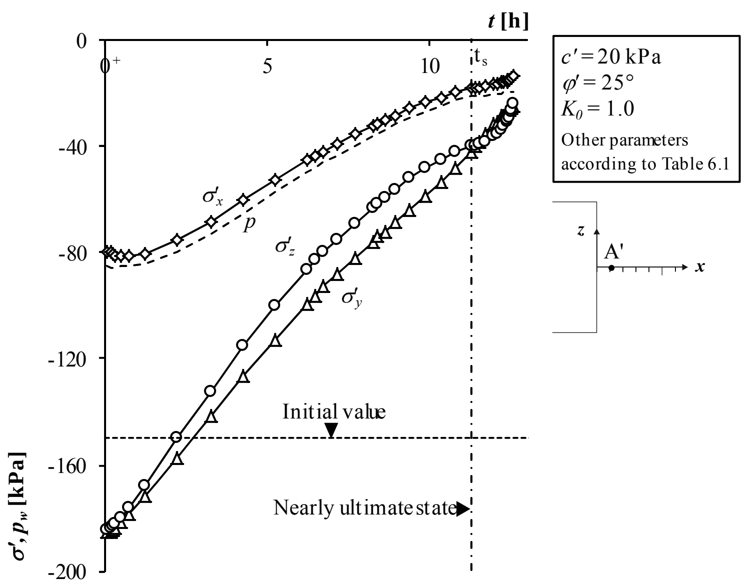

Figure 6.7 *Evolution of the effective stresses (σ'_x, σ'_y, σ'_z) and of the pore pressure (p_w) at point A over time. The dashed vertical line crossing the time axis at t = t_s = 11.3 h indicates the near ultimate state.*

6.5 On the transient tensile failure of the ground

High hydraulic head gradients ahead of the tunnel face may induce tensile stresses in the ground. The latter are statically admissible only if the ground exhibits a tensile strength, which presupposes the presence of cementation bonds between the grains. Otherwise, tensile failure would occur in the form of progressive ravelling of the ground at the face. Under the assumption of the MC-failure criterion the tensile strength of the ground is a function of the friction angle and of the cohesion (see Figure 6.8a). In order to take into account the absence of tensile strength, a tension cut-off has to be considered in the constitutive model (see Figure 6.8b).

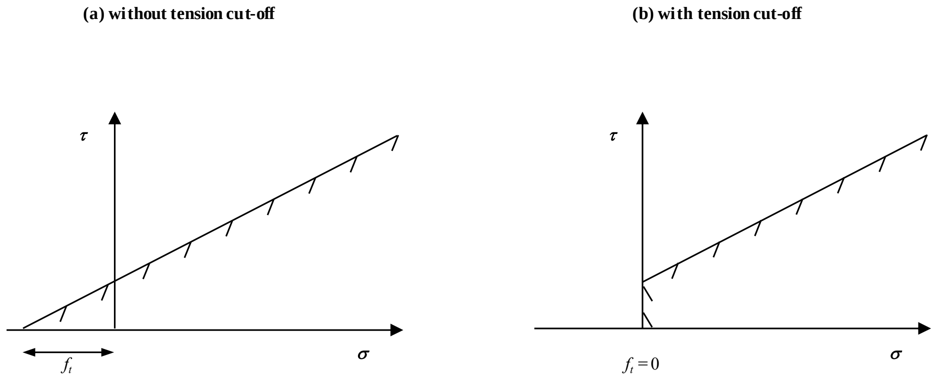

***Figure 6.8** MC-yield surface, (a), without and, (b), with tension cut-off.*

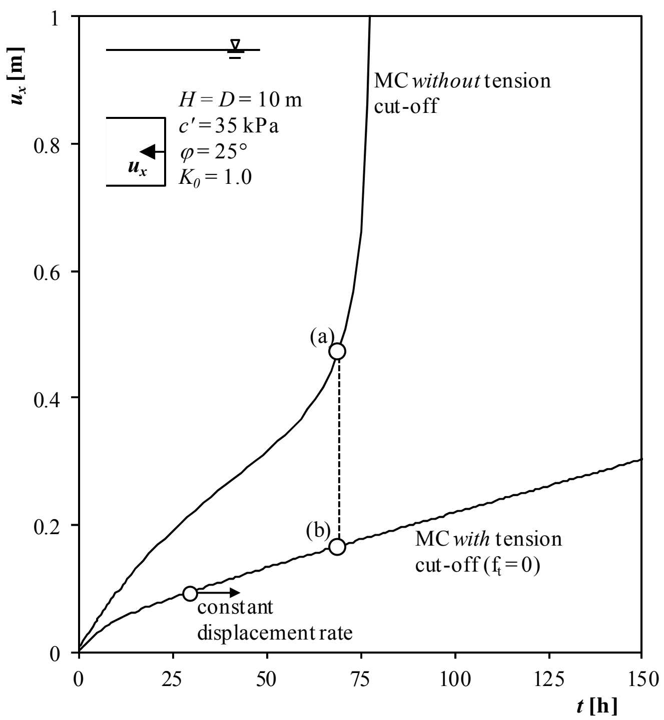

***Figure 6.9** Time-development of the horizontal extrusion of the tunnel face u_x computed without and with tension cut-off in the constitutive model (other parameters according to Table 6.1).*

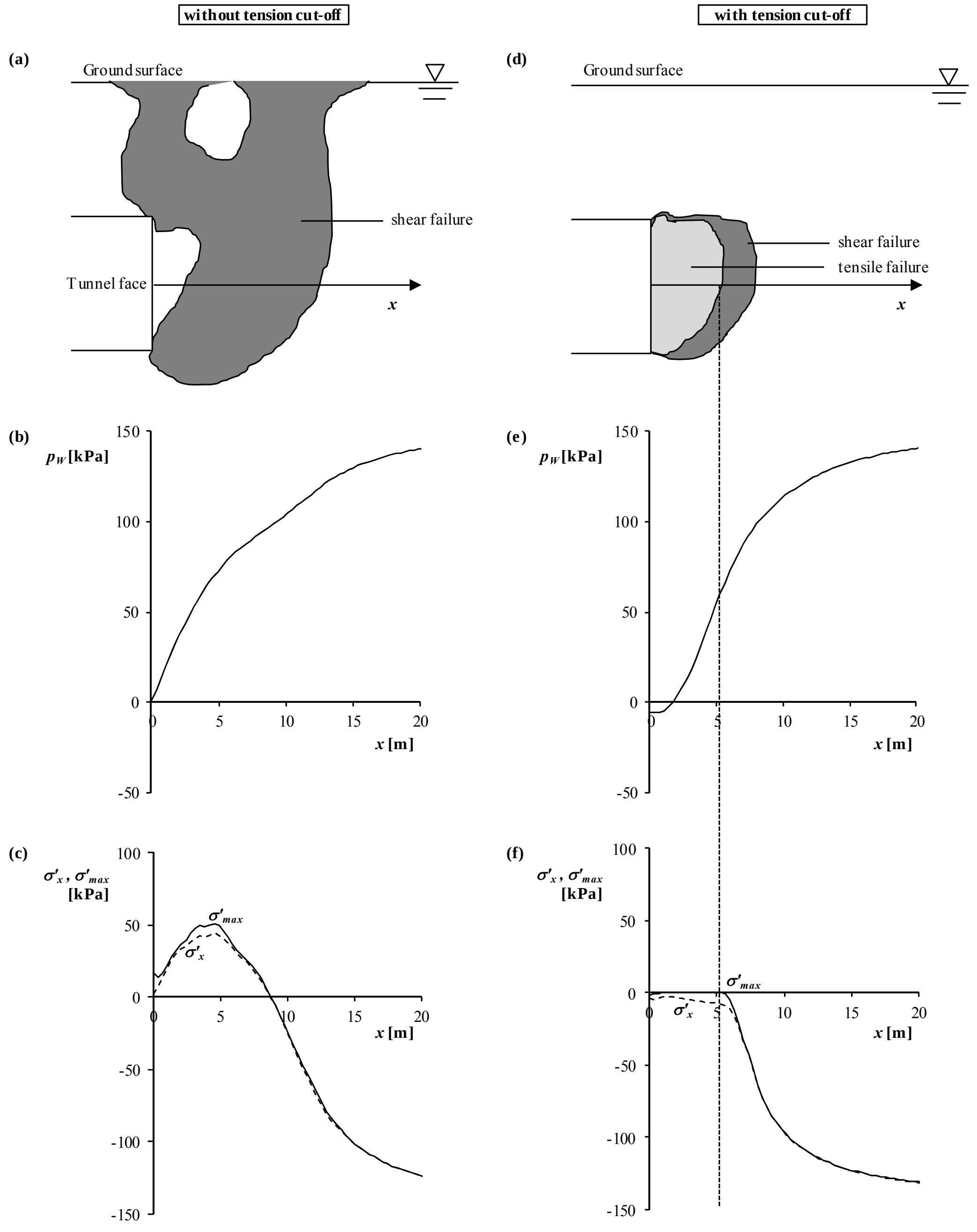

Figure 6.10 *(a) and (d) Plastic zone, (b) and (e) spatial distribution of the pore pressure and (c) and (f) spatial distribution of the maximum and horizontal effective stresses 70 hours after undrained excavation computed. (a) - (c) without and (d) - (f) with tension cut-off in the constitutive model, respectively (φ' = 25°, c' = 35 kPa, K_0 = 1.0, H/D = 1, other parameters according to Table 6.1).*

This section investigates numerically the influence of tension cut-off on the manifestation of failure. With the exception of tension cut-off (which is considered in the constitutive model after Clausen [86]) and of cohesion (which is taken here equal to 35 kPa in order that tensile rather than shear failure occurs), computational model and parameters are the same as in Section 6.4.

Without tension cut-off, failure occurs at about t = 70 h and is characterized – as in all numerical computations with isochoric plastic flow until now – by a rapidly accelerating face extrusion (Figure 6.9, upper line) and a fully developed plastic zone up to the soil surface (Figure 6.10a). Due to the distribution of the pore pressure ahead of the tunnel face (Figure 6.10b) close to failure, seepage forces act towards the tunnel face, thus necessitating tensile effective stresses (Figure 6.10c) in order to fulfil equilibrium in the horizontal direction.

With tension cut-off, however, the model behaviour is qualitatively different with respect both to the time-development of the face extrusion and to the shape of the failure zone: after a certain period of time (about at t = 30 h) the displacement rate becomes constant rather than accelerating (Figure 6.9, lower line). Within about 70 hours after excavation, a tensile failure zone has developed ahead of the tunnel face (Figure 6.10d); it is characterized by zero maximum principal effective stress σ'_{max} (Figure 6.10f) and enclosed by a shear failure zone, which – differently from Figure 6.10a – does not extend to the overburden. In addition, the pore pressure distribution (Figure 6.10e) is slightly different than in Figure 6.10b, with negative values close to the tunnel face. The difference between the results obtained adoption or not a tension cut-off (particularly evident in the evolution over time of the displacement) is due to the irreversible volumetric strains accompanying tensile failure (separation); their effect is the same as that of plastic dilation in the case of shear failure described in Section 2.4 (note also the lower displacement rate, compared to the displacement rate obtained without tension cut-off, in Figure 6.9). In the present case, however, the volumetric strains are due to the associativity of the flow rule at tensile failure (Figure 6.8b).

Physically, the occurrence of tensile failure corresponds to the formation of tensile cracks. The latter, would (on account of the negative pore pressure, Figure 6.10e) desaturate as soon as they reach a free surface (the tunnel face); the stabilizing negative pore pressure would then drop to zero and the face would collapse.

As desaturation is not taken into account and all computations of the present Chapter are carried-out with the MC model without tension cut-off (Figure 6.8a), the stand-up time in a no-tension ground will be taken equal to the time at which tensile stresses start to develop in the model.

6.6 On some factors influencing stand-up time

6.6.1 Cohesion

The stand-up time depends sensitively on the cohesion of the ground; in the example of Figure 6.11, the tunnel face will collapse shortly after undrained excavation for a cohesion of 5 kPa and will remain stable even at long term (*i.e.*, under drained conditions) for a cohesion higher than about 37 kPa, which agrees well with the limit equilibrium prediction after Perazzelli *et al.* (2014) (see Section 6.3.2).

Figure 6.12 shows from top to down the boundary of the plastic zone and the distribution of the horizontal effective stresses σ'_x and of the pore pressure p_w along the horizontal axis ahead of the tunnel face immediately after the undrained excavation (on the l.h.s.) and at the ultimate state (on the r.h.s.) for three cohesion values.

After undrained excavation (Figure 6.12a), the plastic zone extends to the surface for c' = 5 kPa, develops around the entire tunnel face for c' = 20 kPa and is limited to the lower and upper part of the face if c' = 35 kPa. At failure the shape of the plastic zone is similar for all the considered cohesion values (Figure 6.12b).

For a cohesion of c' = 5 kPa, failure occurs shortly after the beginning of the swelling process. Therefore, the effective stresses and the pore pressures at failure are quite close to the undrained values and far away from the steady state distribution (Figure 6.12d and 6.12f).

For c' = 20 kPa, the pore pressure ahead of the tunnel face remains negative at ultimate state (Figure 6.12f), but close to the tunnel face is higher than after undrained excavation.

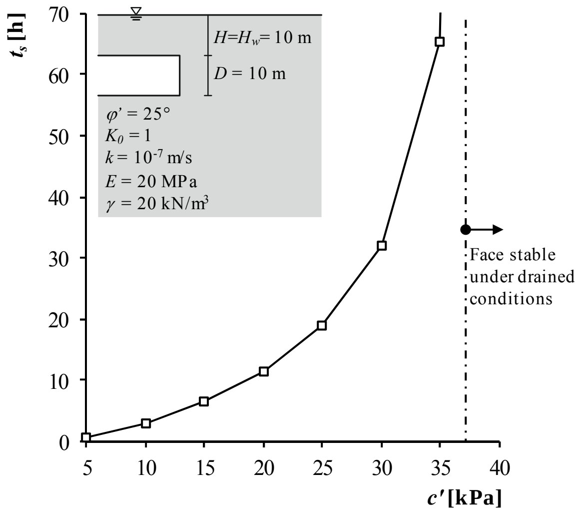

Figure 6.11 *Stand-up time of the tunnel face as a function of the cohesion c'.*

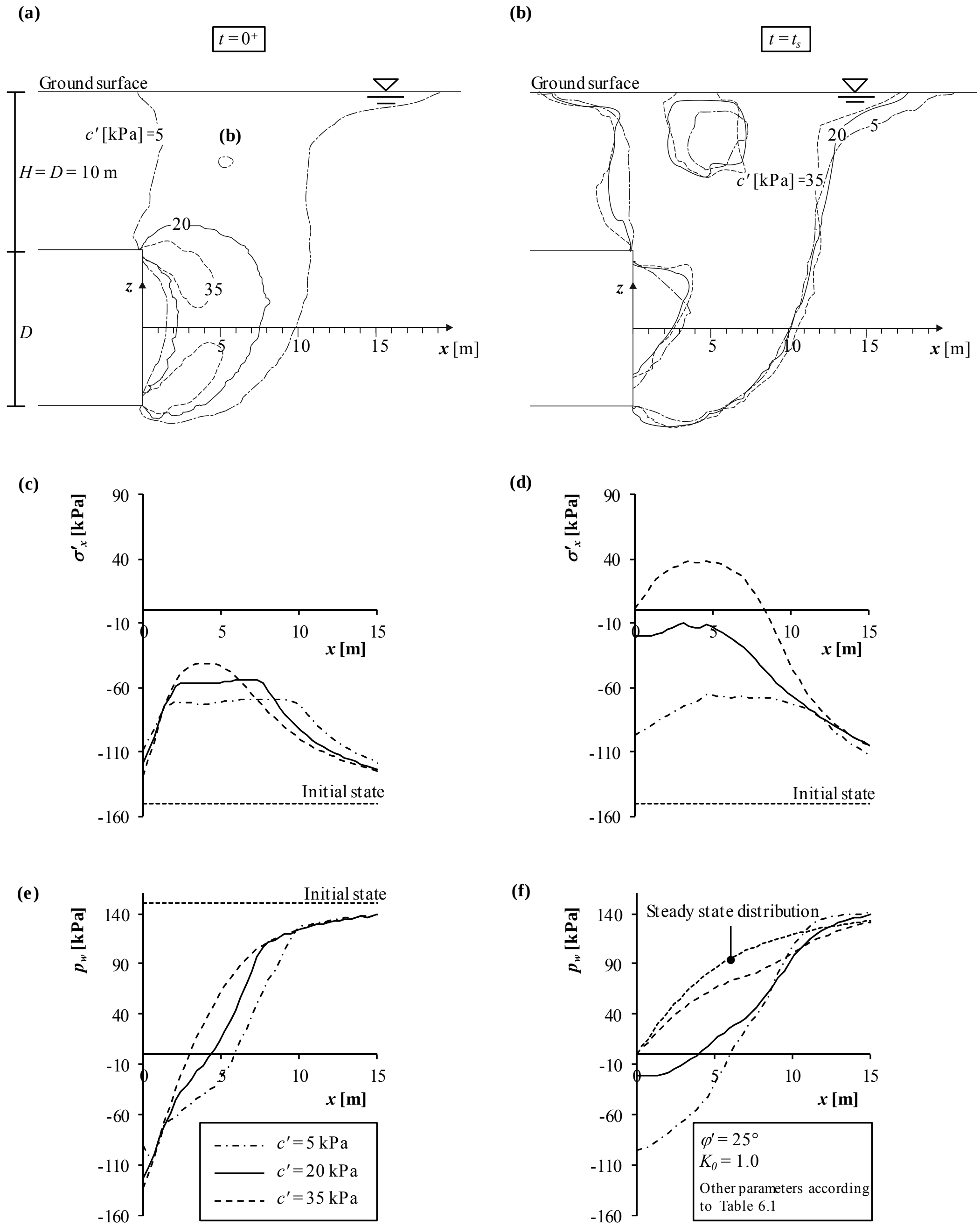

***Figure 6.12** Boundary of the plastic zone (a) immediately after undrained excavation and (b) at ultimate state for c' = 5 kPa, 20 kPa and 35 kPa, and spatial distributions along the x-axis immediately after undrained excavation and at ultimate state of the effective horizontal stress σ'_x (diagrams (c) and (d), respectively) and of the pore pressure p_w (diagrams (e) and (f), respectively) for c' = 5 kPa, 20 kPa and 35 kPa.*

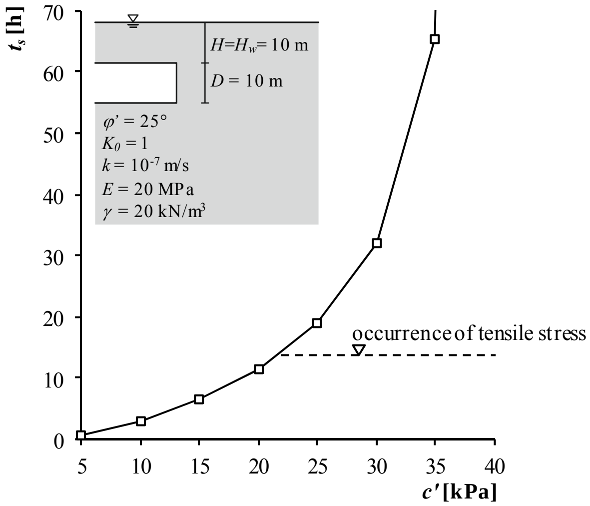

Figure 6.13 *Stand-up time of the tunnel face as a function of the cohesion c' for a ground with (solid line) and without (dashed line) tensile strength.*

For *c'* = 35 kPa, tensile stresses develop ahead the tunnel face close to failure (Figure 6.12d). The development of tensile stresses is due to the pore pressure distribution (Figure 6.12f), which during the dissipation process approaches the steady state distribution and, therefore, causes seepage forces directed towards the face. In the considered example tensile stresses ahead of the tunnel face appear only if the cohesion is higher than about 20 kPa (Figure 6.13). This happens – independently on the cohesion – at approximately 15 hours. As mentioned in Section 6.5, this time is taken as stand-up time for no-tension soils.

6.6.2 Friction angle

Stand-up time increases with friction angle provided that cohesion is less than 30 kPa (Figure 6.14). For higher cohesion values, however, stand-up time decreases with increasing friction angle. The reason is that tensile strength (which is important due to the development of tensile stresses) decreases with the friction angle (the value of cohesion being fixed; Figure 6.15).

For the three values of friction angle, tensile stresses appear in the model about 10 to 15 hours after excavation. This time corresponds, according to the definition given in Section 6.5, to the stand-up time for a non-tension soil.

Furthermore, the critical cohesion (*i.e.* the cohesion for which stand-up time becomes infinite) practically does not depend on friction angle (Figure 6.14).

Finally, the lower the friction angle, the more extended the failure zone both short-term and at failure (Figure 6.16).

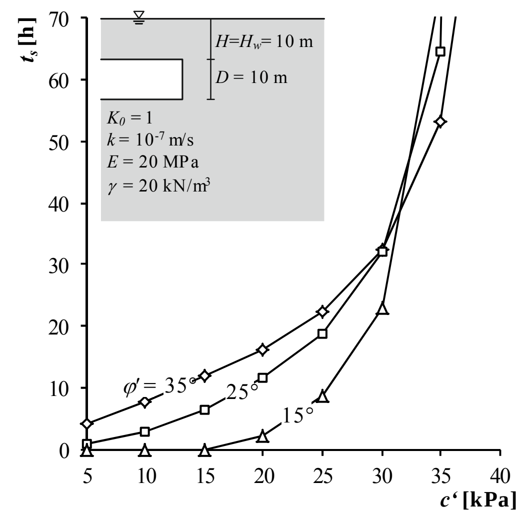

***Figure 6.14** Stand-up time of the tunnel face as a function of the cohesion c' for a friction angle φ' = 15°, 25° and 35°.*

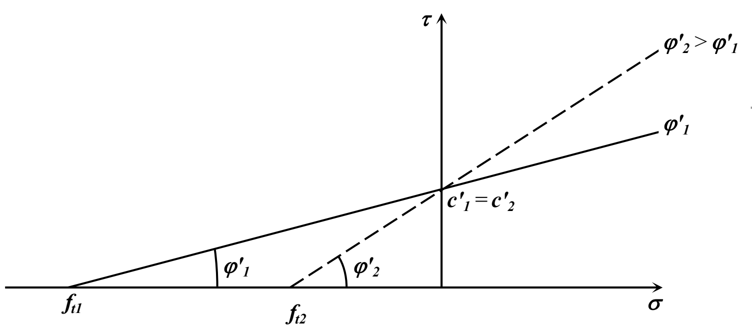

***Figure 6.15** Tensile strength f_t decreasing with increasing friction angle φ' (the cohesion c' being fixed).*

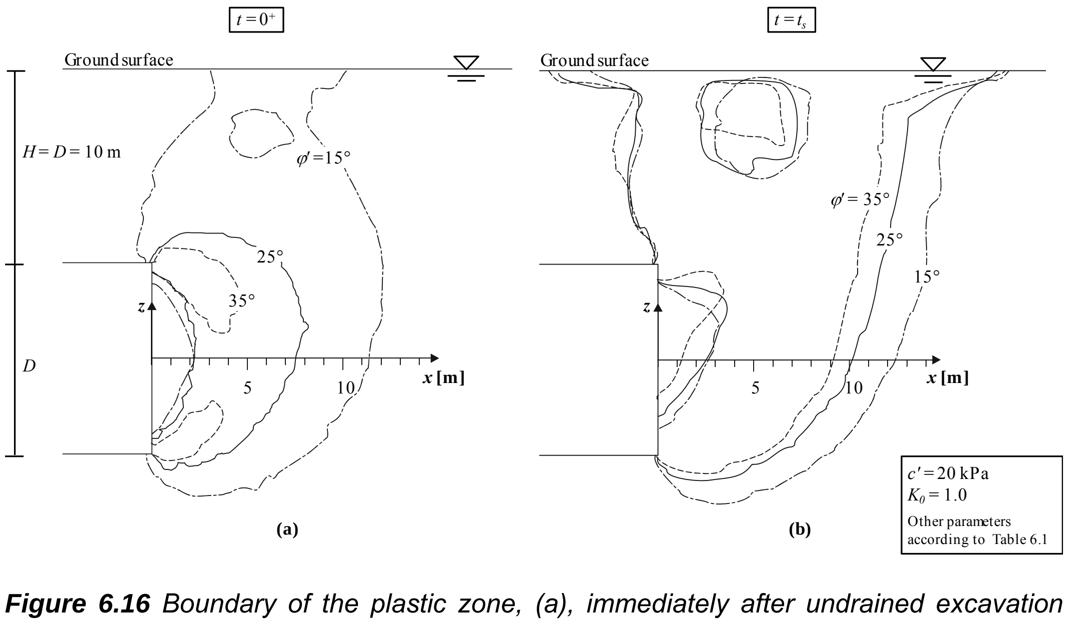

***Figure 6.16** Boundary of the plastic zone, (a), immediately after undrained excavation and, (b), at ultimate state for φ' = 15°, 25° and 35°.*

6.6.3 *In situ* horizontal effective stress

The coefficient of lateral pressure K_0 does not have any influence on stability in the uncoupled problem [87], but stand-up time increases with *in situ* horizontal effective stress (Figure 6.17).

For K_0 = 0.5, the short-term plastic zone (*i.e.*, the one developing under undrained conditions) is more extended (ahead of the face and toward the surface) than for K_0 = 1.0 (Figure 6.18a). This is because under undrained conditions the shear resistance of the ground depends essentially on the mean initial effective stress [88], which is higher in the case of K_0 = 1. Consequently, in spite of the smaller stress change caused by the excavation in the case of a low coefficient of lateral pressure, the latter is unfavourable with respect to the time-development of stability. This is evident considering the stress paths at a point ahead of the face (Figure 6.19). As the initial effective stresses are closer to the *MC*-line in the case of the low K_0, the effective stress change that is needed to reach yielding condition is smaller, necessitates less excess pore pressure dissipation and, consequently, yielding starts earlier. At failure, however, the extent of the plastic zone is practically independent from K_0 (Figure 6.18b).

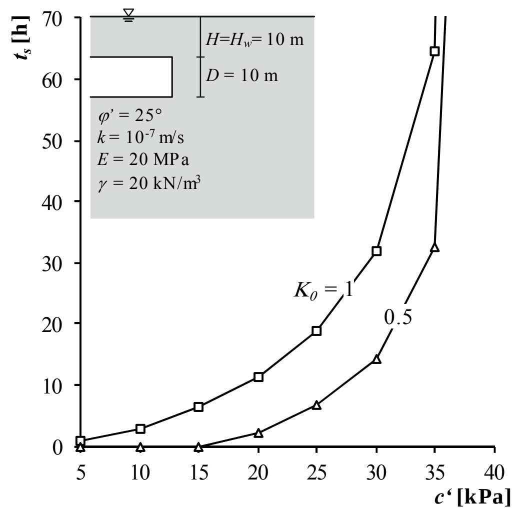

Figure 6.17 *Stand-up time of the tunnel face as a function of the cohesion c' for a coefficient of lateral pressure K_0 of 0.5 and 1.0.*

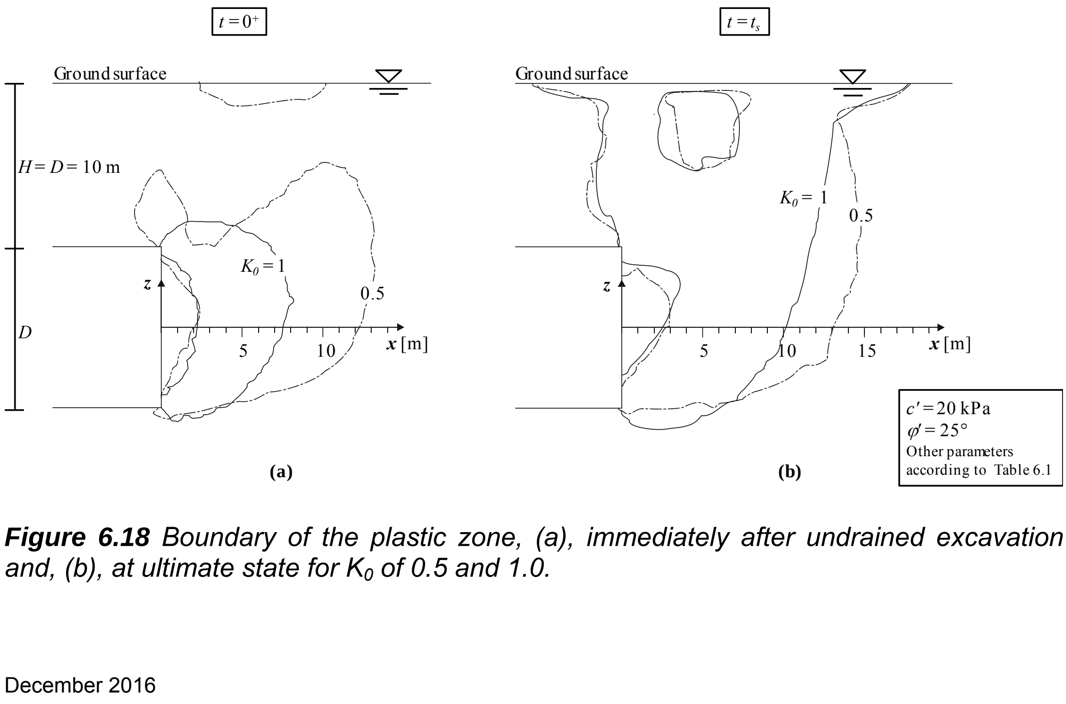

Figure 6.18 *Boundary of the plastic zone, (a), immediately after undrained excavation and, (b), at ultimate state for K_0 of 0.5 and 1.0.*

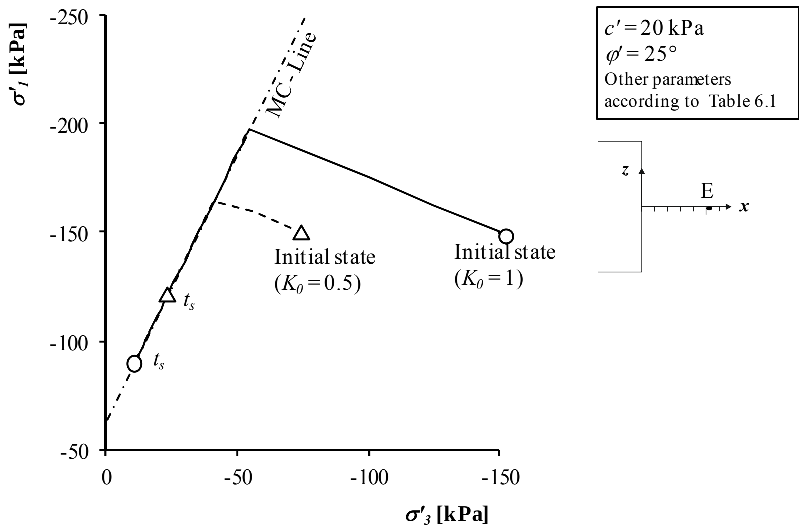

***Figure 6.19** Stress paths in the principal stress plane at point E (see inset in the figure) for K_0 of 0.5 and 1.0.*

6.6.4 Depth of cover

The stand-up time increases with overburden in the case of soils exhibiting low to medium cohesion (*c′* < about 30 kPa, Figure 6.20). This is due to the longer drainage path and to the longer propagation distance of the plastic zone. At higher cohesion values (*c′* > about 30 kPa), however, these effects are overweighted by the effect of the (destabilizing) pore pressure gradients (which increase with the overburden; Figure 6.21a and Figure *6.21*b) so that the stand-up time decreases.

It should be noted that numerical problems did occur in the case the highest considered overburden and for a friction angle of 35°. The numerical analyses aborted long before reaching ultimate state. This is probably due to the combination of high seepage forces and low tensile strength.

Figure 6.22 shows the boundary of the plastic zone after undrained excavation (continuous lines) and at failure (dashed lines) for three depths of cover; the extent of the plastic zone around the tunnel at $t = 0^+$ does not change much with depth. At the ultimate state, however, the extent of the plastic zone ahead of the face increases with depth.

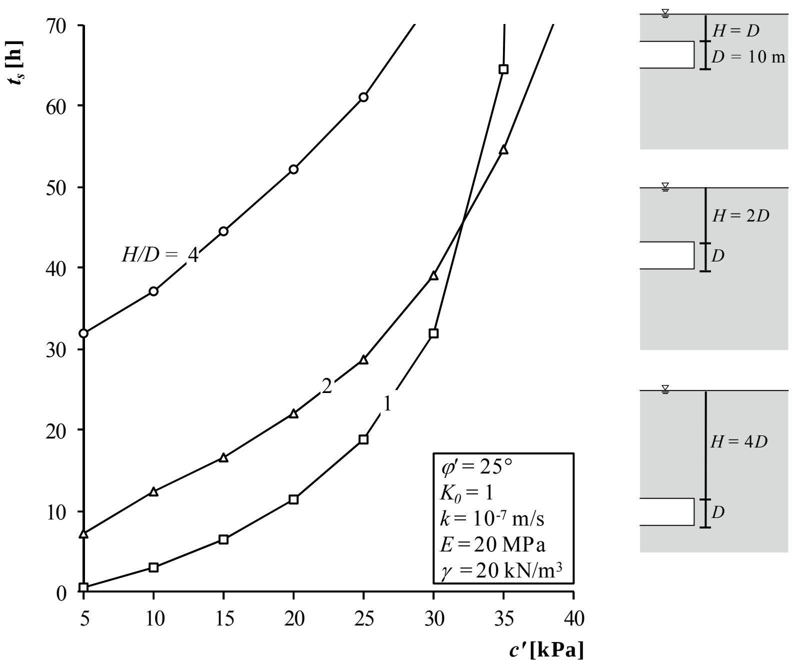

Figure 6.20 *Stand-up time of the tunnel face as a function of the cohesion c' for a depth of cover H/D = 1, 2 and 4.*

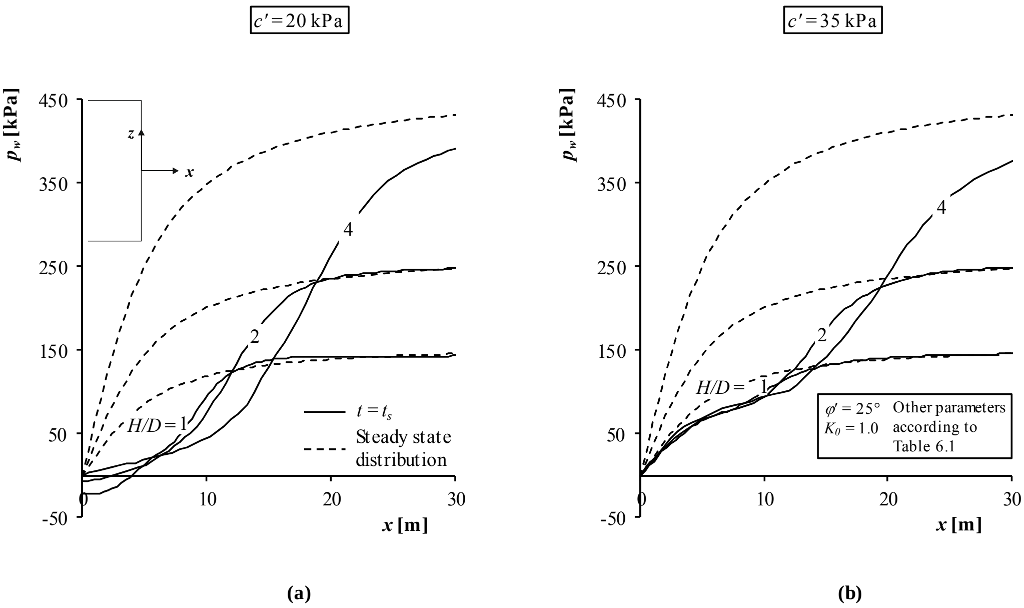

Figure 6.21 *Spatial distributions along the x-axis (see inset in diagram (a)) of the pore pressure p at ultimate state for a ground cohesion c' of 20 kPa and 35 kPa.*

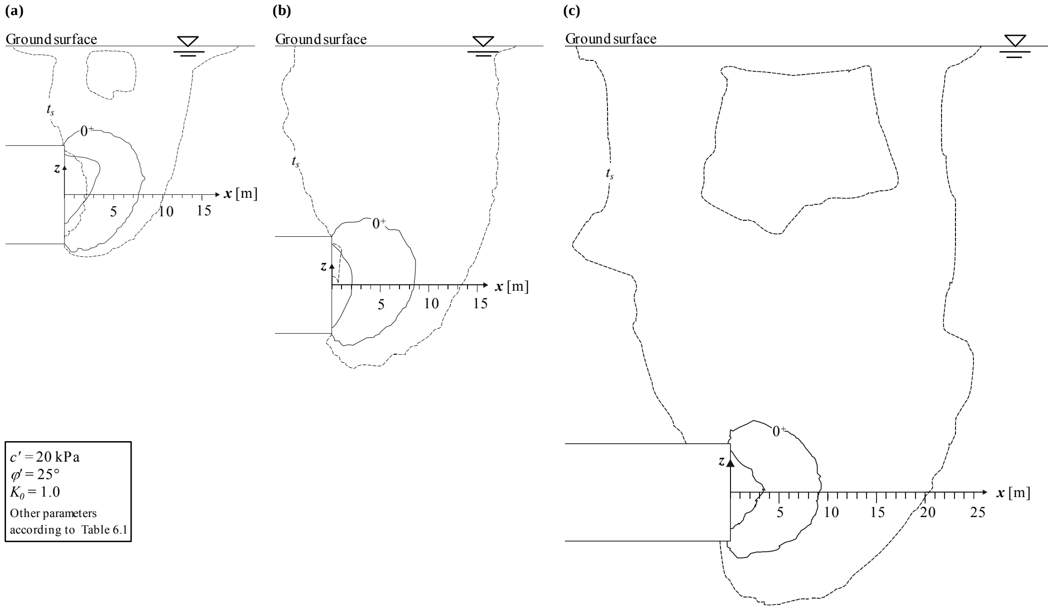

***Figure 6.22** Boundary of the plastic zone immediately after undrained excavation and at ultimate state for H/D = 1, 2 and 4.*

6.7 Design diagrams

A parametric study was performed with the aim to prepare deign charts for the estimation of the stand-up time of the tunnel face. The latter depends, in general, on the geometric parameters of the problem (D, H_w, H), the material constants of the ground (submerged unit weight γ', Young's modulus E, Poisson's ratio ν, ground cohesion c', friction angle φ', dilation angle ψ and coefficient of permeability k), of the unit weight of water γ_w and the coefficient of lateral pressure K_0:

$$t_s = f\left(E, \nu, c', \varphi', \psi, \gamma', \gamma_w, \mathrm{k}, K_0, \mathrm{D}, H, H_w\right). \tag{6.5}$$

For dimensional reasons and due to the structure of the equations underlying consolidation theory, a dimensionless stand-up time T_s can be defined (*cf.* [29]) and Eq. (6.5) can be written in normalized form as follows:

$$T_s = \frac{t_s E k}{\gamma' D^2} = f\left(\frac{c'}{\gamma'\mathrm{D}}, \frac{\gamma_w}{\gamma'}, \varphi', \psi, K_0, \frac{H}{H_w}, \frac{H}{D}, \nu\right). \tag{6.6}$$

The l.h.s. term of Eq. (6.6) shows that if the permeability or the Young's modulus is higher by a factor of ten, then the stand-up time will be ten times shorter.

For working-out a manageable number of design charts, the following values are kept fixed: $\psi = 0$, $\nu = 0.3$, $H_w / H = 1$, $\gamma_w/\gamma' = 1$. Consequently, Eq. (6.6) reduces to

$$T_s = \frac{t_s E k}{\gamma' D^2} = f\left(\frac{c'}{\gamma'\mathrm{D}}, \varphi', K_0, \frac{H}{D}\right). \tag{6.7}$$

On account of the expected mesh dependency (see Chapter 3), the stand-up time was additionally computed with a spatial discretization of 1 and 2 m. As presented in Chapter 3 and as validated in Chapter 5, the obtained results allow to linearly extrapolate the results to a mesh size of zero (remark that the assumption is reasonable considering that the thickness of the shear band, for soil of low permeability, amounts to few millimetres, only).

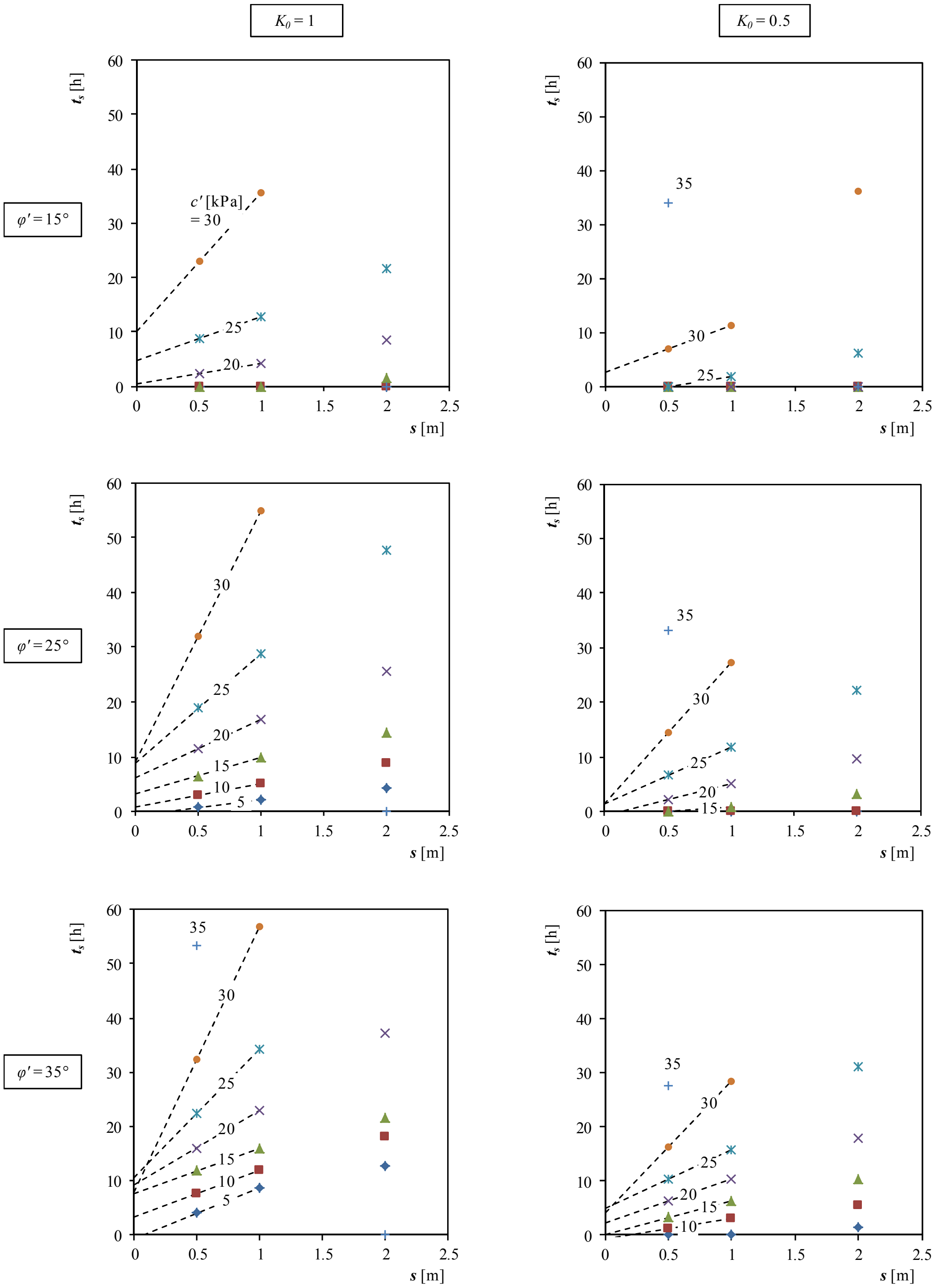

***Figure 6.23** Stand-up time as a function of the mesh size for H/D = 1 (ψ = 0°, ν = 0.3, H_w / H = 1, γ_w / γ' = 1).*

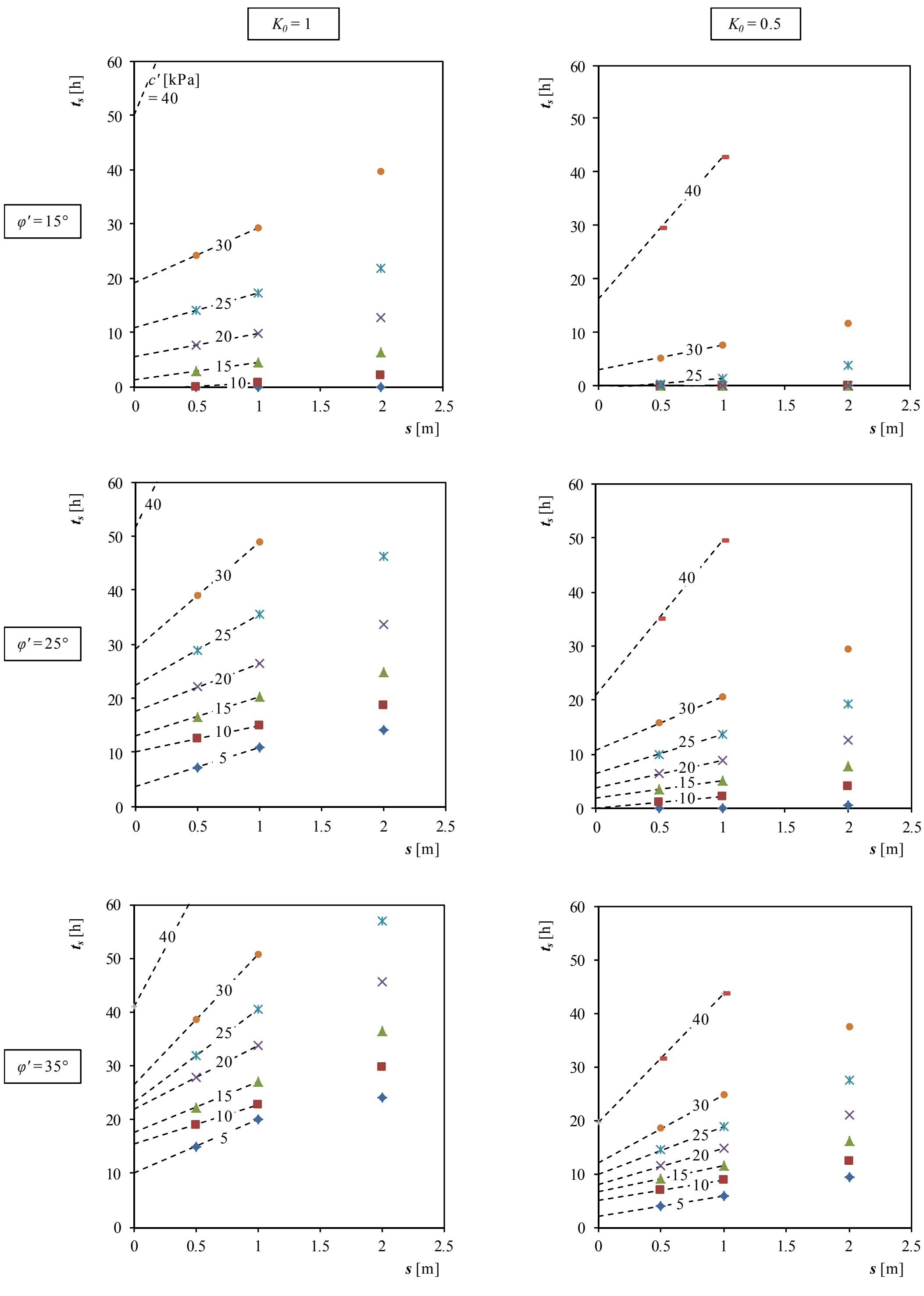

Figure 6.24 *Stand-up time as a function of the mesh size for H/D = 2 (ψ = 0°, ν = 0.3, H_w / H = 1, γ_w / γ' = 1).*

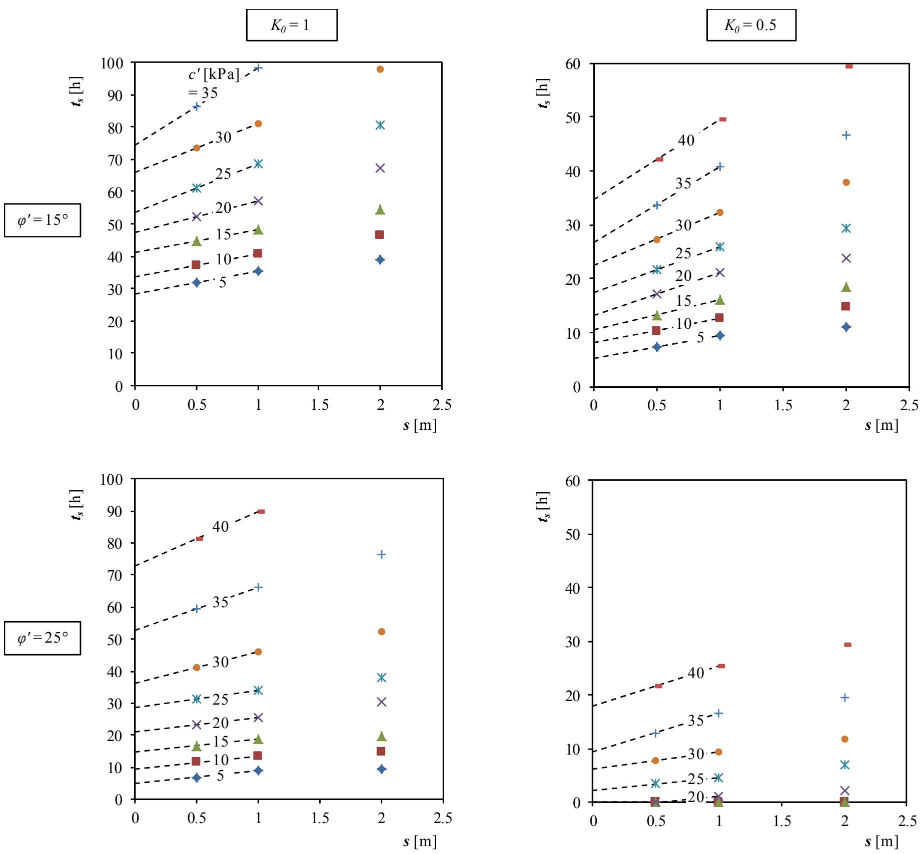

***Figure 6.25** Stand-up time as a function of the mesh size for H/D = 4 (ψ = 0°, ν = 0.3, H_w / H = 1, γ_w / γ' = 1).*

Figure 6.23 to Figure *6.25* present the stand-up time t_s as a function of element size for *H/D* = 1, 2 and 4, respectively. As expected based upon the previous Chapters, the stand-up time increases with increasing element size. The relationship between mesh size and stand-up time is almost linear with the exception of the results obtained for *H/D* = 1 and cohesion values higher than about 20 – 30 kPa. In the latter case, the mesh dependency of stand-up time is strongly non-linear; for *c'* = 35 kPa, for example, the stand-up time is finite for the finer mesh (0.5 m), but becomes infinite (meaning stable face under drained conditions) for the coarser meshes. This model behaviour was already observed on the example of an underwater vertical cut in Section 3.2.2 for cohesion values close to the critical one (leading to drained stability). Callari [44] also observed that there are combinations of strength parameters for which the tunnel face collapses or not depending on the size of the spatial discretization. Consider for example the case *H/D* = 1 and φ' = 25°. As shown in Section 6.3.2, the theoretical cohesion required for drained stability amounts to about 38 kPa. When the cohesion approaches this value, the stand-up time increases asymptotically to infinity. Consequently, a small change of cohesion leads to a large change of stand-up time. As the mobilized shear strength depends on the element size, a change of element size strongly influences the stand-up time. In the extreme case, the mobilized strength parameters are such that the tunnel face remains stable under drained conditions for large elements (not allowing the rotation of the principal axes, and so structural softening), but fails when choosing a finer discretization (which allows the rotation of the principal axes, and so structural softening).

The numerical results of Figure 6.23 to Figure *6.25* were post-processed in order to obtain design diagrams giving the normalized stand-up time T_s as a function of the normalized cohesion (Figure 6.26 and Figure *6.27*). Figure 6.26 is based upon the finite element computations with the finer mesh (*s/D* = 0.05) and partially revises the results presented in Schuerch [64] because it considers additional computations carried-out during this PhD research. On one hand side, the design diagrams of Figure 6.26 overestimate the stand-up time because they are obtained for a mesh size which leads to a shear band thickness larger than the expected one. On the other hand, they underestimate the stand-up time because, they do not consider the plastic dilation, which as shown in Chapters 4 and 5, delays the occurrence of failure. As these two effects are opposite, the design diagrams of Figure 6.26 give a stand-up time which may be close to the real one.

Figure 6.27 was obtained by a linear extrapolation of the numerical results for 0.5 m and 1.0 m to an element size of zero (dashed lines in Figure 6.23 to Figure *6.25*). The extrapolation has been performed only for results exhibiting an almost linear relationship between stand-up time and mesh size. The design nomograms of Figure 6.27 give a *lower limit* of the stand-up time – thus representing a conservative version of the charts of Figure 6.26 – because, (i), they do not consider the plastic dilation, and, (ii), assume a very thin thickness of the shear band.

Generally, considering the uncertainties related to the ground parameters (particularly that of the permeability), the influence of the mesh size on the stand-up time (illustrated by the differences between Figure 6.26 and Figure *6.27*) is not relevant from the practical engineering point of view. Indeed, the mesh-dependency becomes relevant, when the strength is close to the critical cohesion for drained face stability.

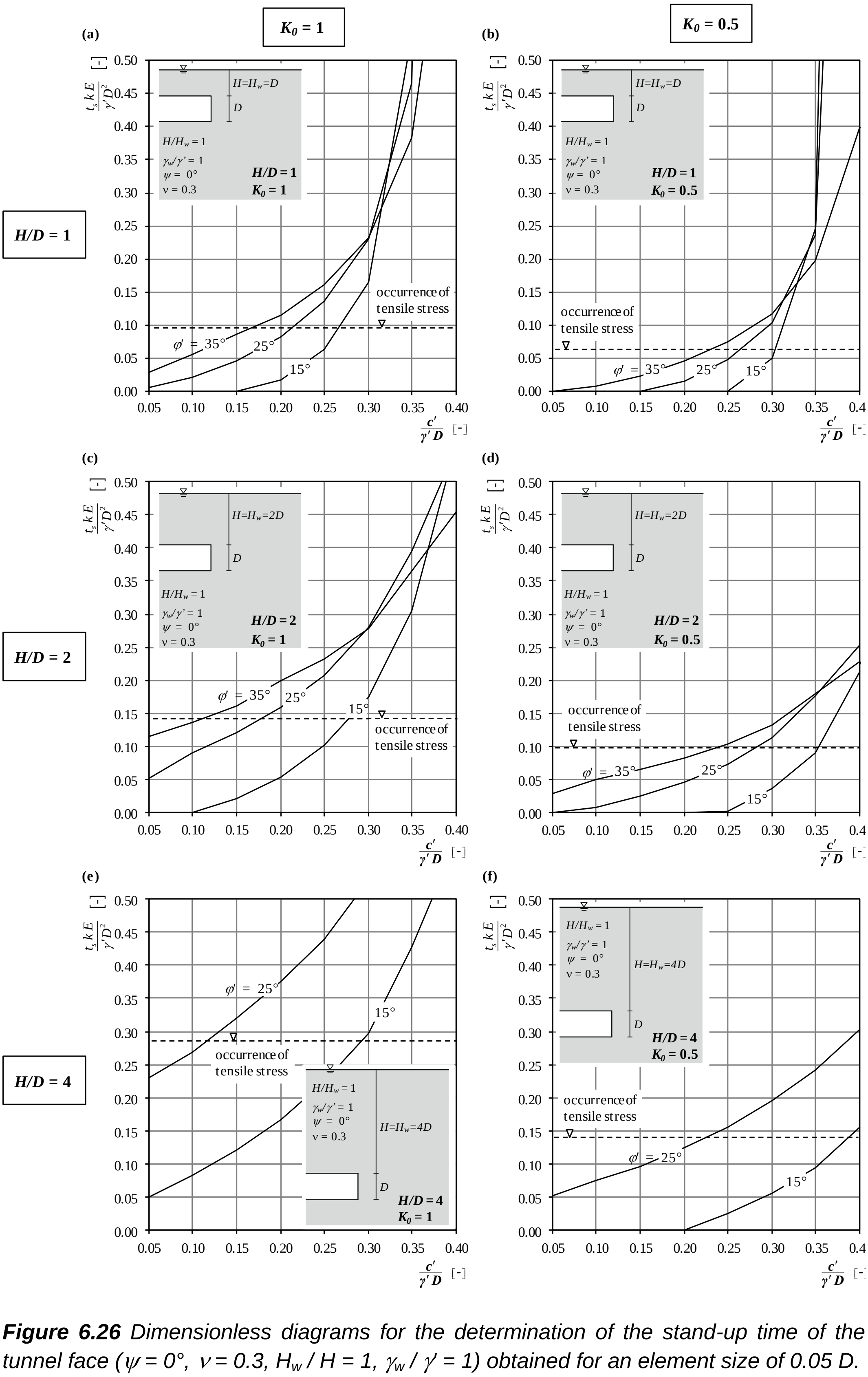

***Figure 6.26** Dimensionless diagrams for the determination of the stand-up time of the tunnel face (ψ = 0°, ν = 0.3, H_w / H = 1, γ_w / γ' = 1) obtained for an element size of 0.05 D.*

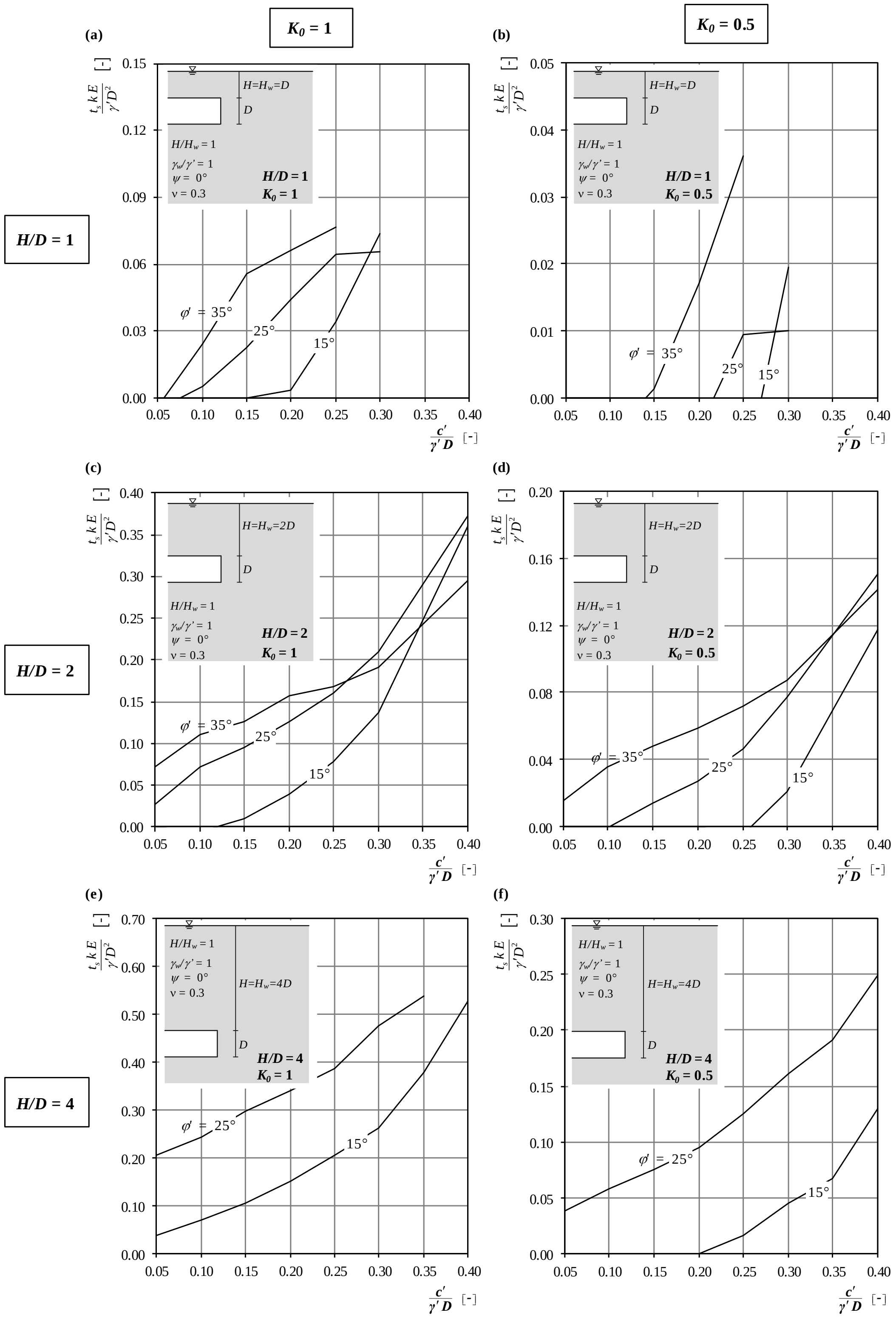

Figure 6.27 *Dimensionless diagrams for the determination of the stand-up time of the tunnel face obtained based upon linear extrapolation to a zero element size ($\psi = 0°$, $\nu = 0.3$, $H_w / H = 1$, $\gamma_w / \gamma' = 1$).*

6.8 Application example

In order to illustrate the utility of the design diagrams let consider the following example, based upon the construction of the tunnel of Line 3 of the Athens Metro. The tunnel is under construction with an EPB machine and runs in the south-west of the city. Under the operational point of view it is advantageous to carry-out inspection and/or maintenance of the cutterhead under atmospheric conditions. For this reason the stability of the unsupported tunnel face is investigated in a specific tunnel location. The ground consists of weak Lower Athens Schists at tunnel elevation, overlayed by a layer of the more competent Upper Athens Schist. The water table is located at the ground surface (Figure 6.28a).

The design nomograms are applied making the conservative assumption of homogenous ground, with the mechanical and hydraulic properties of the particularly weak Lower Athens Schists. Two models are considered: one extending up to the ground surface (Figure 6.28b) and, one extending up to the boundary between the two geological units (Figure 6.28c).

For the parameter set given in Figure 6.28c (normalized cohesion $c'/(\gamma' D)$ = 0.24, friction angle φ' = 25°) the dimensionless stand-up time obtained with Figure 6.26 is equal to 0.05 – 0.075, while tensile stresses would start developing at 0.065 – 0.1. With a simple transformation taking into account the permeability of the ground k, the Modulus of Young E, the submerged unit weight of the ground γ' ant the tunnel diameter D the stand-up time amounts to 10 – 15 hours. The design diagrams of Figure 6.27 provide a stand-up time of 2 – 8 hours. This period is sufficient for depressurizing and emptying the working chamber and carrying-out routine inspection and maintenance works.

The field experience agreed well with the computational predictions: after 6 hours of works inside the excavation chamber under atmospheric conditions the first indications of instability were observed (in form of some ravelling in the upper part of the tunnel face). As a consequence the excavation chamber was evacuated and the pressurized again.

This simple application example shows the usefulness of using the design diagrams: they assist operational decision-making – in the present example related to the feasibility of men entries in the cutterhead chamber under atmospheric conditions.

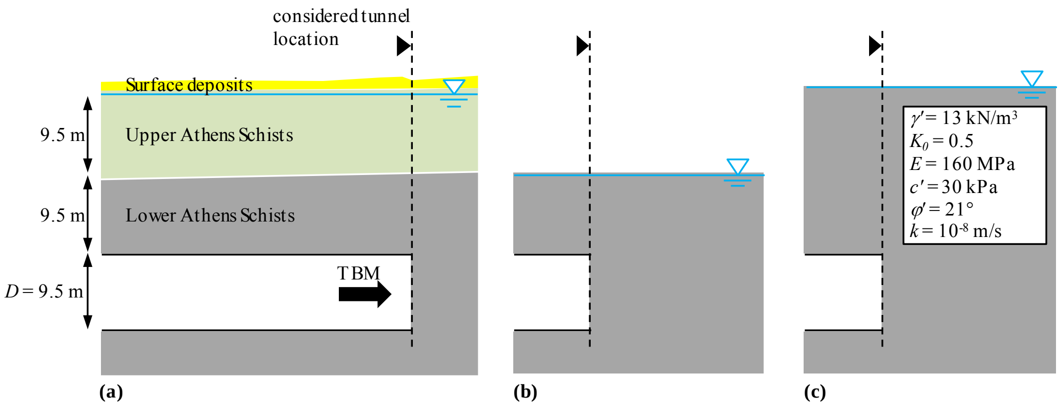

Figure 6.28 *Geological profile; (b, c) simplified models assumed for an estimation of the stand-up time from the design nomograms.*

6.9 The influence of the support pressure on the stand-up time

The design diagrams apply to an unsupported tunnel face, *i.e.* to the worst case with respect stability. The application of a slight support pressure (for example, a low air pressure, partially compensating the in situ hydrostatic pressure, for carrying-out interventions for TBM inspection or maintenance), however, is often operationally not problematic, particularly considering that short stand-up times are disadvantageous, too.

Figure 6.29 shows the influence of the support pressure on the stand-up time for the example of a 20 m deep tunnel with a diameter of 10 m. The solid line are obtained assuming that the applied support pressure acts as effective support, while the dashed lines assumes that the support pressure partially compensate the water pressure. The two conditions are simulated by applying the support pressure as uniform total stress and imposing as hydraulic boundary conditions at the tunnel face either an atmospheric pressure or the support pressure.

The partial compensation of the water pressure is representative for hyperbaric interventions (dashed lines), while the simulation of effective support is representative for a mechanical support of the tunnel face, e.g. by reinforcing the tunnel face with bolts (note that a support pressure of 0.5 to 1 bar amounts – assuming sufficient bolt strength and overlapping length – to a reinforcement density of about 0.25 to 0.5 bolts per square meter, respectively; [89]). The effect of a light support pressure is remarkable: applying an effective support pressure of 0.8 bar, the tunnel face would remain stable even long-term, while in a hyperbaric intervention under 1 bar (40% of the in situ hydrostatic pressure) the stand-up time would be twice as high as in the case of an atmospheric intervention.

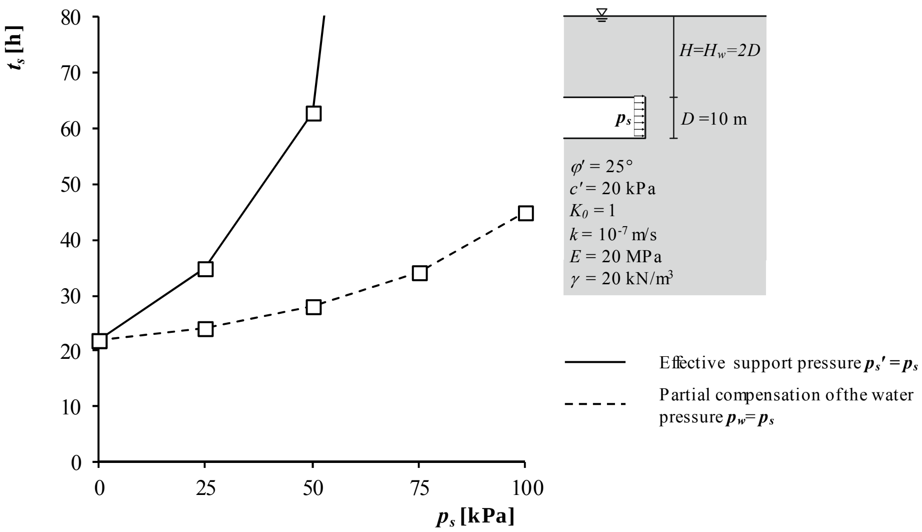

Figure 6.29 *Stand-up time of the tunnel face as a function of the applied support pressure p_s.*

6.10 Critical advance rate

The previous Sections investigated stand-up time during an excavation stand-still, assuming that undrained conditions prevail at the beginning of the stand-still. As explained in Section 6.4, this assumption is reasonable in the case of very fast (compared to the ground permeability) tunnel advance. Otherwise, partially drained conditions would prevail during advance and thus at the beginning of the standstill.

With respect to the question of face stability, "partially drained conditions" means that the permeability of the ground is such that dissipation of excess pore pressures occurs to a certain (practically relevant but nevertheless incomplete) degree simultaneously with the advance of excavation or during a standstill. As explained by Anagnostou [90], a simple dimensional analysis shows that the ratio of soil permeability k to advance rate v will govern whether steady, partially drained or undrained conditions prevail during ongoing excavation. The higher the advance rate v and the lower the permeability k, the less will the pore pressures dissipate in the vicinity of the face and, consequently, the higher will be the shear resistance. If, on the other hand, the permeability is high or the advance slow, drained conditions, which are less favourable for stability, will already prevail around the working face.

Under such conditions, the relevant important question is the estimation of the minimum ("critical") advance rate for which the face would remain stable during excavation.

As detailed presented in Section 1.2.1, the issue of face stability during ongoing excavation was addressed only by Höfle [14], [49] and by Sitarenios and Kavvadas [50].

The design charts presented in Section 6.7 can be used for a simplified estimation of the critical advance rate. Noting that the failure zone ahead is extended up to one diameter ahead of the tunnel face (Figure 6.12 and Figure *6.16*) and that during advance this zone is continuously excavated (Figure 6.30), the critical advance rate v_{cr} can be taken equal to the ratio of tunnel diameter D to the stand-up time t_s :

$$v_{cr} = \frac{D}{t_s}, \tag{6.8}$$

where t_s can be obtained from T_s given by the design charts of Figure 6.26 or Figure *6.27*.

Figure 6.31 shows the critical advance rate as a function of cohesion for a circular tunnel with diameter 10 m located at depth 10 m (same geometry and ground parameters as in Section 6.4). In this example, assuming a cohesion of the ground of 25 kPa, the face would be stable during advance, it the rate amounts to at least to 12 m/day (typical range) or 39 m/day (very high advance speed) with T_s after Figure 6.26 and Figure *6.27*, respectively.

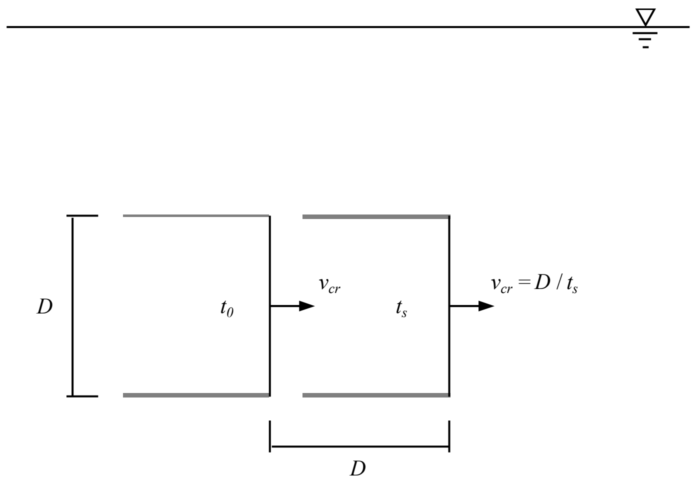

Figure 6.30 *Geometrical definition of critical advance speed.*

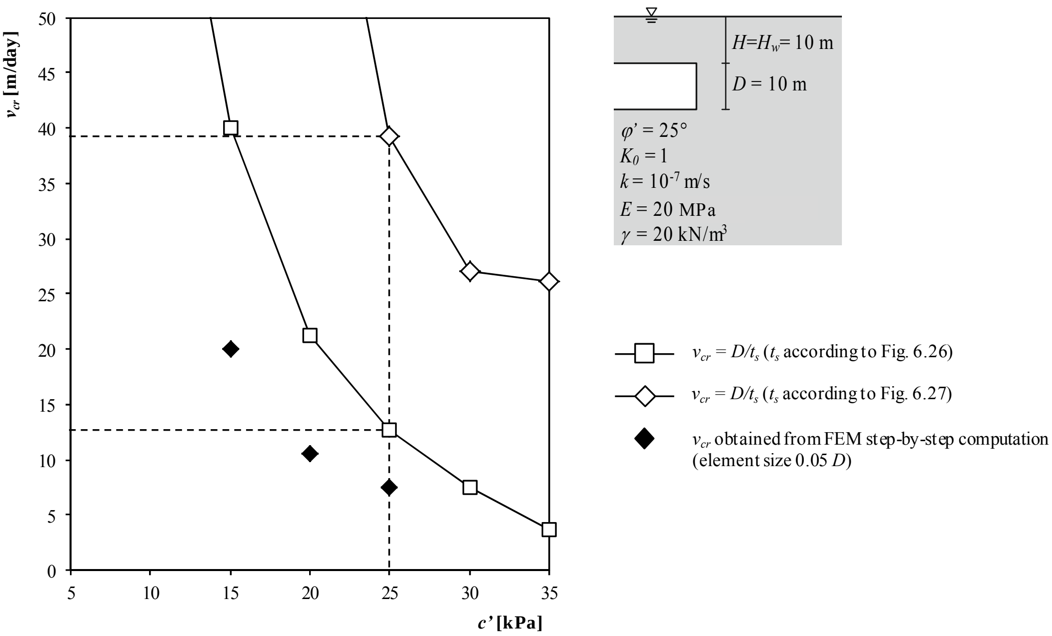

Figure 6.31 *Critical advance rate as a function of the cohesion c'.*

For the same example, a comparative computation was carried-out, simulating numerically the tunnel advance step by step. Figure 6.32 shows the computational model. The excavation is simulated by successively deactivating the ground elements over a total of 15 successive steps of 2 m length. The elements size amounts to 2 m over steps 1 – 9 and to 0.5 m over steps 10 – 15 (being thus the same, *i.e.* equal to 0.05 D, as in the design charts of Figure 6.26). Each step consists in a transient analysis of duration consistent with the imposed advance rate, during which the nodal forces at the tunnel face are progressively reduced to zero (e.g. for advance rate of 10 m/day and step length 2 m, the deactivation of the elements is carried-out over a time step of 0.2 days). The tunnel lining is simulated in a simplified way by fixing the displacements at the excavation boundary just prior to the deactivation of the ground elements. No-flow conditions are imposed to the tunnel wall, while mixed conditions where applied to the tunnel face.

Figure 6.33 shows the boundary of the plastic zones at the end of step 15 obtained for three value of advance speed and for cohesion 20 kPa. The extent of the plastic zone increases with decreasing advance rate. The critical advance speed for the presents example amounts to 10.5 m/day. For lower advance rate the numerical algorithm fails to find an equilibrated solution. Taking into account the stand-up time according to Figure 6.26 (which was based upon the same mesh size as used in the step-by-step calculations) the critical advance speed corresponds to a ratio D / t_s of 0.5.

The black diamonds in Figure 6.31 corresponds to the critical advance speed computed by means of the step-by step FEM analyses for several cohesion values. For the considered example, the critical advance speed varies between about 0.5 – 0.6 D/t_s. This means that the critical advance rate assumed in Equation (6.8) overestimates the one computed numerically, and so, it provides a conservative estimation which can be used in the engineering practice.

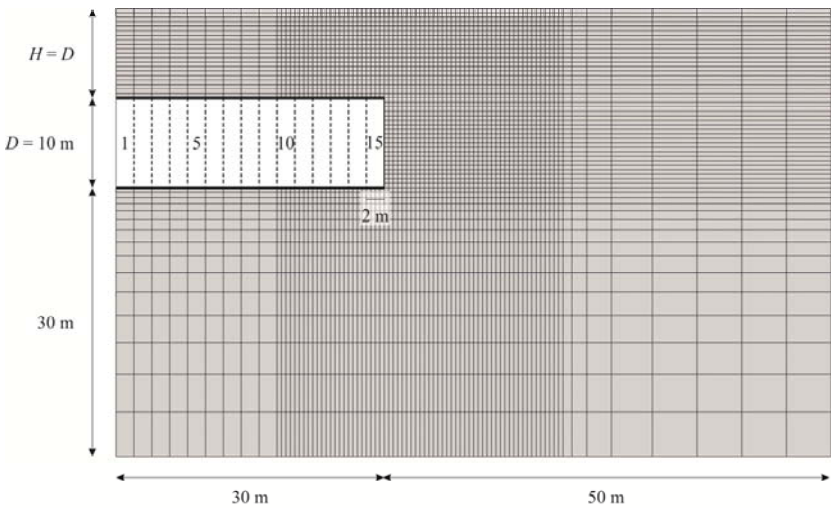

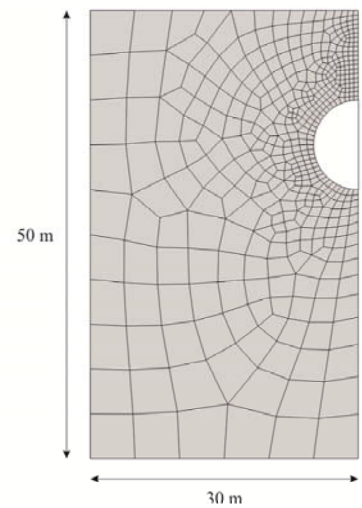

Figure 6.32 *Computational model used for the step-by-step FEM analyses.*

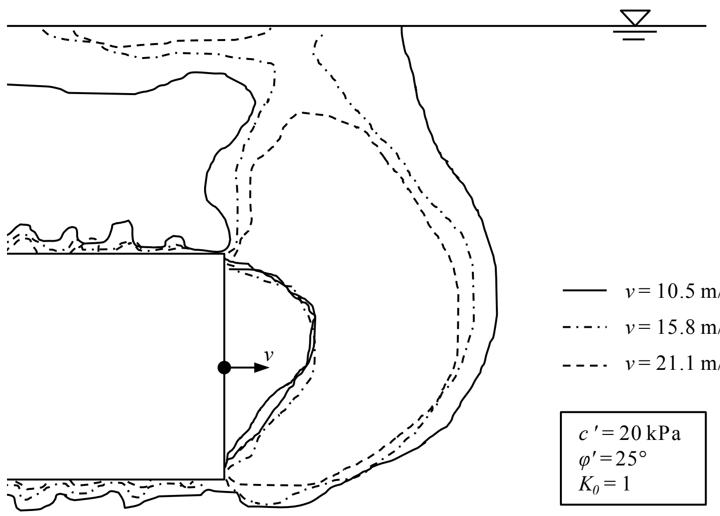

Figure 6.33 *Boundary of the plastic zone for several values of advance rate (other material parameters according to Table 6.1).*

6.11 Conclusions

Experience shows that the tunnel face may be stable in the short term, but collapse after a certain time period. The stand-up time of the tunnel face is important in engineering practice, especially in medium- and low-permeability water-bearing ground.

Numerical models are able to explain the phenomenon of delayed failure; they show that instability occurs more or less rapidly depending on the permeability, stiffness and shear strength of the ground, as well as on the coefficient of lateral pressure.

On the basis of a parametric study, Chapter 6 presented design charts allowing the stand-up time to be estimated for a given geotechnical situation, thus assisting the engineers on-site decision-making. The design diagrams are elaborated for a fixed relatively fine mesh size and for a mesh size of zero (obtained by means of a linear extrapolation of the results to zero, taking into account the linear dependency of the stand-up time to the mesh size). The latter represent a lower limit of the stand-up time expected for an infinitely thin shear band.

In view of the underlying simplifying assumptions (e.g. homogenous ground and undrained conditions up to the beginning of the standstill period) their use presupposes a measure of engineering judgment. Due to the uncertainties related to the computation method and to the heterogeneity of the ground (concerning both structure and material parameters), a sufficiently high safety factor should be applied to the estimated stand-up time, and the face behaviour should be monitored during standstills in order to timely detect the onset of any instability (cracks, extrusion, increasing water inflows, ravelling). In the case of unsatisfactory ground behaviour, re-pressurization of the excavation chamber (mechanized tunnelling) or reinforcement of the face (conventional tunnelling) will be required. Chapter 6 showed that even a small support pressure (0.5 to 1 bar) increase the stand-up time of the tunnel face considerably.

Finally, Chapter 6 gave an estimation of the minimum average advance rate, which allows to excavate without support/reinforcement of the tunnel face. The minimum advance rate can be taken approximately equal to the ratio of tunnel diameter to stand-up time.

7 Surface settlements under transient conditions

7.1 Introduction

The response of water-bearing grounds to tunnelling is typically investigated assuming undrained or drained conditions. These assumptions are correct in the case of very low- or very high-permeability soils, respectively, but do not apply for soils of medium to low permeability, for which partially drained (hereafter referred to as "transient") conditions prevail during advance.

This chapter shows the relevance of transient conditions for the surface settlements by presenting a series of parametric studies carried-out by means of 3D coupled hydraulic-mechanical numerical analyses assuming that the ground obeys either the simple and widely used linearly elastic perfectly plastic Mohr-Coulomb model or the modified Cam Clay model.

Comparative computations highlight the influence of the advance rate, standstill duration and seepage flow conditions at the tunnel boundary and at the excavation face on the tunnelling-induced settlements.

Finally, an easy to use method is presented for estimating whether drained, undrained or partially drained conditions have to be expected during advance as well as for assessing settlements under transient conditions based upon the results of relatively simple drained and undrained analyses.

7.2 Computational models

For the purpose of this study simple numerical models of conventional and TBM tunnels are used. Specifically, the excavation and support installation sequence of a cylindrical tunnel is considered together with various scenarios for the face support pressure during advance (as explained later in detail). Conventional tunnelling with partial excavation and staggered installation of the primary lining (e.g. closing of the ring at a certain distance) or details of shield excavation (e.g. annulus grouting, shield gap) are not taken into account. Although this would be possible, it is not necessary for the purpose of the present study, which aims to highlight the significance of accounting for time-dependency in tunnels through medium-permeability grounds and, on the other hand, to quantify the corresponding range of transient conditions.

The tunnel diameter is taken equal to D = 10 m, which is typical for traffic tunnels, and the overburden H = 1.5D or 3D. Concerning face support, three modes are considered (AD1, AD2 and AD3 in Figure 7.1): excavation under atmospheric pressure without support of the face (applicable both for conventional and shied tunnelling); excavation under atmospheric pressure with face reinforcement or support (common in conventional tunnelling through weak ground); excavation with full compensation of the hydrostatic pressure. The latter is only possible in closed shield tunnelling and consists in the sealing of the excavation chamber (by means the so called filter cake in slurry shield or conditioned muck in EPB shield) and in the application of a support pressure equal or higher than the in situ hydrostatic pressure at the face. The assumed tunnel support consists of a t_l = 0.20 m thick concrete lining. The lining installation follows the advancing heading at a distance l_u of 4 m (Figure 7.2c). Concerning lining permeability, two borderline cases are considered: (a) a highly permeable lining (but with no-flow boundary condition in case of negative pore pressure); (b) an impervious lining (a no-flow boundary condition applies to the supported section of the tunnel boundary). According to Wongsaroj [21], the assumption of highly permeable lining is valid if the ratio of

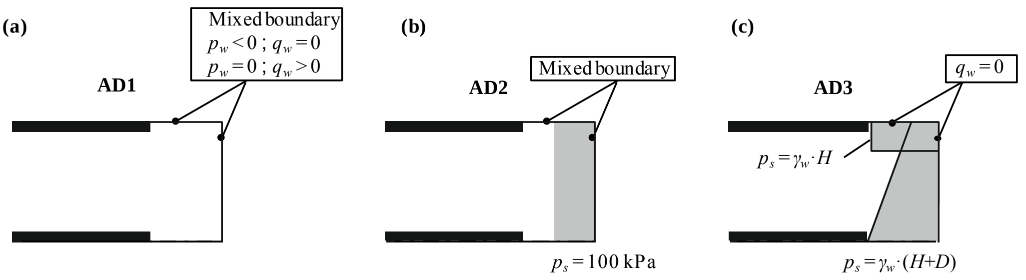

Figure 7.1 *Hydraulic boundary conditions and applied loads for the advance modes, (a), at atmospheric pressure, (b), at atmospheric pressure with face support or reinforcement, (c) with full compensation of the water pressure.*

the soil permeability multiplied by the overburden to the lining permeability multiplied by its thickness is higher than 100, while the assumption of impervious lining is valid if this ratio is lower than 0.1.

Soil-fluid coupled transient and steady state three-dimensional analyses are carried-out using the FEM program Abaqus [66]. Figure 7.2 shows the used FEM meshes. The element size varies from 1.25 m (close to the ground surface) to 50 m (at the model boundary) in the transversal direction. The element size in the longitudinal direction amounts to 2 m between x = 0 and 220 m (Fig. 7.2), while it progressively increases up to 50 m from x = 220 m to x = 400 m (Fig. 7.2).The soil is discretized by 8-node tri-linear displacement and pore pressure brick elements; the lining is discretized by 8-node linear brick elements. All the model vertical boundaries and the bottom boundary are fixed in the direction perpendicular to them.

The water table is taken equal to the elevation of the ground surface (H_w = H). The seepage flow follows Darcy's law with a constant isotropic permeability. The hydraulic potential is fixed to its initial value at the far field boundaries as well as at the level of the water table. The latter is adequate if there is no draw-down of the water table, which presupposes sufficient ground water recharge. No-flow conditions are imposed at the symmetry plane as well as, (i), at the lined tunnel wall in the case of practically impervious lining and, (ii), at the excavation face and at the unlined tunnel wall in the case of advance with full compensation of the water pressure. Mixed conditions (i.e. no-flow in case of negative pore pressure, and seepage face elsewhere) are imposed, (i), at the lined tunnel wall when the lining is assumed practically pervious and, (ii), at the tunnel face and at the unsupported tunnel wall in the case of advance in atmospheric conditions. Mixed conditions allow the water to flow from the ground toward the tunnel, but not vice-versa (flow toward the ground would presuppose a continuous external wetting of the excavation boundary).

In the case of closed shield tunnelling with full compensation of the water pressure, the total pressure acting on the excavation face and at the unlined tunnel wall is taken equal to the initial hydrostatic water pressure (Figure 7.1c). This is a simplifying approximation because in closed shield tunnelling the supporting medium (bentonite slurry or excavated muck) is heavier than water.

In the case of advance under atmospheric conditions, face reinforcement is modelled for simplicity by a uniform total face support pressure of 100 kPa (Figure 7.1b), which applies to a dense face reinforcement consisting of fully grouted bolts spaced at 1 m with big overlapping length.

The lining is modelled as an isotropic, linearly elastic material of Young modulus E_l of 15 GPa and Poisson's ratio ν_l of 0.15. The soil is modelled either as an isotropic, linearly elastic and perfectly plastic material obeying the Mohr-Coulomb yield criterion with a non-associated plastic flow or as a Modified Cam Clay material with associated plastic flow,

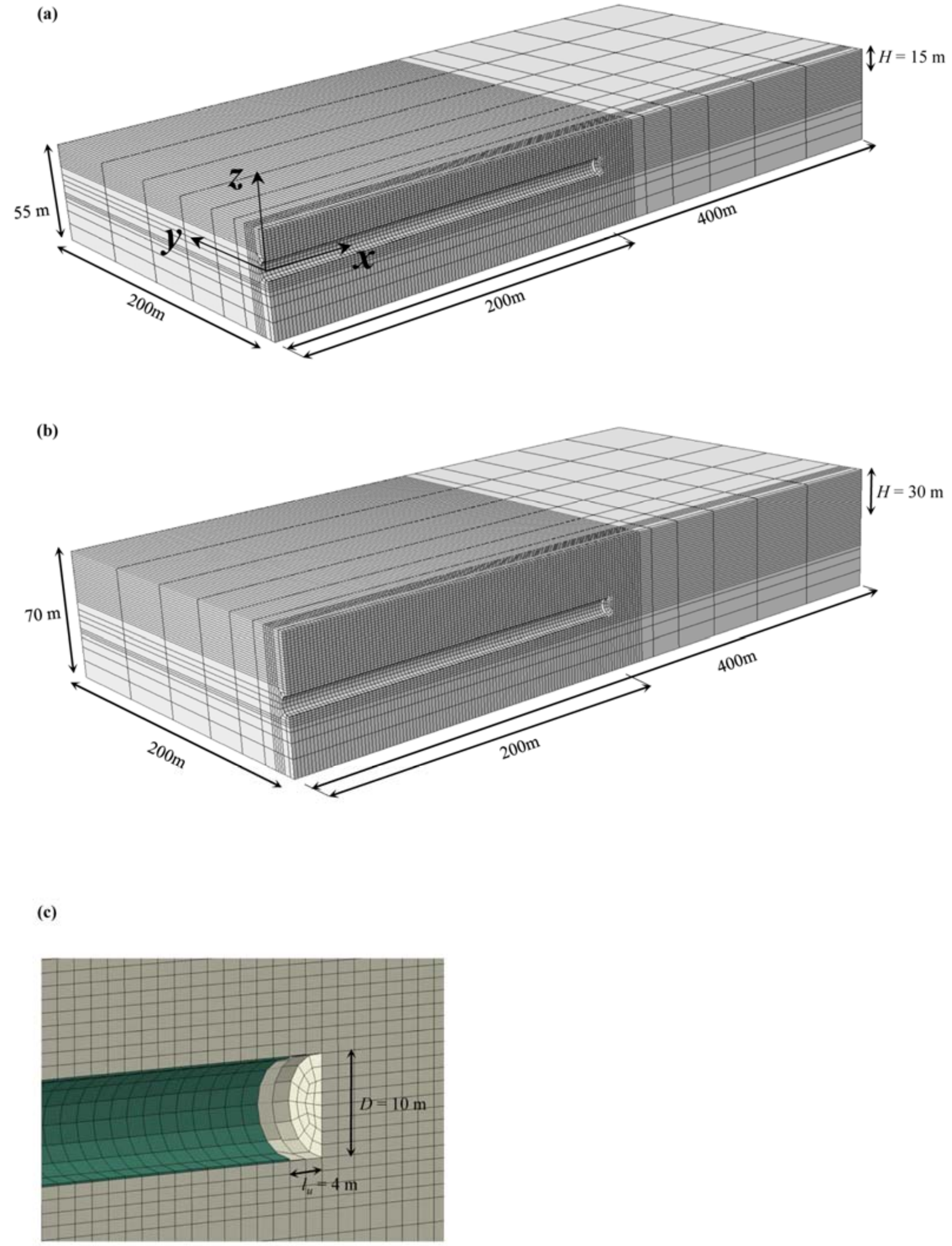

Figure 7.2 *Mesh for overburden, (a), H=15 m and, (b), H=30 m; (c), detail at the excavation face (the support activated before the next excavation step is shown, i.e.* l_u *= 4 m behind the current position of the face).*

and a circular critical state surface in the deviatoric plane. The elasto-plastic constitutive equations are integrated after Clausen [67] (linearly elastic, perfectly plastic material) or using the build-in Abaqus procedure (Modified Cam Clay).

Tables 7.1 and 7.2 show the assumed parameter sets. The study considers Mohr Coulomb soils (of variable cohesion) with dilatancy angle ψ = 5° (see Table 7.1) and slightly or highly overconsolidated Modified Cam Clay soils (see Table 7.2 and Figure 7.4c). The CSL slope *M* of 0.98 (assumed for the Modified Cam Clay soils MCC1-MCC4) corresponds to a friction angle of 25° in triaxial compression (TC), and ~35° in triaxial extension (TE) and in plane strain (PS). The CSL slope *M* of 1.42 (assumed for the Modified Cam Clay soil MCC5) is an extremely large value that corresponds to a friction angle of 35° in TC, 55° in TE and 70° in PS. The analysis simulates the excavation of a 200 m long tunnel portion with a constant advance rate *v* of 1 m/day, followed by a standstill sufficiently long to reach drained conditions in the entire soil model. The excavation process is modelled as a repeated sequence of deactivation of soil elements every 2 m and activation of the lining elements of 2 m long tunnel linings next to the existing tunnel linings. The unsupported span at each step is of 4 m (Figure 7.2c).

For each considered set of soil-mechanical parameters and operational conditions, a parametric study has been performed considering a fixed advance rate (v = 1 m/day) and several soil permeability values k. As it will be shown in Section 7.3, the soil response depends on the v/k-ratio rather than the individual values of advance rate and soil permeability, i.e. varying the advance rate with fixed soil permeability would lead to the same results. The borderline case of "drained excavation" (i.e., of slow excavation through a high permeability soil; hereafter indicated by v/k = 0) was investigated by means of steady state analyses. The borderline case of "undrained excavation" (i.e., of rapid excavation through a low-permeability soil; hereafter indicated by $v/k = \infty$) was investigated by means of transient analyses assuming an extremely low permeability value compared to the advance rate and applying a no-flow hydraulic condition on the tunnel boundaries.

***Table 7.1** Soil parameters (Mohr Coulomb model)*

		MC1	**MC2**	**MC3**	**MC4**	**MC5**
Dry unit weight	γ_d [kN/m^3]	15				
Unit weight of water	γ_w [kN/m^3]	10				
Initial void ratio	e_0 [-]	1				
Effective unit weight	γ' [kN/m^3]	10				
Coeff. of lateral stress	K_0 [-]	0.5				1
Permeability	k [m/s]	***var.***				
Water compressibility	c_w [MPa]	0				
Young's modulus	E [MPa]	50				
Poisson's ratio	ν [-]	0.35				
Cohesion	c' [kPa]	10	50	100	50	
Friction angle	φ' [°]	25			35	25
Dilation angle	ψ [-]	5				

***Table 7.2** Soil parameters (Modified Cam Clay)*

		MCC1	**MCC2**	**MCC3**	**MCC4**	**MCC5**
Dry unit weight	γ_d [kN/m^3]	15				
Unit weight of water	γ_w [kN/m^3]	10				
Surface pressure	σ_{OC} [kPa]	40	300	600	300	
Permeability	k [m/s]	***var.***				
Water compressibility	c_w [MPa]	0				
Gradient of swelling line	κ [-]	0.03			0.06	0.03
Gradient of compression line	λ [-]	0.3				
Poisson's ratio	ν [-]	0.35				
Intercept (void ratio) of the compression line	e_1 [-]	3				
Slope of CSL in axisym. compression	M [-]	0.98				1.42

Table 7.3 gives an overview of the performed analyses. We remark that for the low cohesion soil MC1 and for the slightly overconsolidated soil MCC1 only the case of advance with full compensation of the water pressure has been analysed. The compensation of the water pressure is required in order to avoid the instability of the tunnel face.

Table 7.3 *Overview of the parametric studies*

		Soil	Lining	Advance mode	H [m]
1	MC2_Per_AD1	MC2	Pervious	Atmospheric pressure	15
2	MC2_Imp_AD1		Impervious		
3	MC2_Per_AD2		Pervious	Atmospheric pressure with face reinf.	
4	MC2_Imp_AD2		Impervious		
5	MC2_Imp_AD3			Full compensation of the water pressure	
6	MC1_Imp_AD3	MC1			
7	MC3_Per_AD1	MC3	Pervious	Atmospheric pressure	
8	MC3_Imp_AD1		Impervious		
9	MC4_Per_AD1	MC4	Pervious		
10	MC4_Imp_AD1		Impervious		
11	MC5_Per_AD1	MC5	Pervious		
12	MC5_Imp_AD1		Impervious		
13	MC3_Per_AD1_H30	MC3	Pervious		30
14	MC3_Imp_AD1_H30		Impervious		
15	MCC2_Per_AD1	MCC2	Pervious	Atmospheric pressure	15
16	MCC2_Imp_AD1		Impervious		
17	MCC2_Per_AD2		Pervious	Atmospheric pressure with face reinf.	
18	MCC2_Imp_AD2		Impervious		
19	MCC2_Imp_AD3			Full compensation of the water pressure	
20	MCC1_Imp_AD3	MCC1			
21	MCC3_Per_AD1	MCC3	Pervious	Atmospheric pressure	
22	MCC3_Imp_AD1		Impervious		
23	MCC4_Per_AD1	MCC4	Pervious		
24	MCC4_Imp_AD1		Impervious		
25	MCC5_Per_AD1	MCC5	Pervious		
26	MCC5_Imp_AD1		Impervious		

7.2.1 Initial conditions

The initial conditions represent the equilibrated state just before excavation and they are described by the following variables: saturation degree, void ratio (or porosity), pore water pressure and effective stresses. They must be in equilibrium with the prescribed external loads and consistent with the adopted constitutive model of the ground.

The analyses assume saturated soils (i.e. saturation degree equal to 1). The geostatic conditions, as formulated in Abaqus, read as follows:

$$\frac{dp_{w0}}{dz} = -\gamma_w \ , \tag{7.1}$$

$$\frac{d\sigma'_{z0}}{dz} = -\gamma_d - (n_0 - 1)\gamma_w, \qquad n_0 = \frac{e_0}{1+e_0} \tag{7.2}$$

and

$$\sigma'_{x0} = \sigma'_{y0} = K_0 \sigma'_{z0} \ , \tag{7.3}$$

where z is the vertical direction (see Fig. 7.2), p_{w0} is the initial pore pressure, σ'_{z0} is the initial vertical effective stress (compressive stress as positive), σ'_{x0} and σ'_{y0} are the initial horizontal effective stresses, γ_d is the dry unit weight of the soil, n_0 and e_0 are initial porosity and void ratio respectively, K_0 is the coefficient of lateral stress. We remark that in the so-called 'total pore pressure' coupled hydraulic-mechanical formulation of Abaqus the dry unit weight of the soil is a material constant; for this reason Eq. (7.2) leads to a slightly non-linear initial effective stress distribution when the porosity n_0 is assumed variable along z.

Different initial states have been defined for Mohr-Coulomb (MC) and Modified Cam Clay materials (MCC).

7.2.1.1 MC model

For Mohr Coulomb soils the initial void ratio is assumed constant (e_0 = 1), the initial vertical and horizontal effective stresses increase linearly with depth according to the submerged unit weight ($\gamma' = \gamma_d - 0.5\gamma_w$) and the coefficient of lateral stress K_0. Two values of K_0 are assumed in the parametric study (K_0 =0.5 and 1).

7.2.1.2 MCC model

Overconsolidated Cam Clay soils with an *OCR* that varies with the depth have been considered and the spatial distribution of the initial effective stresses, void ratio and preconsolidation pressure have been numerically computed. This is done in 3 simulation steps:

i) Initialization considering normally consolidated deposit with a surface pressure (Eq. 7.8) corresponding to an effective mean stress at the ground surface of 1 kPa;
ii) Stepwise drained loading of the numerical model up to a certain surface pressure σ_{OC} (see Table 7.2) in order to simulate the maximum vertical effective stress experienced by the material during its geologic history;
iii) Stepwise complete unloading of the ground surface to simulate the mechanical effects of the erosion or deglaciation.

For the initialization of the normally consolidated material at the first step, the value of lateral stress coefficient K_0 is taken consistent with the Modified Cam-clay model (assuming that elastic deviatoric strains are negligible) and is estimated using the relation [91]:

$$K_0 = \frac{3-\eta}{3+2\eta} \quad ; \quad \eta = -\frac{3}{2}\left(1-\frac{k}{\lambda}\right)+\frac{1}{2}\sqrt{9\left(1-\frac{k}{\lambda}\right)^2+4M^2} \quad , \tag{7.4}$$

where λ is the slope of the virgin compression line, κ is the slope of the swelling line and *M* is the slope of the critical state line (or critical stress ratio).

The initial effective vertical stress σ'_{z0} and the initial void ratio e_0 at the first step have to satisfy the equilibrium equation (Eq. 7.2) and, in order to be consistent with the Modified Cam-clay model and the assumption of normally consolidated material (i.e. K_0 according to Eq. 7.4), they have also fulfill the following conditions:

$$e_0 = e_1 - \lambda \ln(p'_{c0}) + \kappa \ln\left(\frac{p'_{c0}}{p'_0}\right), \qquad p'_0 = +\frac{1}{3}(1+2K_0)\sigma'_{z0}\,, \tag{7.5}$$

$$\frac{p'_{c0}}{p'_0} = 1+\left(\frac{\eta}{M}\right)^2, \tag{7.6}$$

where e_1 is the intercept of the virgin compression line (i.e. void ratio for an isotropic effective pressure of 1 kPa), p'_{c0} is the initial preconsolidation pressure and p'_0 is the initial mean effective stress.

The derivation of analytical expressions for the vertical distribution of σ'_{z0} and e_0 considering Eqs. (7.2), (7.4), (7.5) and (7.6) is cumbersome. Therefore, a numerical approach is followed subdividing the soil in a number of discrete layers. Inside each layer the porosity is assumed linearly variable with the depth. The integration of Eq. (7.2) assuming as boundary condition the effective vertical stress at the top of the k-layer $\sigma'_{z0,k}$

leads to the following equation for the effective vertical stress at the bottom of the k-layer $\sigma'_{z0,k+1}$

$$\sigma'_{z0,k+1} = \sigma'_{z0,k} + (\gamma_d - \gamma_w)\Delta z_k + \frac{1}{2}(n_{0,k} + n_{0,k+1})\gamma_w \Delta z_k \,, \tag{7.7}$$

where Δz_k is the thickness of the layer, $n_{0,k}$ and $n_{0,k+1}$ are the porosity at the top and at the bottom of the layer respectively. The top of the first layer coincides with the ground surface; here the effective vertical stress $\sigma'_{z0,1}$ and the porosity $n_{0,1}$ are taken equal to

$$\sigma'_{z0,1} = \frac{3}{(1+2K_0)} p'_{0,1} \text{ with } p'_{0,1} = 1kPa \text{ and} \tag{7.8}$$

$$n_{0,1} = \frac{e_{0,1}}{1+e_{0,1}} \text{and } e_{0,1} = e_1 - (\lambda - \kappa)\ln\left[1 + \left(\frac{\eta}{M}\right)^2\right] \tag{7.9}$$

The vertical stress $\sigma'_{z0,k+1}$ and the initial void ratio $e_{0,k+1}$ must satisfy the Eqs. (7.5), (7.6) and (7.7) and are evaluated iteratively.

Figure 7.3 shows using red markers the effective vertical stress σ'_{z0}, the coefficient of lateral stress K_0, the void ratio e_0 as a function of the depth computed as described above for an example of normally consolidated material. They are taken as initial values of the calculation step i. The dashed lines show the results of the first calculation step i of the numerical stress analysis. We remark that although the differences between the initial values and results of the first calculation step are very small (see red markers and dashed lines), displacements of some millimetres are computed close to the ground surface. This may occur because in this part of the model the material stiffness is very small (due to the low effective stresses) and thus small adjustments of the stresses produce 'visible' displacements. Figure 7.3 shows also the results of the steps ii and iii. The continuous lines refer to the condition prevailing just before the excavation.

Figure 7.4 shows for the different MCC soils considered in the present study (see Table 7.2) the pre-excavation lateral stress coefficient K_0, overconsolidation ratio *OCR* and Young modulus E^* as a function of the depth. The latter was computed according the following equation:

$$E^* = 3(1-2\nu)\frac{p'(1+e)}{\kappa} \tag{7.10}$$

where ν is the Poisson ratio, κ is the slope of the swelling compression lines, *p'* and *e* are the pre-excavation effective stress and void ratio.

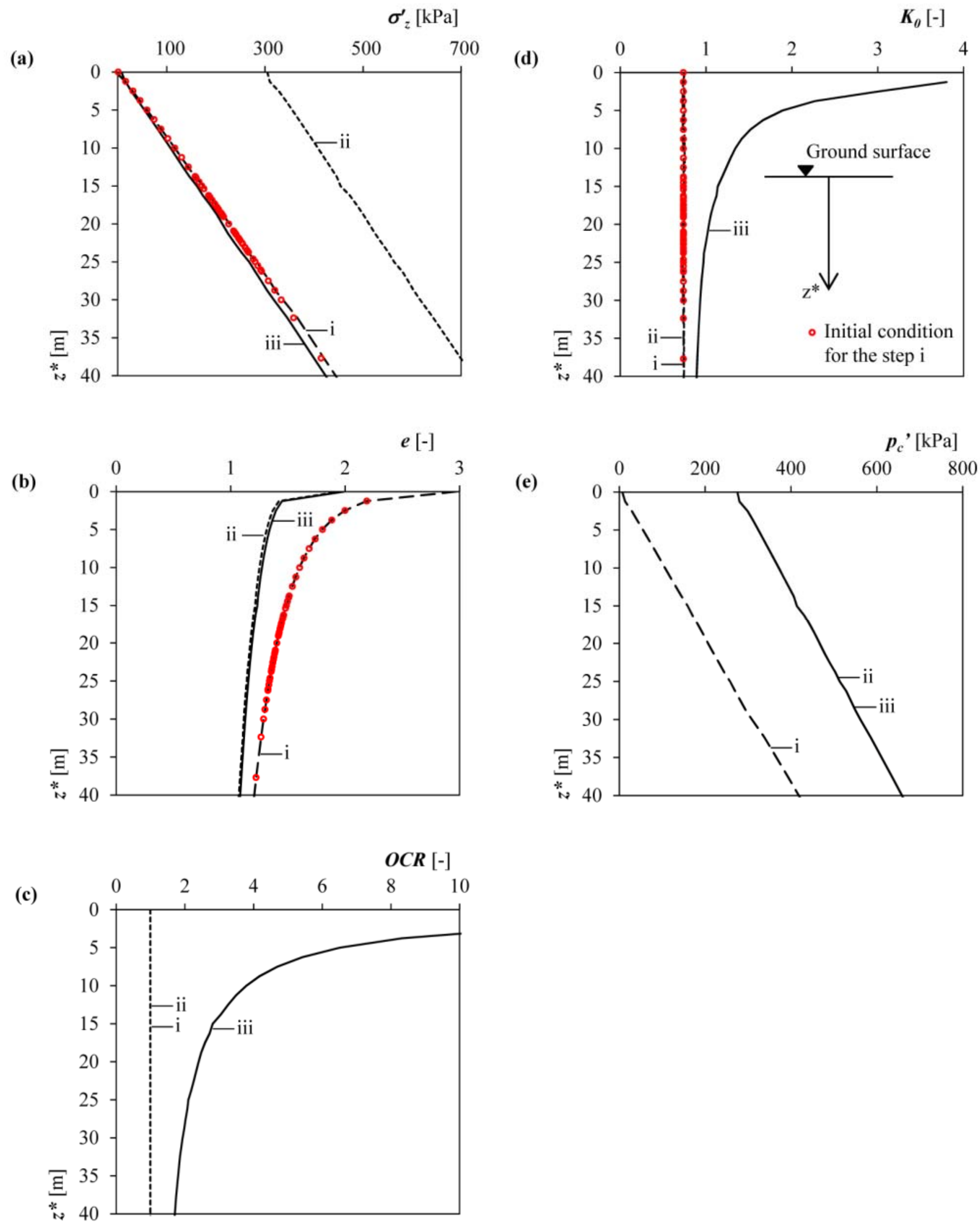

Figure 7.3 *Vertical distribution of, (a), vertical effective stress σ'_z, (b), void ratio e, (c), overconsolidation degree OCR, (d), coefficient of later stress K_0 and, (e), consolidation pressure p'_c at pre-excavation stages i–iii (soil MCC2, parameters according to Table 7.2).*

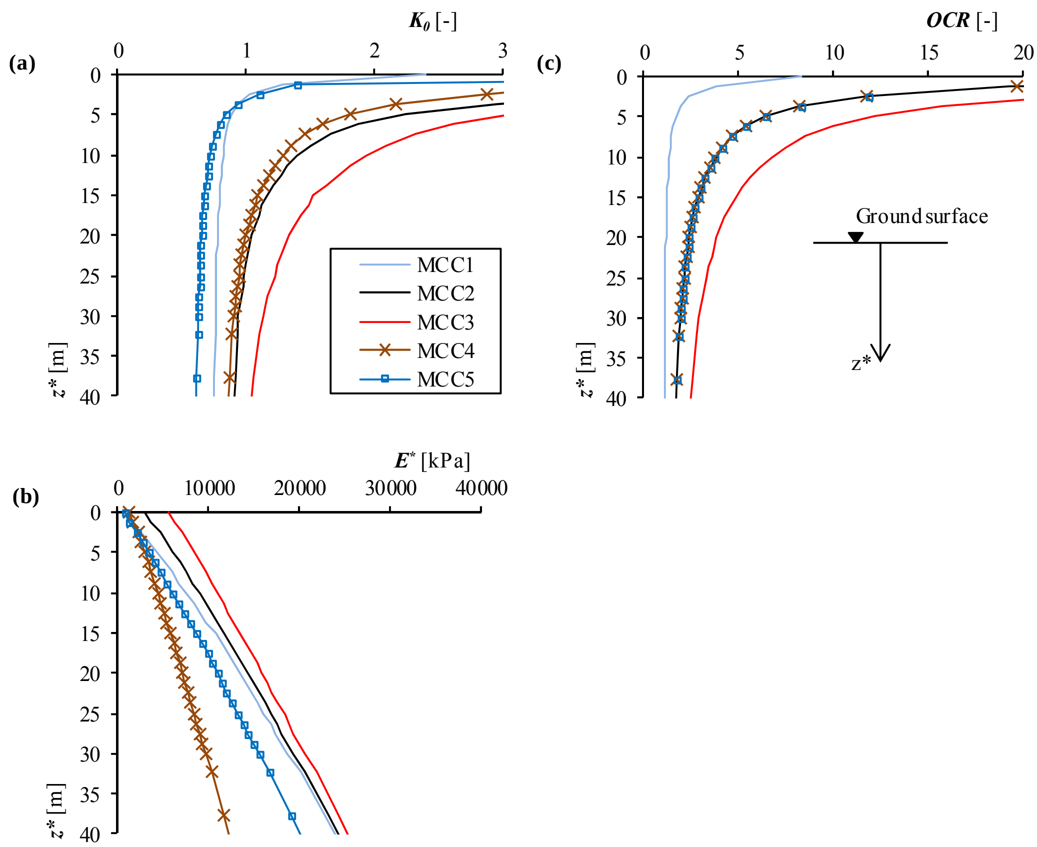

Figure 7.4 *Vertical distribution of, (a), lateral stress coefficient K_0, (b), Young modulus E_0, (c), overconsolidation degree OCR at pre-excavation stage iii (parameters according to Table 7.2).*

The soils MCC1, MCC2 and MCC3 are characterized by different values of the surface pressure σ_{OC} (see Table 7.2), for this reason they exhibit different overconsolidation ratio. At fixed depth, the lateral stress coefficient K_0 and the Young modulus E^* increase with *OCR*.

The soils MCC2 and MCC4 differ only with respect to κ (see Table 7.2). The soil MCC4 has a smaller Young modulus E^* because the Young modulus E^* is inversely proportional to κ (see Eq. 7.10).

The soils MCC2 and MCC5 differ only with respect to the material constant *M* (see Table 7.2). The lateral stress coefficient of a normally consolidate material K_0 decreases with increasing *M* (see Eq. 7.4). This causes the difference between the K_0-values of MCC2 and MCC5. With decreasing K_0 the effective stress decreases and E^* decreases too (see Eq. 7.10). For this reason MCC5 exhibits a smaller modulus E^*.

7.3 Dimensional analysis

7.3.1 MC model

For a specific advance mode, for a fixed point of the surface and a fixed position of the tunnel face, the displacement *u* during continuous excavation (i.e. no standstill) is a function of the following parameters:

$$u = f\left(E, \nu, c', \varphi', \psi, \gamma_w, \gamma', K_0, k, D, H, H_w, t_l, E_l, \nu_l, l_u, \zeta, v\right) \quad (7.11)$$

where ζ is the ratio between the lining permeability and soil permeability (here ζ = 0 and ∞ for the cases of ideally pervious and impervious lining).

For dimensional reasons and due to the structure of the equations underlying consolidation theory a dimensionless advance rate can be defined as follow:

$$v^* = \frac{v\gamma_w D}{kE} \quad (7.12)$$

and the displacement can be written in normalized form:

$$\frac{u}{D} = f\left(\nu, \frac{c'}{\gamma' D}, \varphi', \psi, \frac{\gamma_w}{\gamma'}, K_0, \frac{E}{\gamma' D}, \frac{v\gamma_w D}{kE}, \frac{H}{D}, \frac{H_w}{H}, \frac{t_l}{D}, \frac{E_l}{E}, \nu_l, \frac{l_u}{D}, \zeta\right) \quad (7.13)$$

The dimensionless factors $v\gamma_w D/kE$, $c'/\gamma' D$ φ', K_0 and H/D are considered as variable in the parametric analyses

7.3.2 MCC model

For a Modified Cam Clay (MCC) soil, the displacement *u* is a function of the following parameters:

$$u = f\left(\nu, \lambda, \kappa, e_1, M, \xi, \sigma_{OC}, \gamma_w, \gamma_d, k, D, H, H_w, t_l, E_l, \nu_l, l_u, \zeta, v\right) \quad (7.14)$$

and can be written in normalized form as follows:

$$\frac{u}{D} = f\left(\nu, \lambda, \kappa, e_1, M, \xi, \frac{\sigma_{OC}}{\gamma_d D}, \frac{\gamma_w}{\gamma_d}, \frac{v\gamma_w D}{kE_a^*}, \frac{H}{D}, \frac{H_w}{H}, \frac{t_l}{D}, \frac{E_l}{E_a^*}, \nu_l, \frac{l_u}{D}, \zeta\right) \quad (7.15)$$

where E^*_a is the pre-excavation Young's modulus (Eq. 7.10 and Fig. 7.4b) at the tunnel depth (at z^* = 20 m in Figure 7.4b).

The dimensionless factors $v\gamma_w D/kE^*_a$, κ, $\sigma_{OC}/\gamma_d D$, and M are considered as variable in the parametric analyses

7.4 Surface settlements for the borderline cases of a very high or a very low permeability

The response of water-bearing grounds to tunneling is typically investigated for the following two cases: (a) a high-permeability soil exhibiting drained behaviour right from the start, i.e. even around the advancing tunnel heading (e. [92]); (b) a low-permeability soil exhibiting undrained behaviour during excavation. Case (a) is investigated by means of steady state analyses. Case (b) is typically analysed by means of an undrained analysis (constant water content constraint), which provides the short-term response, followed by a transient analysis which provides the time-dependent post-excavation settlements (e.g. [21]).

Some examples are discussed in the following paragraphs with the main goals to show how the adopted soil models (MC and MCC) behave and how the conditions prevailing in the vicinity of the advancing face (undrained or drained) affect surface settlements.

The examples consider two cases of excavation at atmospheric pressure (i.e., a MC soil with relatively high cohesion, referred to as MC2 in Tab. 7.1, and a highly overconsolidated MCC soil, referred to as MCC2 in Tab. 7.2) and two cases of excavation with full compensation of the water pressure (i.e. a MC soil with relatively low cohesion – MC1 in Tab. 7.1 – and a slightly overconsolidated MCC soil – MCC1 in Tab. 7.2). The computations were performed for overburden H of 15 m (1.5D).

7.4.1 MC model

7.4.1.1 Settlements during advance

Consider first the case of tunnelling under atmospheric pressure through a soil of relatively high cohesion (MC2). Figure 7.5 applies to a low-permeability soil (characterized by undrained conditions during advance) and shows the surface settlements along the longitudinal tunnel axis (Fig. 7.5a); the surface settlements in a fixed cross section at x = 100 m (Fig. 7.5b); the water pressure distribution along the vertical tunnel axis at x = 100 m (Fig. 7.5c). The red and blue lines show the results for two different positions of the tunnel face.

The results for a high-permeability soil (characterized by drained conditions during advance) are presented analogously in Figure 7.6. Figures 7.6a, b and c assume an impervious lining, while Figures 7.6d, e and f assume a pervious lining.

In a low permeability soils (undrained conditions during advance), settlement increases almost monotonously with the distance of the face up to a certain distance, but the ground surface experiences a small heave after the installation of the lining (see red line in Figure 7.5a). This behaviour is caused by the heave of the soil below the tunnel (so called buoyancy effect; cf. [93]) and by the presence close to the face of a practically rigid lining that stops the ovalization of the tunnel cross section. The redistribution of the total stresses induces negative excess pore pressure (i.e. pore pressures lower than the initial hydrostatic values) almost everywhere with exception of a small portion of the model close to the surface (see blue line and markers in Figure 7.5c). The highest negative excess pore pressures develop close to the tunnel before the lining installation, where the soil experiences the biggest reduction in the total average pressure.

In the case of excavation through a high permeability soil (drained conditions during advance) and support by a pervious lining, the pore pressures in a fixed cross section decrease monotonously with the advance of the face (Figure 7.6f) and reach their final values (red line in Figure 7.6f) almost 2D behind the face. The spatial stress redistribution and simultaneously the consolidation (i.e., increase of the effective compression stresses due to the decrease of the pore pressures) induce settlements that increase monotonously with the distance of the face (Figure 7.6d). In particular the transversal settlement trough deepens and widens with the distance from the tunnel face (Figure 7.6e).

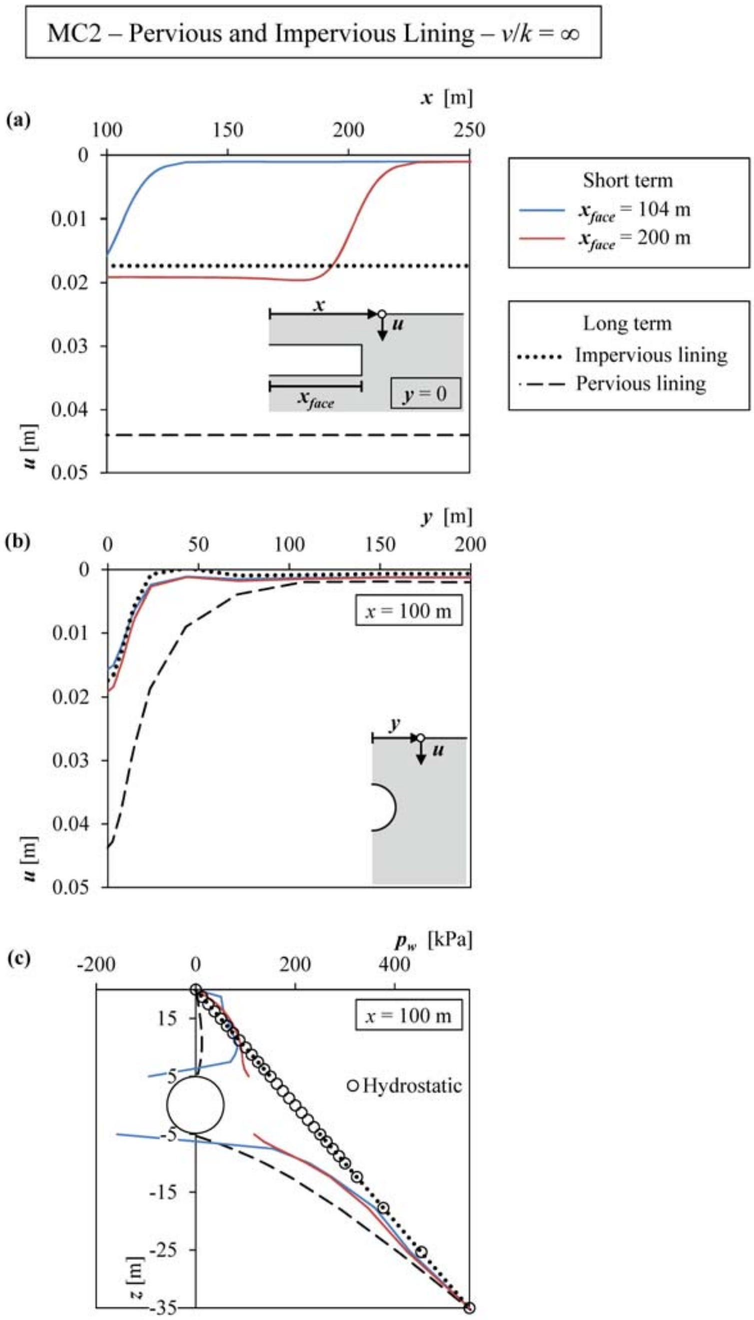

Figure 7.5 *(a), Surface settlements along the longitudinal tunnel axis, (b), surface settlements in a fixed cross section and, (c), vertical distribution of the water pressure, after undrained excavation at atmospheric pressure (short term; solid and dotted lines) and after the subsequent consolidation stage (long term; dashed lines) considering an impervious or pervious lining (soil MC2, parameters according to Table 7.1).*

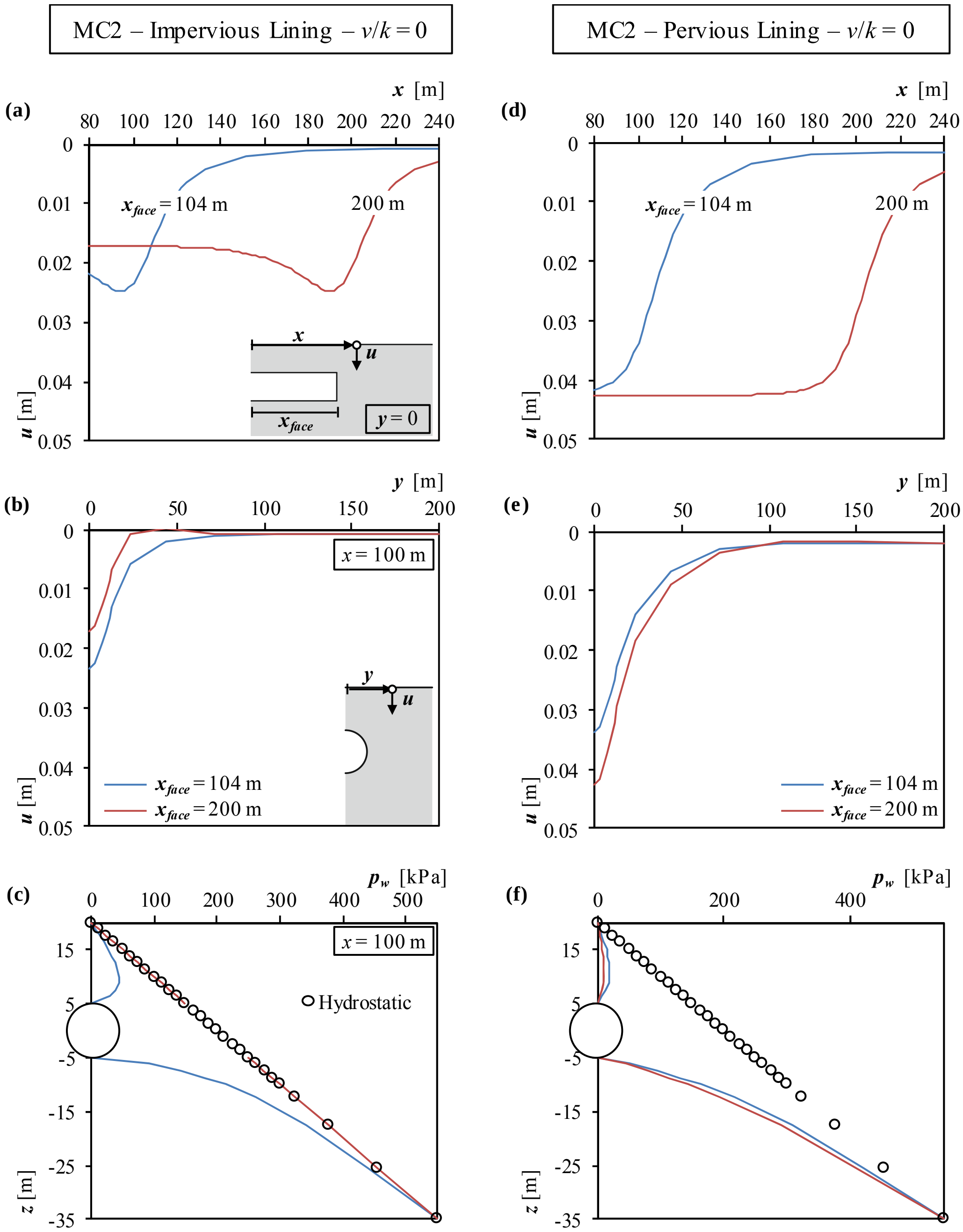

Figure 7.6 *(a, d), Surface settlements along the longitudinal tunnel axis, (b, e), surface settlements in a fixed cross section and (c, f), vertical distribution of the water pressure after fully drained excavation at atmospheric pressure considering an impervious (l.h.s.) and pervious (r.h.s.) lining (soil MC2, parameters according to Table 7.1).*

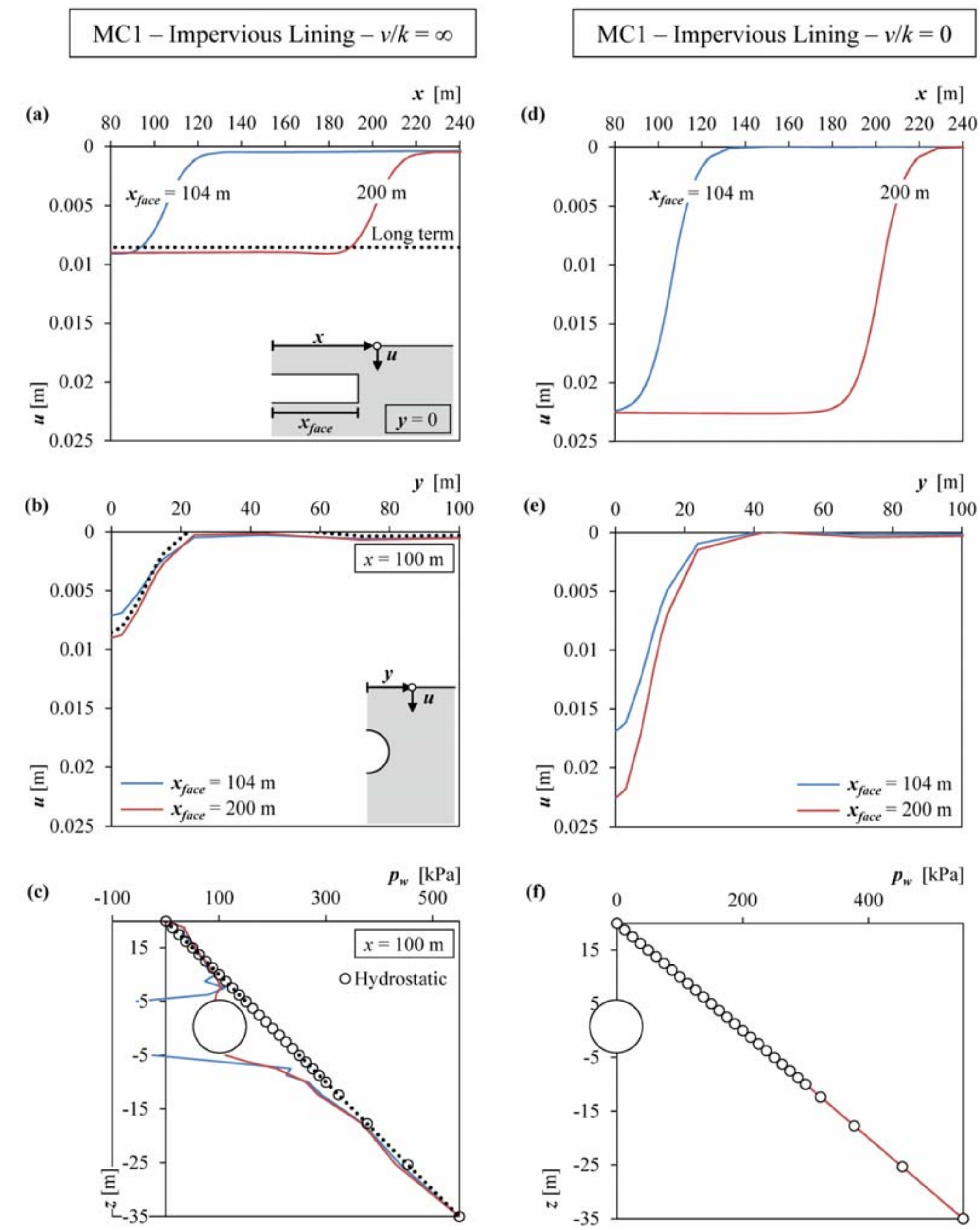

Figure 7.7 *(a, d), Surface settlements along the longitudinal tunnel axis, (b, e), surface settlements in a fixed cross section and (c, f), vertical distribution of the water pressure after undrained (l.h.s.) and fully drained (r.h.s.) excavation with full compensation of the water pressure and impervious lining (soil MC1, parameters according to Table 7.1).*

In the case of excavation through a high permeability soil (drained conditions during advance) and support by an impervious lining,, the pore pressures decrease at the face (blue line in Figure 7.6c) and increase again after the installation of the lining up to reaching the hydrostatic values (red line in Figure 7.6c) almost 6D behind the face. In a fixed cross section the ground surface experiences a subsidence when the tunnel face approaches the section and a heave once the face moves away (Figures 7.6a,b). The subsidence in the vicinity of the face is caused by the stress redistribution induced by the excavation and by the (instantaneous) consolidation. The heave in the lined portion of the tunnel is caused by the swelling which accompanies the re-establishment of the hydrostatic pressure distribution. A crater-like depression of the surface occurs above the tunnel face (Figure 7.6a). Anagnostou [13] observed the same behaviour for an elastic soil model and remarked that with a more realistic material model (taking into account the stiffer ground response to unloading) this depression is expected to be less pronounced. The MC model is able to reproduce a stiffer response in unloading if the material yields in loading. In the investigated case the soil yields before the lining installation only in a small portion of the model and for this reason the heave is still pronounced.

Next, the examples with full compensation of the water pressure in a soil of relatively low cohesion (MC1) will be considered. Figures 7.7a, b and c show (analogously to Figures 7.5a, b and c) the surface settlements and pore pressures for a low permeability soil (undrained conditions during advance); Figures 7.7d, e and f shows the same results for a high permeability soil (drained conditions during advance). Only the case of impervious lining is considered in these examples.

Under undrained conditions the soil can be conceived as a monophasic medium and the face pressure represents a total support pressure; the model behaviour (Figures 7.7a, b and c) is qualitatively similar to the one observed for advance at atmospheric pressure (Figure 7.5). Under drained conditions, however, a very different behaviour is predicted (compare Figures 7.7d, e and f with Figures 7.6a, b and c). The water pressure remains constant during the face advance (Figure 7.7f); surface settlements occur only due to the spatial redistribution of the effective stresses (as in a dry soil) and increase almost monotonously with the face advance (Figures 7.7d, e).

7.4.1.2 Long-term settlements of a very low-permeability soil

In a very low-permeability soil undrained conditions prevail during excavation. The settlements in any given tunnel cross-section continue to increase long after the passage of the face due to the excess pore pressure dissipation until reaching the steady state hydraulic head field.

The settlements at the end of the dissipation process are referred hereafter to as steady-state long-term settlements; they are discussed in this section in order to clarify some important aspects of the model behaviour.

For the examples considered before, the settlements and pore pressures under steady-state long-term conditions are reported in Figures 7.5 and 7.7 (a, b and c). The dashed lines assume a pervious lining while the dotted lines consider an impervious lining.

In the case of impervious lining the long term pore pressures are hydrostatic (dotted lines in Figures 7.5c and 7.7c). In the post-excavation period the pore pressures increase almost everywhere in the model (compare red and dotted lines in Figures 7.5c and 7.7c). As a consequence, the effective (compressive) stresses decrease, thus causing swelling and a heave of the ground surface (the dotted lines are above the red lines in Figures 7.5a, b and 7.7a, b).

In the case of pervious lining, the long term hydraulic field is characterized by a significant pore pressure relief (dashed line in Figure 7.5c). In the post-excavation period, the pore pressures decrease (compare red and dashed lines in Figure 7.5c), the effective (compressive) stresses increase, the ground consolidates and the surface experiences further subsidence (the dashed lines are below the red lines in Fig. 7.5a and b). The long-term transversal settlement trough is deeper and wider than the short-term one (Figure 7.5b).

7.4.1.3 Concluding remarks

(1) According to Figures 7.5, 7.6 and 7.7, the longitudinal and transversal settlement profiles in the vicinity of the advancing face depend significantly on the soil permeability, i.e. on whether drained or undrained conditions prevail around the advancing face

(2) In the case of *full compensation of the water pressure* and impervious lining, significant differences can be observed also with respect to the final (steady-state) settlements far behind the face. They depend on whether the conditions prevailing during advance are drained (red curve in Fig. 7.7e) or undrained (dotted curve in Fig. 7.7b).

(3) In the case of *excavation under atmospheric pressure*, the final settlements are practically independent on the conditions prevailing during advance and on the deformations in the region of the advancing face. They are almost equal for drained and undrained conditions (compare the dashed curve in Figure 7.5b with the red curve in Figure 7.6e and the dotted curve in Figure 7.5b with the red curve in Figure 7.6b, respectively).. This is true both for a pervious and an impervious lining.

(4) The reliability of the MC model with respect to the computed final settlements is questionable in the case of excavation through a high-permeability soil (drained conditions during advance) under atmospheric pressure and support by an impervious lining. Specifically, the MC model predicts a considerable heave in the swelling stage following the lining installation, because of the assumed linearly elastic behaviour and the limited yielding. However, real soil behaviour is characterized by a higher stiffness in unloading (i.e. during the swelling stage) as in loading (i.e. during the consolidation occurring before lining installation). Therefore, settlements are expected to decrease after lining installation less than predicted by the MC model.

7.4.2 MCC model

Figures 7.8 and 7.9 show (analogously to Figures 7.5 and 7.6) the surface settlements and pore pressures for the examples of excavation at atmospheric pressure in a highly overconsolidated soil (MCC2). Figure 7.10 shows (analogously to Figure 7.7) the results for excavation with full compensation of the water pressure in a slightly overconsolidated soil (MCC1).

According to Figures 7.8 and 7.9, the behaviour of the highly overconsolidated MCC soil is qualitatively similar to the one of the high-cohesion MC soil. Under undrained conditions (low-permeability soil), negative excess pore pressures develop around the tunnel (Fig. 7.8c) because of the redistribution of the total stresses and of the constrained plastic dilatancy of the overconsolidated soil. In the case of an impervious lining, swelling and heave of the soil occurs at long term. In the case of pervious lining, consolidation and very large final displacements (~ 125 mm) occur.

In the case of excavation through a high-permeability soil (drained conditions) under atmospheric pressure and support by an impervious lining (Figure 7.9a), a pronounced crater-like depression of the surface above the tunnel face is observed also in the MCC soil. This occurs because almost everywhere in the model (with the exception of a small region around the tunnel and ahead of the face) only elastic deformations occur, i.e. the mean effective stresses and the void ratios move only on the swelling compression line and consequently the response is equally stiff in loading and unloading.

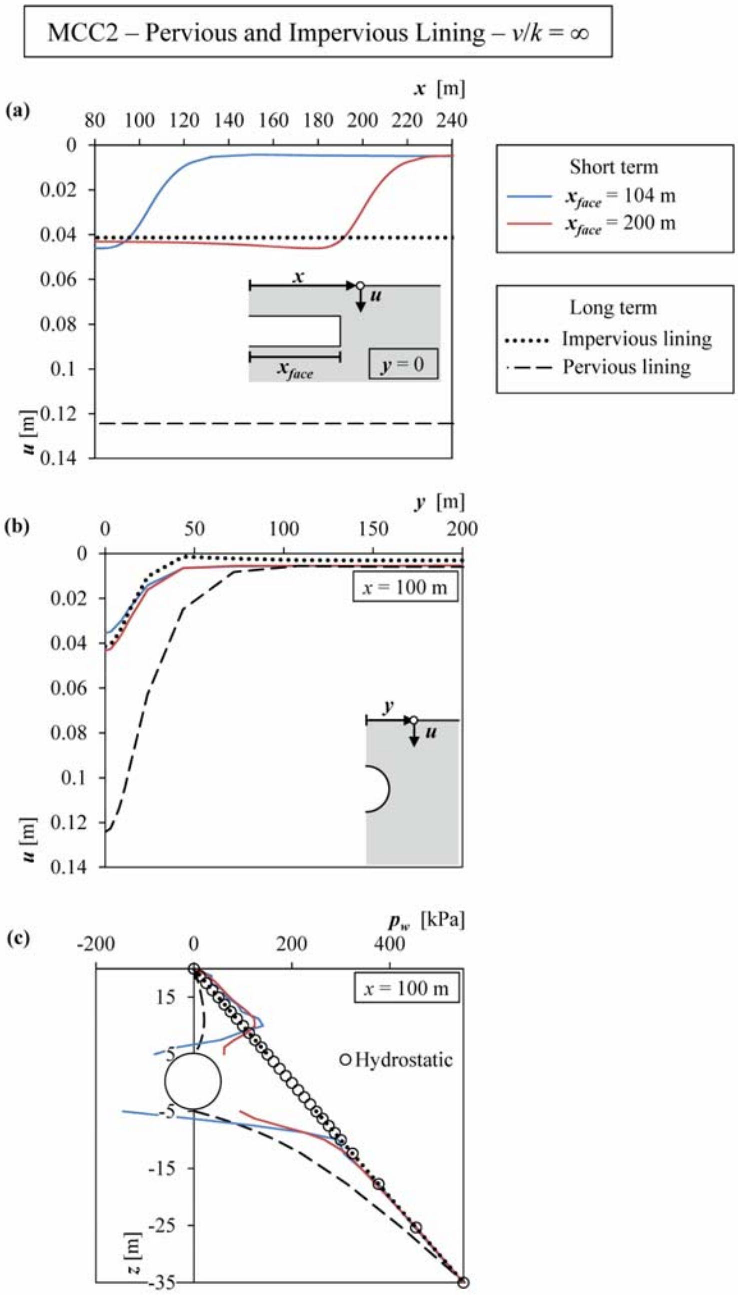

Figure 7.8 *(a), Surface settlements along the longitudinal tunnel axis, (b), surface settlements in a fixed cross section and, (c), vertical distribution of the water pressure, after undrained excavation at atmospheric pressure (short term; solid and dotted lines) and after the subsequent consolidation stage (long term; dashed lines) considering an impervious or pervious lining (soil MCC2, parameters according to Table 7.2).*

If the conditions during excavation are undrained (low permeability soil, high advance rate) the behaviour of the slightly overconsolidated MCC soil (Fig. 7.10) is qualitatively different from that of the MC soil (Figure 7.7). In the MCC soil, positive excess pore pressures (i.e. pore pressures higher than the hydrostatic values) develop above the tunnel at the end of the undrained excavation due to constrained plastic contraction. The subsequent consolidation stage leads therefore to further subsidence at long term, while the opposite occurs in the MC soil (Figures 7.7a, b). This difference is related to the difference in the excess pore pressures caused by the undrained excavation. According to the results of Figures 7.8, 7.9 and 7.10, the conclusions of Section 7.4.1.3 are valid also for the MCC soil model.

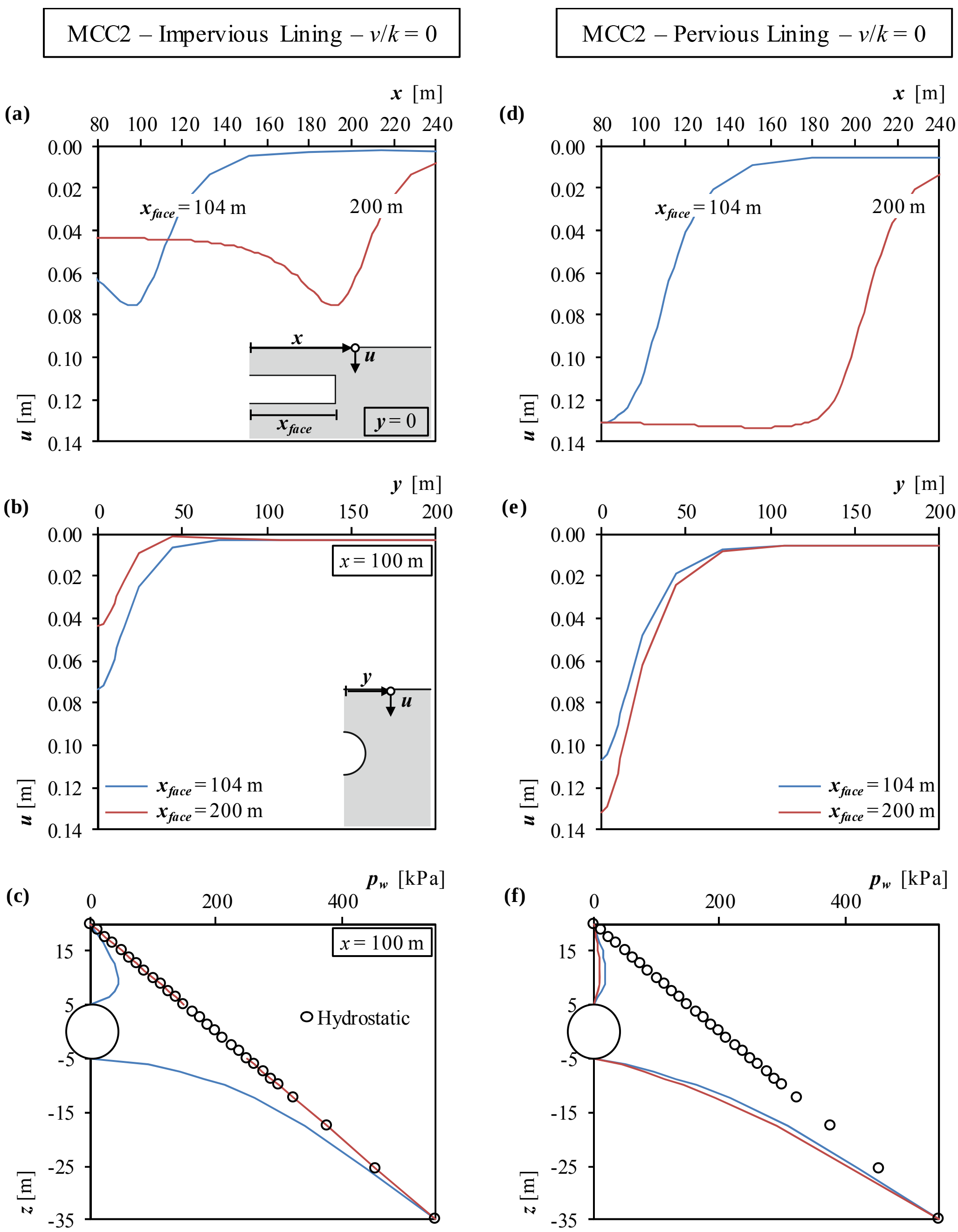

***Figure 7.9** (a, d), Surface settlements along the longitudinal tunnel axis, (b, e), surface settlements in a fixed cross section and (c, f), vertical distribution of the water pressure after fully drained excavation at atmospheric pressure considering an impervious (l.h.s.) and pervious (r.h.s.) lining (soil MCC2, parameters according to Table 7.2).*

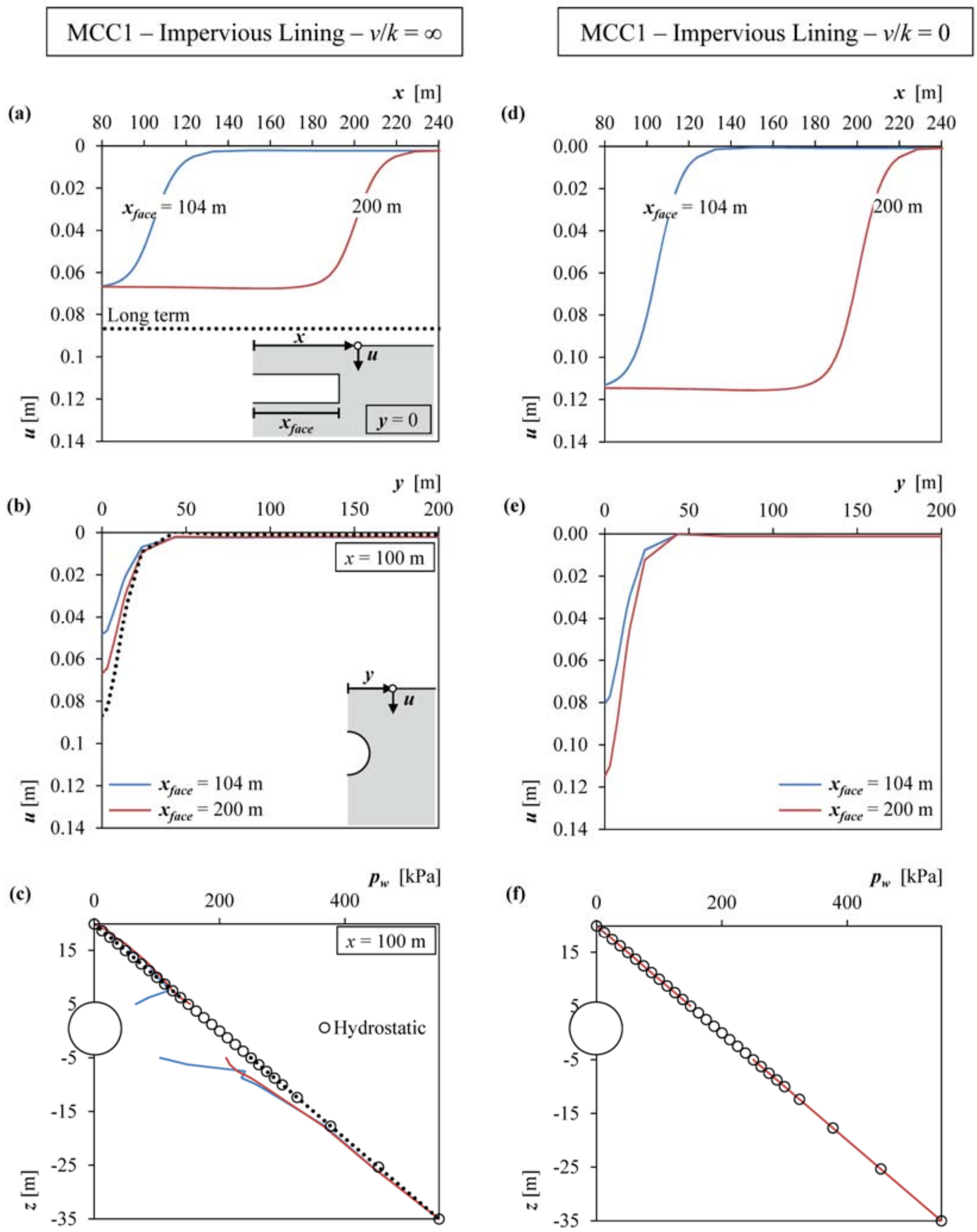

Figure 7.10 *(a, d), Surface settlements along the longitudinal tunnel axis, (b, e), surface settlements in a fixed cross section and (c, f), vertical distribution of the water pressure after undrained (l.h.s.) and fully drained (r.h.s.) excavation with full compensation of the water pressure and impervious lining (soil MCC1, parameters according to Table 7.2).*

7.5 Surface settlements in medium permeability soils

In medium permeability soils transient (or "partially drained") conditions (i.e. conditions somewhere between undrained and drained conditions) prevail during advance. The deformations around the advancing face depend essentially on the ratio of advance rate to soil permeability. The results of a series of parametric studies (Tab. 7.3) into this effect are presented in the following.

7.5.1 MC model

For the same examples presented in Section 7.4.1, Figures 7.11-7.17 show for several *v/k*-ratios: the longitudinal profile of the surface settlements (Figures. 7.11a, 7.12a and 7.13a), the transversal profiles of the surface settlements in a cross section 4 m behind the face (Figures 7.11b, 7.12b and 7.13b), the long term settlements (Figures 7.11c, 7.12c and 7.13c), the spatial distribution of the water pressure in the longitudinal vertical cross section of the tunnel (Figures 7.14 and 7.15), the longitudinal profiles of the surface settlements after standstills of different duration (Figures 7.16 and 7.17).

Figures 7.11, 7.12, 7.14 and 7.16 consider advance at atmospheric pressure in a soil of relatively high cohesion (MC2); Figures 7.13, 7.15 and 7.17 consider advance with full compensation of the water pressure and support by an impervious lining in a soil of relatively low cohesion (MC1).

Depending on the ratio *v*/*k*, the ground response in the vicinity of the advancing face lies somewhere between the undrained and the drained response (Figures 7.11a, 7.12a and 7.13a) with exception of very high *v*/*k*-ratios for which the response is more favourable than the undrained one (i.e. smaller settlements). This behaviour is more pronounced in the case of advance under atmospheric pressure and support by an impervious lining (Figure 7.12a). A similar effect of the ratio v/k can be observed in the investigations of Ramoni and Anagnostou [94] into TBM tunnelling through squeezing ground.

High *v*/*k*-ratios reduce the time available to the consolidation process in the vicinity of the face (Figures 7.14 and 7.15) and result to smaller surface settlements (Figures 7.11a,b, 7.12a,b and 7.13a,b). The longitudinal and transversal settlement profiles in the vicinity of the face deepen and widen with decreasing the *v*/*k*-ratio.

Figure 7.11a shows that for intermediate values of the advance rate to permeability ratio no steady state is reached far behind the face. The reason is that the total time required for the excavation of the 100 m long considered tunnel portion is less than the consolidation time and, consequently, the consolidation process continues far behind the face. Note that the higher the *v*/*k*-ratio, the less the time required to excavate the 100 m and therefore the longer the numerical model has to be in order to reach steady state.

In the case of excavation at atmospheric pressure the final settlements are almost independent on the *v*/*k*-ratio (Figures 7.11c and 7.12c) and thus on the deformations in the vicinity of the advancing face as well (cf. Section 7.4.1). In the case of advance with full compensation of the water pressure (Figure 7.13c) the final settlements increase with decreasing *v*/*k*-ratio.

The crater-like depression of the surface occurs only in the case of advance at atmospheric condition in soils with high permeability (Figure 7.12a) or, equivalently, at low advance rates.

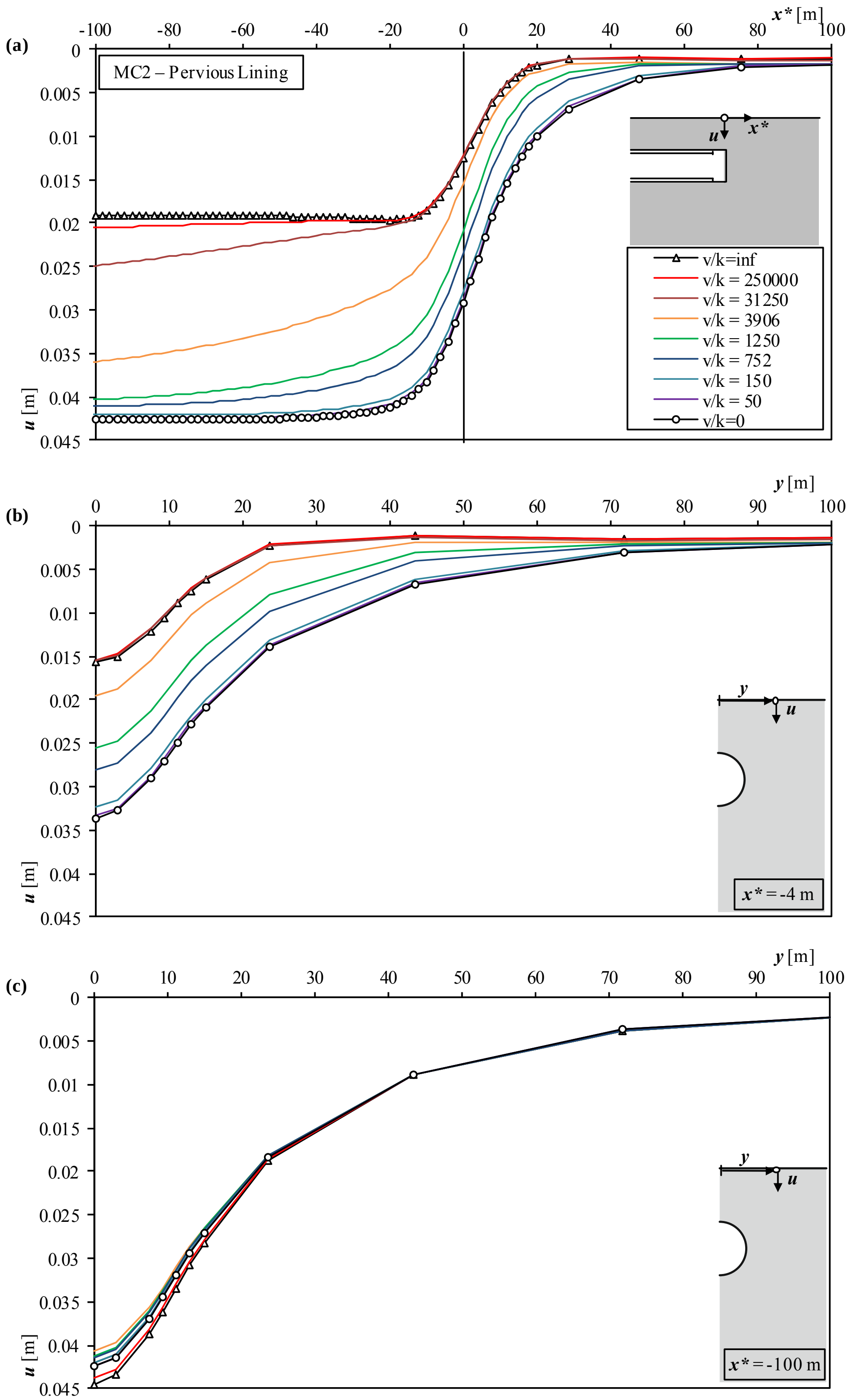

Figure 7.11 *(a), Longitudinal profile of the surface settlements, (b), transversal profile of the surface settlements in a cross section 4 m behind the face and (c), final settlements for advances at atmospheric pressure with pervious lining (soil MC2, parameters according to Table 7.1).*

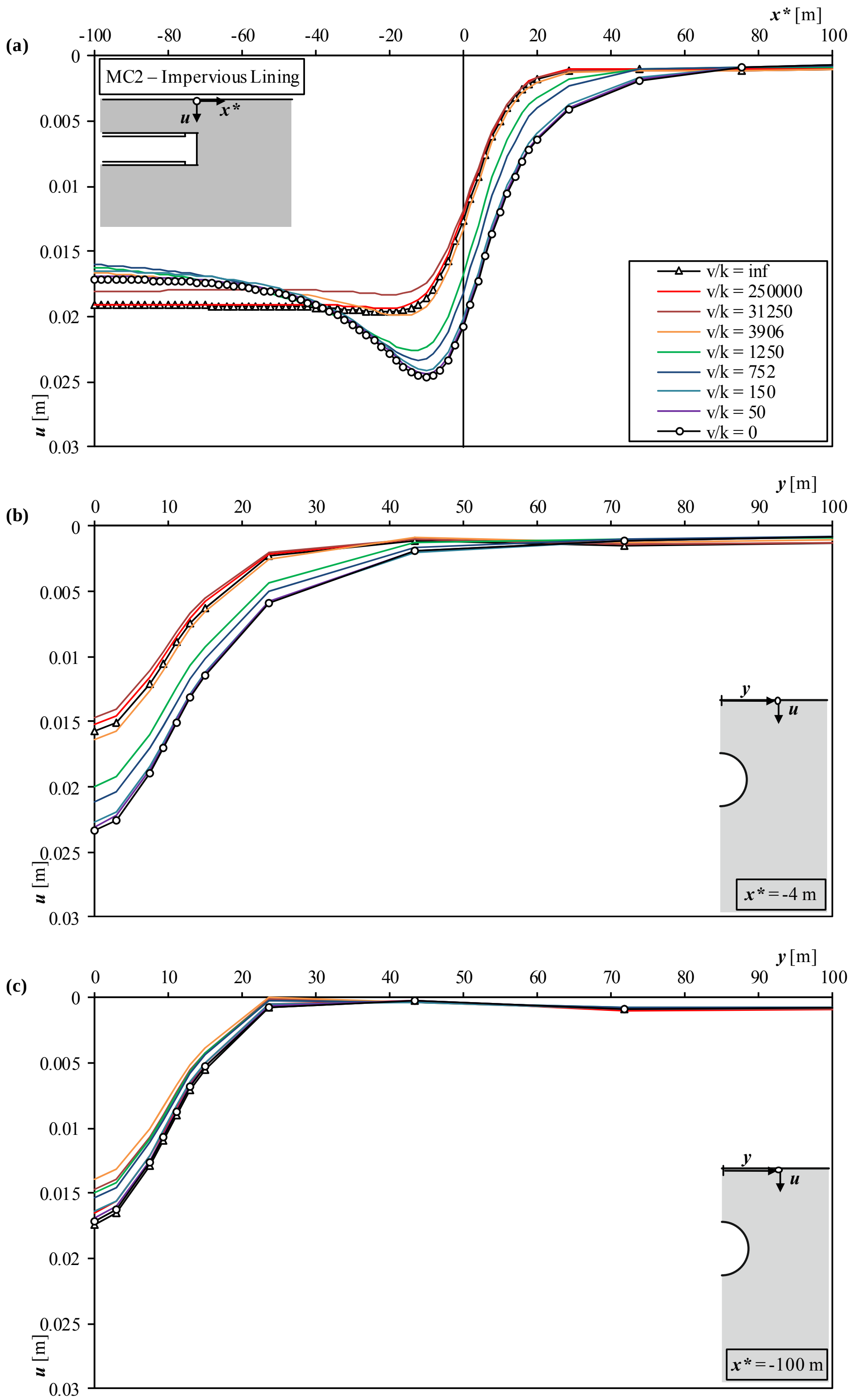

Figure 7.12 *(a), Longitudinal profile of the surface settlements, (b), transversal profile of the surface settlements in a cross section 4 m behind the face and (c), final settlements for advances at atmospheric pressure with impervious lining (soil MC2, parameters according to Table 7.1).*

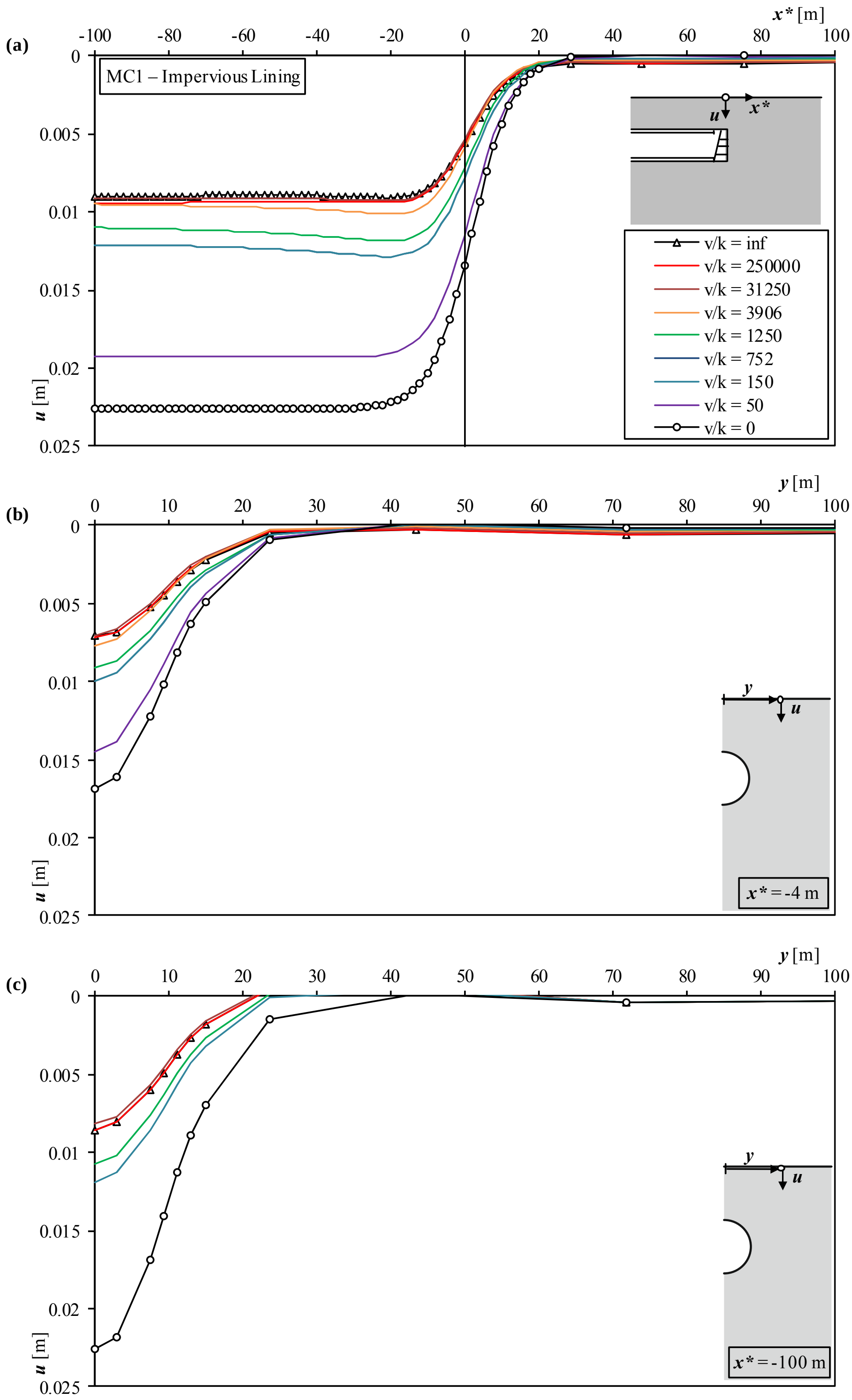

Figure 7.13 *(a), Longitudinal profile of the surface settlements, (b), transversal profile of the surface settlements in a cross section 4 m behind the face and (c), final settlements for advances with full compensation of the water pressure and impervious lining (soil MC1, parameters according to Table 7.1).*

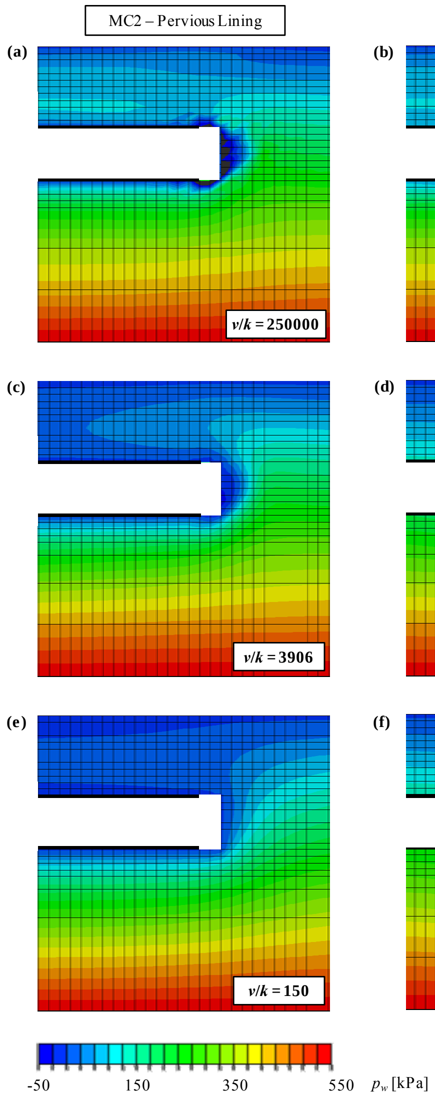

Figure 7.14 *Spatial distribution of the water pressure during advance at atmospheric pressure with pervious (l.h.s) and impervious (r.h.s) lining (soil MC2, parameters according to Table 7.1).*

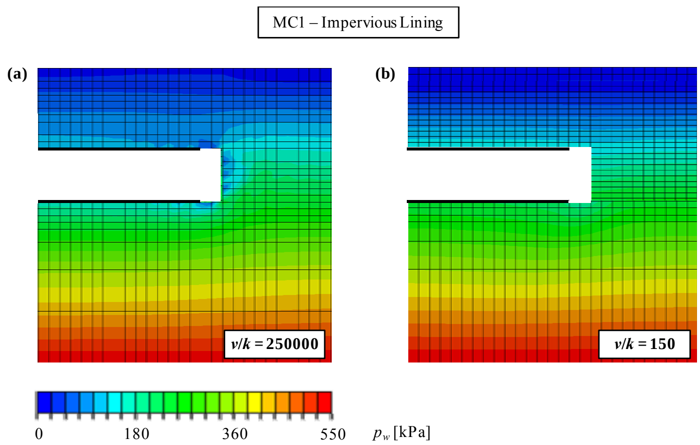

Figure 7.15 *Spatial distribution of the water pressure during advance with full compensation of the water pressure and impervious lining (soil MC1, parameters according to Table 7.1).*

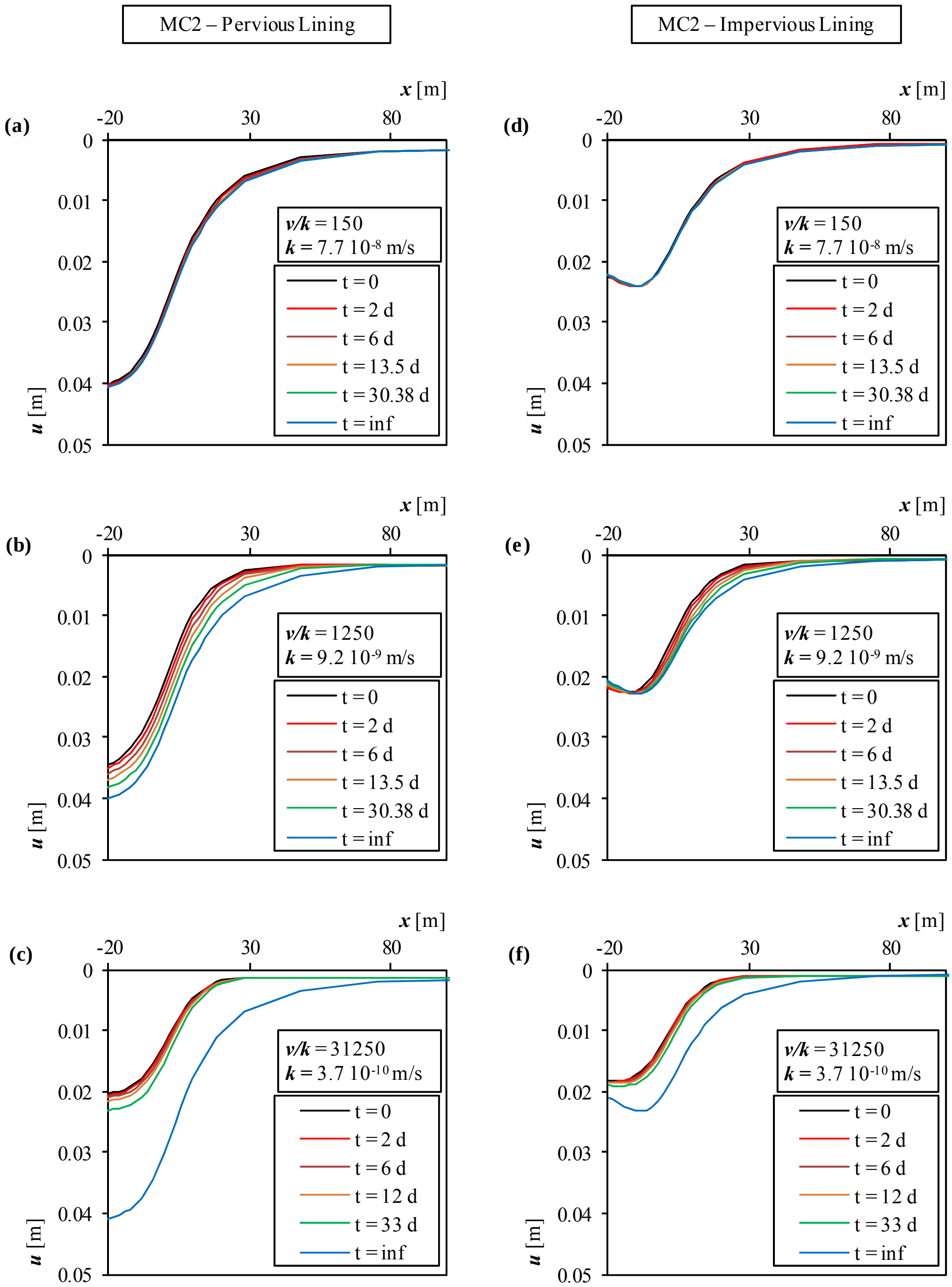

***Figure 7.16** Longitudinal profiles of the surface settlements during standstill at several time points for advances at atmospheric pressure with pervious (l.h.s) and impervious (r.h.s) lining (soil MC2, parameters according to Table 7.1).*

If the conditions prevailing around the advancing face are partially drained, the surface settlements can increase significantly also during short standstills (Figures 7.16b,e). The longitudinal profile deepens and widens with increasing time (Figures 7.16b, e). In the case of undrained conditions, the surface settlements increase only during long standstills (Figures 7.16c,f). If the conditions are almost drained, the surface settlements remain almost constant over time (Figures 7.16a,d).

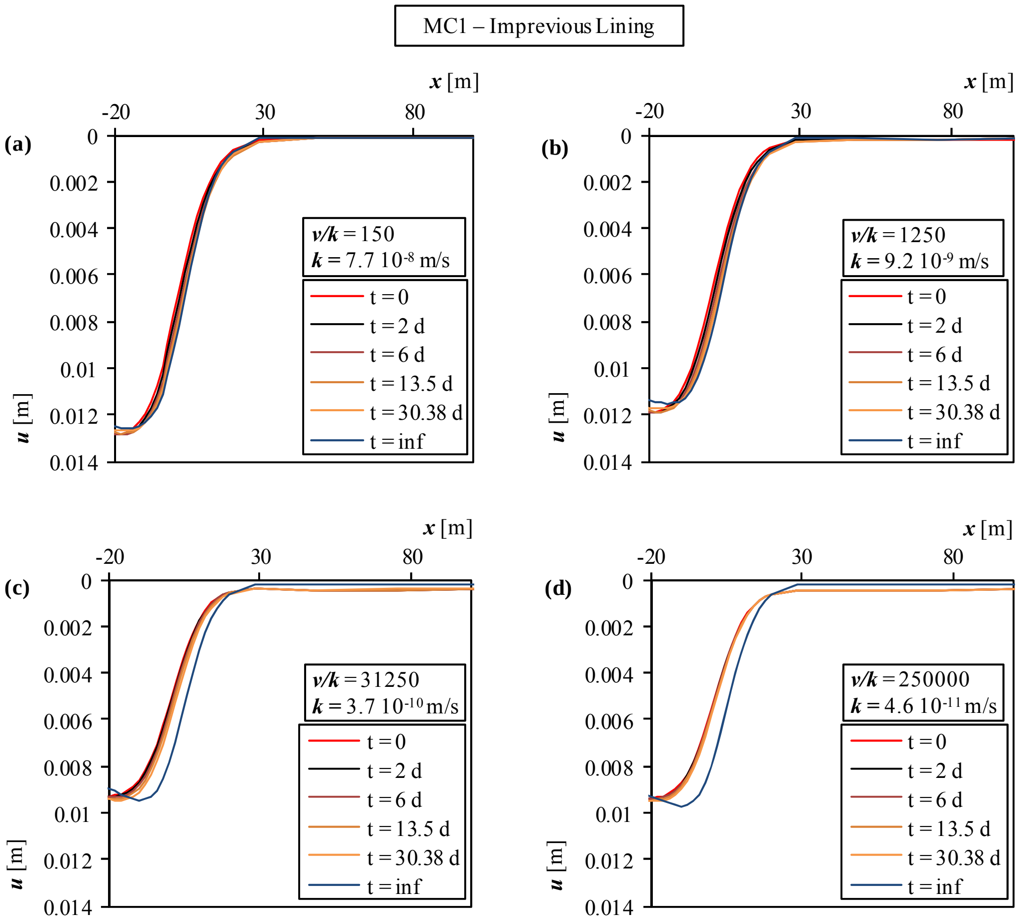

***Figure 7.17** Longitudinal profiles of the surface settlements during standstill at several time points for advances with full compensation of the water pressure and impervious lining (soil MC1, parameters according to Table 7.1).*

The increase in the settlements during short standstills is less pronounced in the case of advance with full compensation of the water pressure (Figure 7.17) than for advance under atmospheric pressure. This is such for two reasons: water pressures decrease less if water pressure is fully compensated; consolidation takes more time as the drainage boundary is far from the tunnel.

The above examples show clearly that the conditions prevailing around the advancing face (drained, undrained or partially drained) are very important for the developing settlements. Knowing which conditions have to be expected would be, therefore, valuable for the design and the decision making process during the tunnel construction (e.g., for evaluating the impact of an eventual standstill on the surface settlements).

7.5.1.1 Determination of the parameter range under which transient behaviour is relevant

Figure 7.18 shows the vertical settlement of a control point of the surface in the vicinity of the tunnel face (here a point on the vertical tunnel axis, located 4 m behind the face) as a function of the ratio *v*/*k* for all the computational examples (assuming MC soil) of the present study (see Table 7.3).

In order to facilitate a comparison, the results are represented in four diagrams that consider several sets of, (a), soil strength parameters, (b), K_0 values, (c) overburdens and, (d), advance modes. The continuous and dashed lines apply to pervious and impervious linings, respectively. They coincide for sufficiently high *v*/*k*-values corresponding to practically undrained conditions.

The surface settlements decrease with increasing of the soil strength (Figure 7.18a) and with increasing of the lateral stress coefficient (Figure 7.18b). The convergences of the tunnel increase with the overburden and consequently also the surface settlements (Figure 7.18c). The advance mode plays a relevant role (Figure 7.18d). The full compensation of the water pressure is a very effective measure to limit the settlements (i.e., in the presented example, the settlement in the case of full compensation of the water pressure is one order of magnitude smaller than the one in the case of atmospheric pressure in the same geotechnical conditions).

In the case of advance under atmospheric pressure, the conditions in the vicinity of the heading are practically undrained for $v/k > 10^6$ and practically drained for $v/k < 10^2$. This is true for all considered examples, independently on the strength parameters, coefficient of lateral stress, overburden and lining permeability (Fig. 7.18). Similar results were obtained by Anagnostou [13] for a tunnel of the same diameter and overburden as in the present study (D = 10 m, H = 15 m), excavated under atmospheric pressure in an elastic soil with stiffness equal to the one considered here (E = 50 MPa).

Figure 7.19 shows for the same control point considered in Figure 7.18 the normalized surface settlement u^* as a function of the dimensionless velocity $v\gamma_w D/kE$,

$$u^* = \frac{u - u_{undr}}{u_{dr} - u_{undr}} \tag{7.16}$$

where u_{undr} and u_{dr} are the settlements in the borderline cases of undrained ($v/k = \infty$) and drained conditions ($v/k = 0$), respectively, while u are the transient settlements reported in Figure 7.18. A normalized displacement u^* close to 1 means that the conditions are practically drained, while a value close to zero indicates practically undrained conditions. Negative values mean that the transient (partially drained) response is more favourable than the undrained one (see Section 7.5.1).

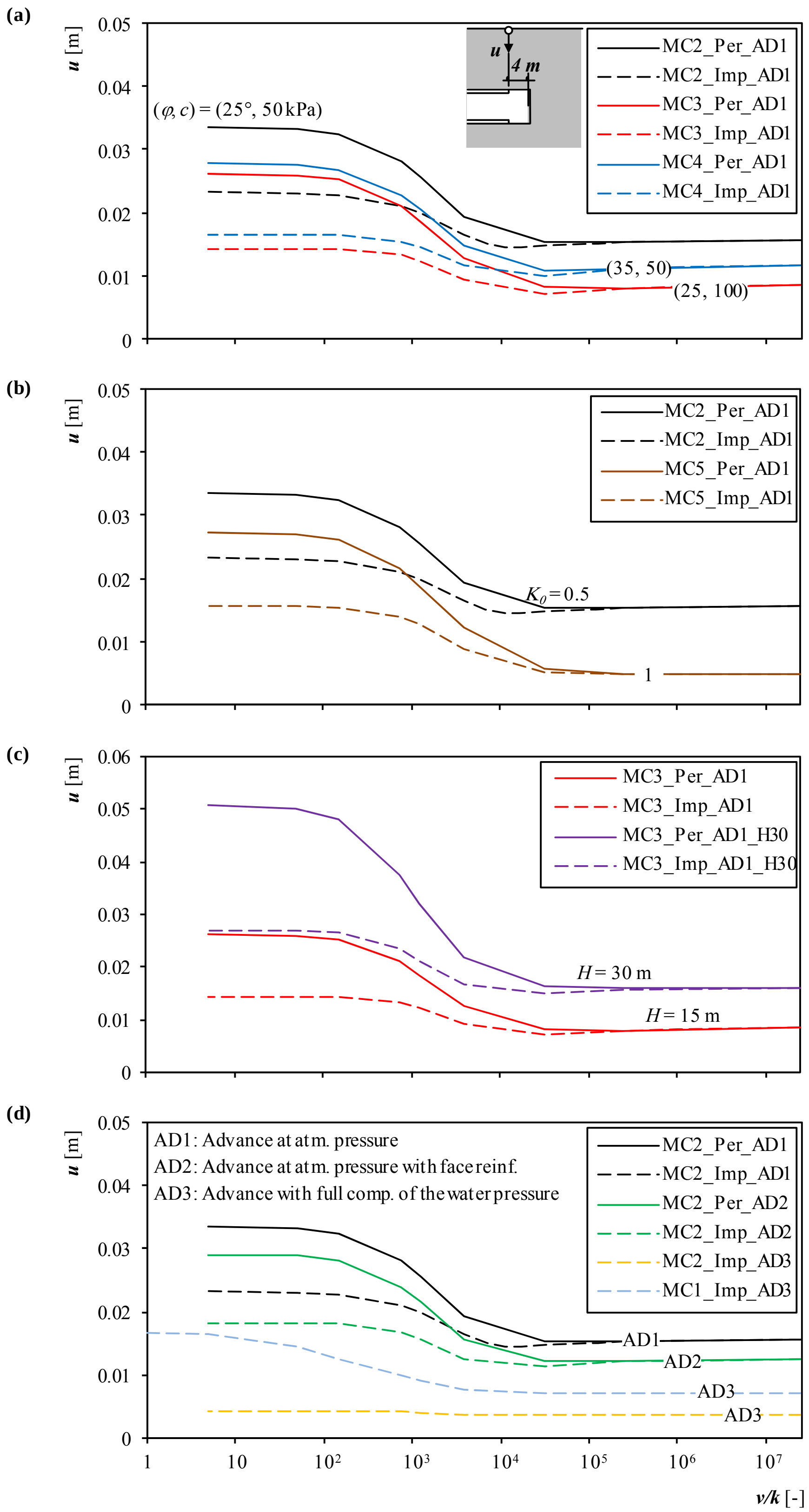

Figure 7.18 *Surface settlement of a point located 0.4D behind the tunnel face as a function of v/k-ratio for different sets of ground parameters and advance modes, for pervious and impervious lining (MC-sets of parameters according to Table 7.1).*

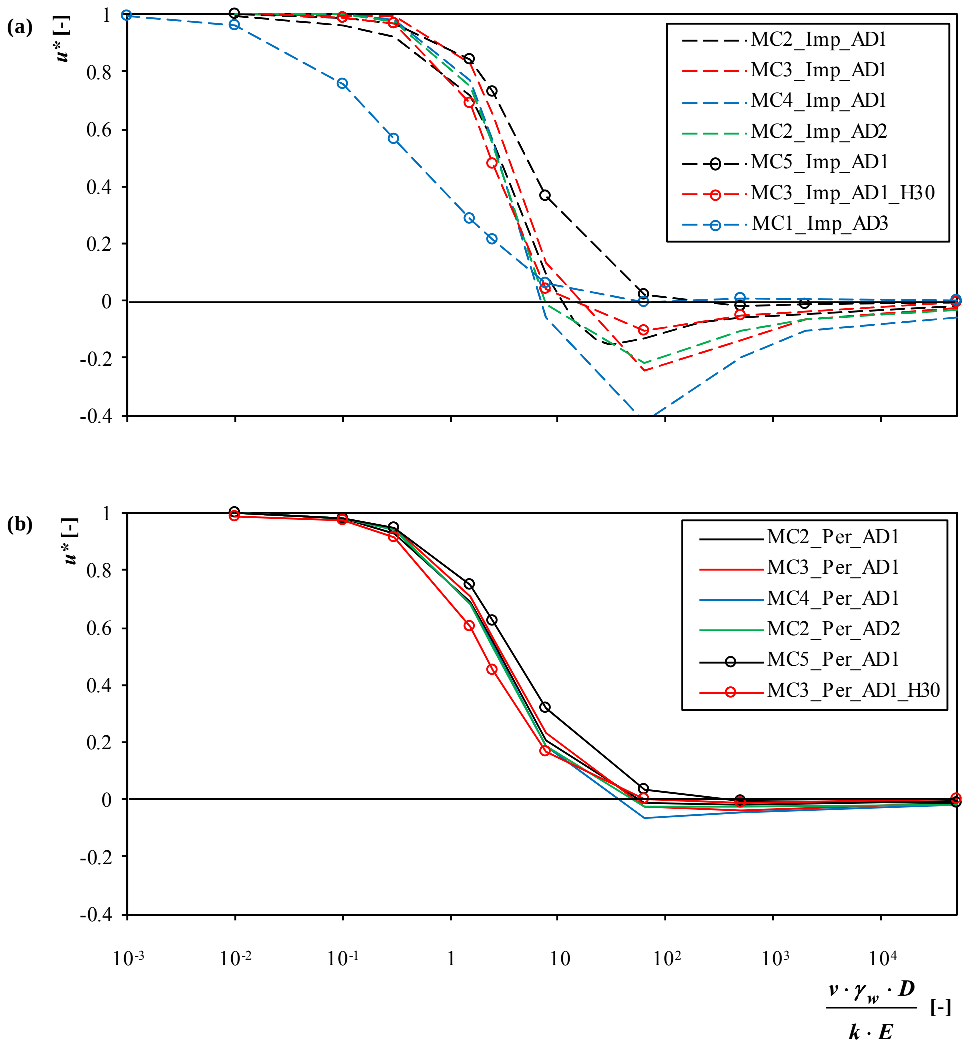

Figure 7.19 *Normalized surface settlement u* of a point located 0.4D behind the tunnel face as a function of dimensionless velocity for (a) impervious lining and (b) pervious lining in MC soils (MC-sets of parameters according to Table 7.1).*

For exacavation under atmospheric pressure, the conditions in the vicinity of the heading are practically undrained for $v\gamma_w D/kE$ > 10^3 and practically drained for $v\gamma_w D/kE$ < 10^{-2}; transient conditions are significant particularly in the range 0.1 < $v\gamma_w D/kE$ < 100 (Fig. 7.19).

In Figure 7.19a the curve for the example of advance in a low cohesion soil (MC1_Imp_AD3) with full compensation of the water pressure is relatively far from the curves considering advance under atmospheric pressure. More specifically, the consolidation process is slower and the advance rate, at which practically drained conditions are reached, is lower in the case of excavation with full compensation of the water pressure than for excavation under atmospheric pressure. A possible explanation is that, in the case of advance with full compensation of the water pressure, the tunnel face and unlined tunnel walls behave like impervious surfaces and, consequently, the water must move far from the tunnel to dissipate the excess pore pressures and it could require longer consolidation times.

7.5.2 MCC model

For the same examples as in Section 7.4.2, Figures 7.20-7.26 show (analogously to Figures 7.11-7.17) the longitudinal profile of the surface settlements (Figures 7.20a, 7.21a and 7.22a), the transversal profiles of the surface settlements in a cross section 4 m behind the face (Figures. 7.20b, 7.21b and 7.22b), the long term settlements (Figures 7.20c, 7.21c and 7.22c), the spatial distribution of the water pressure in the longitudinal vertical cross section of the tunnel (Figures 7.23 and 7.24), the longitudinal profiles of the surface settlements after standstills of different duration (Figures 7.25 and 7.26).

Figures 7.20, 7.21, 7.23 and 7.25 consider advance under atmospheric pressure (either with a pervious or an impervious lining) in a highly overconsolidated soil (MCC2), while Figures 7.22, 7.24 and 7.26 assume a slightly overconsolidated soil (MCC1), advance with full compensation of the water pressure and support by an impervious lining.

The effect of the *v*/*k*-ratio on the surface settlements and pore pressures during advance and standstills, is the same as for MC soils (compare Figures 7.20-7.26 with Figures 7.11-7.17).

Section 7.5.1 (MC analyses; Fig. 7.12a) showed that for very high *v*/*k*-ratios the ground response close to the tunnel face was more favorable than the undrained one, i.e. the predicted settlements were lower. Although this aspect does not appear in Figures 7.20-7.23, it was observed also for some examples with MCC soils (Fig. 7.28).

For low *v*/*k*-ratios, settlements far behind the face are greater than the steady-state ones (Fig. 7.21a). This behaviour was observed also for MC soils (although this aspect does not appear in Figure 7.12a) and also for elastic soils [13].

Figure 7.27 shows (analogously to Fig. 7.18) the vertical settlement of a control point of the surface in the vicinity of the tunnel face (the same point as in Figure 7.18) as a function of the ratio *v*/*k* for all computational examples (assuming MCC soil) of the present study (see Table 7.3).

In order to facilitate a comparison, the results are represented in four diagrams that consider various surface consolidation pressures, critical state line slopes *M*, swelling line slopes and advance modes. The results for pervious and impervious linings are presented using continuous and dashed lines, respectively.

As shown in Section 7.2.1.2 the pre-excavation lateral earth pressure coefficient K_0 and thus the (equivalent) Young's modulus E^* increases with increasing consolidation pressure σ_{OC} and decreasing critical stress ratio *M*. At the same time the yield strength increases with increasing σ_{OC} and *M*. These facts explain why the surface settlements for σ_{OC} = 600 kPa are smaller than those for σ_{OC} = 300 kPa in Figure 7.27a and may explain why the settlements for *M* = 0.98 are smaller than the ones for *M* = 1.42 in Figure 7.27b (considering that yielding around the tunnel is restricted, the elastic response can be dominant).

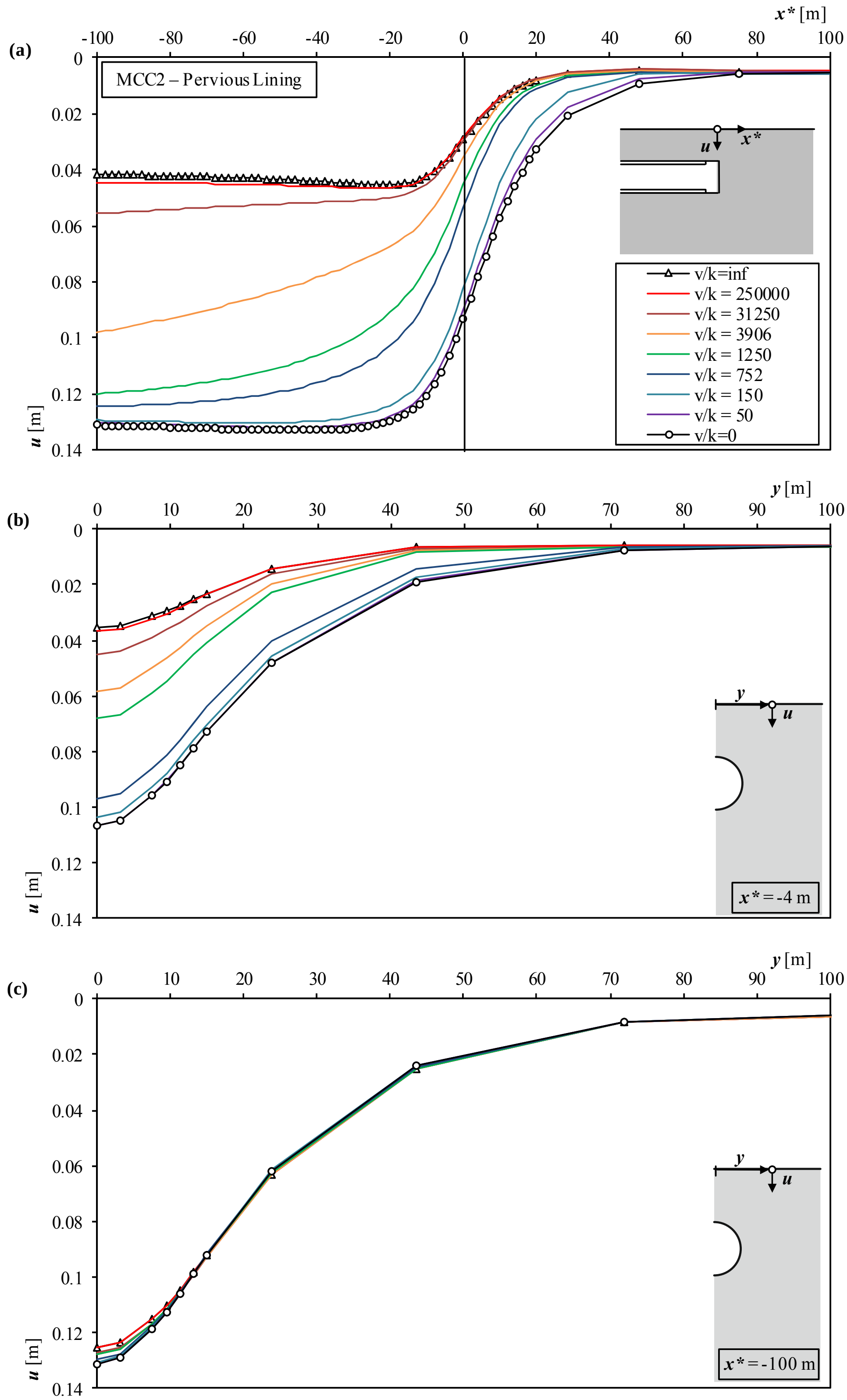

Figure 7.20 *(a), Longitudinal profile of the surface settlements, (b), transversal profile of the surface settlements in a cross section 4 m behind the face and (c), final settlements for advances at atmospheric pressure with pervious lining (soil MCC2, parameters according to Table 7.2).*

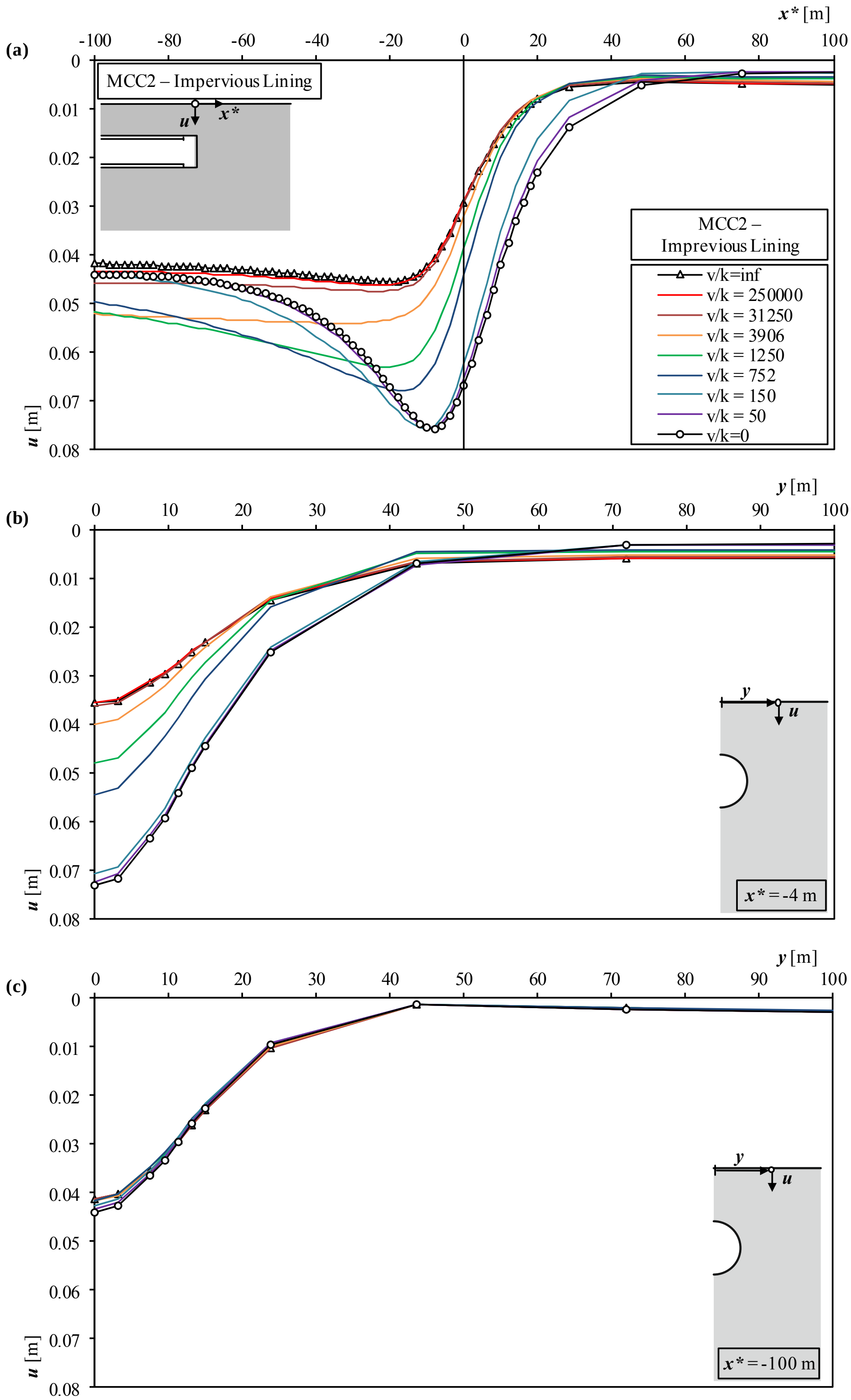

Figure 7.21 *(a), Longitudinal profile of the surface settlements, (b), transversal profile of the surface settlements in a cross section 4 m behind the face and (c), final settlements for advances at atmospheric pressure with impervious lining (soil MCC2, parameters according to Table 7.2).*

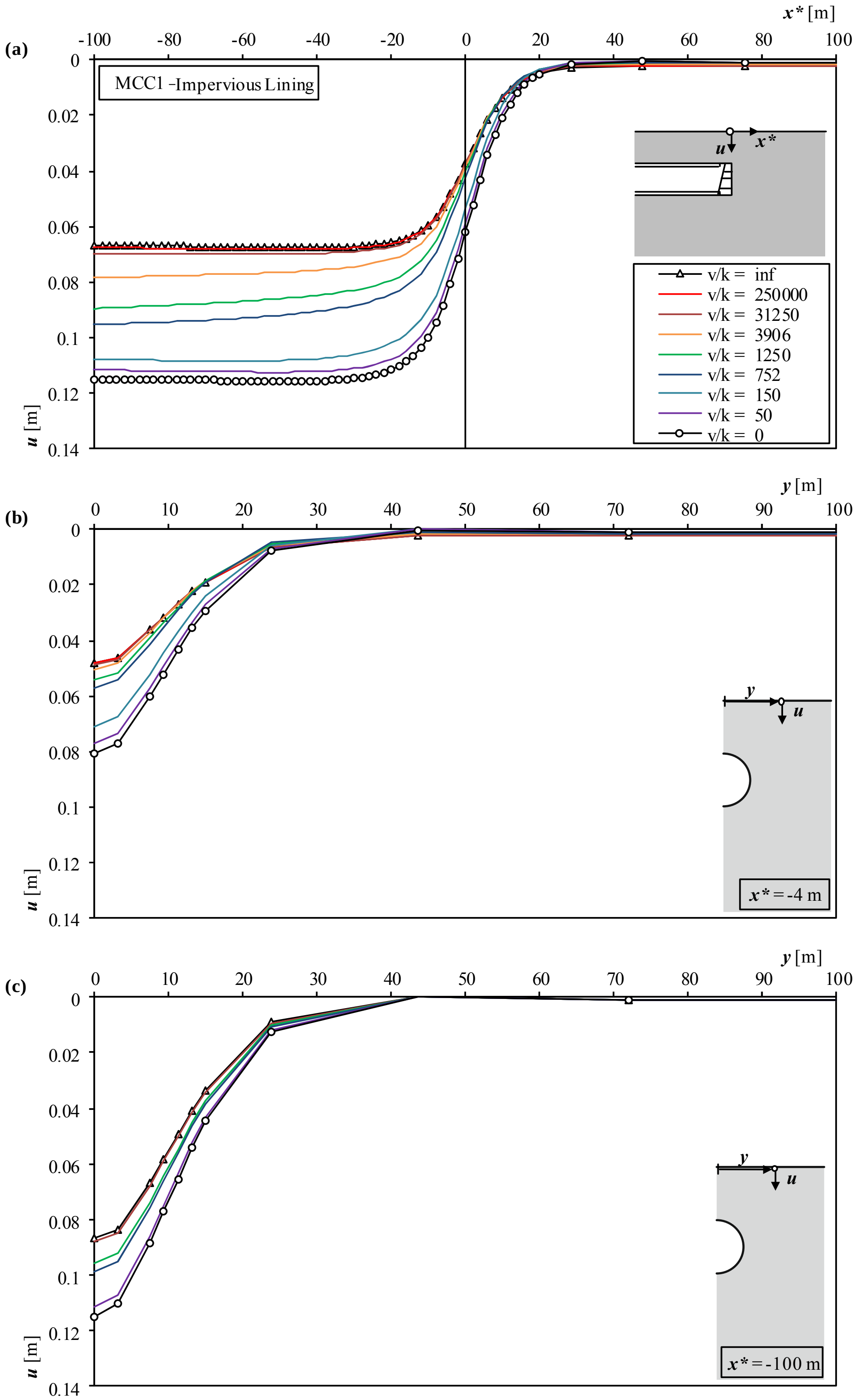

Figure 7.22 *(a), Longitudinal profile of the surface settlements, (b), transversal profile of the surface settlements in a cross section 4 m behind the face and (c), final settlements for advances with full compensation of the water pressure and impervious lining (soil MCC1, parameters according to Table 7.2).*

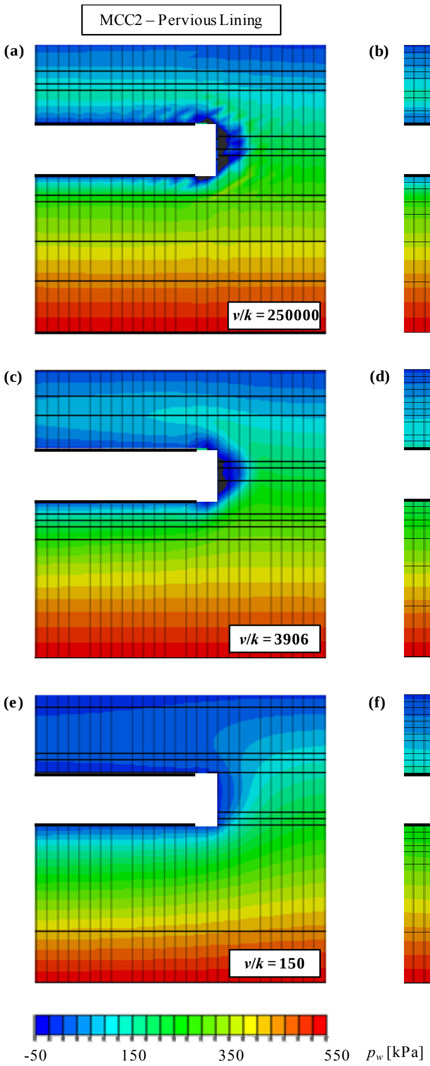

Figure 7.23 *Spatial distribution of the water pressure during advance at atmospheric pressure with pervious (l.h.s) and impervious (r.h.s) lining (soil MCC2, parameters according to Table 7.2).*

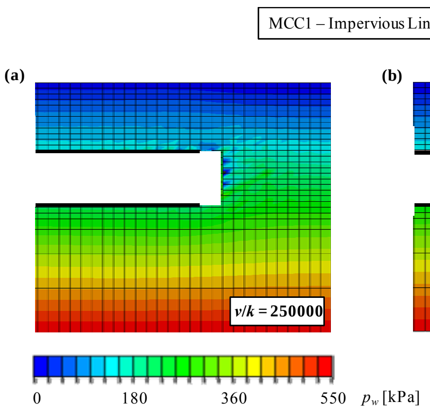

Figure 7.24 *Spatial distribution of the water pressure during advance with full compensation of the water pressure and impervious lining (soil MCC1, parameters according to Table 7.2).*

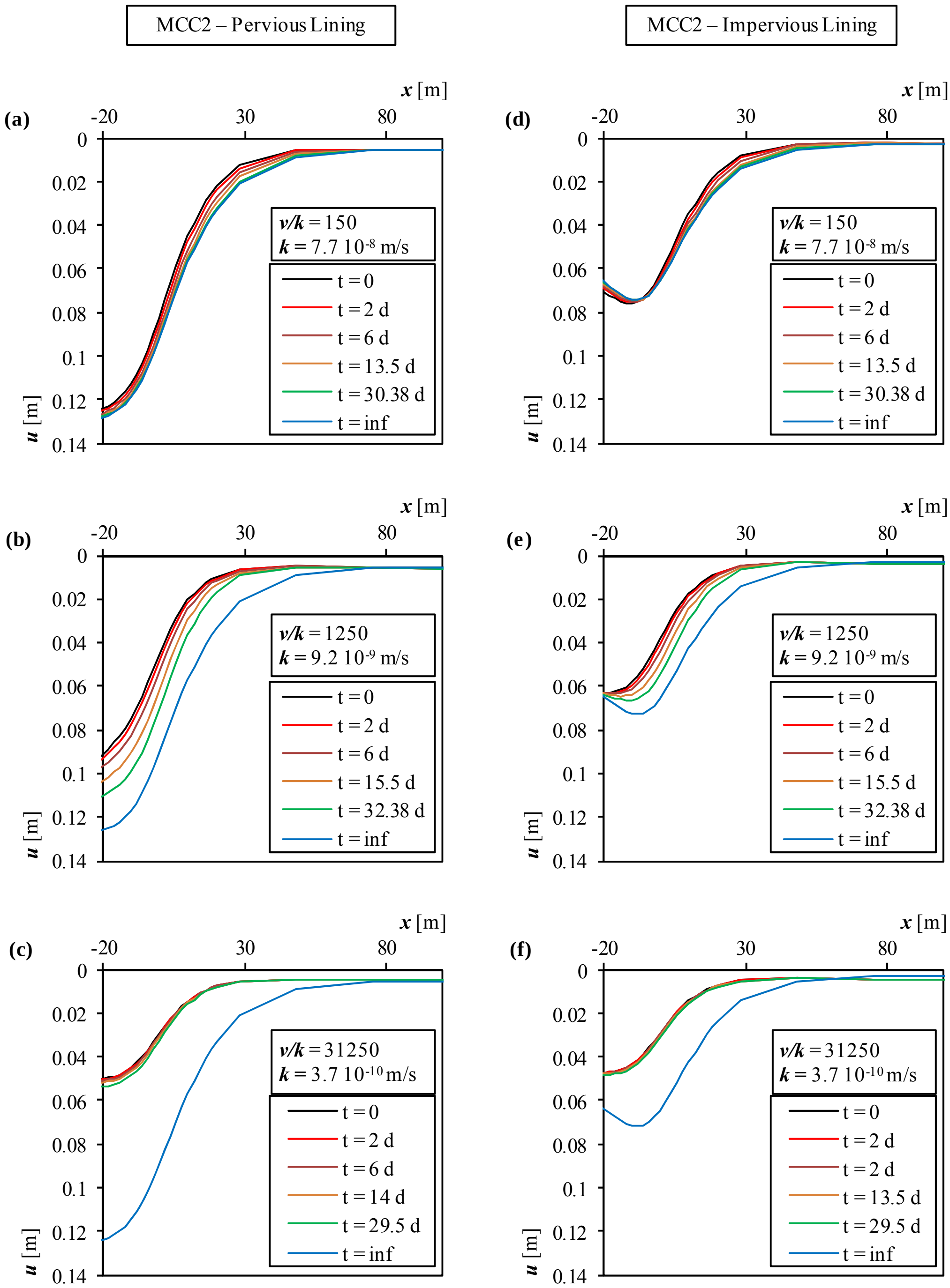

***Figure 7.25** Longitudinal profiles of the surface settlements during standstill at several time points for advances at atmospheric pressure with pervious (l.h.s) and impervious (r.h.s) lining (soil MCC2, parameters according to Table 7.2).*

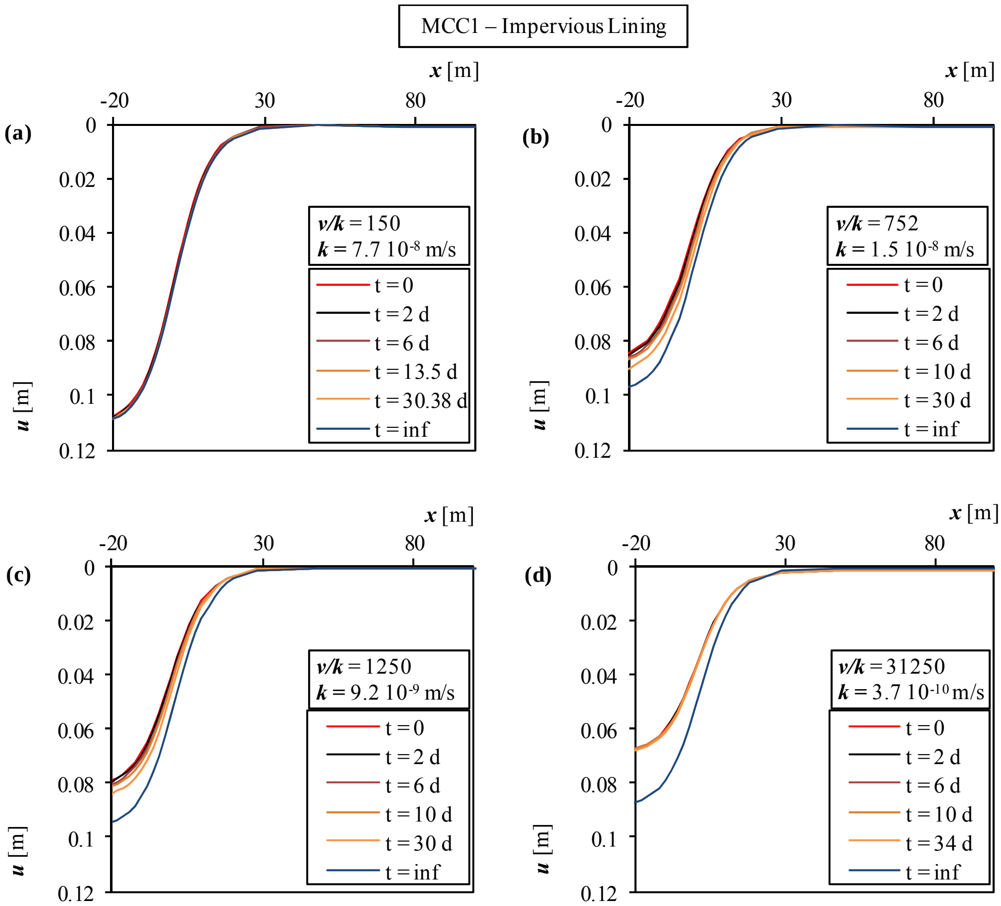

***Figure 7.26** Longitudinal profiles of the surface settlements during standstill at several time points for advances with full compensation of the water pressure and impervious lining (soil MCC1, parameters according to Table 7.2).*

As the Young modulus E^* is inversely proportional to the slope of the swelling line (Section 7.2.1.2), the surface settlements increase with increasing κ (Figure 7.27c). Under atmospheric pressure (and even if the face is supported) the surface settlements are one order of magnitude higher than the settlements developing in the case of full compensation of the water pressure.

Figure 7.28 shows (for the same control point as Fig. 7.27) the normalized surface settlement u^* as a function of the dimensionless velocity $v\gamma_w D/kE^*_a$. The limits for practically undrained response, for practically drained response and for significant transient conditions are almost the same as for MC soils.

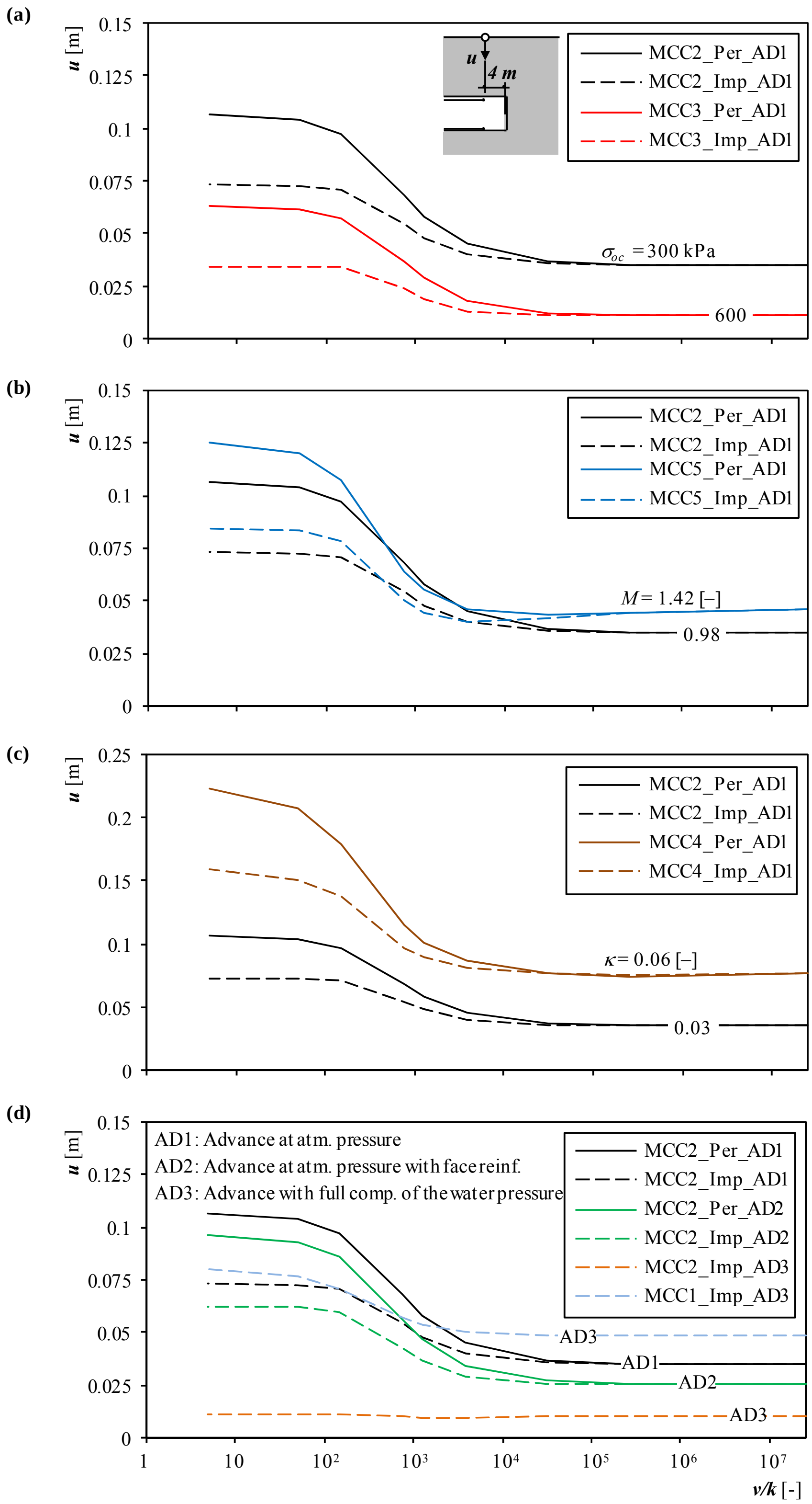

***Figure 7.27** Surface settlement of a point located 0.4D behind the tunnel face as a function of v/k-ratio for different sets of ground parameters and advance modes, for pervious and impervious lining (MCC-sets of parameters according to Table 7.2).*

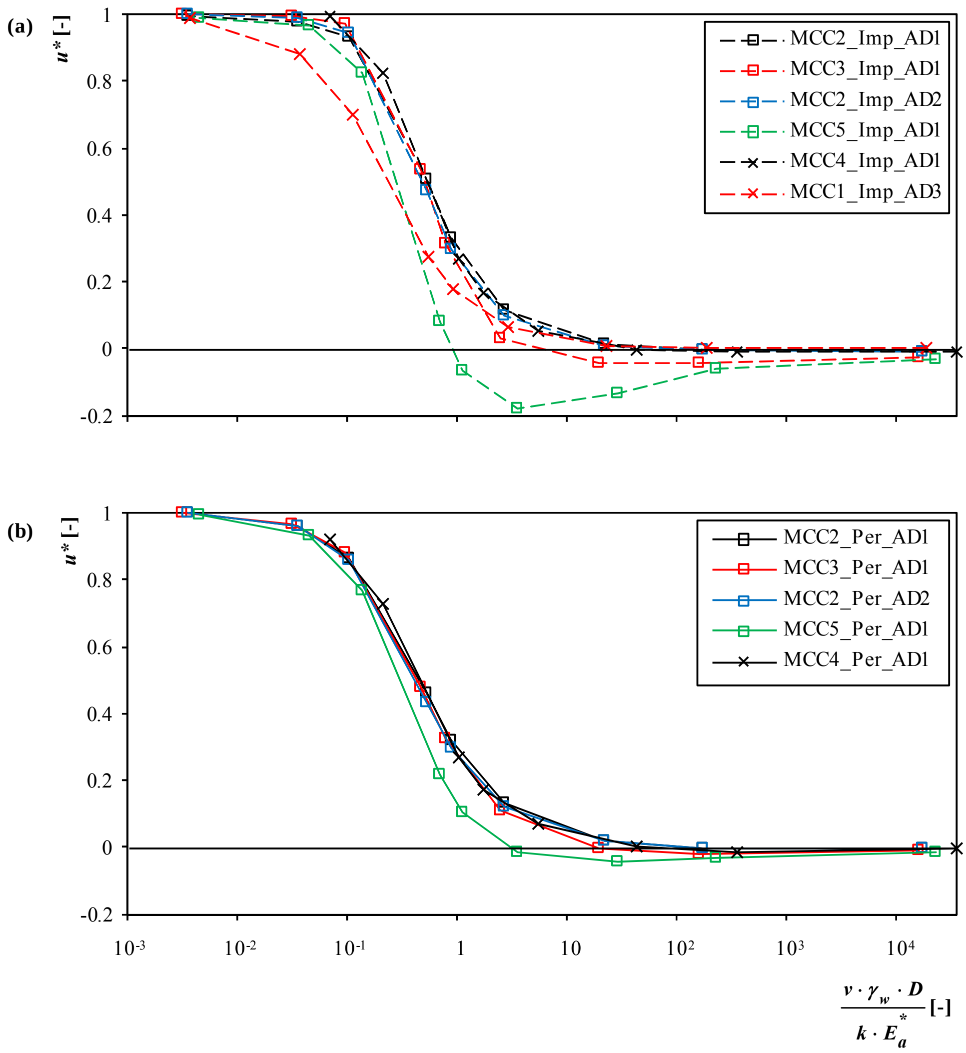

Figure 7.28 *Normalized surface settlement u* of a point located 0.4D behind the tunnel face as a function of dimensionless velocity for (a) impervious lining and (b) pervious lining in MCC soils (MCC-sets of parameters according to Table 7.2).*

7.6 Practical estimation of transient settlements

Figure 7.29 shows the normalized displacement *u** as a function of the dimensionless advance rate for all the computational examples of the present study, assuming advance at atmospheric pressure. The results of Figure 7.29 can be used together with the settlements computed under the simplest assumptions of undrained and drained excavation for a preliminary and quick assessment of the surface transient settlement in the vicinity of the face:

$$u = u_{undr} + u^*(u_{dr} - u_{undr}). \tag{7.17}$$

The factor *u** depends on the dimensionless advance rate and can be evaluated according to the following equation (see red curve in Figure 7.29):

$$u^* = \exp\left(-\frac{v\gamma_w D}{6kE_{eq}}\right), \tag{7.18}$$

where E_{eq} is the Young's modulus for a MC soil and the initial elastic stiffness at the tunnel axis for a MCC soil (see Eq. 7.10). The proposed equation does not account for the negative values of u*, which arise under certain conditions (see Section 7.5.1 as well as Fig. 7.29). In such cases Eq. (7.18) is conservative.

Eq. (7.18) is useful from a practical point view as it allows for a quick estimation of the transient settlements developing during excavation above the face in medium permeability soils based upon the settlements developing under undrained or drained conditions. The latter can be estimated by means of relatively simple numerical analyses, represent a lower and an upper limit, respectively, of the transient settlement and, as shown by the performed analyses, can be different by a factor of 1.5÷3.

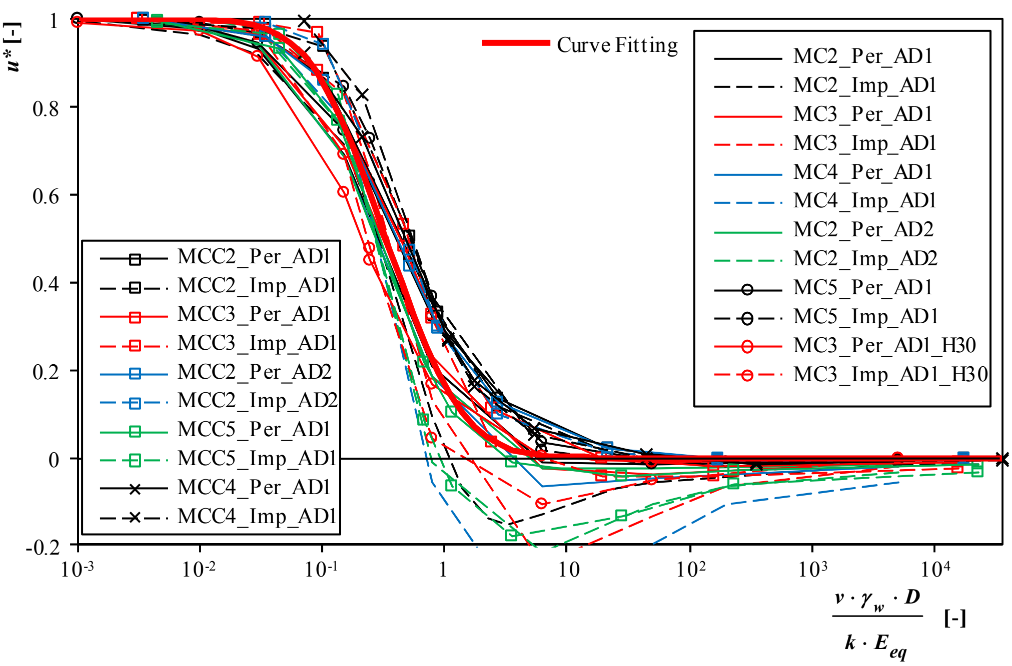

Figure 7.29 *Normalized surface settlement u* of a point located 0.4D behind the tunnel face as a function of dimensionless velocity for advances at atmospheric pressure considering impervious and pervious lining, MC and MCC soil models (MC and MCC sets of parameters according to Tables 7.1 and 7.2).*

7.7 Conclusions

The present computations have highlighted the role played by the drainage conditions at the tunnel boundary and the tunnel face in the control of tunnelling-induced settlements. Specifically:

(1) Seepage flow toward a pervious lining induces a long-term pore pressure distribution around the tunnel, which is significantly different from the initial hydrostatic one and may lead to relatively large deformations and surface displacements. When high pore pressures are expected at the excavation depth, the water drainage through the lining must be avoided even if this might result to higher lining loads.

(2) If the permeability of the ground is high (and, consequently, drained conditions are expected during advance), compensation of the water pressure may be indispensable for settlement limitation even in soils of relatively high shear strength exhibiting stable face behaviour. Comparative calculations show that, for the same geotechnical conditions, the settlements developing under full compensation of the water pressure can be one order of magnitude smaller than those occurring during advance at atmospheric pressure.

(3) The relevance of the transient conditions on the tunnelling-induced surface settlements was highlighted. In the case of a rapid excavation with short standstills only a limited time is available to the consolidation process in the vicinity of the advancing face and, consequently, only small consolidation-induced surface settlements occur.

(4) The conditions around the advancing face (drained, undrained or transient) affect also quantitatively the longitudinal and transversal settlement profiles close to the face independently of the lining permeability.

(5) Based upon a series of parametric studies with the MC and MCC models, considering several soil parameters, overburdens and hydraulic conditions at the tunnel walls (i.e. pervious or impervious lining), we can conclude that for tunnels excavated at atmospheric pressure, the conditions in the vicinity of the face are practically undrained as long as $v\gamma_w D/kE_{eq} > 10^3$ and practically drained as long as $v\gamma_w D/kE_{eq} < 10^{-2}$, while transient conditions are significant when $v\gamma_w D/kE_{eq}$ is between 0.1 and 100.

(6) A simple equation for estimating settlements under transient conditions based upon the results of relatively simple drained and undrained analyses has been developed.

Notation

b	Width of the sample
c, c'	Cohesion
$c'_{D,lim}$	Limit cohesion under drained condition
$c_{u,lim}$	Limit cohesion under undrained condition
c_w	Water compressibility
D	Diameter of the tunnel
e	Void ratio
E	Young's Modulus of MC soils
E^*	Pre-excavation value of the elastic stiffness of MCC soils (Eq. 7.10)
E^*_a	Pre-excavation value of the elastic stiffness of MCC soils at the depth of tunnel axis
e_0	Initial void ratio
e_1	Intercept of the compression line
E_{eq}	Equivalent Young's Modulus
E_l	Young's Modulus of the lining
f_t	Tensile resistance
$g, n{\cdot}g$	Ground acceleration, centrifugal acceleration
h	Height of model scale
H	Overburden
H_w	Water table above the tunnel crown
i, j, m	Dummy index
I_P	Plasticity index
k	Coefficient of permeability
K_0	Lateral pressure coefficient
l_u	Installation distance of the lining
M	Slope of the critical state line
n	Porosity
n_0	Initial porosity
N_1	Normalized face advancement rate
N_s	Stability number.
OCR	Over-consolidation ratio
p, p'	Mean effective and total stress
p'_0	Initial absolute value of the mean effective stresses
p'_c	Preconsolidation pressure
p'_{c0}	Initial preconsolidation pressure
p_s, p'_s	Total and effective support pressure

p_w	Pore pressure
p_{w0}	Initial pore pressure
q	Deviatoric stress
q_n	Normal flow
q_v	Vertical load
q_w	Water flow
q_x	Water flow in x-direction
q_y	Vertical flow in y-direction
r	Radial distance
s	Mesh size
s_u	Undrained shear strength
s_x, s_y	Boundary traction
t	Time
t_∞	Time at the end of the consolidation process
t_l	Lining thickness
T_s	Dimensionless stand-up time
t_s	Stand-up time
u	Displacement
$U(t_s)$	Consolidation degree
u^*	Normalized surface settlement
$u_{A,x}$	Horizontal displacement at point A
$u_{A,y}$, $u_{A,y}$	Vertical displacement at point A
u_{dr}	Settlement under drained conditions
u_{undr}	Settlement under undrained conditions
u_x	Horizontal displacement
u_y, u_z	Vertical displacement
$u_{z,0}$	Initial vertical displacement
v	Advance rate
v	Velocity vector of the sliding wedge (tangential to the shear band)
v^*	Normalized advance rate
v_{cr}	Critical advance rate
w_l	Liquid limit
w_p	Plastic limit
x^*	Distance from the tunnel face
x, y, z	Coordinates
x_{Face}	Position of the tunnel face
z^*	Depth
Δt	Time increment

Δz_k	Thickness of the layer in Eq. 7.7

Greek symbols

Φ	Water potential
ε^{el}_{vol}	Elastic component of the volumetric strain
ε^{pl}_{eq}	Equivalent plastic strain
ε^{pl}_{vol}	Plastic component of the volumetric strain
ε_{vol}	Volumetric strain
ε_{xy}	Shear strain
γ	Saturated unit weight
γ'	Submerged unit weight of the ground
γ_d	Dry unit weight
γ_w	Unit weight of water
η	Reduction factor
φ, φ'	Effective friction angle
κ	Slope of the swelling line in the semi-logarithmic compression plane
λ	Slope of the compression line in the semi-logarithmic compression plane
ν	Poisson's ratio
ν_l	Poisson's ratio of the lining
θ	Inclination of the sliding plane
θ_L	Lode's angle
σ'_{max}	maximum effective stress
σ_{n0}, σ'_{n0}	Initial total and effective stress normal to the tunnel face
σ_n, σ'_n	Total and effective normal stress
σ_{OC}	Overconsolidation pressure
σ_v , σ'_v	Total and effective vertical stress
σ_{x0}, σ'_{x0}	Initial horizontal total and effective stress
σ_x, σ'_x	Total and effective horizontal stress (2D, 3D)
σ_{y0}, σ'_{y0}	Initial total and effective vertical stress
σ_y, σ'_y	Total and effective vertical stress (2D) / horizontal transversal stress (3D)
σ'_z	Total and effective vertical stress (3D)
σ'_{z0}	Initial vertical effective stress
ω	Angular speed
ψ	Dilation angle
ζ	Ratio between lining and soil permeability

References

[1] Atkinson, J.H., Mair, R.J. (1981). Soil mechanics aspects of soft ground tunnelling. Ground Eng. 14, No. 5, 20–28.

[2] Sevaldson, R.A. (1956). The slide in Lodalen, October 6th, 1954. *Géotechnique* **6**, No. 4, 167–182.

[3] Skempton, A.W. (1964). Long-term stability of clay slopes. *Géotechnique* **14**, No. 2, 77–101.

[4] Skempton, A.W. (1977). Slope stability of cuttings in brown London Clays. *Proc. 9th int. conf. on Soil Mechanics and Foundation Engineering*, 261–270, Tokyo.

[5] Vaughan, P.R., Walbancke, H.J. (1973). Pore pressure changes and the delayed failure of cutting slopes in overconsolidated clay. *Géotechnique* **23**, No. 4, 531–539.

[6] Hughes, D., Sivakumar, V., Glynn, D., Clarke, G. (2007). A case study: delayed failure of deep cutting in lodgement till. *Geotechnical Engineering* **160**, No. 4, 193–202.

[7] Potts, D.M., Kovacevic, N., Vaughan, P.R. (1997). Delayed collapse of cut slopes in stiff clay. *Géotechnique* **47**, No. 5, 953–982.

[8] Lollino, P., Santaloia, F., Amorosi, A., Cotecchia, F. (2011). Delayed failure of quarry slopes in stiff clays. *Géotechnique* **61**, No. 10, 861–874.

[9] Ellis, E.A., O'Brien, A.S. (2007). Effect of height on delayed collapse of cuttings in stiff clay. *Geotechnical Engineering* **160**, No. 2, 73–84.

[10] Davis, E.H., Gunn, M.J., Mair, R.J., Seneviratne, H.N. (1980). The stability of shallow tunnels and underground openings in cohesive material, *Géotechnique* **30**, No. 4, 397–416.

[11] Shahin, H.M., Nakai, T. (2005). Finite element analysis of 3D full scale tunnel excavation using subloading t_{ij} model. *Pipelines 2005*. 101–115.

[12] Callari, C., Casini, S. (2005). Three-dimensional analysis of shallow tunnels in saturated soft ground. In: *Geotechnical Aspects of Underground Construction in Soft Ground.* Taylor & Francis, 2006, 495–501.

[13] Anagnostou, G. (2008). The Effect of Tunnel Advance Rate on the Surface Settlements. In: *Proc. 12th IACMAG*, 579–586, Goa.

[14] Höfle, R., Fillibeck, J., Vogt, N. (2008) Time dependent deformations during tunnelling and stability of tunnel faces in fine-grained soils under groundwater. *Acta Geotech* **3**, 309–316.

[15] Callari, C. (2009). Three-dimensional Effects of Ground Desaturation due to Tunneling. In: *Proc. EURO: TUN 2009, 2nd International ECCOMAS Conference on Computational Methods in Tunneling* 517–524, Bochum.

[16] Sterpi, D. (1999). An analysis of geotechnical problems involving strain softening effects. *Int J. Numer. Anal. Meth. Geomech.* **23**, 1427–1454.

[17] Davis, E.H. (1968). Theories of plasticity and the failure of soil masses. In: *Soil Mechanics: Selected Topics*, (Editor: I. K. Lee), Butterworths, London, 341–380.

[18] O'Reilly, M.P., Mair, R.J., Alderman, G.H. (1991). Long-term settlements over tunnels: an eleven-year study at Grimsby. In: *Proc: of Tunneling '91 symposium, Institute of Mining and Metallurgy*, 1991 London, 55–64

[19] Bowers, K.H., Hiller, D.M., New, B.M. (1996). Ground movement over three years at the Heathrow Express Trail Tunnel. In: *Geotechnical aspects of underground construction in soft ground*. Mair & Taylor, Balkema, Rotterdam, 1996, 647–652.

[20] Wongsaroj, J. (2005). Three-dimensional finite analysis of short- and long-term ground response to open face tunnelling in stiff clay. Ph.D Thesis, Cambridge University.

[21] Wongsaroj, J., Soga, K., Mair, R.J. (2013). Tunneling-induced consolidation settlements in London Clay. *Géotechnique* **63**, No. 13, 1103–1115.

[22] Kasper, T., Meschke, G. (2006). A numerical study of the effect of soil and grout material properties and cover depth in shield tunnelling. . *Computers and Geotechnics* **33**, 234–247.

[23] Shin, J.H., Addenbrooke, T.I., Potts, D.M. (2002). A numerical study of the effect of groundwater movement on long-term tunnel behaviour. *Géotechnique* **52**, No. 6, 391–403.

[24] Culmann, C. (1875). *Die graphische Statik*. Meyer & Zeller, Zurich.

[25] Taylor, D.W. (1937). Stability of earth slopes. *J. Boston Soc. Civ. Engng* **24**, No. 3, 197–246.

[26] Bishop, A.W. (1955). The use of the slip circle in the stability analysis of slopes. *Géotechnique* **5**, No. 1, 7–17.

[27] Michalowski, R.L. (2002). Stability charts for uniform slopes. *J. Geotech. Geoenviron. Engng.* **128**, No. 4, 351–355.

[28] Anagnostou, G., Kovári, K. (1994). The face stability of slurry-shield driven tunnels. *Tunn. Undergr. Space Technol.* **9**, No. 2, 65–174.

[29] Eisenstein, Z., Samarasekera, L. (1992). Stability of unsupported tunnels in clay. *Can. Geotech. J.* **29**, 609–613.

[30] Bjerrum, L., Kjaernsli, B. (1957). Analysis of the stability of some Norwegian natural clay slopes. *Géotechnique* **7**, No. 1, 1–16.

[31] Banerjee, P.K., Kumbhojkar, A.S., Yousif, N.B. (1988). Finite element analysis of the stability of a vertical cut using an anisotropic soil model. *Can. Geotech. J.* **25**, 119–127.

[32] Borges, J.L. (2008). Cut slopes in clayey soils: consolidation and overall stability by finite element method. *Geotech. Geol. Engng.* **26**, 479–491.

[33] Holt, D.A., Griffiths, D.V. (1992). Transient analysis of excavation in soil. *Comput. Geotech.* **13**, No. 2, 159–174.

[34] Griffiths, D.V., Li, C.O. (1993). Analysis of delayed failure in sloping excavations. *J. Geotech. Eng.* **119**, No. 9, 1360–1378.

[35] Kovacevic, N., Hight, D.W., Potts, D.M. (2007). Predicting the stand-up time of temporary London Clay slopes at Terminal 5, Heathrow Airport. *Géotechnique* **57**, No. 1, 63–74.

[36] Kirkebø, S. (1994). *A numerical study of excavation in low permeable soils*. Dr. Ing. thesis Dept. of geotechnical Eng., The Norwegian Institute of Technology.

[37] Sanavia, L. (2009). Numerical modelling of a slope stability test by means of porous media mechanics. *Engng Computation.* **26**, No. 3, 245–266.

[38] Vermeer, P.A., Van Langen, H. (1989). Soil collapse computations with finite elements. *Ing. Archiv* **59**, No. 3, 221–236.

[39] Kovacevic, N. (1994). Numerical analyses of rock fill dams, cut slopes and road embankments. Ph.D. thesis, University of London.

[40] Griffiths, D.V. (1989). Computation of collapse loads in geomechanics by finite elements. *Ing. Archiv* **59**, 237–244.

[41] Griffiths, D.V., Lane, P.A. (1999). Slope stability analysis by finite elements. *Géotechnique* **49**, No. 3, 387–403.

[42] Griffiths, D.V., Hicks, M.A., Li, C.O. (1991). Transient passive earth pressure analyses. *Géotechnique* **41**, No. 4, 615–620.

[43] Ng, C.W.W., Lee, G.T.K. (2002). A three-dimensional parametric study of the use of soil nails for stabilizing tunnel faces. *Computers and Geotechnics* **29**, 673–697.

[44] Callari, C. (2015). Numerical assessment of tunnel face stability below the water table. In: *Proc. 14th IACMAG*, 2007–2010, Kyoto.

[45] Vaughan, P.R. (1994). Assumption, prediction and reality in geotechnical engineering. *Géotechnique* **44**, No. 4, 573–609.

[46] Potts, D.M., Zdravković, L.T. (2001b). *Finite element analysis in geotechnical engineering: Application*. Thomas Telford Limited, London.

[47] Kovacevic, N., Miligan, G.W.E., Menkiti, C.O., Long, M., Potts, D.M. (2008). Finite element analyses of steep man-made cuts in Dublin boulder clay. *Can. Geotech. J.* **45**, No. 4, 549–559.

[48] Kovacevic, N., Jardine, R.J., Potts, D.M., Clukey, C.E., Brand, R.J., Spikula, D.R. (2012). A numerical simulation of underwater slope failures generated by salt diapirism combined with active sedimentation. *Géotechnique* **62**, No. 9, 777–786.

[49] Höfle, R., Fillibeck, J., Vogt, N. (2009). Time depending stability of tunnel face. In: *Proc. 35th ITA–AITES General Assembly*, Budapest.

[50] Sitarenios, D.L., Kavvadas, M. (2016). The interplay of face support pressure and soil permeability on face stability in EPB tunneling. In: *Proc. WTC,* 2016, San Francisco.

[51] Cooper, M.R., Bromhead, E.N., Petley, D.J., Grant, D.I. (1998). The Selborne cutting stability experiment. *Géotechnique* **48**, No. 1, 83–101.

[52] Davies, M.C.R. (1985). Centrifuge model of an embankment failure. In: *Proc. Failure in earthworks*. Thomas Telford Ltd, 451–453, London.

[53] Deepa, V., Viswanadham, V.S. (2009). Centrifuge model tests on soil-nailed slopes subjected to seepage. *Ground improvement* **162**, No. 13, 133–144.

[54] Franzius, J. N., Potts, D. M. (2005). Influence of mesh geometry on three-dimensional finite-element analysis of tunnel excavation. *Int. J. Geomech.*, 5(3), 256–266.

[55] Stallebrass, S.E., Jovičić, V., Taylor, R.N. (1994). Short-term and long-term settlement around a tunnel in stiff clay. *Numerical Method in Geotechnical Engineering, Smith, I.M. (eds)*, Balkema, Rotterdam, 235–240.

[56] Wongsaroj, J., Soga, K., Mair, R.J. (2007). Modelling of long-term ground response to tunnelling under St James's Park, London. *Géotechnique* **57**, No. 1, 75–90.

[57] Cattoni, E., Miriano, C., Boco, L., Tamagnini, C. (2016). Time-dependent ground movements induced by shield tunneling in soft clay: a parametric study. *Acta Geotech.* **11**, No. 6, 1385–1399.

[58] Mair, R.J. (2008). Tunnelling and geotechnics: new horizons. *Géotechnique* **58**, No. 9, 695–736.

[59] Schuerch, R., Anagnostou, G. (2012). Tunnel face stability under transient conditions: stand-up time in low permeability ground. In: *Proceedings of the 22nd European Young Geotechnical Engineers Conference*, Gothenburg.

[60] Schuerch, R., Anagnostou, G. (2013a). Analysis of the stand-up time of the tunnel face. *In Proc. ITA-AITES World Tunnel Congress*, *WTC,* 2013, Geneva.

[61] Schuerch, R., Anagnostou, G. (2013b). The influence of the shear strength of the ground on the stand-up time of the tunnel face. In: *Proc. TU-Seoul 2013 International Symposium on Tunnelling and Underground Space Construction for Sustainable Development*, Seoul.

[62] Schuerch, R., Anagnostou, G. (2015a). Delayed failure identification by coupled hydraulic-mechanical numerical analyses. In: *Proc. 14th IACMAG*, 1061–1066, Kyoto.

[63] Schuerch, R., Anagnostou, G. (2015b). Failure propagation and mesh-dependency in coupled hydraulic-mechanical transient problems. In: *Proc. 14th IACMAG*, 329–334, Kyoto.

[64] Schuerch, R., Poggiati, R., Anagnostou, G. (2016). Design diagrams for estimating tunnel face stand-up time in water-bearing ground. In: *Proc. WTC*, 2016, San Francisco.

[65] Schuerch, R. (2016). On the delayed failure of geotechnical structures in low permeability ground. Ph.D Thesis Nr. 23681, ETH Zurich.

[66] Dassault Systèmes (2012). Abaqus 6.12, *Theory and Analysis User's Manual.*

[67] Clausen, J., Damkilde, L., Andersen, L. (2007). An efficient return algorithm for non-associated plasticity with linear yield criteria in principal stress space. *Computers and Structures* **85**, No. 23–24, 1795–1807.

[68] Wehnert, M. (2006). *Ein Beitrag zur drainierten und undrainierten Analyse in der Geotechnik*. Universität Stuttgart, Mitteilung 53 des Instituts für Geotechnik.

[69] Drescher, A., Detournay, E. (1993). Limit load in translational failure mechanisms for associative and non-associative materials. *Géotechnique* **43**, No. 3, 443–456.

[70] Lambe, T.W., Whitman, R.V. (1979). *Soil mechanics - SI version*. Chichester: John Wiley.

[71] Rice, J.R. (1975). On the stability of dilatant hardening for saturated rock masses. *J. Geophys. Res.* **80**, 1531–1536.

[72] Han, C., Vardoulakis, I. (1991). Plane-strain compression experiments on water-saturated fine-grained sand. *Géotechnique* **41**, No. 1, 49–78.

[73] Atkinson, J.H., Bransby, P.L. (1978). *The mechanics of soils*. McGraw-Hill Book Company (UK).

[74] Weber, T.M. (2007). *Modellierung der Baugrundverbesserung mit Schottersäulen*. Ph.D Thesis Nr. 17321, ETH Zurich.

[75] Jardine, R.J. Potts, D.M., Fourie, A.B., Burland, J.B. (1986). Studies of the influence of non-

linear stress-strain characteristics in soil-structure interaction. *Géotechnique* **36**, No. 3, 377–396.

[76] Potts, D.M., Zdravković, L.T. (2001a). *Finite element analysis in geotechnical engineering: Theory*. Thomas Telford Limited, London.

[77] Lambe, T.W. (1973). Predictions in soil engineering. *Géotechnique* **23**, No. 2, 149–202.

[78] Springman, S.M., Laue, J., Boyle, R., White, J., Zweidler, A. (2001). The ETH Zürich Geotechnical drum centrifuge. *International Journal of Physical Modelling in Geotechnical Engineering* **1**, No.1, 59 – 70.

[79] Schofield, A.N. (1980). Cambridge geotechnical centrifuge operations. *Géotechnique* **30**, No. 3, 227–268.

[80] Vermeer, P.A. (1990). The orientation of shear bands in biaxial tests. *Géotechnique* **40**, No. 2, 323–336.

[81] Gudehus, G. (1973). Elastoplastische Stoffgleichungen für trockenen Sand. *Ingenieur Archiv* **42**, 151–169.

[82] Jaky, J. (1948), Pressure in silos, The 2nd International Conference on Soil Mechanics and Foundation Engineering, **1**, 103 – 107.

[83] Shin, J.H., Potts, D.M., Zdravković, L.T. (2005). The effect of pore-water pressure on NATM tunnel linings in decomposed granite soil. *Canadian Geotechnical Journal* **42**, 1585-1599.

[84] Perazzelli, P., Leone, T., Anagnostou, G. (2014). Tunnel face stability under seepage flow conditions. *Tunnelling and Underground Space Technology* **43**, 459–469.

[85] Berg, C.A. (1972). A note on construction of the equivalent plastic strain increment. *Journal of Research* **76**, 197–213.

[86] Clausen, J., Damkilde, L., Andersen, L., (2005). An efficient return algorithm for non-associated Mohr-Coulomb plasticity. In: *Proc.10th Int. Conf. Civil, Structural and Environmental Engineering Computing*, United Kingdom.

[87] Vermeer, P.A., Ruse, N. (2001). Die Stabilität der Tunnelortsbrust in homogenem Baugrund. *Geotechnik* **24**, No. 3, 186–193.

[88] Broms, B.B., Bennermark, H. (1967). Stability of vertical openings. *Journal of the Soil Mechanics and Foundations Division* **93**, 71–94.

[89] Anagnostou, G., Perazzelli, P. (2015). Analysis method and design charts for bolt reinforcement of the tunnel face in cohesive-frictional soils. *Tunnelling and Underground Space Technology* **47**, No. 1, 162–181.

[90] Anagnostou, G. (2007). Practical consequences of the time-dependency of ground behaviour in tunnelling. In: *Proc. RETC*, 255–265, Toronto.

[91] Roscoe, K.H., Burland, J.B. (1968). On the generalised stress-strain behaviour of ‘wet’ clay, *Engng Plasticity,* Cambridge Univ. Press, 535–609.

[92] Dias, D., Kastner, R. (2013). Movements caused by the excavation of tunnels using face pressurized shields – Analysis of monitoring and numerical modelling results. *Engineering Geology*, **152**, 17–25

[93] Pinto, F., Whittle, A.J. (2013). Ground Movements due to Shallow Tunnels in Soft Ground. I: Analytical Solutions. *J. Geotech. Geoenviron. Eng.,* 10.1061/(ASCE)GT.1943-5606.0000948, 04013040

[94] Ramoni, M., Anagnostou, G. (2011). The effect of consolidation on TBM shield loading in Water-Bearing squeezing ground. *Rock Mech Rock Eng*., **44**, 63–83.

Projektabschluss

Schweizerische Eidgenossenschaft
Confédération suisse
Confederazione Svizzera
Confederaziun svizra

Eidgenössisches Departement für
Umwelt, Verkehr, Energie und Kommunikation UVEK
Bundesamt für Strassen ASTRA

FORSCHUNG IM STRASSENWESEN DES UVEK

Version vom 09.10.2013

Formular Nr. 3: Projektabschluss

erstellt / geändert am: 06.12.2016

Grunddaten

Projekt-Nr.: FGU 2012/002

Projekttitel: Ortsbruststabilität und Oberflächensetzungen infolge Tunnelvortrieb unter transienten Bedingungen

Enddatum: Dezember 2016

Texte

Zusammenfassung der Projektresultate:

Das vorliegende Forschungsprojekt schliesst Wissenslücken betreffend Ortsbruststabilität und Oberflächensetzungen beim Tunnelbau in wasserführenden Lockergesteinen mittlerer-niedriger Durchlässigkeit. Die Beherrschung der Ortsbrust und die Beschränkung der Geländesetzungen stellen wichtige Voraussetzungen jedes erfolgreichen Tunnelvortriebs im überbauten Gebiet dar. Lockergesteine mittlerer-niedriger Durchlässigkeit kommen beispielsweise oft im Schweizerischen Mittelland vor (Moränen, siltige Ablagerungen). Ein Hauptaspekt ihres Verhaltens ist, dass sie zeit verzögert auf den Tunnelvortrieb reagieren. Ihr kurzfristiges Verhalten ist günstiger als das langzeitige Verhalten: die Setzungen nehmen mit der Zeit zu; die Ortsbrust kann anfänglich stabil sein und erst nach einer gewissen Zeit instabil werden.
Instabile Verhältnisse können eine Baugrundverbesserung oder das Aufbringen eines Stützdrucks erfordern. Da derartige Massnahmen kostspielig, zeitaufwändig und baubetrieblich folgenreich sein können, ist die Frage der Standzeit – definiert als Zeit zwischen Ausbruch und dem Auftreten einer Instabilität – für die Praxis wichtig.
Bei der Durchführung des Projektes sind fundamentale Fragen über die zugrundeliegenden physikalischen Mechanismen und die numerischen Berechnungsverfahren aufgetreten, deren Klärung vertiefte theoretische und experimentelle Untersuchungen erforderten. Mit den theoretischen Untersuchungen konnten jene Aspekte des mechanischen Verhaltens der Lockergesteine identifiziert werden, deren Berücksichtigung für die rechnerische Erfassung des Phänomens einer verzögerten Instabilität unabdingbar ist. Ferner konnte gezeigt werden, wie die Standzeit anhand von numerischen Berechnungen bestimmt werden kann. Mit den experimentellen Untersuchungen wurde festgestellt, dass die numerischen Berechnungsverfahren ausreichend genaue Prognosen erlauben.
Nach dem erfolgreichen Abschluss dieser grundlegenden Untersuchungen wurde das Problem der Standzeit der Ortsbrust systematisch untersucht. Anhand der Ergebnisse einer umfassenden Parameterstudie, eine grosse Bandbreite von geotechnischen Bedingungen abdeckend, wurden dimensionslose Bemessungsdiagramme erstellt. Letztere ermöglichen eine Abschätzung der Standzeit von oberflächennahen Tunnels für eine gegebene geotechnische Situation. Sie stellen somit eine nützliche Entscheidungshilfe für die Planung und die Durchführung von Tunnelvortrieben im Lockergestein dar.

Das zweite Hauptthema des Forschungsprojektes, die transienten Oberflächensetzungen betreffend, wurde durch eine Serie von 3D hydraulisch-mechanisch gekoppelten zeitabhängigen numerischen Analysen untersucht. Je nach Gebirgsdurchlässigkeit und Vortriebsgeschwindigkeit sind die Bedingungen während des Vortriebs undrainiert, drainiert oder teilweise drainiert und die Oberflächensetzungen mehr oder weniger gross. Deshalb ist es wichtig beurteilen zu können, welche der o.g. Bedingungen beim Vortrieb zu erwarten sind. Im Forschungsprojekt konnte gezeigt werden, dass die Bedingungen im Bereich der Ortsbrust anhand eines einzigen Parameters (einer dimensionslosen Vortriebsgeschwindigkeit) charakterisiert werden können. Liegt dieser Parameter innerhalb eines gewissen Bereichs, so sind aufwändige und anspruchsvolle transiente numerische Berechnungen für die Setzungsabschätzung unabdingbar. Anhand einer umfangreichen Reihe solcher Berechnungen konnte jedoch eine einfache Gleichung aufgestellt werden, welche eine Abschätzung der Setzungen mit einfacheren numerischer Berechnungen erlaubt.

Forschung im Strassenwesen des UVEK: Formular 3 Seite 1 / 3

Schweizerische Eidgenossenschaft
Confédération suisse
Confederazione Svizzera
Confederaziun svizra

Eidgenössisches Departement für
Umwelt, Verkehr, Energie und Kommunikation UVEK
Bundesamt für Strassen ASTRA

Zielerreichung:

Die Projektziele wurden erreicht indem basierend auf vertieften theoretischen und experimentellen Untersuchungen einfach anwendbare Methoden zur Abschätzung der Standzeit der Ortsbrust und der vortriebsbegleitenden Oberflächensetzungen in wasserführenden Lockergesteinen mittlerer Durchlässigkeit ausgearbeitet wurden.

Folgerungen und Empfehlungen:

Bei oberflächennahen Tunneln im Lockergestein (c' < 30 kPa, E < 50 MPa) mittlerer Durchlässigkeit (k = 10exp-6 bis 10exp-8 m/s) beträgt die Standzeit zwischen 0 und einigen Tagen. Je höher die Scherfestigkeit des Baugrunds, je grösser die Überlagerung, je höher die horizontalen, effektiven Primärspannungen, je niedriger die Durchlässigkeit und die Steifigkeit des Baugrunds und je höher der Stützdruck der Ortsbrust desto höher ist ihre Standzeit. Sie kann anhand der im vorliegenden Bericht dargestellten dimensionslosen Bemessungsdiagramme abgeschätzt werden. Diese können auch zur Beurteilung der Stabilität der Ortsbrust während eines laufenden Vortriebs in Abhängigkeit der Vortriebsgeschwindigkeit herangezogen werden.
In Lockergesteinen mittlerer Durchlässigkeit hängen auch die Setzungen in der Umgebung der Tunnelortsbrust von der Vortriebsgeschwindigkeit und der Gebirgsdurchlässigkeit ab. Die im Bericht vorgeschlagene Gleichung erlaubt eine Setzungsabschätzung anhand der Ergebnisse relativ einfacher Berechnungen für die Grenzfälle eines hochdurchlässigen oder eines praktisch undurchlässigen Baugrunds, d.h. ohne Rückgriff auf anspruchsvolle transiente numerische Analysen.

Publikationen:

- Schuerch, R., Anagnostou, G. (2012). Tunnel face stability under transient conditions: stand-up time in low permeability ground. In: Proceedings of the 22nd European Young Geotechnical Engineers Conference, Gothenburg.
- Schuerch, R., Anagnostou, G. (2013a). Analysis of the stand-up time of the tunnel face. In Proc. ITA-AITES World Tunnel Congress, WTC, 2013, Geneva.
- Schuerch, R., Anagnostou, G. (2013b). The influence of the shear strength of the ground on the stand-up time of the tunnel face. In: Proc. TU-Seoul 2013 International Symposium on Tunnelling and Underground Space Construction for Sustainable Development, Seoul.
- Schuerch, R., Anagnostou, G. (2015a). Delayed failure identification by coupled hydraulic-mechanical numerical analyses. In: Proc. 14th IACMAG, 1061–1066, Kyoto.
- Schuerch, R., Anagnostou, G. (2015b). Failure propagation and mesh-dependency in coupled hydraulic-mechanical transient problems. In: Proc. 14th IACMAG, 329–334, Kyoto.
- Schuerch, R., Poggiati, R., Anagnostou, G. (2016). Design diagrams for estimating tunnel face stand-up time in water-bearing ground. In: Proc. WTC, 2016, San Francisco.
- Schuerch, R. (2016). On the delayed failure of geotechnical structures in low permeability ground. Ph.D Thesis Nr. 23681, ETH Zurich.

Der Projektleiter/die Projektleiterin:

Name: Anagnostou Vorname: Georgios

Amt, Firma, Institut: Institut für Geotechnik, ETH Zürich

Unterschrift des Projektleiters/der Projektleiterin:

Forschung im Strassenwesen des UVEK: Formular 3 Seite 2 / 3

Schweizerische Eidgenossenschaft
Confédération suisse
Confederazione Svizzera
Confederaziun svizra

Eidgenössisches Departement für
Umwelt, Verkehr, Energie und Kommunikation UVEK
Bundesamt für Strassen ASTRA

FORSCHUNG IM STRASSENWESEN DES UVEK

Formular Nr. 3: Projektabschluss

Beurteilung der Begleitkommission:

Beurteilung:

Die Forschungsarbeit bearbeitet das bautechnisch relevante Thema der Ortsbruststabilität von oberflächennahen Tunnels in wassergesättigten Böden. Instabilitäten in der Ortsbrust können zu Setzungen oder sogar Tagbrüchen führen. Die theoretischen Kenntnisse der dynamischen Effekte in sehr durchlässigen resp undurchlässigen Böden sind recht gut bekannt, doch für die in der Schweiz oft angetroffenen Böden, die dazwischen liegen, fehlten die entsprechenden Analysen. Die Forschungsarbeit hatte zum Ziel, diese Lücke zu schliessen.

Umsetzung:

Die Umsetzung erwies sich als wesentlich schwieriger. Insbesondere zur Modellierung des verzögerten Bruches verlangte nach sehr vertieften Analysen der nummerischen Modellbildung, die anschliessend durch umfangreiche physikalische Versuche zu verifizieren waren. Es mussten damit grundlegende Kenntnisse erarbeitet werden, die es aber anschliessend erlaubten, vereinfachte und daher praxistaugliche Modellparameter zu definieren, so dass die Problemstellung ohne vertiefte theoretische Kenntnisse ingenieurtechnisch bearbeitet werden kann.

weitergehender Forschungsbedarf:

Die Forschungsarbeit zeigt keinen unmittelbaren weitergehenden Forschungsbedarf auf.

Einfluss auf Normenwerk:

Die Forschungsarbeit hat keinen Einfluss auf Normen.

Der Präsident/die Präsidentin der Begleitkommission:

Name: Amberg Vorname: Felix

Amt, Firma, Institut: Amberg Engineering AG

Unterschrift des Präsidenten/der Präsidentin der Begleitkommission:

Forschung im Strassenwesen des UVEK: Formular 3 Seite 3 / 3

Verzeichnis der Berichte der Forschung im Strassenwesen

Das Verzeichnis der in der letzten Zeit publizierten Schlussberichte kann unter www.astra.admin.ch (Forschung im Strassenwesen → Downloads → Formulare) heruntergeladen werden.